Seismic design and assessment of resilient post-tensioned steel frames with viscous dampers

by

Athanasios I. Dimopoulos

Thesis Submitted to the University of Warwick for the degree of Doctor of Philosophy

School of engineering, University of Warwick

June 2016

Summary

Conventional seismic-resistant structural systems are currently designed to develop a global sway plastic mechanism under strong earthquakes, which is achieved by allowing the development of controlled inelastic deformations in specific locations of main structural members such as beams, bases of columns and braces. Inelastic deformations in structural members result in damage and residual drifts, and therefore, in economic losses such as repair costs and downtime. Moreover, earthquake reconnaissance reports reveal large economic losses related to non-structural damage, e.g. failure of walls due to large storey drifts or failure of acceleration-sensitive equipment due to large peak floor accelerations. These losses highlight the need for resilient structures with the potential to remain intact after frequently occurred earthquakes and return to service within an acceptable short, if not immediate, time after strong rare earthquakes. Moreover, resilient structures should provide a very low probability of collapse (i.e. increased life safety) under very rare maximum considered earthquake.

Steel self-centering moment-resisting frames using post-tensioned beam-column connections are a promising class of resilient structures. They exhibit softening force-drift behaviour and eliminate inelastic deformations and residual drifts as the result of gap openings developed in beam-column interfaces and elastic post tensioned bars which clamp beams to columns and provide self-centering capability. Also, post tensioned connections use energy dissipation devices, which are activated when gaps open and can be easily replaced if damaged. Steel frames equipped with passive dampers are another class of resilient structures. Dampers provide supplemental damping to control drifts, and thus, provide an effective means to achieve economical designs with high performance.

The main goal of this PhD is to develop a seismic design and assessment procedure for steel self-centering moment-resisting frames (SC-MRFs) with viscous dampers within the framework of Eurocodes 3 and 8. To achieve this goal, nonlinear models of post-tensioned connections, able to capture the strength and stiffness deterioration due to local buckling, are developed. These models

enable the assessment of the seismic behaviour of SC-MRFs with viscous dampers up to collapse with the aid of nonlinear dynamic analysis. A seismic design method, which incorporates a robust way to estimate rotation demands in post-tensioned connections, is then formulated. Different SC-MRFs with viscous dampers are designed using the proposed design procedure to study different design scenarios. The accuracy of the design procedure is evaluated through nonlinear dynamic analysis. In addition, the superior collapse resistance of SC-MRFs with viscous dampers is validated through incremental dynamic analysis. The thesis concludes with the implementation of an advanced probabilistic framework for direct economic seismic loss estimation and its application to confirm the potential of SC-MRFs with viscous dampers to significantly reduce economic seismic losses.

Table of Contents

List of Tables

List of figures

Abbreviations and Symbols

Abbreviation	Definition
BFFD	Bottom flange friction device
BRED	Buckling-restrained energy dissipator
CBF	concentric-braced frame
CFT	Concrete filled tube
CSED	Cross shaped energy dissipator
CP	Collapse prevention
CT	Contact springs
DS	Damage state
DM	Damage measure
DV	Decision variable
DBE	Design basis earthquake
EBF	Eccentric-braced frames
EDP	Engineering demand parameter
ED	Energy dissipation device
FD	Web friction device
FED	Friction energy dissipation device
FEM	Finite element model
FOE	Frequently occurred earthquake
FR	Friction springs
FR-MRF	Special MRF with welded connections

IDA	Incremental dynamic analysis
IM	Intensity measure
IO	Immediate occupancy
MAF	Mean annual frequency
MCE	Maximum considered earthquake
MDOF	Multi degree of freedom systems
MRF	Moment resisting frame
PBEE-2	2nd generation performance based earthquake engineering
PFA	Peak floor accelerations
PFDC	Post-tensioned friction damped connection
PFDC-MRF	SC-MRF using PFDC
PT	Post-tensioned
RFP	Reduced flange plate
SCFR	Self centering friction damped steel frame
SC-MRF	Self-centering moment resisting frame
SDOF	Single degree of freedom system
WHP	Web hourglass shape steel pin
WMRF	Welded moment resisting frame

Symbol	Definition
A_{PT}	Truss element cross-section area simulating PT bars
A_{rp}	Reinforcing plate area
B	Damping reduction factor (Whittaker et al 2003)
b_f	Width of the beam flange
C_1	Columns comprising steel WMRFs
C_F	Compressive force in the beam-column interface of a PT connection
c_j	Damper constant
d_{1l}	Distances of the lower WHP from the center of rotation in a PT connection
d_{1u}	Distance of the upper WHP from the center of rotation in a PT connection
d_2	Distance of the PT bars from the center of rotation
D_e	Equivalent external diameter of half a WHP
D_i	Diameter at the mid-length of half a WHP
d_{PT}	PT bar diameter
E	Modulus of elasticity
E_{comp}	Compression stiffness
E_{PT}	PT bars elastic modulus
E_{WHP}	Young's modulus of WHP material
F_a	Yield force of a damper (slip force or a friction

	damper)
F_b	PT connection beam axial compressive force after gap opening
F_{Dj}	Slab inertia forces
f_j	Cosine of the angle of the damper centerline to the horizontal
f_u	Ultimate strength
$F_{WHP,l}$	Force in the lower WHP
$F_{WHP,u}$	Force in the upper WHP
$F_{WHP,y}$	Yielding force of one WHP
$F_{x,des}$	Equivalent lateral forces at each floor
f_y	Yielding strength
$f_{y,PT}$	Yielding strength of PT bars material
$f_{y,rp}$	Yielding strength of the reinforcing plate material
$F_{y,WHP}$	Yield force of a WHP
$f_{y,WHP}$	Yielding strength of WHP material
G	shear modulus
$G(DM\|EDP)$	Probability of exceedance a value of DM given an EDP
$G(dv\|DM)$	Probability of exceedance a value of DV given a DM
$G(EDP\|IM)$	Probability of exceedance a value of EDP given an IM
G_1	Beams comprising steel WMRFs

G_{WHP}	Shear modulus of WHP material
K_b	Beams axial stiffness
K_{fe}	Elastic stiffness of a WHP
K_{fp}	Post-yield stiffness of a WHP
$K_{f\Delta}$	Initial elastic frame stiffness
K_j	Horizontal storey stiffness of a SC-MRF
K_{PT}	PT bars axial stiffness
L_{PT}	Total length of PT bars
L_{rp}	Reinforcing plate length
L_{WHP}	Clear length of the bending parts of half a WHP
M	Moment of a PT connection
M_a	Moment of a PT connection at yielding of the FED
M_b	PT connection beam bending moment after gap opening
M_{cap}	Beam's capping moment strength
M_c	Moment in column
M_d	Decompression moment of a PT connection
M_{DBE}	Moment under the DBE
M_{des}	Beams moment at the columns face under the design response spectrum
M_{FR}	PT connection moment contribution from friction devices
M_{Gap}	PT connection gap opening moment

M_{IGO}	PT connection moment when the upper WHPs yield
m_j	Storey mass
M_N	Moment contribution of a PT connection from N
$M_{p,n}$	Nominal beam plastic moment capacity
M_{pl}	Plastic moment resistance of a WHP
$M_{pl,b}$	plastic moment resistance of a beam
$M_{pl,WHP}$	Plastic moment resistance of a WHP cross-section,
M_r	Residual moment
M_{SC}	Beam moment at the maximum drift where self-centering is provided
M_{WHP}	Moment contribution of a PT connection from WHPs
M_y	Effective yield moment
N	Horizontal clamping force transferred to the beam-column interface of a PT connection
N_c	total building replacement cost values
N_{dem}	Number of cost values representing the total building replacement cost because of demolition
N_{rec}	Number of ground motions used to conduct the IDA
n_{WHP}	number of upper and lower WHPs
P	Column cross section axial force
$P(D\|\theta_{s,res})$	Probability of demolition given no collapse

P_y	Column cross section yielding axial force
P-Δ	Second-order effects
q	Force reduction factor
r	Radius of round-shaped part of WHP
S	Rotational stiffness of a PT connection
$S_a(5\%)$	Design response spectrum for 5% damping
$S_a(T_1)$	Spectral acceleration at T_1
$S_{a,MCE}$	Spectral acceleration at T_1 under the MCE
S_F	Additional rotational stiffness of the frame due to the columns restraint that opposes gap opening
S_N	Rotational stiffness of a PT connection from N
S_{WHP}	Rotational stiffness of a PT connection from WHPs
T	Total force in both PT bars;
T_0	Initial PT force
T_1	Fundamental period of vibration
t_f	Thickness of the beam flange
T_y	Yielding force of PT bars,
V	base shear
v	Reduction factor
V/W	Base shear coefficient
V_{C1l}	Shear force in lower column of a PT connection
V_{C1u}	Shear force in upper column of a PT connection

V_{DBE}	Base shear under the DBE
V_{des}	Design base shear
V_{MCE}	Base shear under the MCE
V_{pl}	Plastic shear resistance of a WHP
V_{WHP}	Yield strength of half a WHP
W	Seismic weight
α	Velocity exponent of nonlinear viscous damper
α_p	Post yield stiffness ratio of a PT connection
α_{vd}	Non-linear viscous damping constant
α_α	factor to determine the required connection moment at yield of the FED
β	Energy dissipation factor
γ	Parameter for the combined isotropic-kinematic hardening law
γ_{PT}	Safety factor against PT bars yielding
$\Delta_{el\text{-}des}$	Elastic displacement under the design response spectrum
$\Delta G(DS\|EDP_k)$	Probability of a structure's component to experience damage equal to that associated with a DS
Δ_{gap}	PT connection gap opening
$\Delta_{roof,\ DBE}$	Roof displacement under the DBE
$\Delta_{roof,MCE}$	Roof displacement under the MCE
ε	Constant used for sizing of viscous dampers to satisfy a simple stiffness proportional distribution

	i.e. $c_j=\varepsilon K_j$
ε_c	Maximum compressive strain in the beam flange of a PT connection, at the end of the reinforcing plate
ε_y	Steel yield strain
η	Damping reduction factor (Eurocode 8 2013)
θ	PT connection relative rotation
θ_2	PT connection relative rotation when the upper WHPs yield
θ_3	PT connection relative rotation when the lower WHPs yield
θ_{DBE}	Relative rotation under the DBE
θ_{MCE}	Relative rotation under the MCE
θ_p	pre-capping plastic rotation for monotonic loading;
θ_{pc}	post-capping plastic rotation
θ_r	Roof drift
θ_s	Interstorey drift
$\theta_{s,DBE}$	Interstorey drift under the DBE
$\theta_{s,e}$	Elastic interstorey drift
$\theta_{s,max}$	Maximum interstorey drift
$\theta_{s,MCE}$	Interstorey drift under the MCE
$\theta_{s,res}$	Maximum residual storey drift
$\theta_{s,SC}$	The maximum interstorey drift where self-

	centering is provided
$\theta_{s,y,MRF}$	Elastic interstorey drift of a corresponding MRF
θ_{SC}	Desired relative rotation up to which, a PT connection provides self-centering behaviour
$\theta_{s\text{-}max}$	Maximum interstorey drifts
$\theta_{s\text{-}res}$	Maximum residual interstorey drift
θ_u	Ultimate rotation capacity
θ_y	Yielding rotation
$\lambda(IM)$	MAF of exceedance of an IM value
$\lambda_{DV}(DV \geq dv)$	MAF of exceeding a value of DV
μ	Statistical mean
ξ_s	Supplemental damping ratio
ξ_t	Total damping ratio
σ	Statistical standard deviation
φ_j	Modal coordinate of the first mode shape
Ω_{DBE}	Over strength factor under the DBE
Ω_{MCE}	Over strength factor under the MCE

Acknowledgements

This PhD thesis is the outcome of hard personal work during the last four years. The completion of this thesis wouldn't be possible without the support of many people to whom I feel the need to express my gratitude. I am really grateful to my PhD supervisor, Professor Theodore Karavasilis, for his endless support at both scientific and personal level. I express also my sincere thanks to Dr Vamvatsikos, Dr Vasdravellis, and Dr Tzimas for their valuable and fruitful scientific collaboration. The School of Engineering of the University of Warwick kindly provided the financial support to carry out my PhD research. I am grateful for that support. Finally, I would like to express my gratitude to my friends, my parents and my sister for their encouragement and personal support throughout these years.

Declaration

This thesis is submitted to the University of Warwick in support of my application for the degree of Doctor of Philosophy. It has been composed by myself and has not been submitted in any previous application for any degree.

The work presented was carried out by the author.

Parts of this thesis have been published in the following international journals:

Dimopoulos AI, Karavasilis TL, Vasdravellis G, Uy B. Seismic design, modelling and assessment of self-centering steel frames using post-tensioned connections with web hourglass shape pins. *Bulletin of Earthquake Engineering* 2013; 11:1797–1816.

Tzimas AS, Dimopoulos AI, Karavasilis TL. EC8-based seismic design and assessment of self-centering post-tensioned steel frames with viscous dampers. *Journal of Constructional Steel Research* 2015; 105:60-73.

Dimopoulos AI, Tzimas AS, Karavasilis TL, and Vamvatsikos D. Probabilistic economic seismic loss estimation in steel buildings using post-tensioned moment resisting frames and viscous dampers. *Earthquake engineering and structural dynamics* 2016; DOI: 10.1002/eqe.2722.

1 Introduction

1.1 Conventional seismic-resistant steel structural systems

Steel structures are a suitable construction solution in areas of high seismicity. The reason is the very good material properties of steel (strength and ductility) and that the industrial production of steel shapes guarantees high quality assurance. The most commonly used seismic resistant steel frames for multi-story buildings are classified as steel moment resisting frames (MRFs), concentric-braced frames (CBFs), and eccentric-braced frames (EBFs). Figures 1.1-1.3 show examples of structures designed using the aforementioned steel frames.

Figure 1.1 Building with MRFs (All structure engineering LLC webpage)

Figure 1.2 Building with EBFs (Ogren engineering Web page)

Figure 1.3 Building with CBFs (Ogren engineering web page)

According to the current seismic design practice, which in Europe is based on EC8 (Eurocode 8 2013), structures can be designed to develop non-dissipative or dissipative behaviour. The design of structures to respond elastically is limited into structures of special use, or areas of low seismicity. In all other cases structures are designed to have dissipative behaviour, where significant inelastic deformations are developed during high severity seismic events.

The design for dissipative behaviour of regular structures is usually performed by assigning a structural behaviour factor (i.e. force reduction or modification factor)

which is used to reduce the code-specified forces resulting from idealised elastic response spectra. This is carried out in conjunction with the capacity design concept which requires an appropriate determination of the capacity of the structure based on a pre-defined plastic mechanism (often referred to as failure mode), coupled with the provision of sufficient ductility in plastic zones and adequate over-strength factors for other regions. Figure 1.4 shows the elastic and the design response spectra, using a behaviour factor "*q*" equal to 3 in soil type B according to EC8 (Eurocode 8 2013). Figure 1.5 shows the predefined plastic mechanism of steel MRFs, with plastic hinges developed at the end of beams and at the columns bases according to EC8 (Eurocode 8 2013).

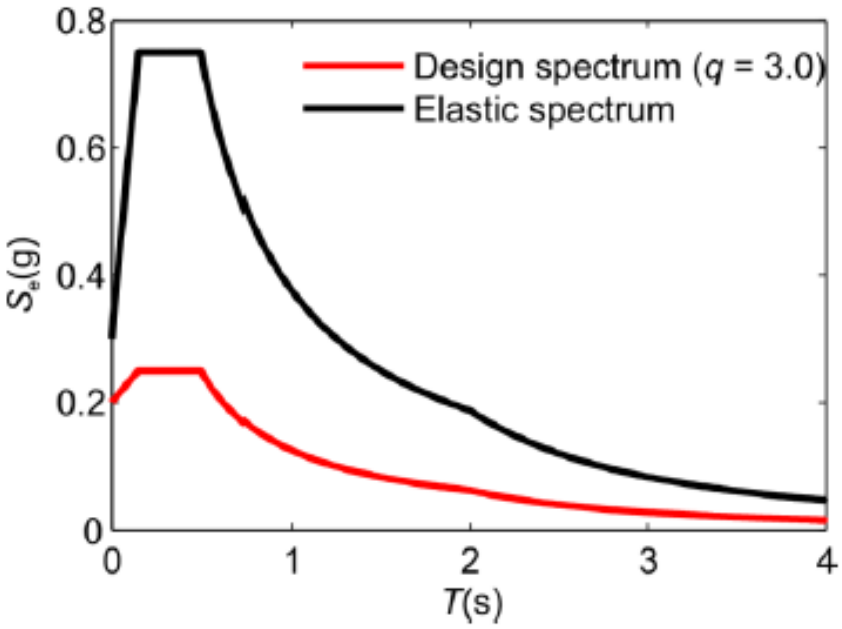

Figure 1.4 Elastic and design response spectra (Eurocode 8 2013)

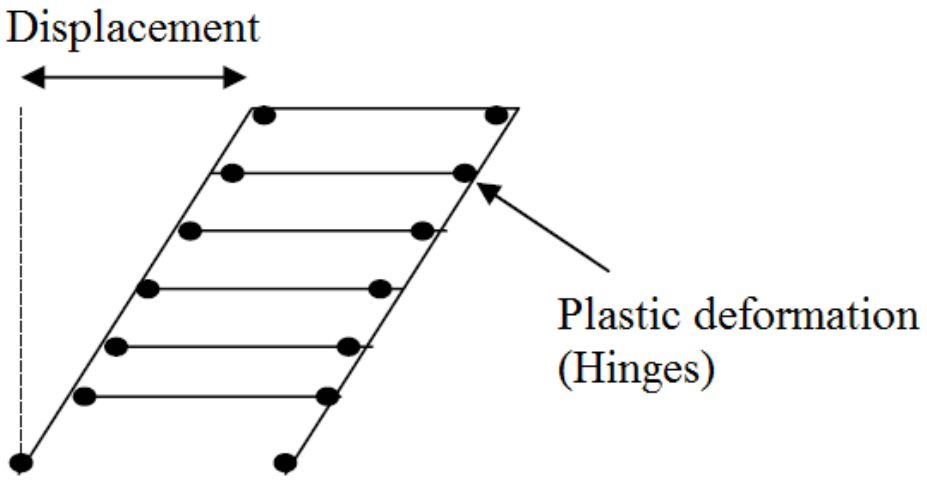

Figure 1.5 Collapse plastic mechanism of a steel MRF designed according to modern seismic codes (Eurocode 8 2013)

1.2 Need for resilient structures

The ideal earthquake resistant structure must be able to develop inelastic deformations during an earthquake while sustaining its integrity (Christopoulos and Filiatrault 2002a,b). This way the disadvantages of buildings withstanding earthquakes elastically can be avoided and residual drifts are eliminated. Structures that respond elastically during earthquakes develop high floor accelerations resulting in non-structural elements and contents damage, and so cost associated with loss of business operation and repair of damage. On the other hand, excessive residual drifts can result in the total loss of a structure if second order effects induced by gravity loads bring the system near collapse (Christopoulos et al 2003). Also, non-structural systems start to lose functionality under certain values of residual drifts (McCormick et al 2008) and there is a probability of buildings to be demolished because of residual (permanent) drifts.

The design of conventional earthquake resistant systems is intended to ensure serviceability under a frequent earthquake and life safety level while avoiding catastrophic failures under a severe earthquake. If the structure does not collapse under a design basis earthquake (DBE; 475 years return period) (FEMA-368 2000a) and the occupants can evacuate it safely, this structure fulfils its function even if it will be never functional again. The socio-economic needs in modern societies have

pushed the barrier of seismic design of buildings considerably higher. In particular, important structures such as hospitals and major bridges must be designed to achieve higher performance levels under severe earthquakes (Christopoulos and Filiatrault 2006).

Previous studies on seismic design and evaluation of conventional seismic-resistant systems, such as steel MRFs (Sanchez and Plumier 2008, Elghazouli 2012, Tzimas et al 2013), showed that these systems experience significant inelastic deformations in structural members under the DBE (Eurocode 8 2013). Inelastic deformations result in structural damage and residual drifts, and therefore, in economic losses such as repair costs and downtime. Moreover, earthquake reconnaissance reports reveal large economic losses related to non-structural damage, e.g. failure of walls due to large story drifts (Dolce and Manfredi 2009, FEMA-P695 2008).

The cost of a new structure designed to meet higher performance levels is weighted against the estimated losses associated with damage, loss of property and downtime in the event of a severe earthquake. So, the need for resilient structures with the inherent potential to minimize structural and non-structural damage is highlighted. By resilient structures we mean that these structures result in lower damage of the structural elements. Structural damage can be isolated in elements that can be easily removed after a strong earthquake, and so repair cost and downtime is minimised. Also the change of use for the structural elements can be easily carried out since they are damage free. Such structures should remain intact under the frequently occurred earthquake (FOE; return period of 95 years) (FEMA-368 2000a) and return to service within an acceptable short, if not immediate, time after the DBE. A resilient structure should also provide a low probability of collapse under the maximum considered earthquake (MCE; return period of 2500 years) (FEMA-368 2000a). The ATC-63 (FEMA-P695 2008) project sets a limit on the permissible probability of collapse under the MCE equal to 10%. As this limit has been primarily set for conventional structural systems, lower probabilities of collapse should be offered by resilient structures.

Two promising classes of resilient structures are (a) steel self-centering moment resisting frames (SC-MRFs) using post-tensioned (PT) beam-column connections;

and (b) steel MRFs equipped with passive dampers. Steel SC-MRFs are discussed in section 1.3 and steel frames with passive dampers are discussed in section 1.4.

1.3 Self-centering moment resisting frames

Steel SC-MRFs experience inelastic behaviour under earthquakes, and so have limited seismic forces and floor accelerations. Moreover, SC-MRFs allow the structural system to return to or near to its original position after an earthquake, and reduce or eliminate cumulative damage to the main structural elements.

SC-MRFs use elastic pre-tensioning elements (e.g., high strength steel bars) which clamp beams to the columns. PT connections use carefully designed energy dissipation devices which are activated when gaps open and can be classified into yielding devices which dissipate energy through inelastic deformations and devices which dissipate energy through friction.

Yielding devices were proposed as (1) angles bolted on the top and bottom flanges of the beam and on the column flanges, dissipating energy through inelastic bending (Ricles et al 2001, 2002; Garlock et al 2005); (2) buckling restrained steel bars placed between the beam flanges and welded on the beam and column, dissipating energy through axial deformations (Christopoulos et al 2002a); (3) reduced flange plates welded around a square-hollow-section column and bolted on the beam flanges (Chou et al 2006); and (4) reduced-section or cross-shaped steel plates placed below the bottom flange of the beam (Chou and Lai 2009). Friction-based devices were proposed as friction bolted surfaces placed on the top and bottom flanges of the beam (Rojas et al 2005; Kim and Christopoulos 2008; Kim and Christopoulos 2009a,b), on the web of the beam (Tsai et al 2008) or on the bottom flange of the beam (Wolski et al 2009).

A new steel PT connection using web hourglass shape steel pins (WHPs) has been recently developed, modelled in ABAQUS and experimentally validated (Vasdravellis et al 2013a,b). The connection isolates inelastic deformations in WHPs, avoids damage in other connection parts as well as in beams and columns, and, eliminates residual drifts. WHPs do not interfere with the composite slab and

are very easy-to-replace without bolting or welding, and so, the connection enables non-disruptive repair and rapid return to building occupancy in the aftermath of a strong earthquake. Figure 1.6 shows a SC-MRF using PT connections with WHPs, and Figure 1.7 shows an exterior PT connection with WHPs. Two high strength steel bars located at the mid depth of the beam, one at each side of the beam web, pass through holes drilled on the column flanges. The bars are post-tensioned and anchored to the exterior columns. WHPs are inserted in aligned holes on the beam web and on supporting plates welded to the column flanges. Energy is dissipated through inelastic bending of the WHPs that have an optimized hourglass shape (Figure 1.8) with enhanced fracture capacity (Vasdravellis et al 2015)

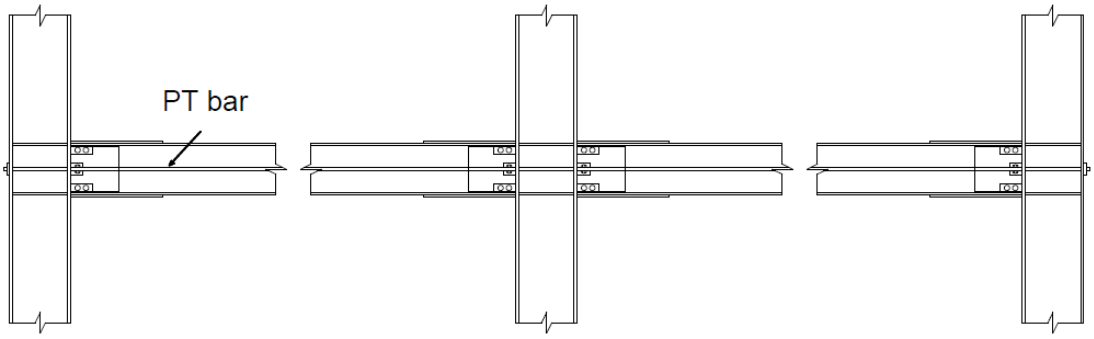

Figure 1.6 SC-MRF

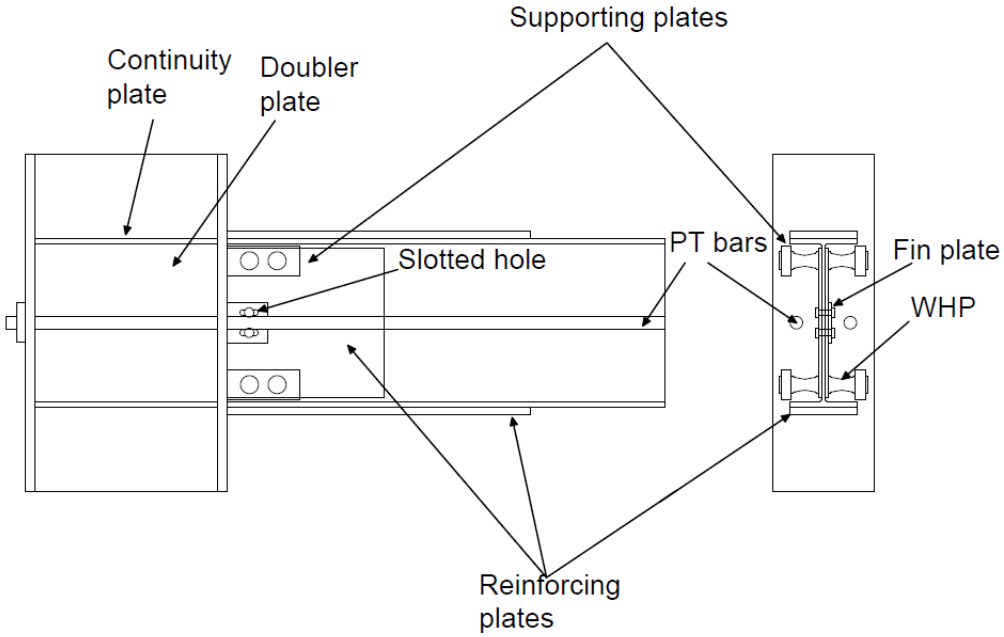

Figure 1.7 Exterior PT connection with WHPs

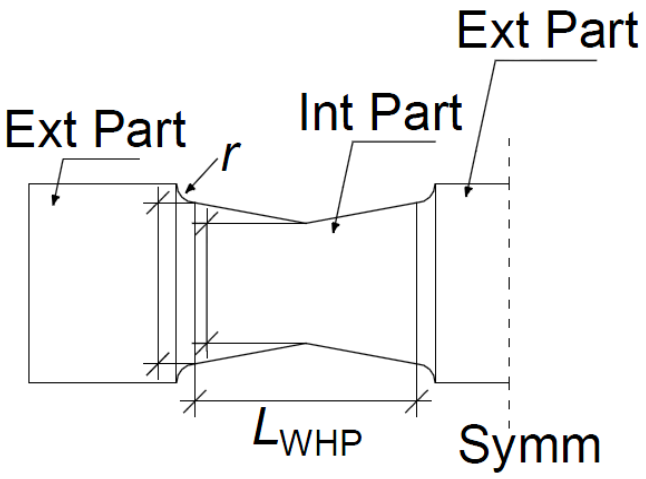

Figure 1.8 Half WHP geometry

1.4 Steel frames with passive dampers

The development of supplemental damping has been attributed to the pioneering work of (Housner 1956) who laid out the foundations for the seismic design of structures based on energy concepts. The use of separate elements in order to increase the damping in a structure was firstly developed by Muto 1969, Kelly et al 1972, Skinner et al 1975. A variety of supplemental dampers has been used in hundreds of buildings around the world in the last twenty years. Passive dampers are types of supplemental dampers which dissipate a part of the energy induced in a structure during an earthquake without using power supplies, actuators or computers. So, instead of using external power sources, passive dampers are activated by the structural system movements. Passive dampers include metallic dampers, friction dampers, visco-elastic dampers, and viscous dampers.

Metallic and friction dampers (Tyler 1977, Pall 1980) are displacement activated, so they dissipate energy through the relative displacements that occur between their connected points. The maximum forces developed in these dampers occur simultaneously with the structure's maximum internal forces during an earthquake.

Metallic and friction dampers exhibit hysteretic behaviour that can be simulated by an elastic-perfectly plastic load displacement as shown in Figure 1.9. For metallic damper, the force F_a corresponds to the yield force of the damper. For a friction damper, the force F_a corresponds to the slip force, also the elastic stiffness of a friction damper is very steep and its behaviour is associated with a rigid-perfectly plastic response.

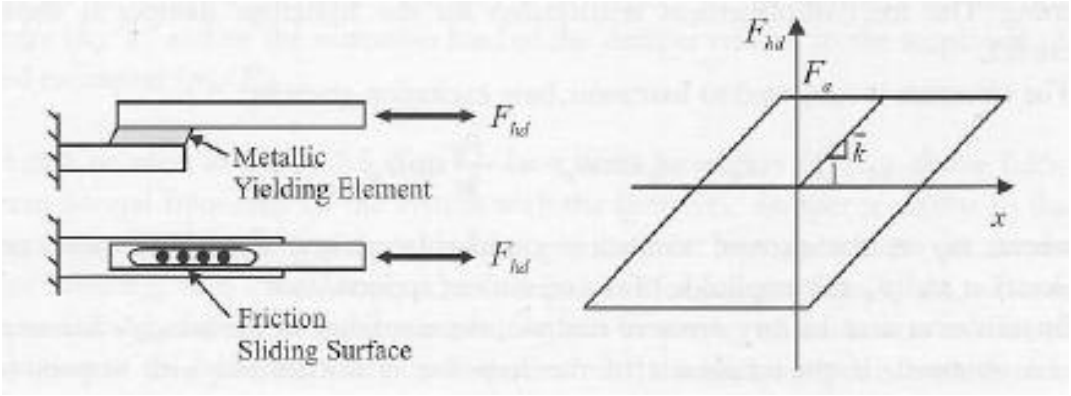

Figure 1.9 Idealized Load-Displacement relationship for metallic and friction dampers (Christopoulos and Filiatrault 2006)

Viscous dampers (Constantinou and Symans 1992) are velocity activated, so they dissipate energy through the relative velocities that occur between their connected points. The maximum forces developed in these dampers do not occur simultaneously with the maximum drifts that a structure experiences during an earthquake. There are two types of viscous dampers, i.e. linear viscous dampers and non-linear viscous dampers. Figure 1.10 shows the hysteretic behaviour and the force-velocity behaviour of a linear viscous damper, while figure 1.11 shows the hysteretic behaviour and the force-velocity behaviour of a non-linear viscous damper. The effect of velocity, expressed by the non-linear viscous damping constant (α_{vd}), increases the energy dissipation and more details can be found in (Christopoulos and Filiatrault 2006).

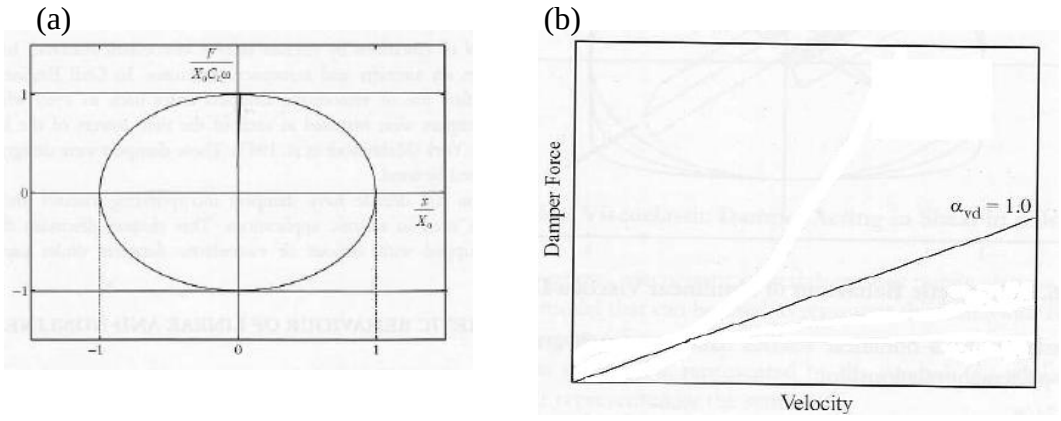

Figure 1.10 (a) Hysteretic behaviour; (b) force-velocity behaviour of linear viscous damper; (Christopoulos and Filiatrault 2006)

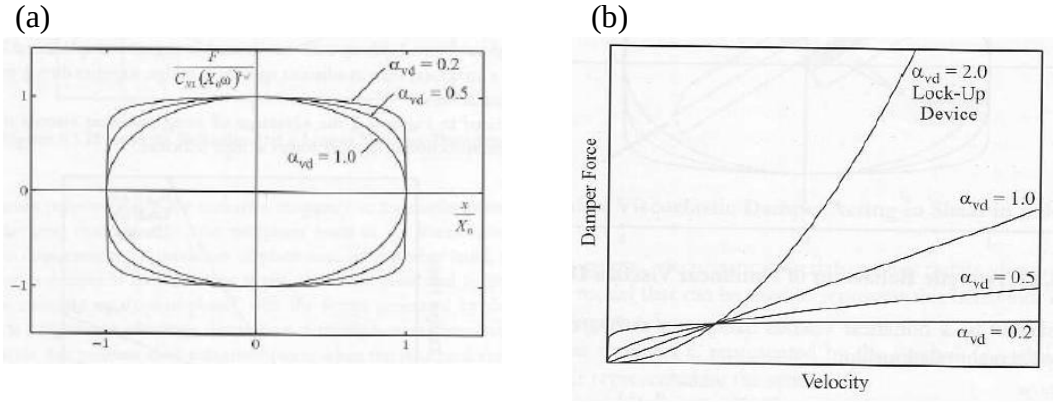

Figure 1.11 (a) Hysteretic behaviour; (b) force velocity behaviour of non-linear viscous damper (Christopoulos and Filiatrault 2006)

Visco-elastic dampers provide both velocity and displacement dependent forces. Figure 1.12 shows the configuration of a visco-elastic damper, which dissipates energy by the shear deformation of the visco-elastic material. Figure 1.13 shows the hysteretic behaviour of a visco-elastic damper, which depends both on deformation and velocity.

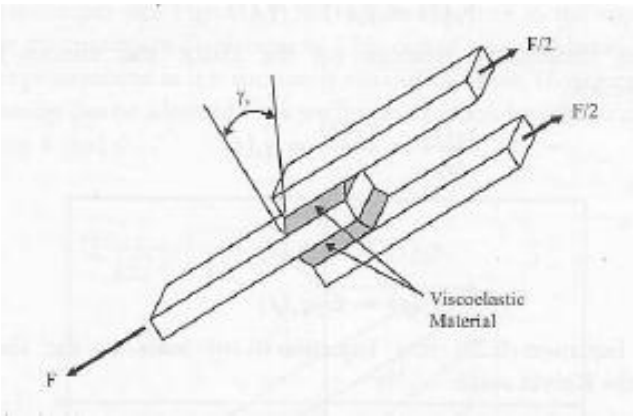

Figure 1.12 Typical visco-elastic damper acting in shear in a bracing member (Christopoulos and Filiatrault 2006)

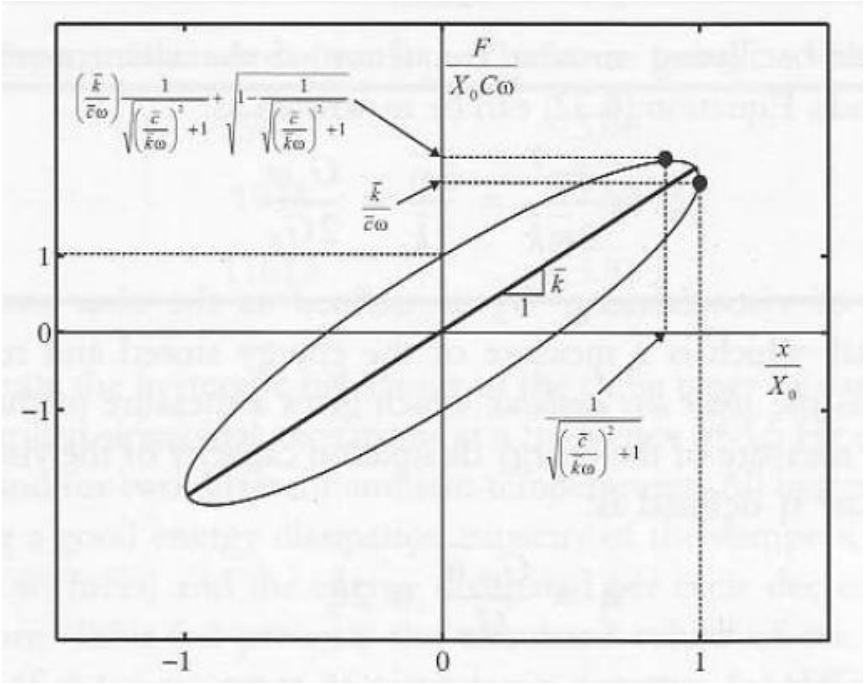

Figure 1.13 Hysteretic behaviour of a visco-elastic damper (Christopoulos and Filiatrault 2006)

Previous analytical and experimental research showed that steel MRFs with visco-elastic dampers can be designed to be lighter and perform better than conventional steel MRFs under the DBE (Karavasilis et al 2011, Karavasilis et al 2012). However, it was shown that it is generally not feasible to design steel MRFs with passive dampers at a practical size to eliminate inelastic deformations in main structural members under the DBE (Karavasilis et al 2011, Karavasilis et al 2012). To address this issue, a seismic design strategy for steel MRFs, which isolates damage in

removable steel energy dissipation devices and uses in parallel viscous dampers to reduce drifts, has been proposed (Karavasilis et al 2012). A study shows that supplemental viscous damping does not always ensure adequate reduction of residual drifts (Karavasilis and Seo 2011). A recent work evaluates the seismic collapse resistance of steel MRFs with viscous dampers and shows that supplemental viscous damping does not always guarantee a better seismic collapse resistance when the strength of the steel MRF with dampers is lower or equal to 75% of the strength of a conventional steel MRF (Seo et al 2014).

1.5 Combined systems

The use of viscous dampers in parallel to self-centering precast concrete base rocking walls has been proposed as an effective way to control peak story drifts and residual drifts (Kurama 2000). The parallel combination of hysteretic and viscous energy dissipation along with a friction slip mechanism in series connected to the viscous energy dissipation mechanism were found to achieve high levels of seismic performance for self-centering systems (Kam et al 2010). A displacement-based seismic design procedure for self-centering frames using combinations of energy dissipation mechanisms has been proposed and evaluated in (Kam et al 2008).

A seismic design procedure of steel SC-MRFs and viscous dampers within the framework of Eurocode 8 (EC8) is presented in Tzimas et al (2015). In this work performance levels are defined with respect to drifts, residual drifts, and limit states in the PT connections. Several design scenarios are implemented in a prototype building combining SC-MRFs with or without viscous dampers. The results of this work show that SC-MRFs with viscous dampers can be designed for less steel weight (resulting in less strength) without compromising their DBE and MCE drift performance. Supplemental damping is very effective in improving the residual drift performance of SC-MRFs. Also the supplemental damping along with strict design criteria for the PT connections can significantly improve the collapse resistance of SC-MRFs. The potential of SC-MRFs with viscous dampers to reduce the economic seismic losses in steel buildings has been evaluated in (Dimopoulos et al 2016).

1.6 Summary

This chapter briefly describes conventional seismic-resistant steel frames and the existing seismic design methodology followed by EC8 (Eurocode 8 2013). The need of resilient structures, which could minimize structural and non-structural damage and the associated losses due to repair cost and downtime, is highlighted. A brief literature review of several types of resilient structural systems like SC-MRFs and passive dampers is briefly presented and several types of PT connections and passive dampers are discussed. Moreover, combined systems using self-centering frames equipped with passive dampers are also briefly discussed.

2 Literature review, research objectives and thesis structure

2.1 Introduction

In this chapter an extensive review of all the existing PT connections in literature is presented. Drawings, design procedures, numerical models, and experimental setups of existing PT connection are outlined and discussed. All the available design procedures of SC-MRFs in literature are presented and discussed. Results from numerical simulations, shaking table tests, and hybrid tests of SC-MRFs in the existing literature are presented and discussed. Also, a preliminary assessment study of SC-MRFs with PT connections and web hourglass shaped pins is presented. The research needs and objectives of this PhD thesis are provided and the PhD thesis structure is outlined.

2.2 Existing PT connections in literature

Figure 2.1 shows the PT connection proposed in the work of Ricles et al (2001). The connection uses high strength steel strands that are post-tensioned after bolted top and seat angles are installed. Contact stresses are developed at the interface between beams and columns under the action of post-tensioning force. Moment resistance is provided by the pre-stressed contact surface, and shear resistance is provided by friction at the contact surface. The PT strands run through the column and are anchored outside the connection region. Shim plates are used between the end of the beam and the column face for construction fit up, with additional steel plates used to reinforce the beam flanges.

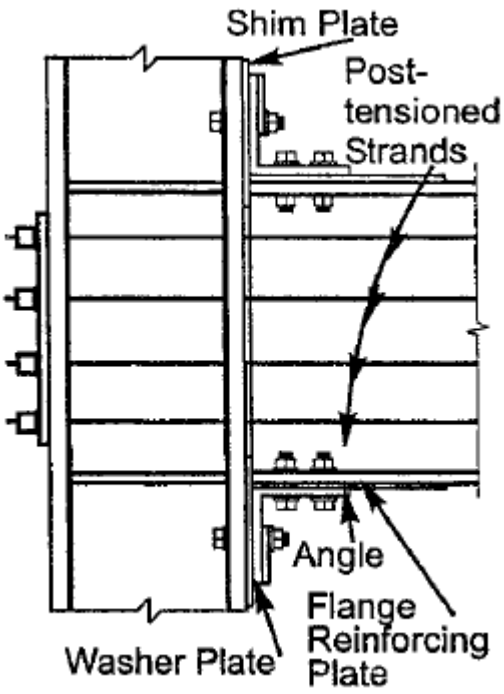

Figure 2.1 Post-tensioned connection (Ricles et al 2001)

An analytical study was undertaken to model the PT connection in the computer program DRAIN-2DX (Prakesh et al 1993). Fiber beam-column elements were used to model the beams and columns. Multi-linear stress strain behaviour is assigned on the beam and column fibers. Compression-only stress strain behaviour is assigned on the fibers of the beam end segment that models the portion of the beam initially in contact with the shim plate at the beam-column interface. Using this modelling procedure the gap-opening behaviour is simulated. Parallel springs are used to model the angles. Each PT strand is modelled using a truss element. The proposed modelling procedure has been validated against experimental cyclic tests. Figure 2.2 shows the analytical model for an interior PT connection and figure 2.3 shows the comparison between the experimental tests and analytical results.

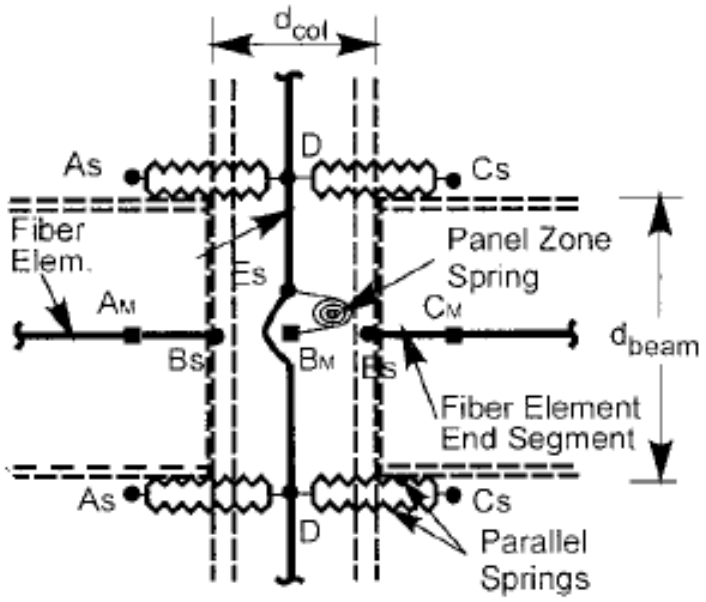

Figure 2.2 Analytical model for an interior PT connection (Ricles et al 2001)

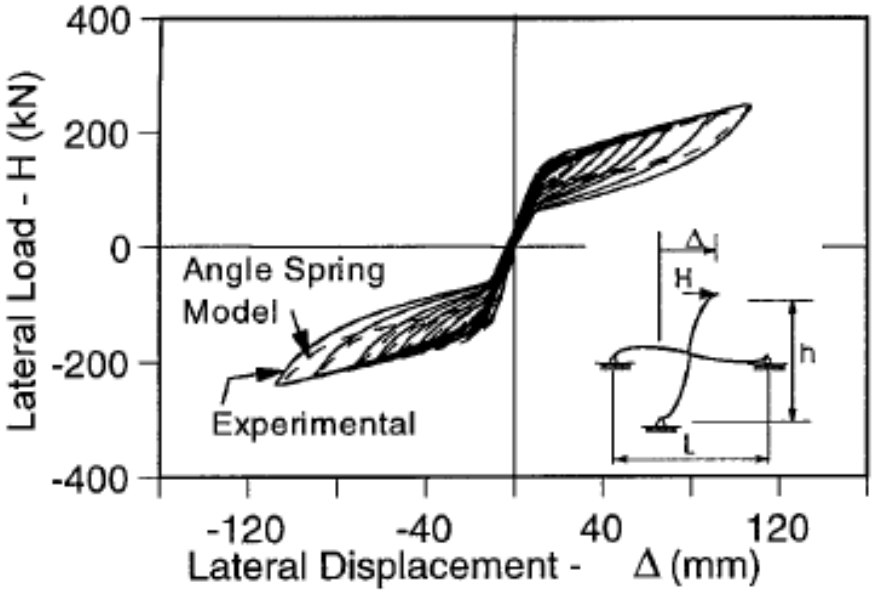

Figure 2.3 Lateral load-Displacement behavior of pot-tensioned connections (Ricles et al 2001)

Nine large-scale PT connection subassemblies were tested under inelastic cyclic loading in (Ricles et al 2002). Figure 2.4 shows the PT connection subassembly test setup. The test results demonstrated that PT connections provide excellent elastic

stiffness, strength and ductility under cyclic loading with energy dissipation occurring primarily in the angles. The study showed that the PT connection has an initial stiffness similar to that of a fully restrained welded connection, and that the PT connection is self-centering without residual deformation. Also the beams and columns remain essentially elastic while inelastic deformation is isolated to the top and seat angles.

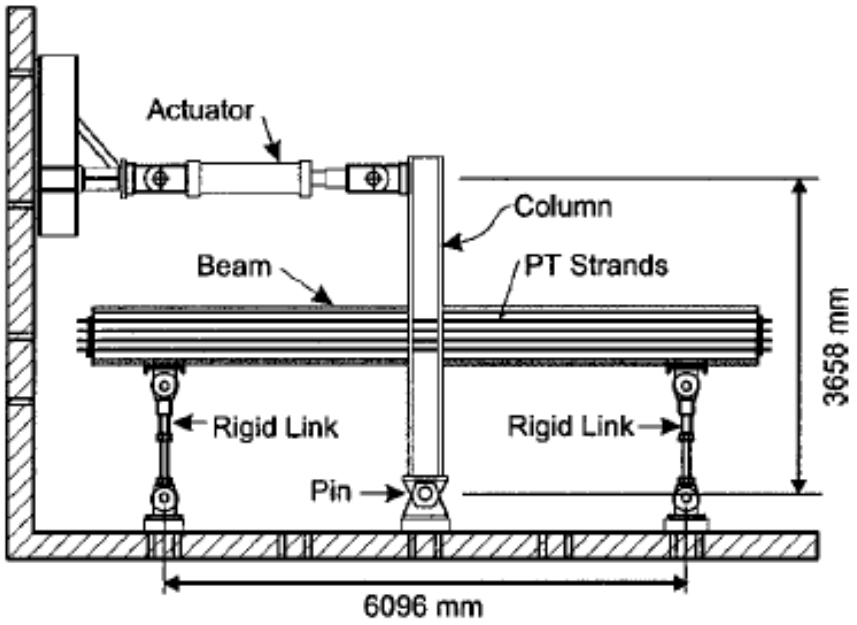

Figure 2.4 PT connection subassembly setup (Ricles et al 2002)

In the work of (Garlock et al 2005) six full-scale interior connection subassemblies of PT connections as shown in figure 1 were subjected to inelastic cyclic loading up to 4% story drift to simulate earthquake loading effects. The experimental setup is similar to that in figure 2.4. The test results show that PT connections exhibit stable self-centering hysteretic behaviour when beam local buckling and strand yielding do not occur. Beam local buckling prevents the specimen from self-centering and limits the ductility, so the connection should be designed to avoid this limit state, by using longer reinforcing plates or using smaller PT force. For the prevention of strand yielding, a larger number of strands, with a smaller initial PT force per strand is recommended.

In (Garlock et al 2005) it was found that plane sections do not remain plane along the length of the reinforcing plate, but do remain plane beyond the end of the

reinforcing plate. It was also found that when the yield strain ε_y is exceeded by two times in the beam flanges at the end of the reinforcing plate, a significant increase of plastic strain was occurred, indicating the onset of beam local buckling.

A post-tensioned friction damped connection (PFDC) for steel MRFs was developed in the work of (Rojas et al 2005). Figure 2.5 shows that PFDC has PT high strength strands running parallel to the beam and anchored outside of the connection. Figure 2.6 shows that reinforcing plates are placed on the beam flanges to limit beam compression yielding, and so to minimize structural damage. Shim plates are placed between the column flange and the beam flanges so that only the beam flanges and reinforcing plates are in contact with the column, and so protecting the beam web from yielding under bearing stress.

Figure 2.6 shows that the friction devices are located at the beam flanges. Friction devices consist of a friction plate sandwiched by two brass shim plates that are inserted between the beam flange reinforcing and outer plates. All plates are bolted to the beam flanges, and long slotted holes are drilled in the friction plate. The friction plate is attached to a tee flange that also serves as a shim plate. A shear tab is bolted to the beam web (with slotted holes) and welded to the column flange to transmit the beam gravity shear forces.

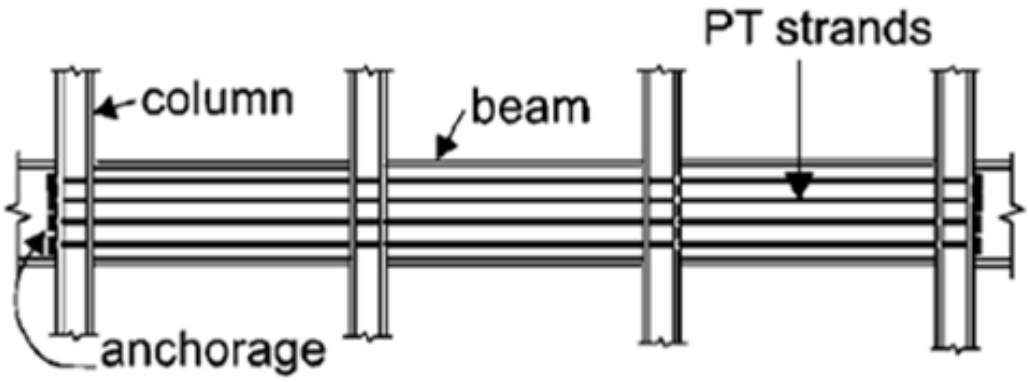

Figure 2.5 Schematic elevation of one floor of frame with PT friction damped connections (Rojas et al 2005)

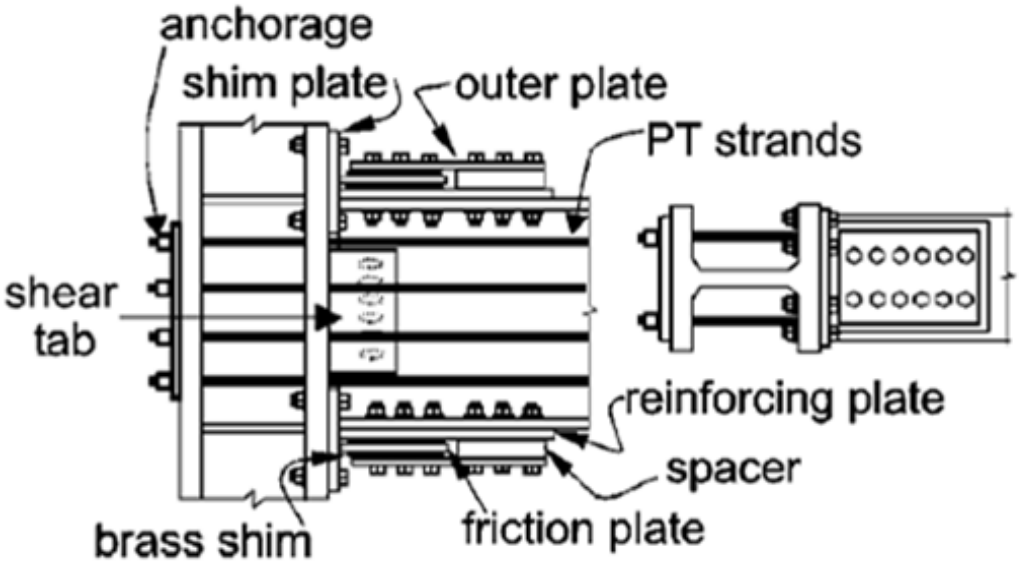

Figure 2.6 PT friction damped connection details (Rojas et al 2005)

In Rojas et al (2005), appropriate formulas for the calculation of the connection moment capacity are provided as a function of the connection relative rotations (θ). Also simplified formulas for the estimation of the relative rotation demands under the DBE and the MCE are presented. Once θ is known, the parameters needed to design the PT connections can be estimated since they are directly or indirectly related to it. A modelling procedure similar to that in (Ricles et al 2001) was also developed for the PT connections and implemented in a six storeys frame.

In the work of Christopoulos et al (2002a) a PT connection with energy dissipating devices (EDs) for steel MRFs is presented and evaluated both experimentally and analytically. High strength PT bars are used in the connections in order to provide self-centering capability and ED bars provide energy dissipation.

Figure 2.7 shows the geometric configuration of a frame incorporating the PT connection. Figure 2.8 shows the detail of an exterior beam to column PT connection. The PT force T is provided by two high strength bars located at mid-depth of the beam one on each side of the web. Four ED bars are symmetrically placed to provide energy dissipation. The ED bars are threaded into couplers which are welded to the inside face of the beam flanges and continuity plates of column. Holes are drilled on the column flange, for the PT and ED bars to pass through. ED

bars are inserted into confining steel cylinders that are welded to the beam flanges, and so are prevented from buckling in compression under cyclic loading.

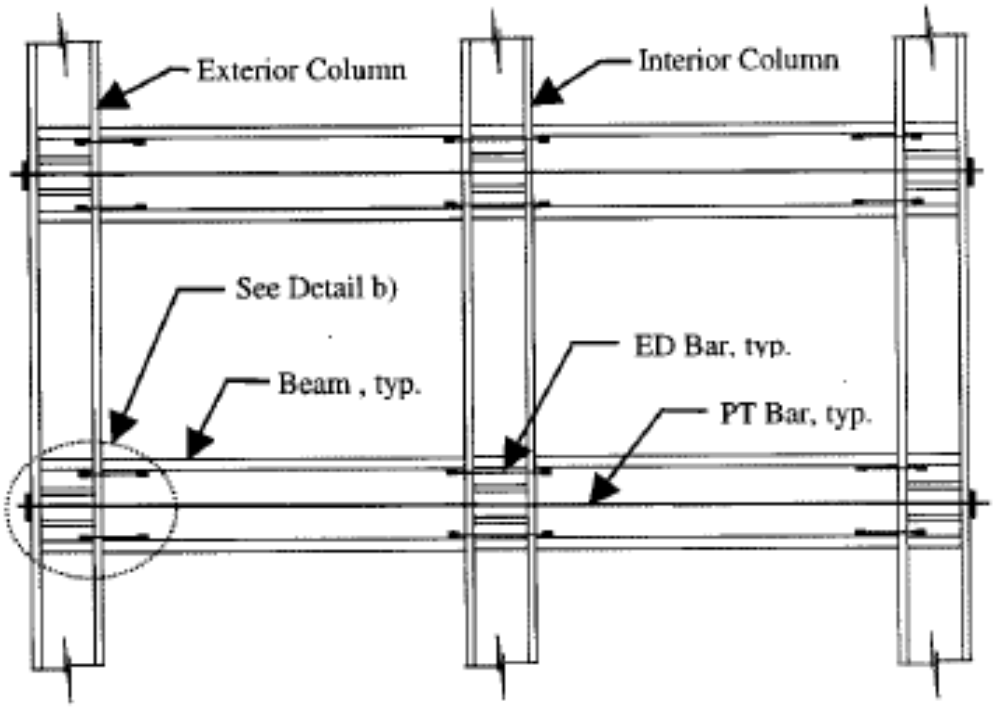

Figure 2.7 Steel frame with post-tensioned energy dissipating steel connection (Christopoulos et al 2002a)

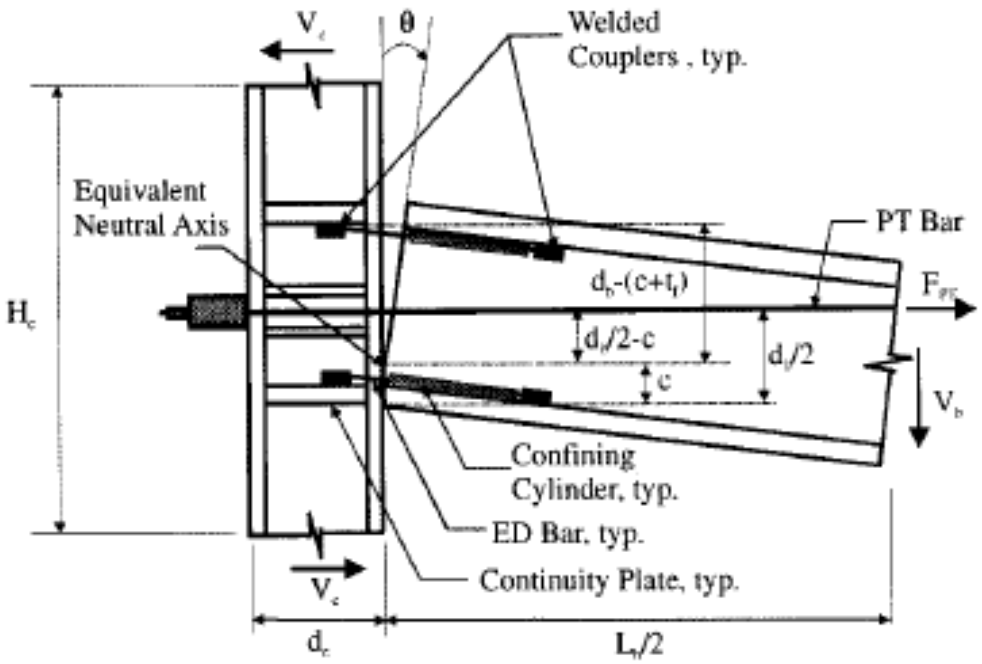

Figure 2.8 Geometric configuration and free body diagram of exterior post-tensioned energy dissipating connection (Christopoulos et al 2002a)

An analytical study was undertaken to develop the relationship between moment and rotation of the PT connection. Using this analytical study a design procedure for the PT connection was developed. According to this design procedure PT bars must remain elastic. Bending moment generated by EDs must remain smaller than that of PT bars, and so self-centering capability is provided. Beams must be designed for combination of gravity loads, PT force and PT connection moment. Shear force must be transferred from beam to column though friction force at the interface between beam and column. The panel zone's shear force comes from PT bars force, ED bars force and contact force between beam and column. The flexural design of column is based on weak beam – strong column philosophy.

An experimental study was also undertaken. In the experimental study, a cyclic component test was performed on two energy dissipating bars to ensure that welded couplers were sufficient to develop the full axial strength of the bars, and to see if the confinement cylinders could prevent buckling of the ED bars. A cyclic loading test was also undertaken on PT connection up to an inter-story drift equal to 5%. Figure 2.9 shows the experimental setup and figure 2.10 shows both the analytical

and experimental the Moment – gap opening angle behaviour. Experimental tests show that the PT connection is capable of self-centering and provides adequate energy dissipation through ED bars yielding. Figure 2.10 also shows that the analytical model is able to accurately predict the experimental behaviour.

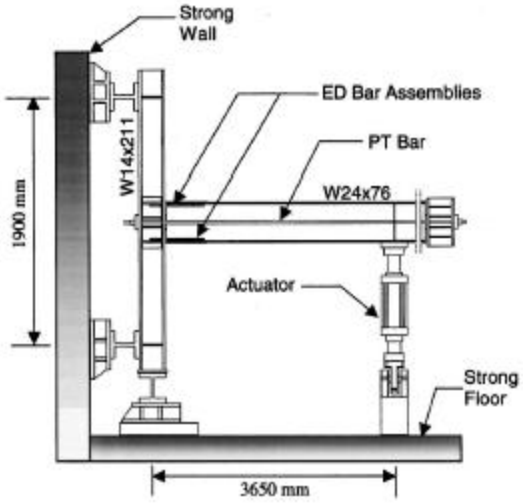

Figure 2.9 Experimental setup for PT connection with EDs (Christopoulos et al 2002a)

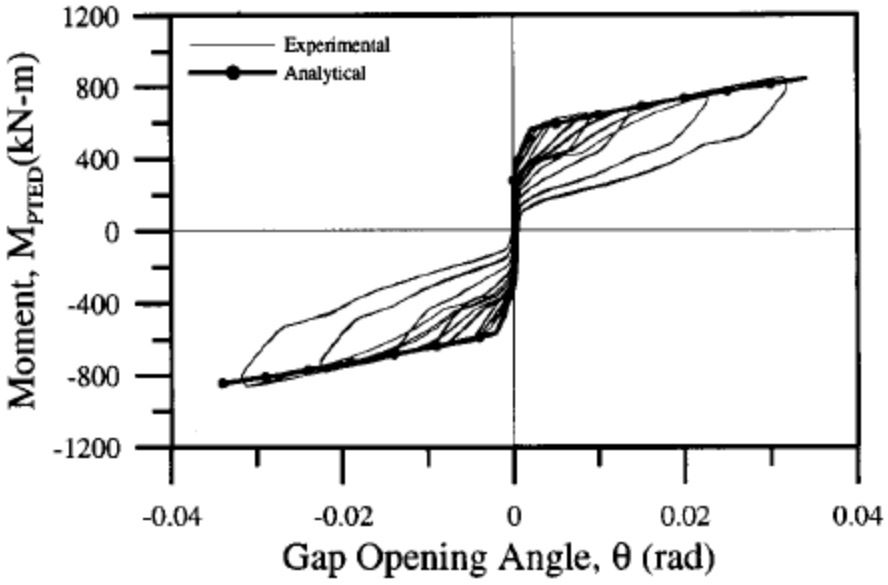

Figure 2.10 Moment (M_{PTED}) – gap opening angle behaviour of PT connection

In the work of Chou et al (2006), the seismic performance of a steel PT connection for MRFs was examined experimentally and analytically. Figure 2.11 shows a frame, which incorporates high-strength steel strands that are anchored outside the exterior concrete filled tube (CFT) column and reduced flange plates (RFPs) that are

used to increase energy dissipation of the connection. Figure 2.12 shows section B-B of the frame in figure 2.11.

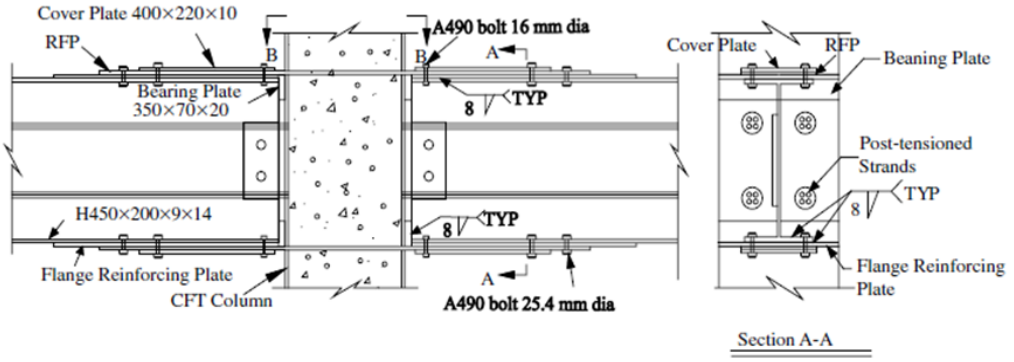

Figure 2.11 Proposed PT beam to CFT column connection (Chou et al 2006)

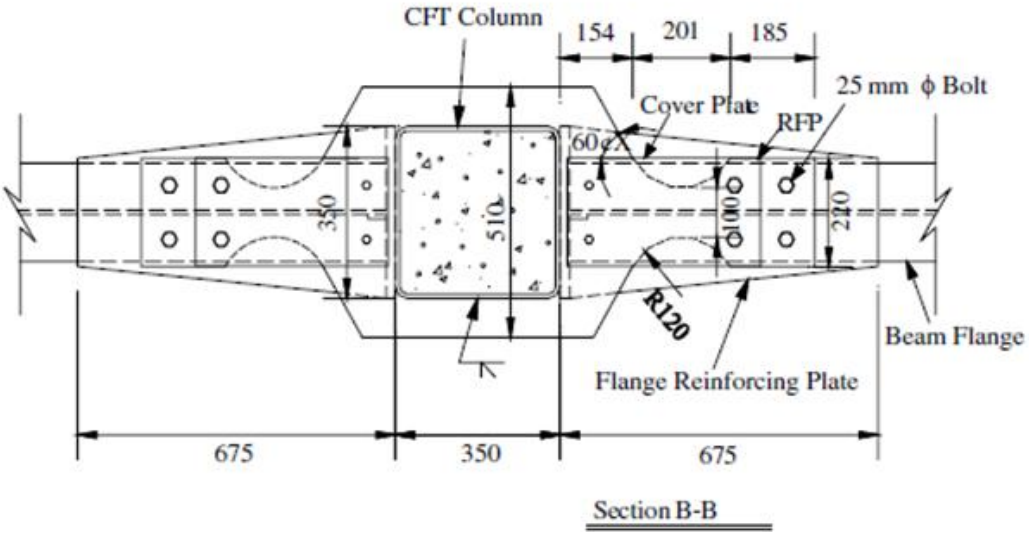

Figure 2.12 Section B-B of the PT beam to CFT connection (Chou et al 2006)

Formulas estimating the moment rotation behaviour of the proposed PT connection and the forces developed on the beam, PT strands, and RFPs are provided. The length of the flange reinforcing plate is determined to limit the beam flange strain at the end of the flange reinforcing plate to the yield strain at the target rotation angle of 0.02 rad. Design steps required to determine the size of the RFPs, corresponding to the target gap opening angle are provided. RFPs are sized based on their expected moment contribution and a tensile strain (0.08) at the target rotation angle.

Cyclic tests were conducted on three full scale subassemblies, which had two steel beams, post tensioned to a CFT column with high-strength strands to provide re-centering response. The tests results indicated that the proposed RFPs provide adequate energy dissipation. The subassemblies could reach 4% interstorey drift without strength degradation. Also buckling of the beam occurred at 5% interstorey drift, causing loss of the strand force, recentering response and maximum capacity. The beam flange strain, near the end of the flange reinforcing plate, was measured to be $1.4\varepsilon_y$, when beam local buckling occurred. This strain value is slightly less than $2\varepsilon_y$ based on the experiments of Garlock et al (2005). One of the specimens in this study was modelled with the non-linear finite element analysis program ABAQUS (ABAQUS 2010) to study the behaviour of the steel beam under combined post-tensioning and flexural loadings. Figure 2.13 shows that the predicted beam-moment-deflection relationship agrees with the experimental results.

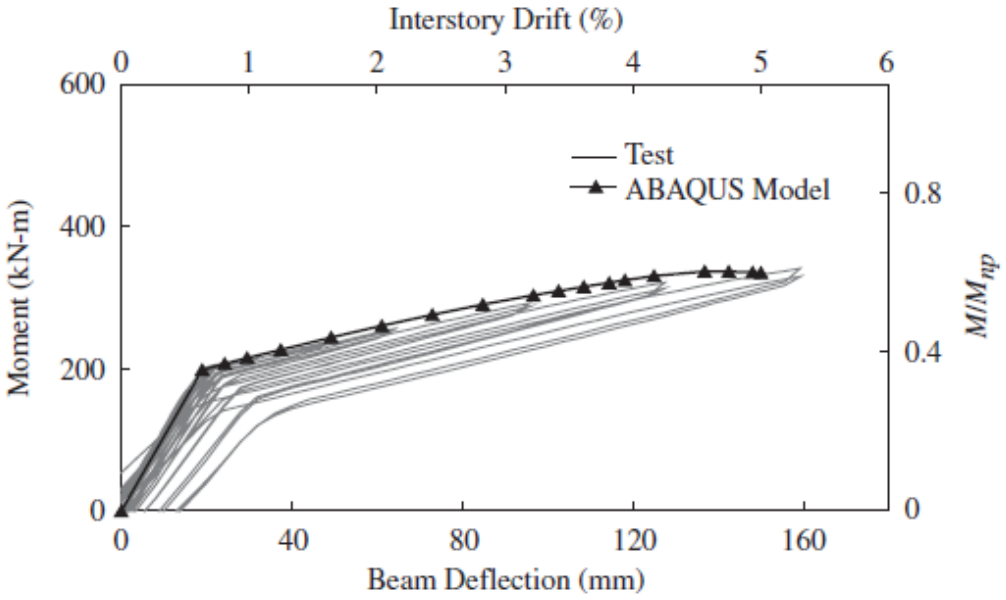

Figure 2.13 ABAQUS prediction versus test results (Chou et al 2006)

In the work of Wolski et al (2009) a new beam-to-column connection for earthquake resistant MRFs is introduced. The connection has a beam bottom flange friction device (BFFD) and PT high-strength steel strands running parallel to the beam. The BFFD provides energy dissipation to the connection and avoids interference with the floor slab. Also when properly designed the BFFD would not have to be replaced after the DBE. Figure 2.14 shows a schematic representation of steel MRF with PT

connections with BFFDs and figure 2.15 shows details of a PT connection with BFFD (Wolski et al 2009).

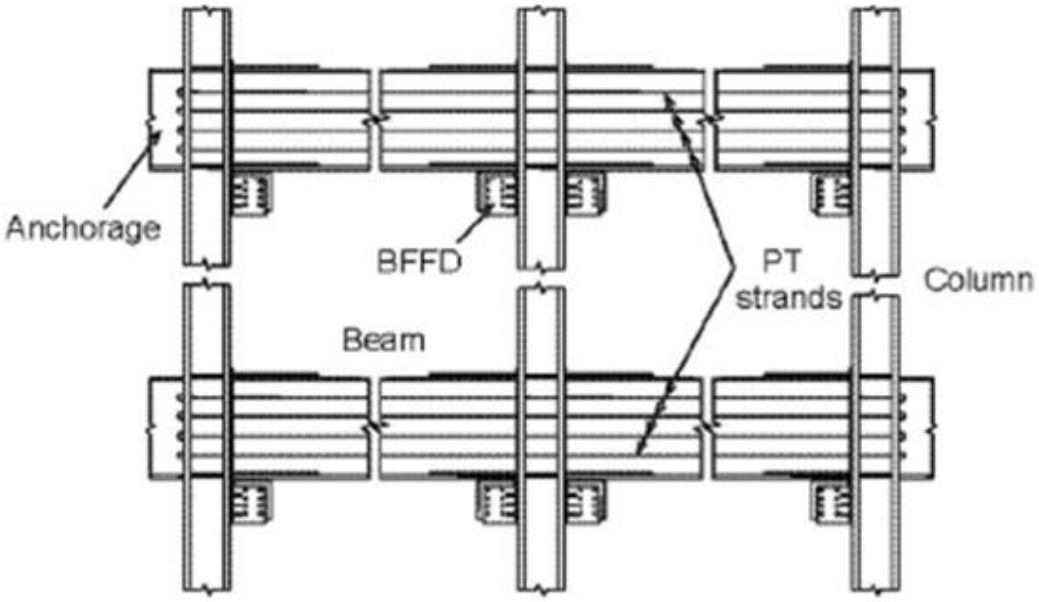

Figure 2.14 Schematic representation of a steel MRF with PT connections with BFFDs

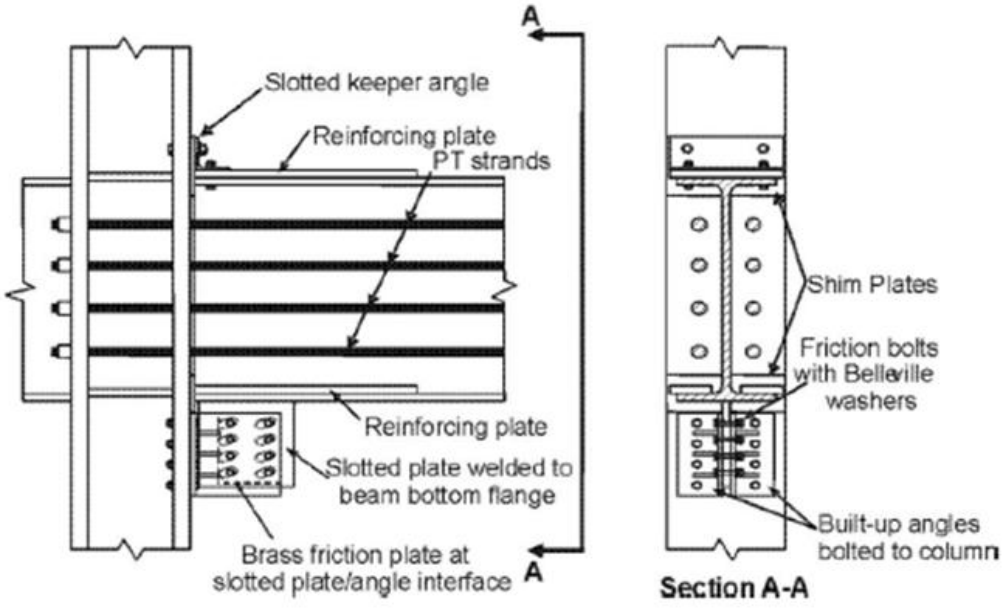

Figure 2.15 Details for a PT connection with BFFD (Wolski et al 2009)

Formulas estimating the moment rotation behaviour of the proposed PT connection and the forces developed on the beam, PT strands, and BFFDs as a function of the rotation angle are provided. Figure 2.16 shows that the moment rotation behaviour of the proposed PT beam to column connection is un-symmetric.

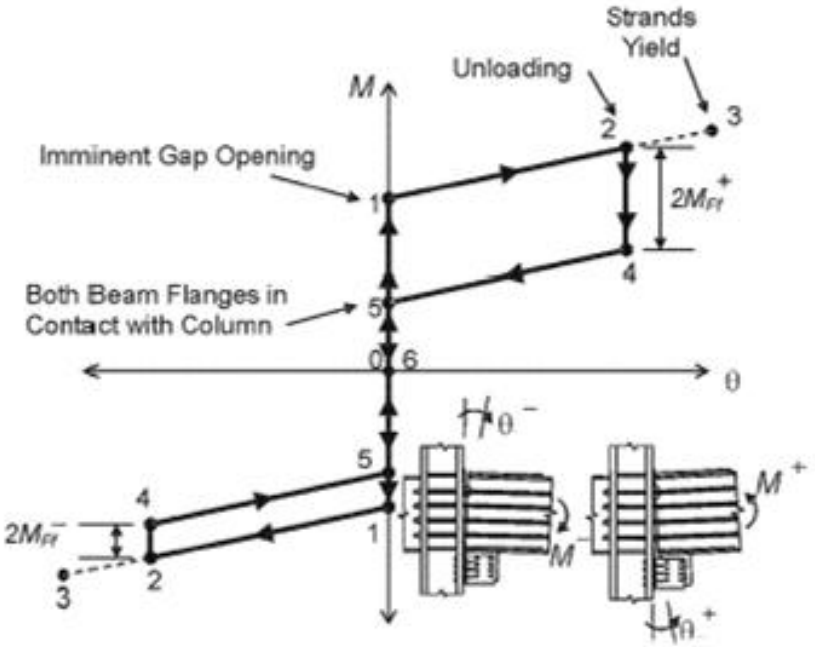

Figure 2.16 Conceptual moment – rotation cyclic response of a one sided PT connection with a BFFD (Wolski et al 2009)

A design approach, preserving self-centering behaviour under the DBE is suggested, and so the moment in the imminent gap opening of the connection must be greater than two times the moment developed by the BFFD. A maximum relative rotation equal to 0.035 under the DBE was selected, based on time history analyses results by (Rojas 2003). The size of the slotted bolt holes in the BFFD was based on this relative rotation angle. The PT strands were designed to remain elastic (i.e., with the PT force less than 80% of the strand tensile strength) for relative rotation up to 0.07.

Figure 2.17 shows the test setup in which experiments of the PT connections with BFFDs were conducted. A series of seven large-scale tests were performed to investigate the effect of the BFFD friction force. The effects of several parameters on the cyclic loading behaviour of the connection are investigated such as 1) the

level of friction force in the BFFD; and 2) the friction bolt bearing against the end of the slotted bolt holes. The test results show that the BFFD provides reliably energy dissipation to the PT beam to column connections. The energy dissipation characteristics were predictable, consistent and repeatable under different loading histories. However, the flexibility of the outstanding leg of the column angles which attached the BFFD to the column reduced the PT connection stiffness under load reversal and consequently reduced the energy dissipation in the BFFD.

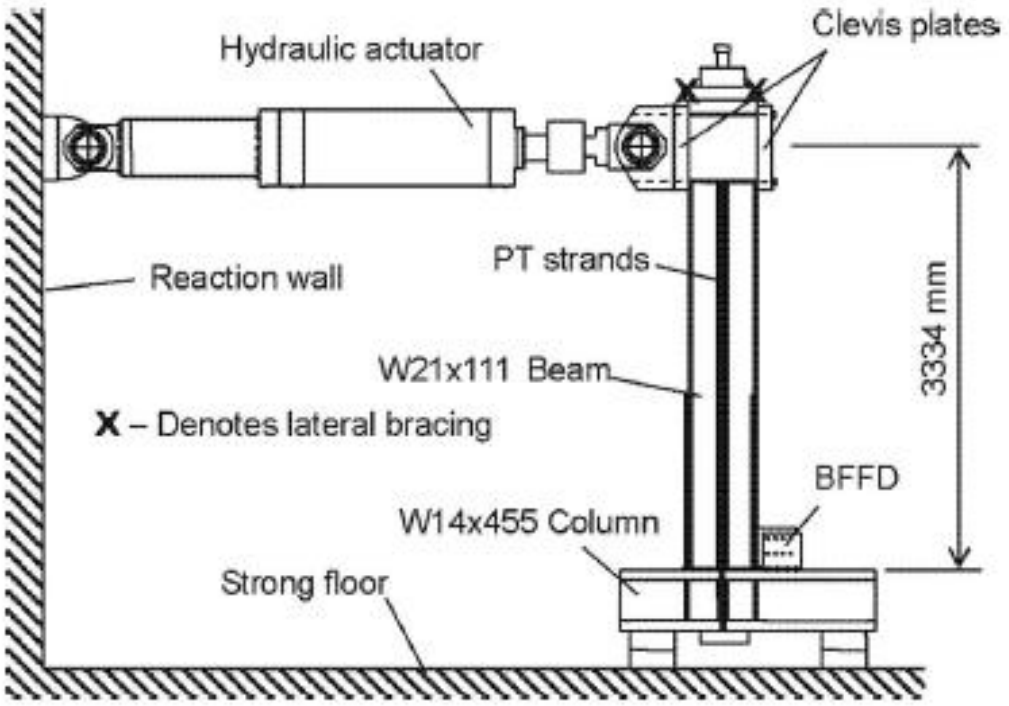

Figure 2.17 PT connection with a BFFD subassembly test setup

In the work of Chou and Lai (2009) experimental and analytical studies of a PT connection are presented. Figure 2.18 shows the geometric configuration of a frame incorporating the proposed beam flange energy dissipators, while figure 2.19 shows the proposed PT connection details. The steel beam web is first positioned to a splice plate, which is embedded in the concrete column and has slotted holes for bolted connection. Beams are post-tensioned to columns via high-strength steel strands before the energy dissipators are bolted below the beam bottom flange and column. Two types of energy dissipators are proposed 1) buckling-restrained energy dissipators (BREDs), which have a reduced section plate restrained by two cover

plates; (2) and cross shaped energy dissipators (CSEDs), which have a reduced section plate welded with two plates in transverse direction.

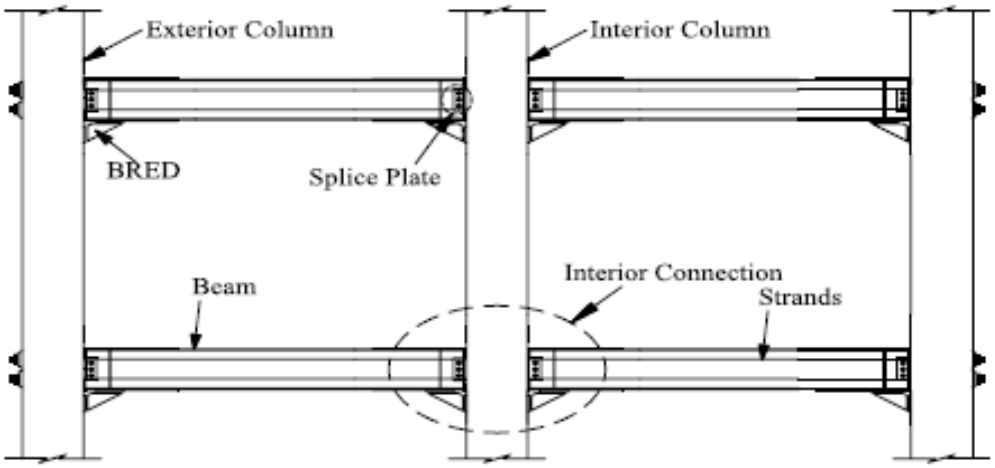

Figure 2.18 The proposed SC-MRF (Chou and Lai 2009)

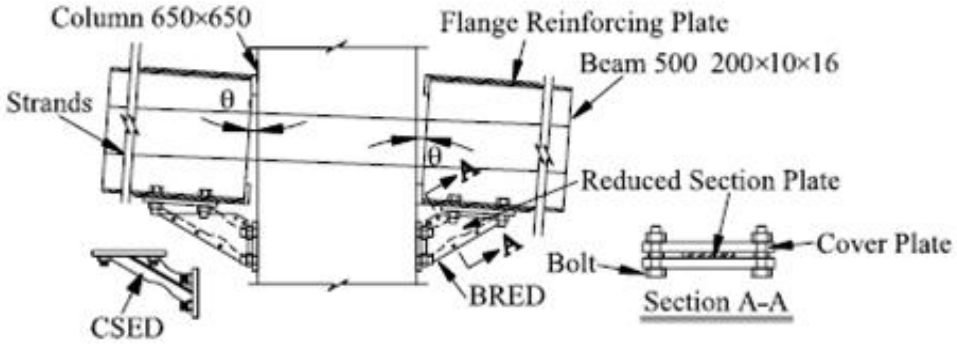

Figure 2.19 The proposed PT connection details (Chou and Lai 2009)

Formulas estimating the moment rotation behaviour of the proposed PT connection are presented. Also an iterative procedure for the prediction of the forces developed in the beam, PT strands, and energy dissipators as a function of the rotation angle is provided. Since no energy dissipator is located on the beam top flange, the hysteretic loop in un-symmetrical and beam decompression in the negative bending occurs earlier than that in the positive bending. Figure 2.20 shows the moment versus relative rotation gap opening angle relationship of the proposed PT connection.

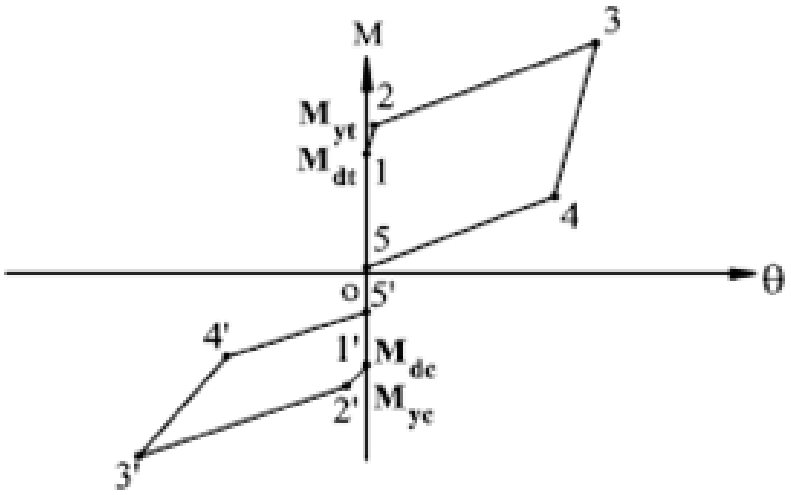

Figure 2.20 Moment provided by strands and energy dissipators (Chou and Lai 2009)

Figure 2.21 shows the test setup of cyclic tests that have been conducted on three full scale PT connection subassemblies and six energy dissipators. The relative rotation angles predicted by the iterative procedure differ by 10% from the experimental ones after n interstorey drift of 1.5%. The iterative analytical steps were reasonably predicted the test response. In the two specimens using BREDs, their fracture occurred at 3% interstorey drift, while in the specimen using CSED the fracture occurred at 4% interstorey drift. These drift values are relatively low. Also in this study six BREDs were tested and analysed in Abaqus to evaluate their cyclic performance.

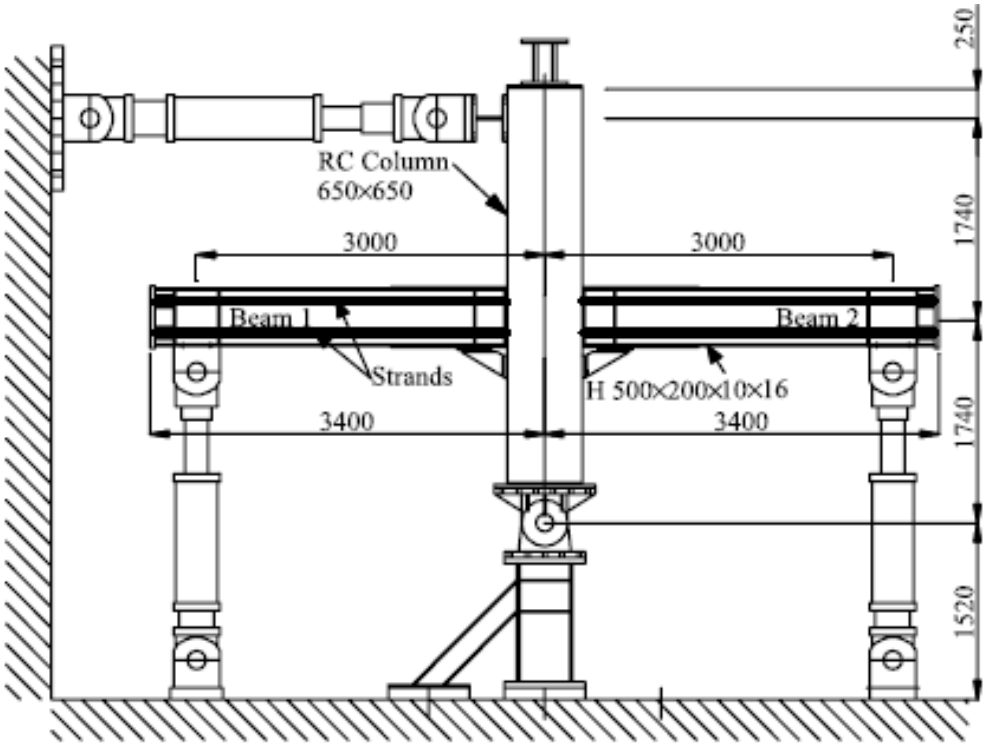

Figure 2.21 Test setup (Chou and Lai 2009)

Figure 2.22 shows a steel beam to column PT connection, constructed with web friction devices (FDs), as proposed in the work of (Tsai et al 2008). Two wide flange beams are connected to a wide flange column through two beam web FDs. Each FD consists of two web clamping plates welded to the column flange and connected to the beam web using slip-critical bolts. PT tendons run along two sides of the beam web and run through the column flanges.

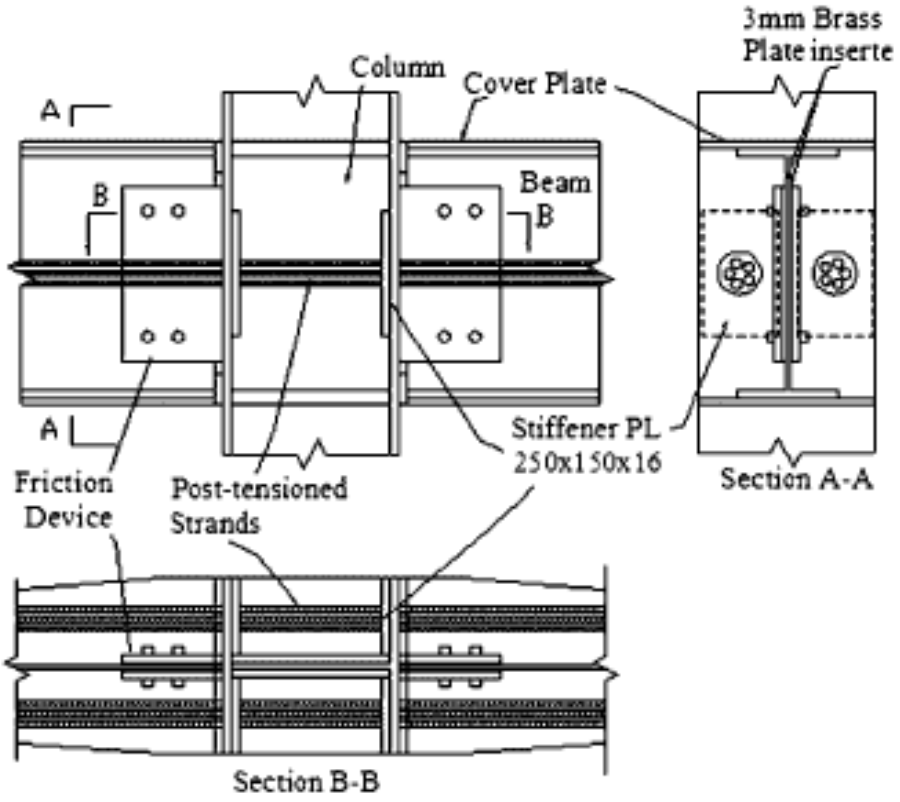

Figure 2.22 Schematic representation of beam to column connection using FDs (Tsai et al 2008)

Formulas estimating the moment rotation behaviour of the proposed PT connection and the forces developed on the beam, PT tendons, and FDs as a function of the rotation angle are provided. In this work experimental cyclic tests were performed on four bolted FDs and on four full-scale PT beam to column connections subassemblies. Figure 2.23 shows the experimental setup of the PT connection. Cover plates were added to the beam flanges to ensure that the beam remained elastic. The size of the overused circular bolt holes on the beam web was determined from the requirement of a maximum beam rotation of 0.05 rad. In order to ensure the re-centering mechanism, the lower bound of the initial PT tendon force is determined from the peak friction force. The upper bound of the initial PT force is determined based on a number of factors, including the beam peak rotation demand, the maximum allowed tendon stress, and the combined axial-flexural capacity of the beam.

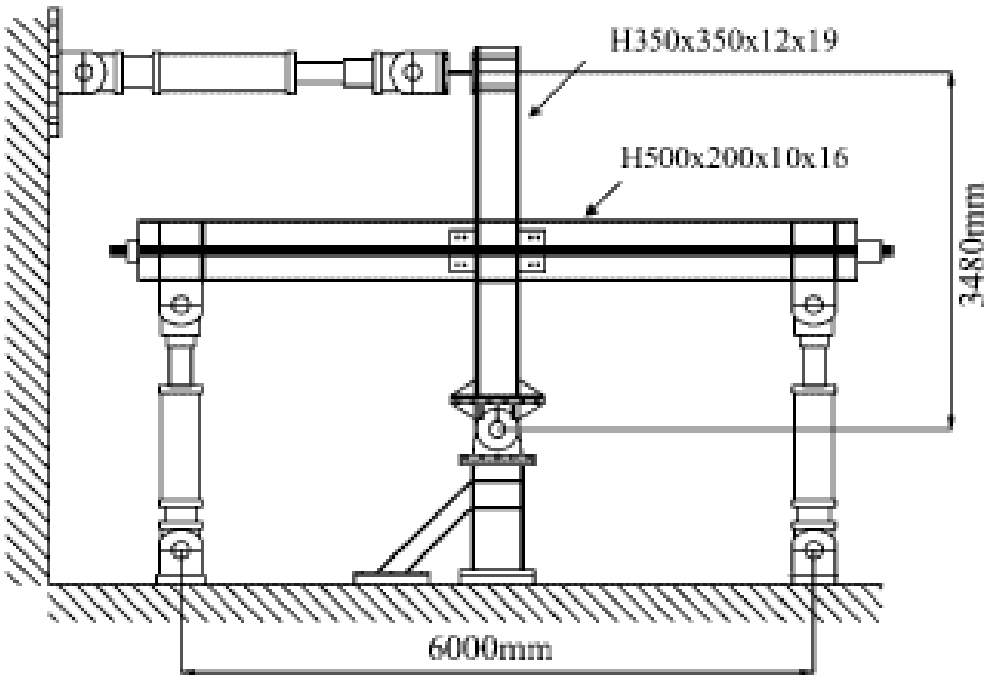

Figure 2.23 PT connection experimental setup (Tsai et al 2008)

In general the decompression moments obtained from the analytical expressions overestimated the experimental responses. The flexural contributions of the PT tendons and the FDs can be reasonably predicted by the proposed analytical expressions. Also, the cyclic response of the PT connection can be accurately predicted using the analytical methods outlined in this study. It has been also concluded that if the beams and the columns are designed to remain elastic, the proposed PT connections can sustain repeated large cyclic deformations without evidence of stiffness or strength deterioration.

A new PT connection that incorporates PT elements to provide self-centering capacity along with friction mechanisms to dissipate energy is proposed in (Kim and Christopoulos 2008; Kim and Christopoulos 2009a,b). Figure 2.24 shows the proposed PT connection. Initial PT force is provided by PT bars, passing through the interior column flanges and are anchored outside the flange faces of the exterior columns. The friction energy dissipation devices (FEDs) are symmetrically installed on the top and bottom beam flanges.

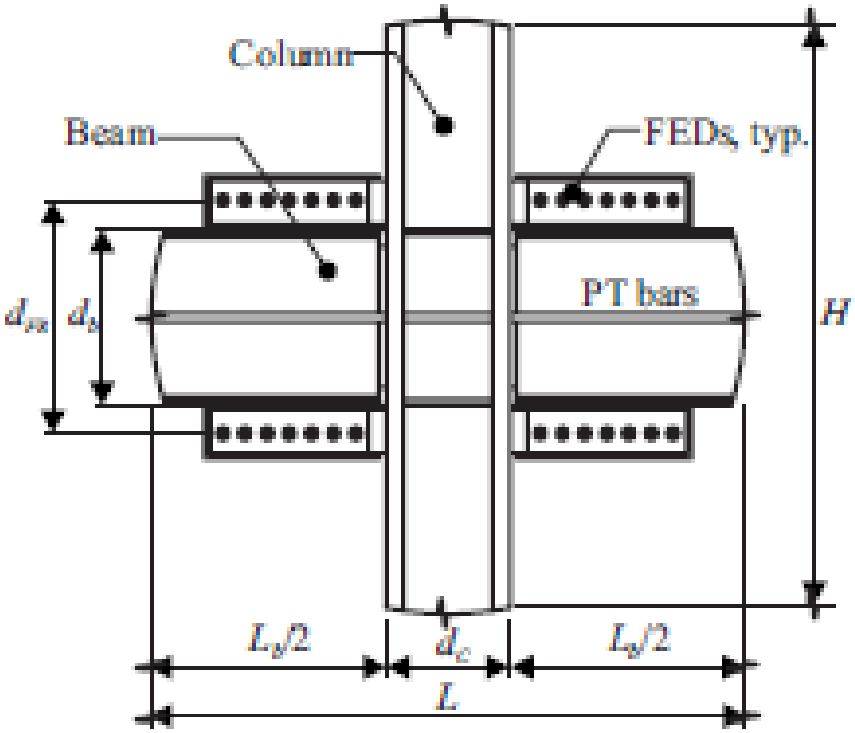

Figure 2.24 Proposed PT connection (Kim and Christopoulos 2008)

Formulas, estimating the forces of the beams, PT bars and FEDs are proposed as a function of the relative rotation angle. Also the relation between the relative rotation angle and the drift is provided. Three different friction materials were investigated under direct dynamic axial cyclic loading. Cyclic tests of the PT connections were conducted to investigate the efficiency of the proposed friction interface and its performance under loading conditions that are expected during seismic loading. Figure 2.25 show the testing setup for an interior beam-column assembly for the proposed PT connection and the geometry of an interior PT connection. Figure 2.26 shows details of the beam column interface, and figure 2.27 shows the elements comprising an FED.

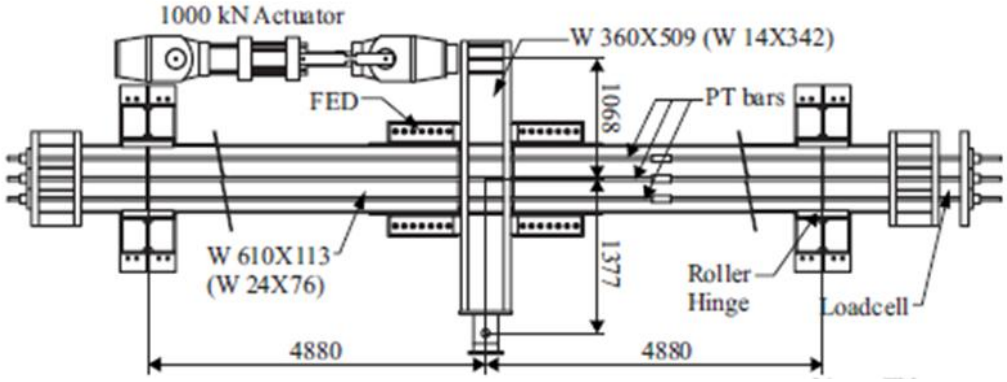

Figure 2.25 Test specimen for interior beam-column assembly (Kim and Christopoulos 2008)

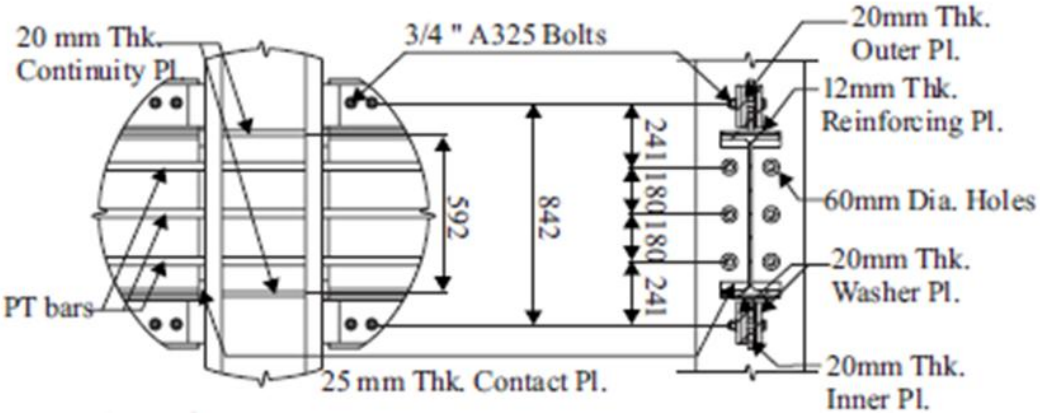

Figure 2.26 Details of beam column interface (Kim and Christopoulos 2008)

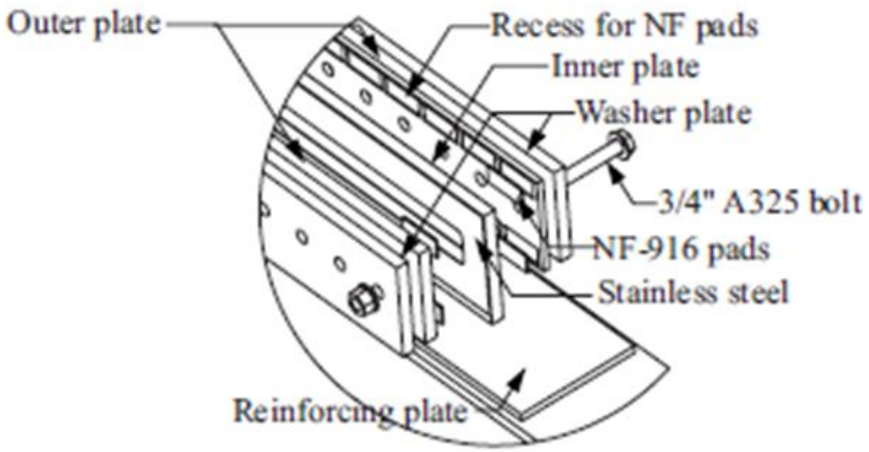

Figure 2.27 Elements comprising FEDs (Kim and Christopoulos 2008)

Within the self-centering limit, no residual drift was observed in the test results, as well as no structural damage. The tests also demonstrated the system's stability and good energy dissipation capacity.

A numerical model was developed using the commercial computer program RUAUMOKO (Carr 2005). Figure 2.28 shows the proposed numerical model in an interior connection and figure 2.29 shows the proposed model in an exterior connection. The proposed model consists of a number of one-dimensional contact (CT), friction (FR) and PT springs that are used to simulate the gap-opening response, the friction dissipative mechanisms and the PT elements.

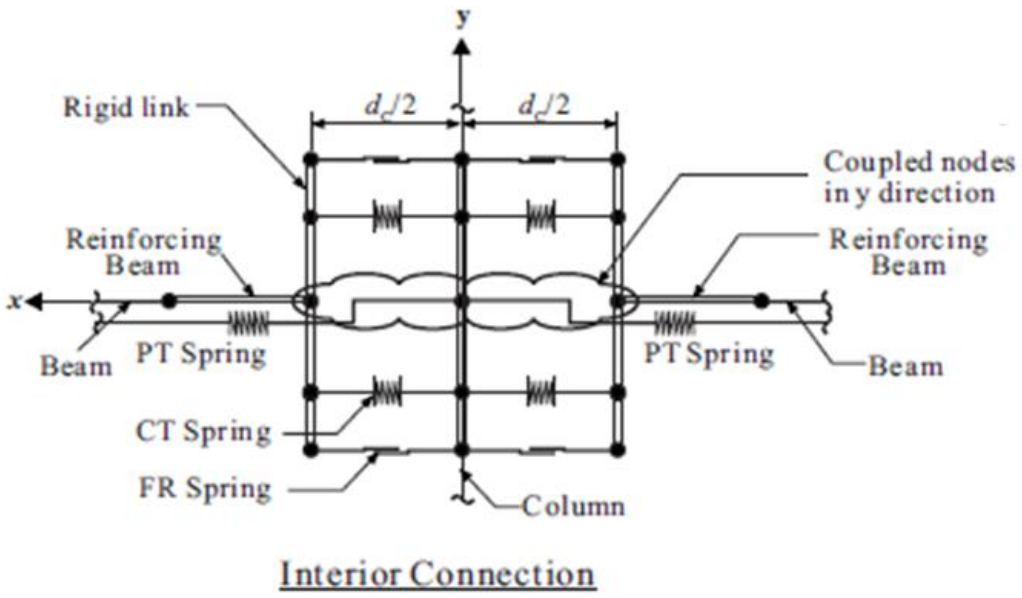

Figure 2.28 Numerical model for an interior PT connection (Kim and Christopoulos 2009a)

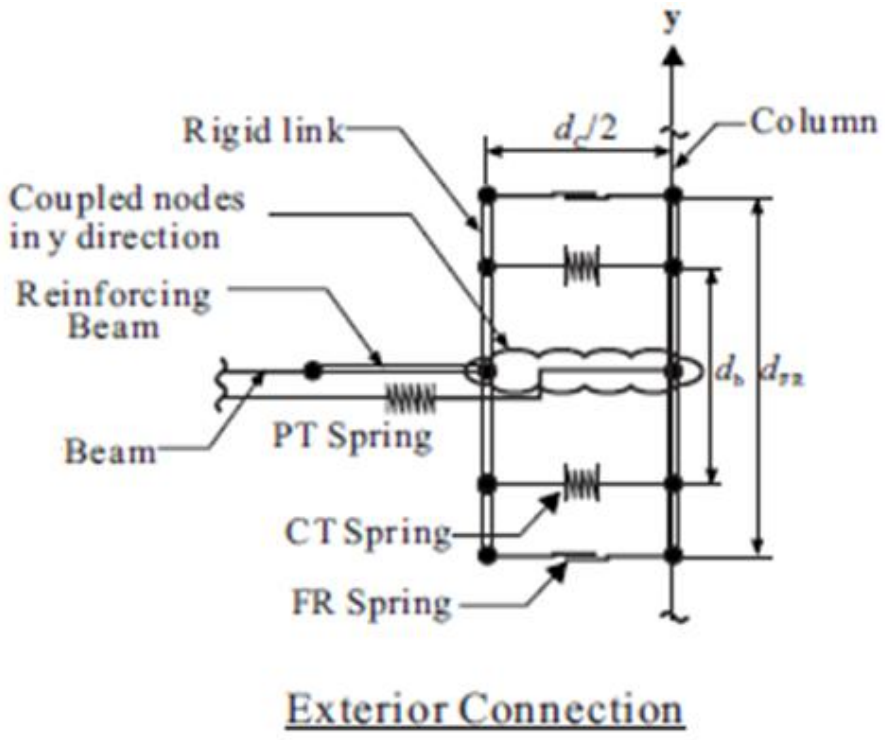

Figure 2.29 Numerical model for exterior PT connection (Kim and Christopoulos 2009a)

The experimental response of the proposed PT connection was also investigated at the ultimate stage. One PT connection specimen was subjected up to 6.2% drift. The web and compression flange of beam around the end of the longitudinal stiffeners abruptly suffered local buckling at a maximum drift 6.2%. Further detailing requirements are proposed in (Kim and Christopoulos 2009a) to assure that flexural hinges form in the beams in order to improve the cyclic response of steel PT connections when drifts exceeding the design drifts are imposed to the system.

In (Kim and Christopoulos 2009a) a non-linear solid finite element model (FEM) was developed, able to predict the PT connection response at ultimate deformation levels. The FEM consisted of solid elements and a number of spring elements to represent the gap-opening and closing phenomena and the frictional energy dissipation capabilities characterizing PT connections.

2.3 Design procedures for SC-MRFs

In the work of Garlock et al (2007) a performance based seismic design approach for SC-MRFs is presented. Seismic performance levels, seismic input levels, structural limit states and capacities and structural demands for a SC-MRF are defined. Design criteria to enforce the design objectives and a step by step design procedure are outlined. Figure 2.30 shows that the gap opening in the PT connections causes a SC-MRF to expand, as mentioned in Garlock et al (2007). This SC-MRF expansion increases with the number of bays. This SC-MRF expansion is accommodated by the floor system and the collector elements that transmit inertial forces from the floor system to the SC-MRF. Figure 2.31 shows the floor system and collector element configuration that accommodates SC-MRF expansion. The SC-MRF must be designed to accommodate the forces that develop as the floor system partially restrains the expansion. It is also mentioned that first story columns can restrain the expansion of the first floor beams, since the SC-MRFs does not expand at the ground floor. Above the first floor, this interaction between floor levels through the columns is small as the frame expansion is similar at each floor. For this reason, the restraint by the columns is neglected in Garlock et al (2007).

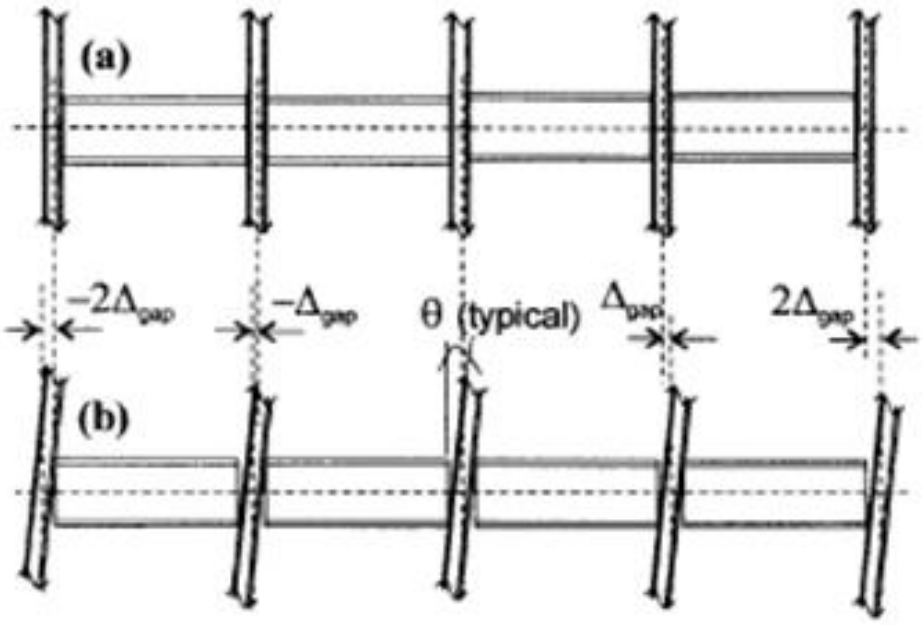

Figure 2.30 Elevation of one floor of a SC-MRF: (a) un-deformed (b) deformed shame (Garlock et al 2007)

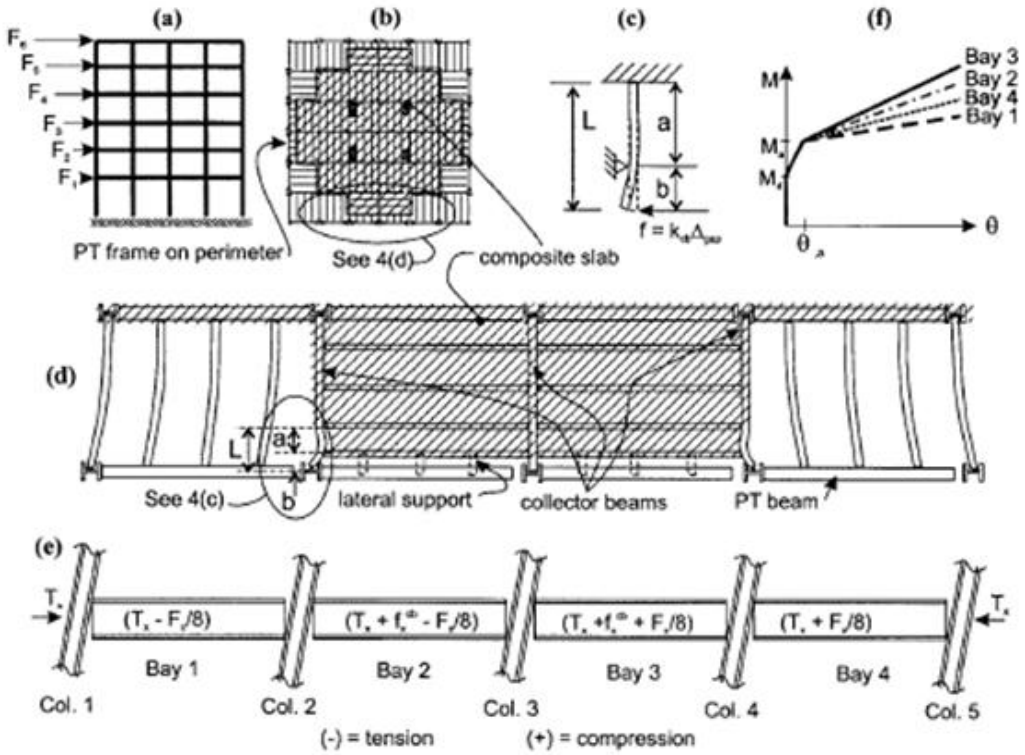

Figure 2.31 (a) Floor inertia forces on building elevation; (b) plan of hypothetical building; (c) deformation of collector beam; (d) interaction of SC-MRF with gravity system; (e) beam axial forces (P) on each bay of floor x; and (f) idealized moment-relative rotation plot of the connection moments on floor x. (Garlock et al 2007)

The design approach for SC-MRFs outlined in Garlock et al (2007) uses two performance levels: Immediate occupancy (IO) and collapse prevention (CP). The design approach has 2 objectives that relate the seismic performance levels to the seismic input levels. Damage to the SC-MRF under the DBE must conform to the IO performance level and damage to the SC-MRF under the MCE must conform to the CP performance level. Structural demands are used to enforce these design objectives. Structural demands quantify the deformations, forces and moments in SC-MRF for the DBE and MCE seismic input levels.

The iterative seismic design procedure for SC-MRFs presented in Garlock et al (2007) is briefly described in the following steps.

Step 1: From appropriate seismic design provisions the design response spectrum for 5% damping ($S_a(5\%)$), the design base shear (V_{des}), the force reduction factor (q), the equivalent lateral forces at each floor ($F_{x,des}$) and the story allowable drift limit are obtained.

Step 2: It is assumed that the beams moment under the DBE (M_{DBE}) equal to the nominal beam plastic moment capacity ($M_{p,n}$). Also it is assumed that the beams moment at the columns face under the design response spectrum (M_{des}) is lower than $0.55 \cdot M_{p,n}$.

Step 3: Beams and columns are selected considering the strong column –weak beam design criterion ($\Sigma M_c > \Sigma M_b$). Formulas for the estimation of M_c and M_b are provided in Garlock et al (2007).

Step 4: An elastic analysis of the frame is performed under the $F_{x,des}$ where rigid beam-column connections have been assumed but the panel zones flexibility and the beam reinforcing plated have been considered. The frame must satisfy the story allowable drift limit otherwise the beams and columns are increased and step 3 is repeated. At the end of this step M_{des}, the initial elastic frame stiffness ($K_{f\Delta}$), V_{des}, the elastic displacement under the design response spectrum ($\Delta_{el\text{-}des}$), and the roof displacement demands under the DBE and MCE ($\Delta_{roof,\ DBE}$, $\Delta_{roof,MCE}$) are obtained. Formulas estimating $\Delta_{roof,\ DBE}$ and $\Delta_{roof,MCE}$ based on the equal displacement rule are provided in (Garlock et al 2007).

Step 5: Collector beams are designed according to the following principles. The initial PT force, T_0, should be greater than the force causing a plastic hinge in the outer collector beam. Also the outer collector beams should not yield under the DBE. A formula estimating the PT connection rotation when the collector beam forms a plastic hinge is provided in Garlock et al (2007)

Formulas estimating the PT connections relative rotation demands under the DBE and MCE (θ_{DBE} and θ_{MCE}) are provided in Garlock et al (2007). These values are obtained by subtracting the elastic story drift ($\theta_{s,e}$) from the total story drift demand ($\theta_{s,DBE}$ or $\theta_{s,MCE}$). $\theta_{s,e}$ is estimated based on the solid assumptions (Garlock 2002)

that the beams, columns and panel zones of SC-MRFs remain elastic under the DBE. $\theta_{s,DBE}$ and $\theta_{s,MCE}$ are obtained by the $\Delta_{roof,\ DBE}$ and $\Delta_{roof,MCE}$ based on studies by (Rojas et al 2005) indicating that the ratio between interstorey drift (θ_s) to roof drift (θ_r) approximately equals to 1.5. Also base shear demands V_{DBE} and V_{MCE} are estimated by multiplying V_{des} by over strength factors (Ω_{DBE}, Ω_{MCE}). Suggested Ω values are given in Garlock et al (2007).

Step 6: The structural demands (V_{DBE}, V_{MCE}, $\theta_{s,DBE}$, $\theta_{s,MCE}$, θ_{DBE} and θ_{MCE}) are estimated using formulas provided in Garlock et al (2007).

Step 7: M_{des} is multiplied by a selected α_α factor to determine the required connection moment at the yield of the FED ($M_a \geq \alpha_\alpha \cdot M_{des}$), which is an angle (see Figure 2.1). The PT strands number, size and T_0 and the FEDs (top and seat angles) properties are selected.

Step 8: The reinforcing plate length (L_{rp}) and reinforcing plate area (A_{rp}) are iteratively selected in order to satisfy certain design criteria. L_{rp} must satisfy the criterion for beam local buckling and the criterion for beam horizontal shear strength, while A_{rp} must satisfy the criterion for yielding under bearing stresses. Beam local buckling under the MCE is prevented by limiting the beam flange strain at the end of the reinforcing plate to two times the yield strain ($2\varepsilon_y$) (Garlock et al 2005). The design criterion for beam horizontal shear strength, is provided in Garlock et al (2007) based on equilibrium of horizontal forces under the DBE. The criterion for yielding under bearing stresses is provided in Garlock et al (2007) under the DBE. If design criteria are not satisfied after several selections of L_{rp} and A_{rp} a new connection is selected. If the beam size needs to be modified the procedure continues from step 3 otherwise from step 6.

Step 9: The panel zones properties are selected, by applying the panel zone yield criterion under the DBE, which is provided in Garlock et al (2007).

Step 10: A nonlinear pushover analysis is performed to evaluate the Ω values, and if these values are significantly different than those assumed the connection design is checked by returning to step 6.

The proposed design procedure is evaluated via comparisons with time history analysis results. SC-MRFs designed using the design approach satisfied the design criteria for the limit states of connection strength, angle fracture, and strand yield. The other design criteria were not always satisfied for a few beams or columns in the frame

In the work of Kim and Christopoulos (2009b) a comprehensive step by step seismic design procedure of SC-MRFs with PT connections presented in Kim and Christopoulos (2008), and Kim and Christopoulos (2009a) that is adapted from current seismic design practices and that can be extended to any other SC-MRF with different PT connections is proposed. A formula for the PT connection gap opening moment (M_{Gap}) is provided. Formulas for the beam axial compressive force (F_b) and bending moment (M_b) after the PT connection gap opening are provided. In these formulas the beams and PT bars axial stiffness (K_b, K_{PT}) are considered as well as the restraint effect on the SC-MRF expansion from the columns and the floor slab. Also, formulas for the bending stiffness of columns in the direction of the beam member axis are provided.

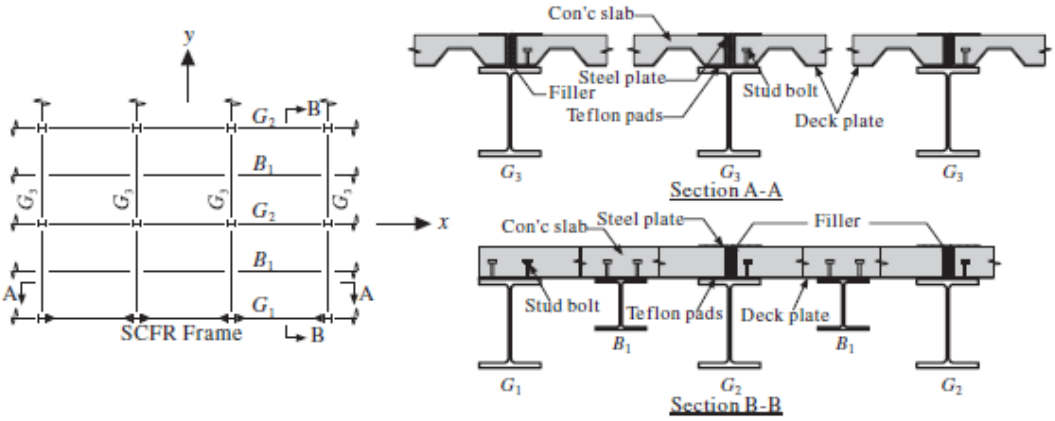

Figure 2.32 Detailing between concrete slab and SC-MRF to eliminate the restraining effect of slabs (Kim and Christopoulos 2009b).

Figure 2.32 shows the proposed in Kim and Christopoulos (2009b) detailing along the boundaries of the slabs that allow for the gap opening to be accommodated. Two of the four sides are restrained by the shear connectors while the other side moves

along with the frame expansion. To allow for a smooth sliding motion, Teflon pads are placed underneath the slab at the sides where sliding of the slab is allowed.

According to the design strategy of Kim and Christopoulos (2009b), SC-MRFs are designed to respond within their self-centering range with no damage to any structural elements and no residual deformation (except for minor residuals caused by the yielding of the column bases) under the DBE level earthquake. While, under the MCE level earthquake, SC-MRFs are designed to form a ductile mechanism with significant inelastic deformation reserve through the flexural yielding of beams at carefully detailed locations.

In Kim and Christopoulos (2009b) a formula estimating the beam moment M_{SC} at the maximum drift where self-centering is provided ($\theta_{s,SC}$), is proposed. By assuming that the elastic drift of the corresponding MRF ($\theta_{s,y,MRF}$) equals to 1%, M_{SC} is provided as a function of M_{Gap}, $\theta_{s,SC}$, and post yield stiffness ratio (α_p). $\theta_{s,SC}$ must be equal to or larger than a target design drift θ_{DBE} to ensure self-centering behavior under DBE level earthquakes. The maximum drift $\theta_{s,max}$ of SC-MRFs is considered as $\theta_{s,SC}$ + 3% rad since properly detailed beam sections allow for a plastic rotation of 3% rad. Therefore the target drift $\theta_{s,MCE}$ of a SC-MRF must be less than $\theta_{s,max}$ to prevent a sudden loss of stiffness and strength due to local buckling at critical beam sections and/or yielding of PT bars. Figure 2.33 shows the moment – interstorey drift relations for self centering systems without ultimate ductile mechanism. Figure 2.34 shows the moment – interstorey drift relations for self centering systems designed according to the procedure proposed in Kim and Christopoulos (2009b). Considering that $\theta_{s,y,MRF}$ equals to 1% rad and that the gap opening angle $\theta_{s,SC}$ for SC-MRFs is approximately 3% rad, we get $\theta_{s,SC}$ equal to 4% rad, which is significantly larger than the drift $\theta_{s,DBE}$ of 2% of a common building under DBE level earthquakes.

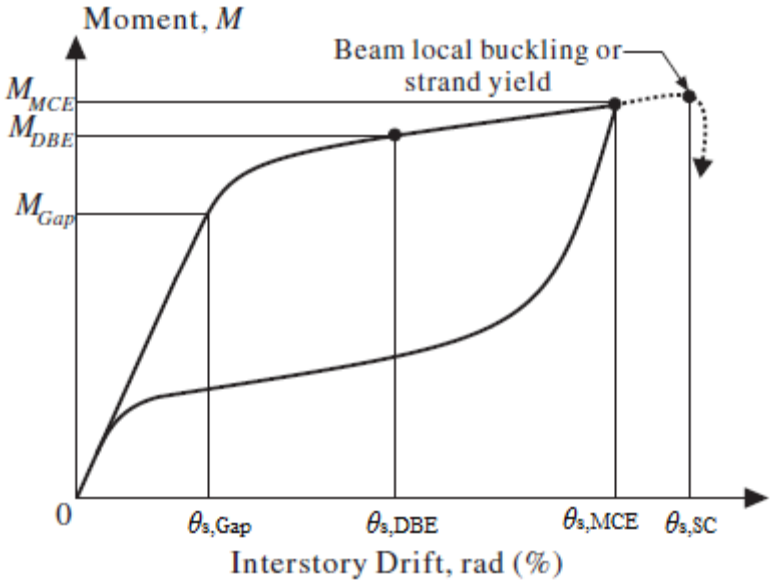

Figure 2.33 Moment-interstorey drift relations for self-centering systems without ultimate ductile mechanism (Kim and Christopoulos 2009b)

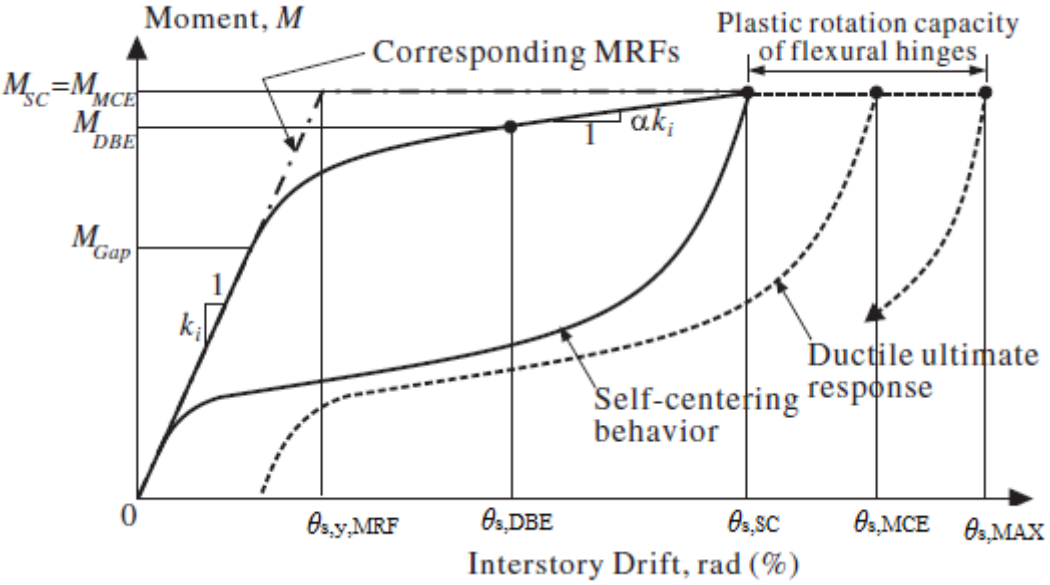

Figure 2.34 Moment-interstorey drift relations for self-centering systems, designed according to procedure proposed in (Kim and Christopoulos 2009b)

In Kim and Christopoulos (2009b) a range of values for α_p and energy dissipation factor (β), where $\beta=2M_{FR}/M_{Gap}$ and M_{FR} is the moment contribution of the friction devices (FEDs) are suggested. So, values of $0.1< \alpha_p <0.15$ and (0.2 for the first story) and values of $0.7<\beta<1$ are suggested. If α_p and β valued are in the recommended range we ensure that self centering is provided, and that SC-MRFs

have similar drifts with MRFs. The last observation has been investigated using both multi degree of freedom systems (MDOF) and single degree of freedom systems (SDOF) (Christopoulos et al 2002a,b).

The steps of the design procedure presented in (Kim and Christopoulos 2009b) are the following.

Step 1: Size the initial beams and columns sections using typical design procedures for MRFs

Step 2: Determine the target drifts, $\theta_{s,DBE}$ and $\theta_{s,MCE}$ for a given seismic hazard level and choose Δ_{SC} consequently.

Step 3: Set to about 0.1 the post yield stiffness ratio (α_p) and between 0.7 and 1 the energy dissipation factor.

Step 4: Design of the main components of the PT connections, PT bars and FEDs. For the sizing of the PT bars, the beams section design moment capacity, considering the reinforcing plates thickness should be met under the $\theta_{s,SC}$ drift limit. The PT bars force should be less than 75% of the ultimate strength of the PT bars under the $\theta_{s,SC}$ drift limit. The moment M_{Gap} should be greater than the moment caused by gravity and wind load effects to prevent any gap opening under such loading conditions. By selecting β, the M_{FR} is obtained and so the friction devices are designed to achieve this moment.

Step 5: Size the reinforcing plates. If reinforcing plates greater than 2 times the beam depth are required, iterate from step 1 with bigger beam sections. Seismic demands, such as the design base shear should be re-calculated since a decrease in the structural period is expected. The reinforcing plate thickness is taken as the thickness of the beam flange. The reinforcing plate length is chosen in order to meet the design capacity (axial force and bending moment) of the beam, reduced with a safety factor, at the end of the reinforcing plates under the $\theta_{s,SC}$ drift limit.

Step 6: Design longitudinal stiffeners welded on the beam webs according to equations presented in (Kim and Christopoulos 2009b). Beams flexural plastic hinges are developed under $\theta_{s,SC}$ = 4% drift limit, at the end of the reinforcing plates. The beam detailing equations provided in (Kim and Christopoulos 2009b) ensure 3% additional inelastic rotation capacity without sudden loss of stiffness and strength due to beam local buckling.

Step 7: Size and detail the other structural members of the SC-MRFs according to capacity design principles to remain elastic at the target design drift. Panel zones are designed to prevent inelastic behavior under shear force equal to the beam axial forces. Also, continuity plates in the columns can be used to minimize local yielding of the columns flanges.

2.4 Assessment of the seismic response of SC-MRFs (numerical simulations, shaking table tests, hybrid tests)

In Rojas et al (2005) a six storey, four bay perimeter MRF was designed as a SC-MRF using post tensioned friction damped connections PFDC-MRF, according to the criteria described in Rojas et al (2005). A second six storey, four bay perimeter special MRF (FR-MRF) with welded connections was designed using the IBC 2000 provisions (ICC 2000). Figure 2.35 shows the layout of the gravity frames and seismic resisting frames when the prototype building is design with FR-MRFs and figure 2.36 shows the layout when the prototype building is designed with PFDC-MRFs. More details for the design properties of the frames are given in Rojas et al (2005).

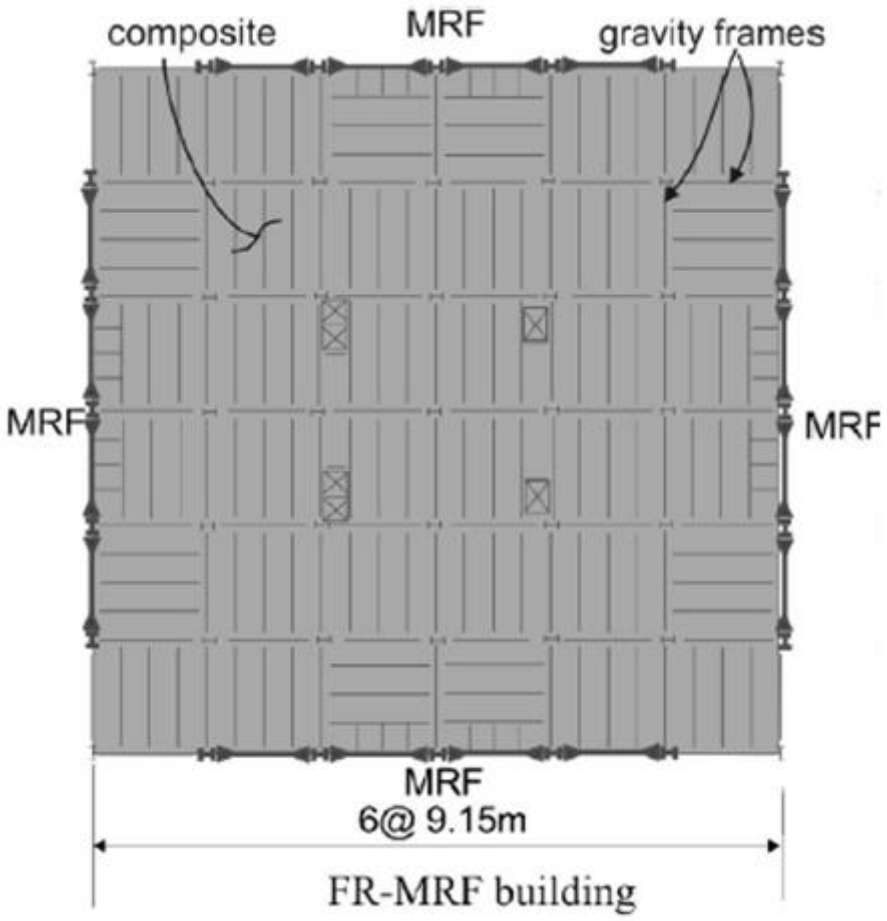

Figure 2.35 Gravity frames and FR-MRFs of prototype building (Rojas et al 2005)

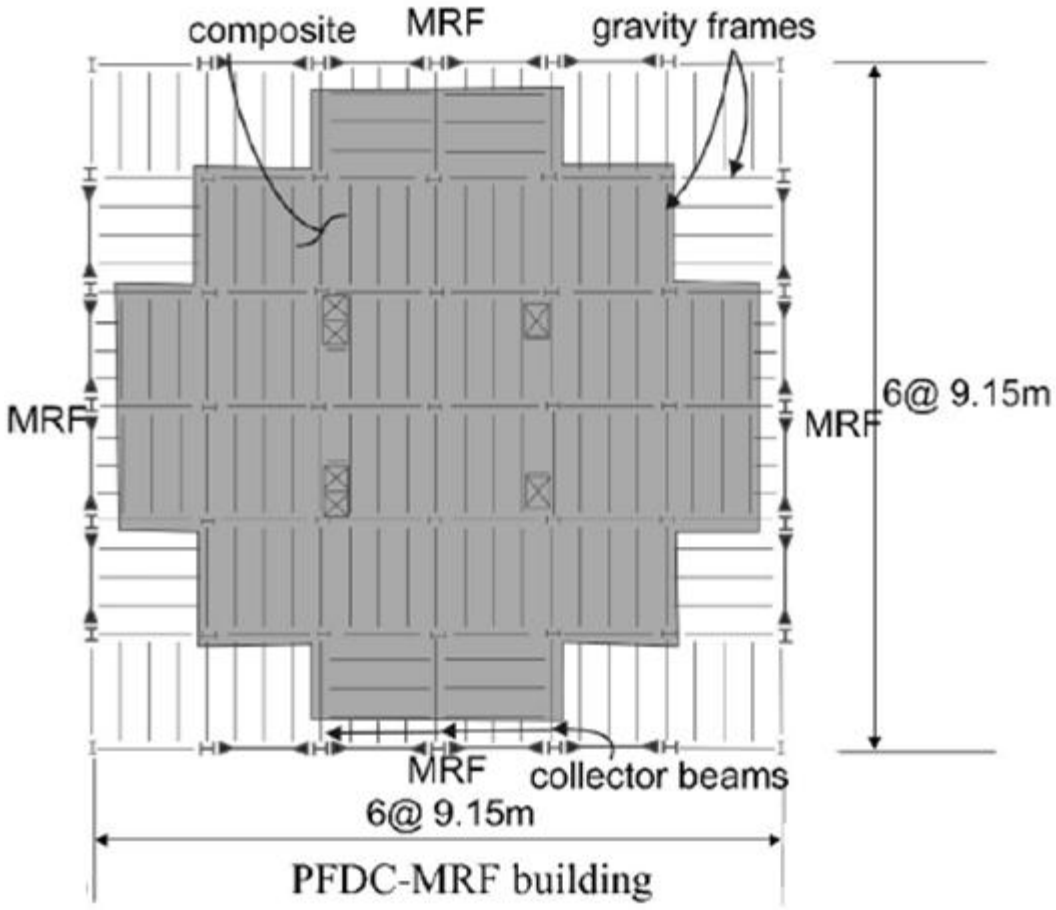

Figure 2.36 Gravity frames and PFDC-MRFs of prototype building (Rojas et al 2005)

Figure 2.37 shows the model in Drain-2DX for FR-MRF and figure 2.38 shows the model for PDFC-MRF used in this study. A beam plastic hinge model, considering strength degradation due to local buckling was used to the FR-MRF beams. Leaning columns were used into the models, incorporating P-Delta effects. Masses are located as shown in figure 2.37 and gravity loads are located in both the leaning columns and MRFs of both frames. The rotational flexibility of the foundation was also considered. PT connections have been modelled according to Ricles et al (2001) modelling approach, and initial stress condition was imposed to account for the initial post tensioning. Springs were used to model the interaction between the floor diaphragm and the PFDC-MRF. Link elements were used to keep the initial post tensioning forces from entering into the collector beam elements during the post

tensioning, since the construction sequence of a PFDC-MRF assumes that the beams are post tensioned before the slab is poured.

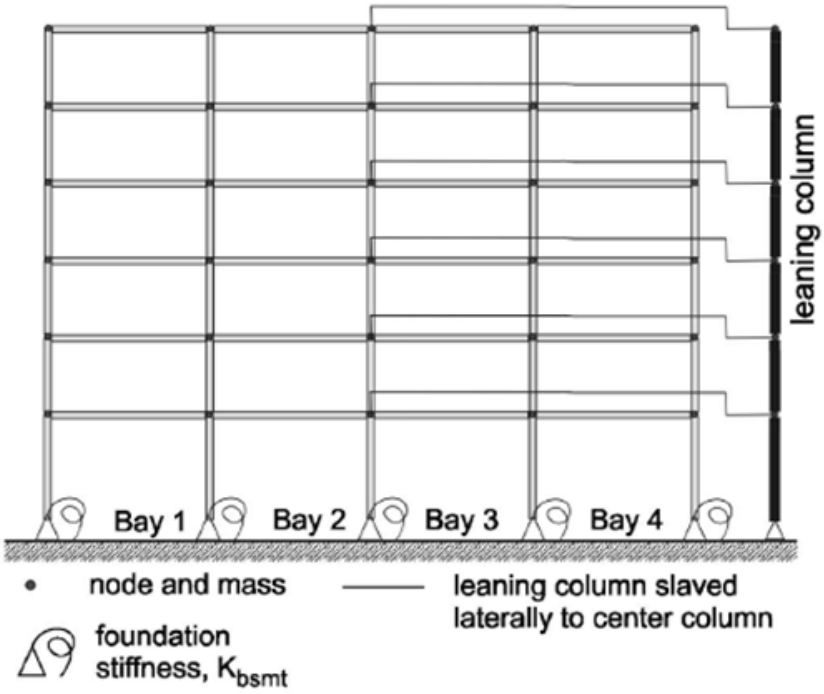

Figure 2.37 Frame model for fully restrained-moment resisting frame (Rojas et al 2005).

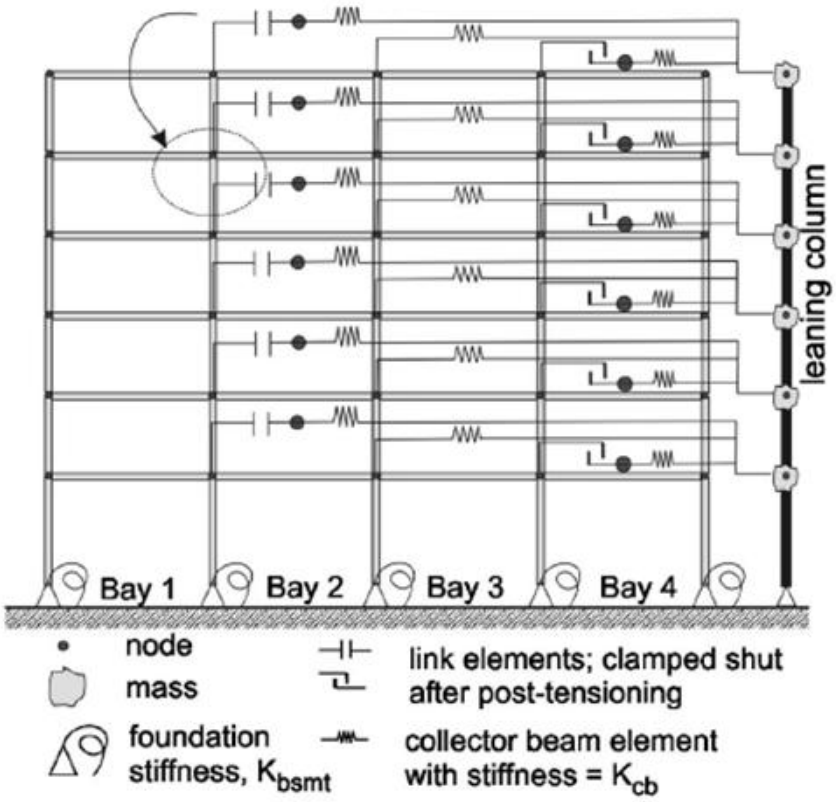

Figure 2.38 post tensioned friction damped connection-moment resisting frame (Rojas et al 2005).

Figure 2.39 shows the results of nonlinear static pushover analysis of each frame. The PFDC-MRF has a larger initial stiffness than the FR-MRF. The first gap opening in the PFDC-MRF occurs when the roof drift is 0.27%, but the reduction in the lateral stiffness due to gap opening at several locations occurs at roof drift equal to 0.53%. Beam compression yielding at the ends of the reinforcing plates of the PFDC-MRF begins when roof drift is 1.90%.

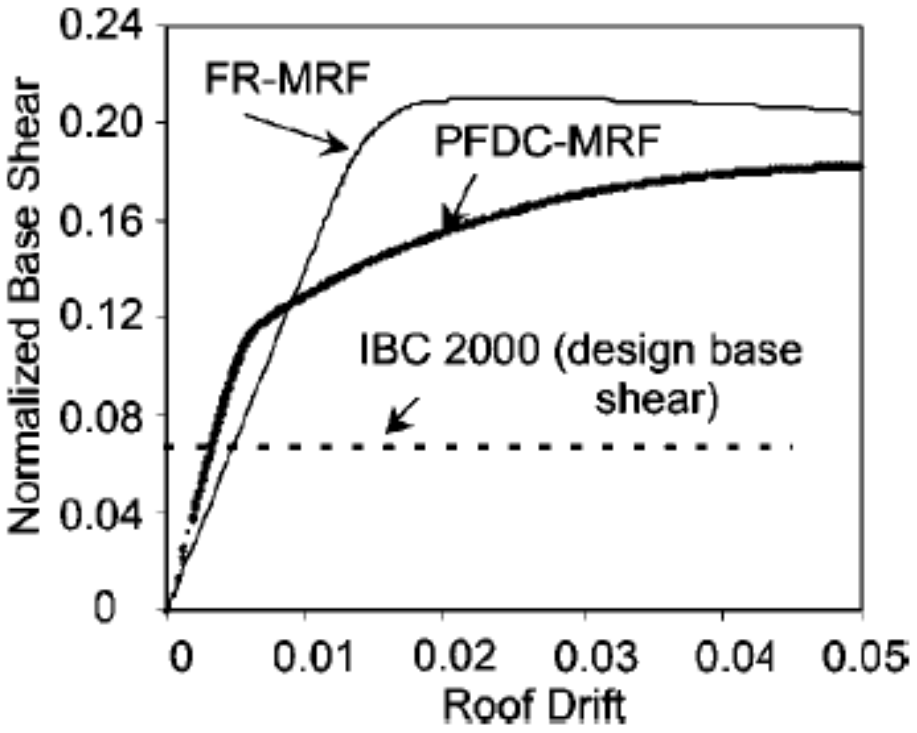

Figure 2.39 Static pushover results for fully restrained moment resisting frames and post tensioned friction damped connection moment resisting frames and comparison with design base shear (Rojas et al 2005)

Nonlinear dynamic time history analyses were conducted using eight ground motions, scaled to the DBE and MCE level, according to the Somerville (1997) approach. Figure 2.40-41 show the mean and mean plus one standard deviation of the maximum story drifts under the DBE and MCE respectively. Under the DBE the FR-MRF has higher drifts in the upper stories and lower drifts in the lower stories than the PFCD-MRF, while under the MCE the FR-MRF has lower drifts in all stories.

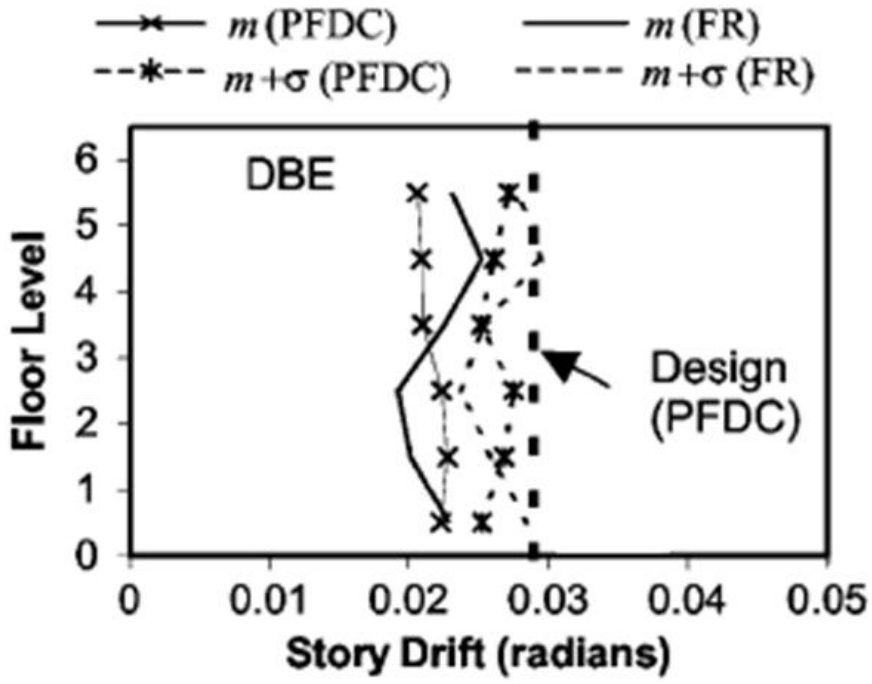

Figure 2.40 Maximum story drifts for DBE considered earthquake records (Rojas et al 2005)

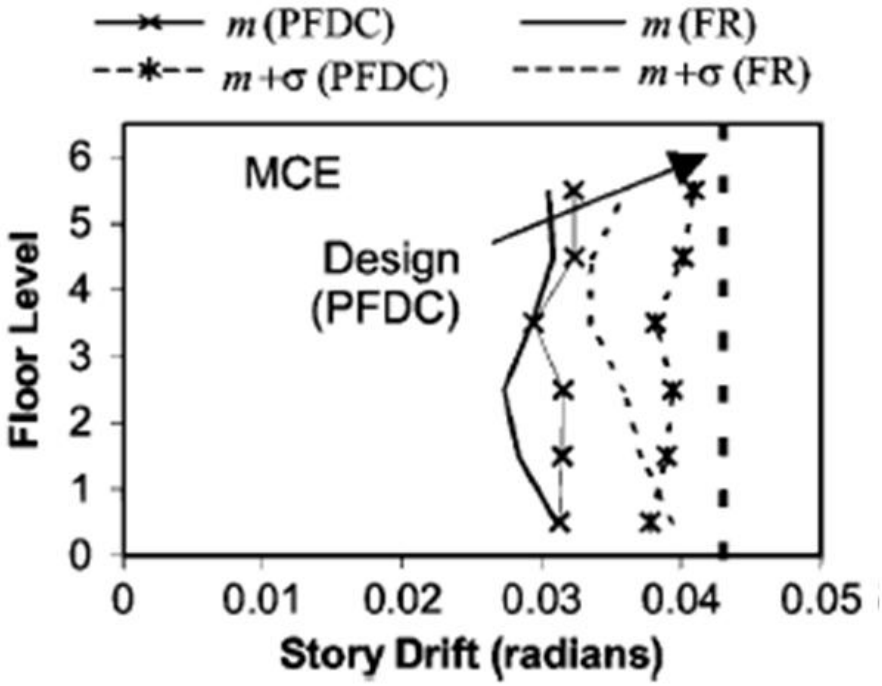

Figure 2.41 Maximum story drifts for MCE considered earthquake records (Rojas et al 2005)

Figure 2.42-43 shows the mean and mean plus one standard deviation of the residual story drifts under the DBE and MCE respectively. The PFDC shows negligible residual story drifts both under the DBE and MCE, which means that inelastic behavior (damage) is minimal.

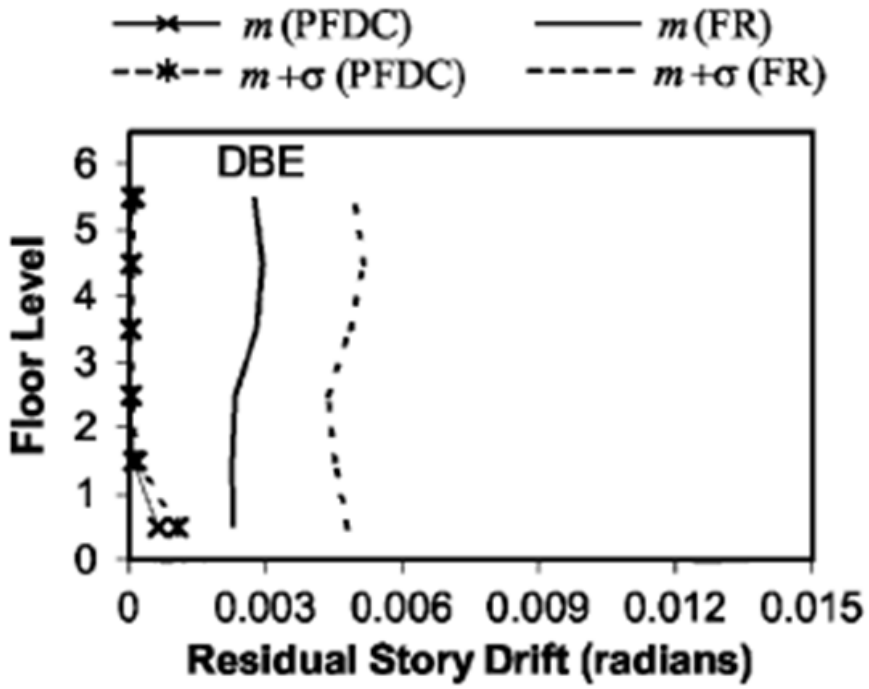

Figure 2.42 Maximum residual story drifts for DBE considered earthquake records (Rojas et al 2005)

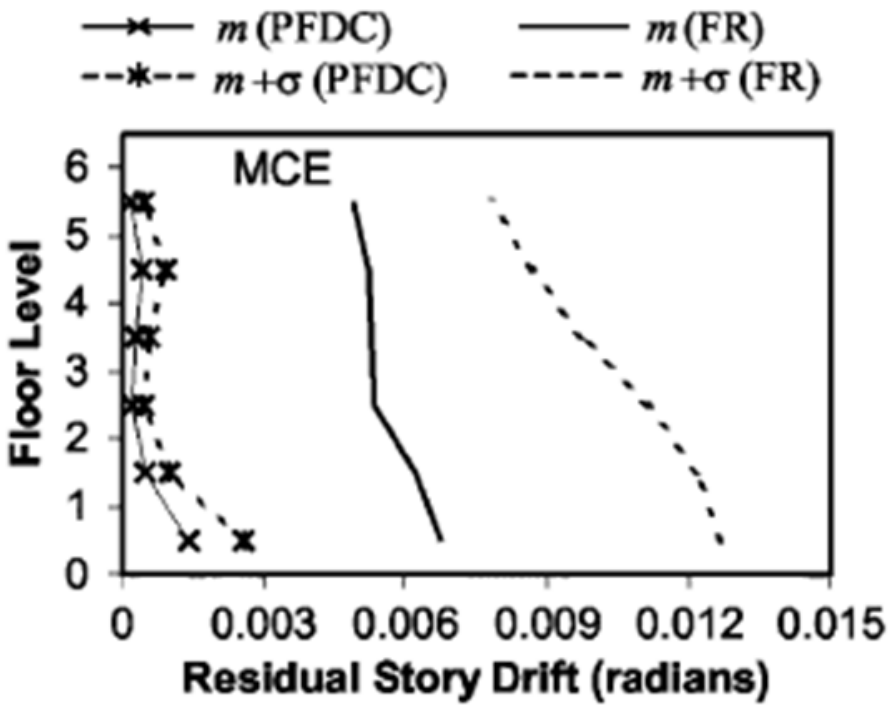

Figure 2.43 Maximum residual story drifts for MCE considered earthquake records (Rojas et al 2005)

A six storey six bay building is designed according to the recommended procedure in Garlock et al (2007) and nonlinear time history analyses were conducted using 3 ground motions, scaled on the DBE and MCE level. Figure 2.44 shows the prototype building which consist of four bay perimeter SC-MRFs. Two different designs of SC-MRFs are considered, by selecting two different α_α values, which control the yielding moment of the FEDs, which are angles (see Figure 2.1). The use of larger α_α results in larger beams and columns and a stiffer and stronger frame, which results in smaller story drifts.

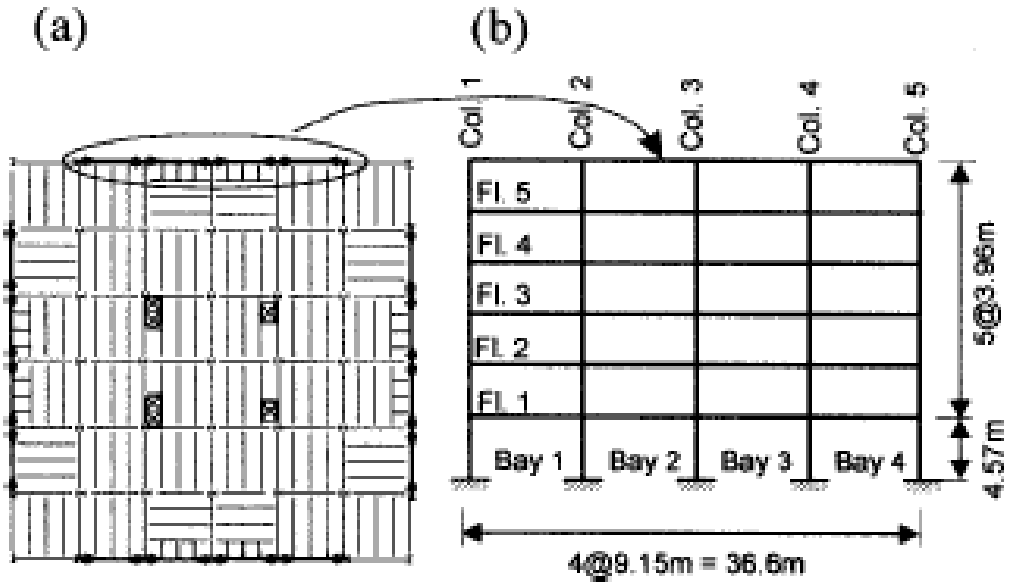

Figure 2.44 (a) Plan of prototype building; (b) Elevation of prototype frame (Garlock et al 2007)

The story drift and relative rotation design values agree with the time history results. Also time-history results indicate that the steel strain (ε) at the end of the reinforcing plates under the DBE approximately equals to two times the yield strain ($2{\cdot}\varepsilon_y$) as expected by the design procedure. The beam axial force and bending moment design values underestimate the time-history results. The design criteria for the limit states of PT connections strength, angles fracture and PT strands yielding were satisfied, but the remaining criteria of the design procedure proposed in Garlock et al (2007) were not always satisfied.

A six story building incorporating welded moment resisting frames (WMRFs) in the east-west direction was designed and a similar building incorporating self centering friction damped steel frames (SCFR) was re-designed by the proposed seismic design procedure in Kim and Christopoulos (2009b). Figure 2.45 shows the plan view of the prototype building. The columns and the beams comprising the steel WMRFs were denoted as C_1 and G_1 respectively. Design properties of frames used in this study are giver in more detail in Kim and Christopoulos (2009b). An important observation is that in the first floor of the SCFR, a higher post yielding stiffness ratio (α_p) was used in the PT connections, because of the amplified column restraining effects, resulting from the fixity at the column bases. This increase in α_p

resulted in higher PT bars area, and so premature yielding of the beam sections, which was addressed by reducing the initial PT force.

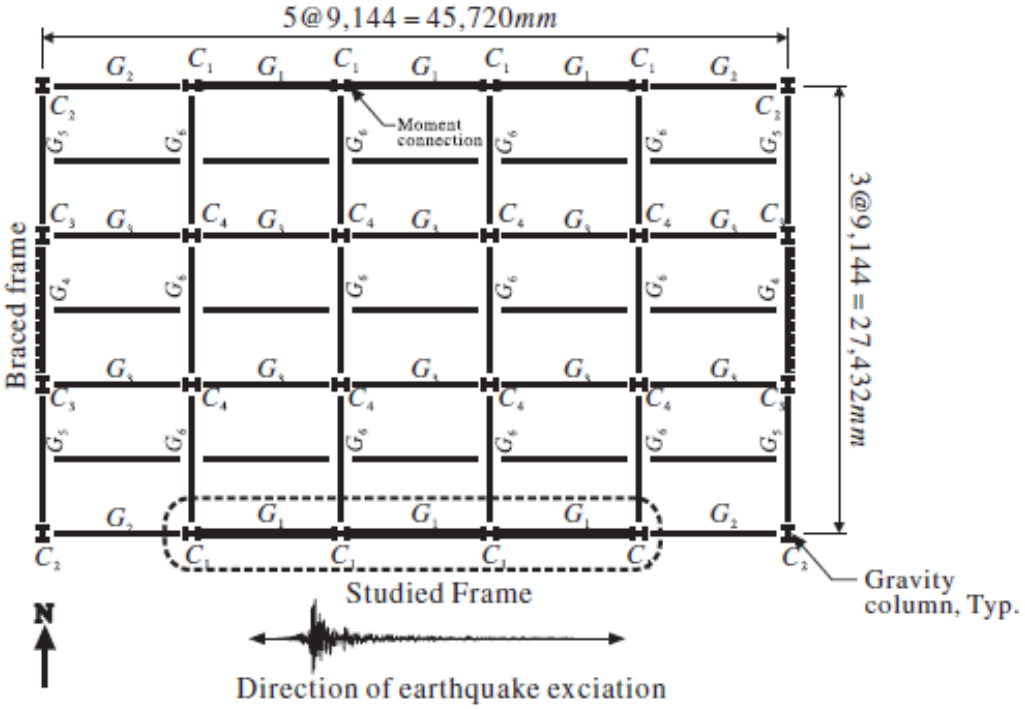

Figure 2.45 Plan view of a six-story framed prototype building (Kim and Christopoulos 2009b)

Numerical models of both the WMRF and the SCFR were developed in RUAUMOKO (Carr 2005). Figure 2.46 shows the numerical model of the SCFR, used in Kim and Christopoulos (2009b). Gravity loads were modelled by applying axial forces on columns and fixed moments and shear forces on the beams. Four leaning columns were used to count for the P-Δ effects. Each leaning column nodes were slaved to one SCFR column nodes, to allow the frame expansion resulting from the gap opening at the beam column interfaces. The strength and stiffness degradation due to local buckling on the beams was not considered. Columns and beams were modelled using beam column elements and PT connections were modelled using the modelling approach of Kim and Christopoulos (2009a) (see figure 2.28-29).

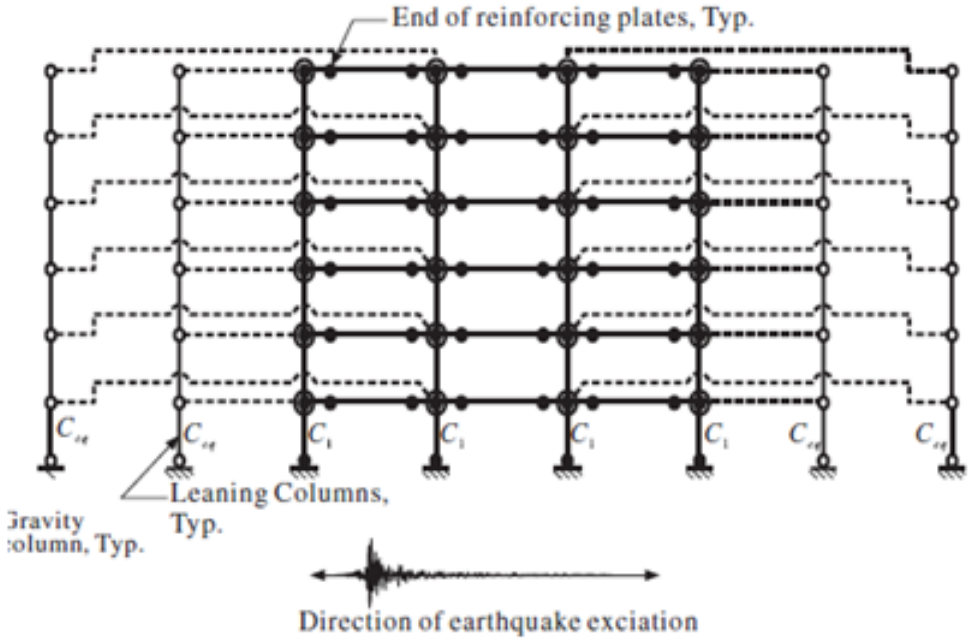

Figure 2.46 Modelling of a SCFR (Kim and Christopoulos 2009b)

Figure 2.47 shows the normalised base shear-roof drift diagrams (pushover curves) for the WMRF and SCFR. Strength deterioration of SCFR does not initiate in roof drifts up to 8%, even if P-Δ effects were considered, since this modelling does not count for stiffness and strength deterioration due to local buckling. The initial stiffness of both frames was almost the same, since they consist of same beams and columns. For roof drifts beyond 1% the SCFR resulted in small residual drifts due to yielding at the column bases. After a roof drift of 4.5%, plastic hinges were developed at the beam sections of the SCFR.

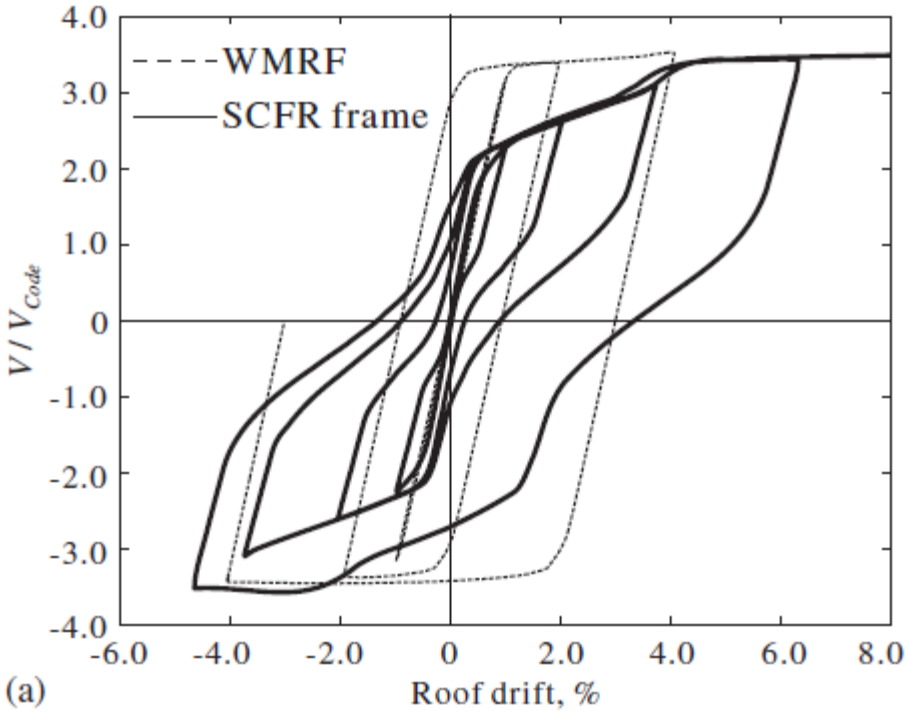

Figure 2.47 Cyclic pushover curved of WMRF and SCFR (Kim and Christopoulos 2009b)

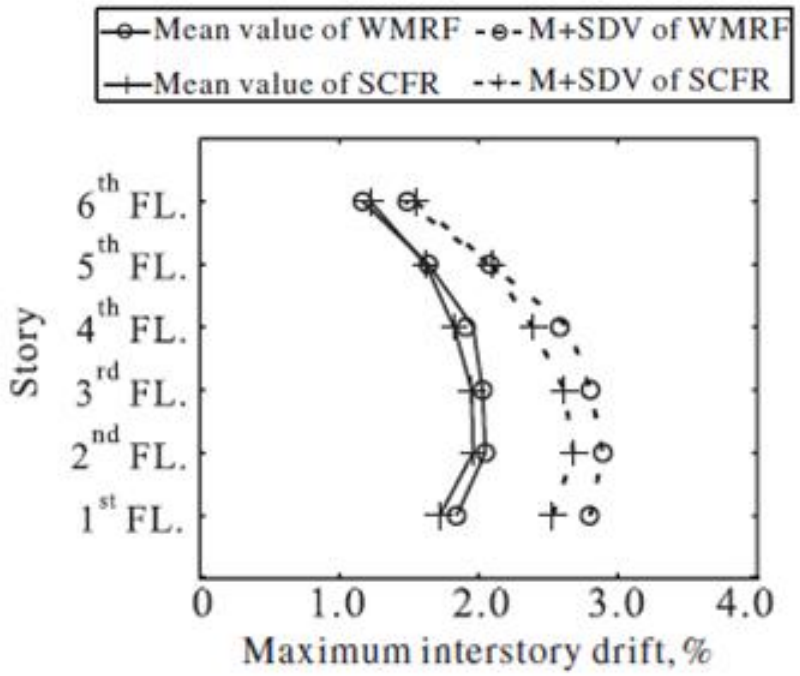

Figure 2.48 Mean plus one standard deviation values of maximum interstorey drift under the DBE ground motions (Kim and Christopoulos 2009b)

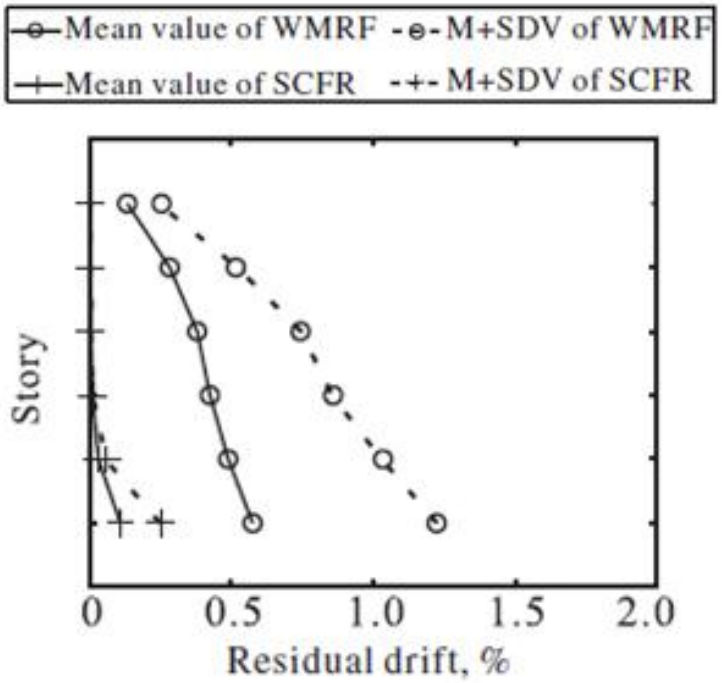

Figure 2.49 Mean plus one standard deviation values of residual drift under the DBE ground motions (Kim and Christopoulos 2009b)

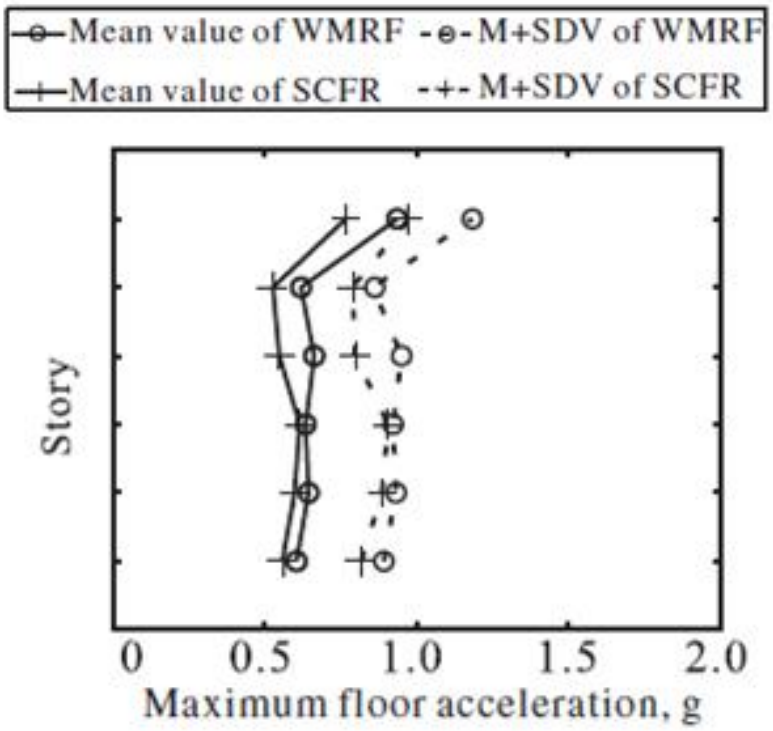

Figure 2.50 Mean plus one standard deviation values of maximum floor accelerations under the DBE ground motions (Kim and Christopoulos 2009b)

Time history anayses were conducted in both frames using set of ground motions scaled to the DBE and MCE level. Figures 2.48-50 show the mean and mean plus one standard deviation values of the maximum storey driftt, residual storey drifts and peak floor acceleration for borth the WMRF and SCFR under ground motions scaled to the DBE. While figures 2.51-53 show the same values under ground motions scaled to the MCE. The SCFR has similar storey drifts with the WMRF, satisfying the design drift demand (2%) both under the DBE and MCE level. The SCFR has almost eliminated residual drifts apart from the first storey due to yielding at the column bases, under both the DBE and the MCE level. Both frames have similar peak floor accelerations. The SCFR beam plastic rotations range from minor yielding to 0.4% under the MCE. The maximum M plus one standard deviation story drift value of the SCFR under the MCE is 4.6%,which highlights the need to ensure a ductile response (without strength and stiffness deterioration) of the SCFR.

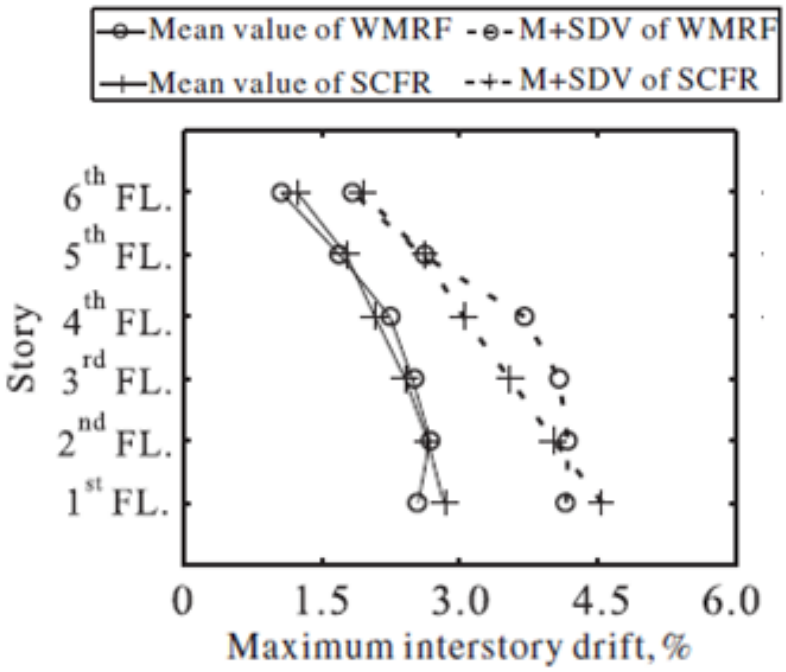

Figure 2.51 Mean and M+SDV values of maximum interstorey drift under the MCE ground motions (Kim and Christopoulos 2009b)

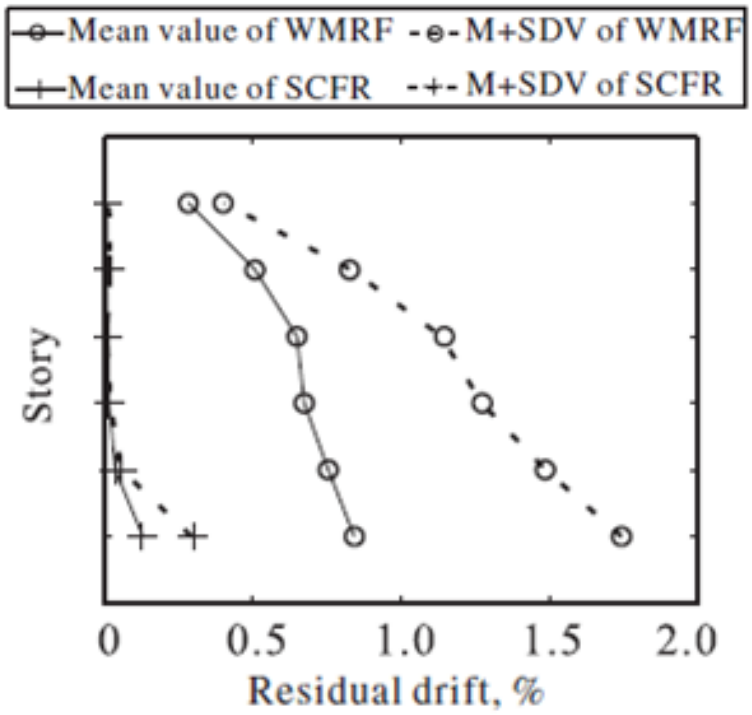

Figure 2.52 Mean and M+SDV values of residual drift under the MCE ground motions (Kim and Christopoulos 2009b)

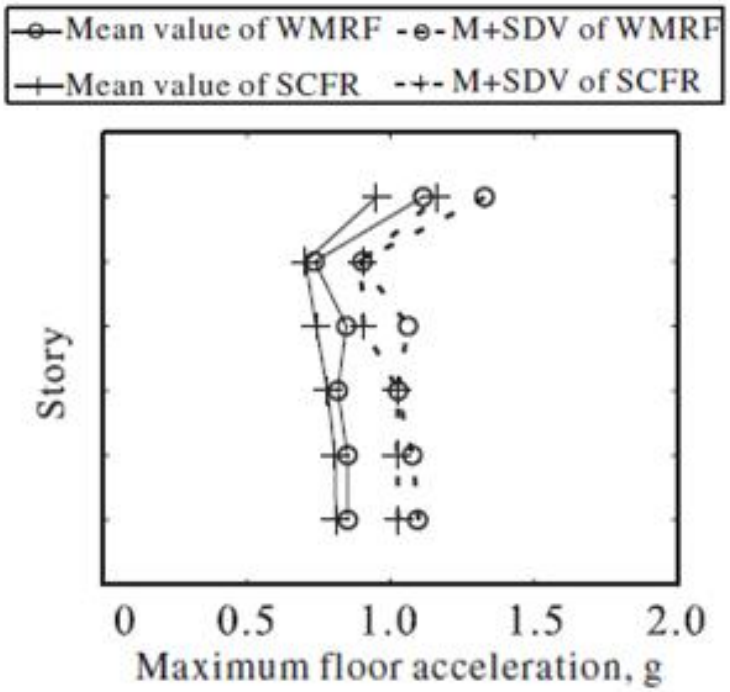

Figure 2.53 Mean and M+SDV values of maximum floor accelerations under the DBE ground motions (Kim and Christopoulos 2009b)

In (Lin et al 2013) a 7 bay, 4 story prototype office building was designed using perimeter SC-MRFs with PT connections and web friction devices (FDs). Figure 2.54 shows the FD, which includes two channel sections welded to column flanges. Brass plates are installed between the channels and the beam web, to provide a reliable brass-steel friction interface. Channels are clamped to the beam web by friction bolts, which are tightened and produce a normal force on the friction interface.

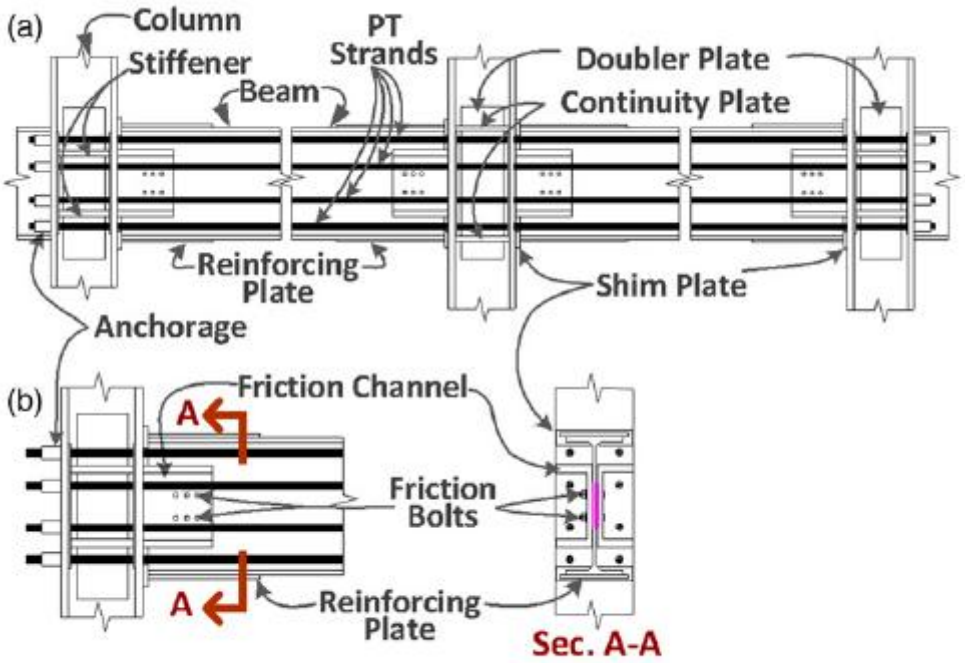

Figure 2.54 (a) Elevation of a 2-bay SC-MRF with PT strands and FDs; (b) connection details (Lin et al 2013a, b)

Figure 2.55 (a) shows the plan view of the 7x7 bay, 4 story prototype office building. Each perimeter frame has two 2 bay steel SC-MRFs with PT connections and FDs. The prototype building was designed according to (ASCE 2005) and the design procedure of (Garlock et al 2007).

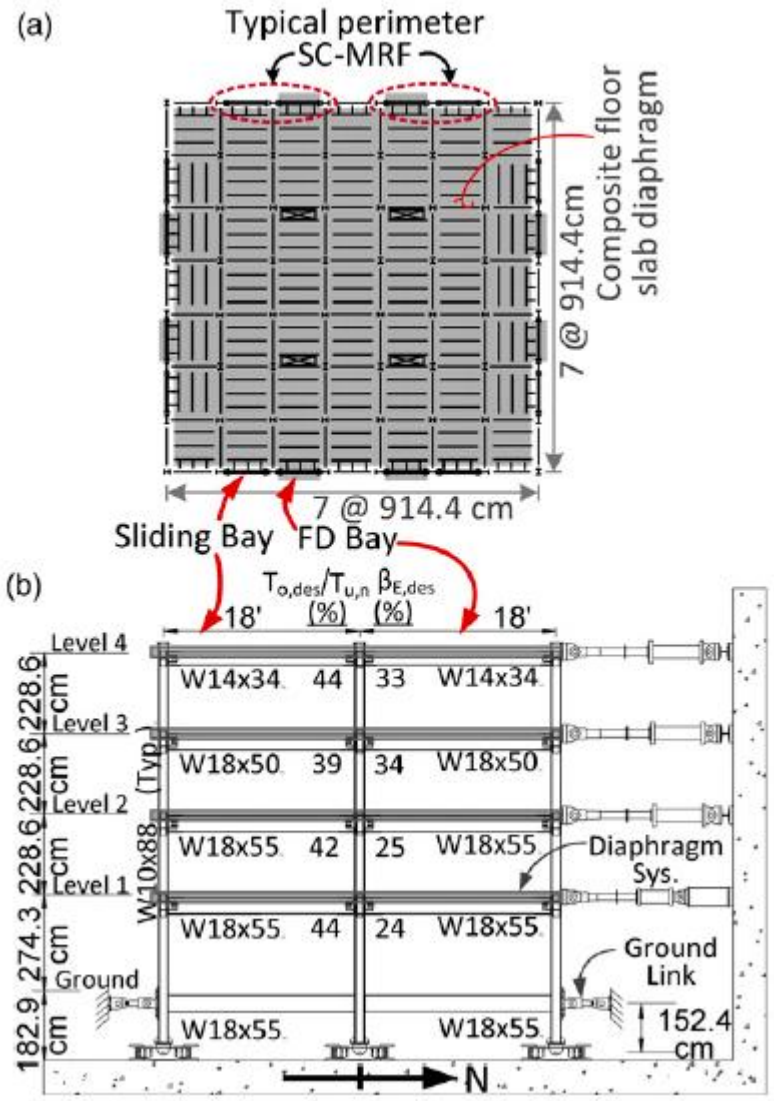

Figure 2.55 (a) prototype building plan; (b) SC-MRF test frame elevation (Lin et al 2013a,b)

One quarter of the building was simulated using the hybrid simulation method, considering the symmetry of the plan. The experimental substructure consisted of one 2 bay SC-MRF acting in one direction of the building, while the remaining one quarter of the building was simulated as an analytical substructure. Figure 2.55 (b) shows the SC-MRF test frame elevation, which has a 0.6 scale factor. A pin support is installed at the columns base, representing the inflection point of the basement story column. Welded beam-column connections are used for the ground level beams and PT connections are used for the beams above ground level.

The floor diaphragm is attached to the beam in one bay ("FD" bay). The beam in the other bay ("sliding" bay) and the columns are free to move horizontally relative to the FD to avoid restraining gap opening of the PT connections. The floor diaphragm is simulated through a concrete slab, connected to the test frame with shear studs. To accommodate the relative movements between the slab and the columns, equations for the sizing of cutouts on the slab are provided in Lin et al (2013a,b).

The tested SC-MRF was subjected into 4 ground motions scaled to the DBE level and 2 ground motions scaled to the MCE level. Figure 2.56-59 show the displacement time histories of all floors of the SC-MRF under 4 ground motions scaled to DBE.

Under the DBE ground motions all floors displacements return to zero, so residual drifts are eliminated and self-centering behaviour is demonstrated. The design demands (relative rotation, interstorey drift) have been exceeded in two of the four DBE ground motions. Also the DBE results indicate that the ratio between the interstorey drift and roof drift which is assumed equal to 1.5 in the design procedure of Garlock et al (2007), appears to be conservative for the lower stories. Minor yielding occurred on the beams under the DBE ground motions, since the maximum recorded steel strain was $1.02\varepsilon_y$.

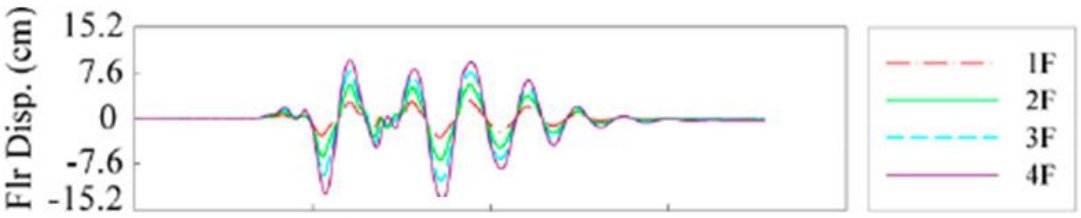

Figure 2.56 Floor displacement time histories from one ground motion scaled to DBE (Lin et al 2013a)

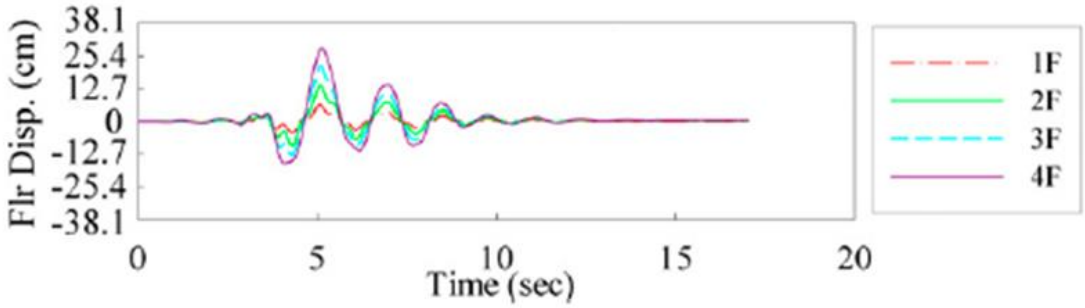

Figure 2.57 Floor displacement time histories from one ground motion scaled to DBE (Lin et al 2013a)

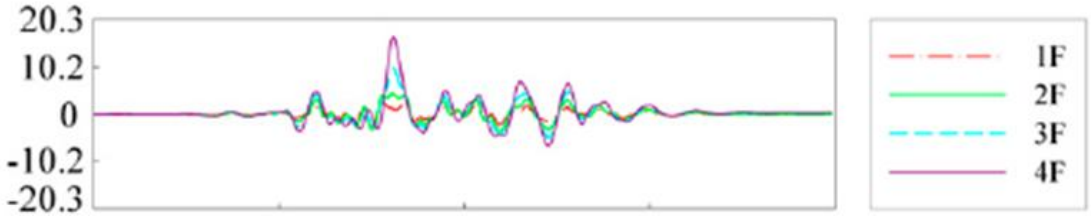

Figure 2.58 Floor displacement time histories from one ground motion scaled to DBE (Lin et al 2013a)

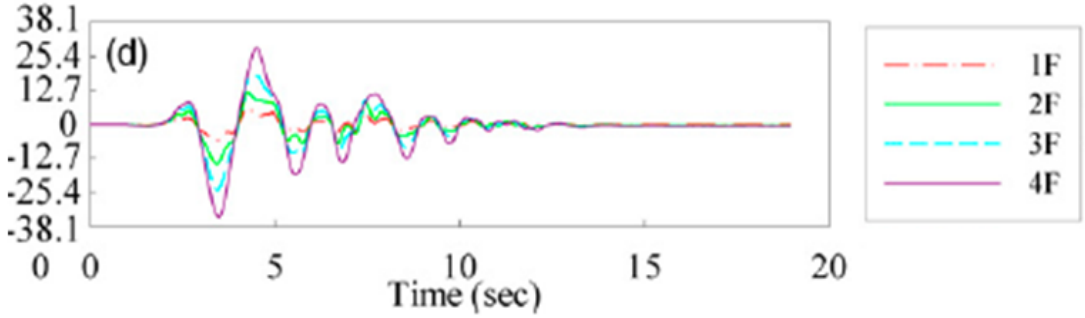

Figure 2.59 Floor displacement time histories from one ground motion scaled to DBE (Lin et al 2013a)

Figure 2.60-61 show the displacement time histories of all floors of the SC-MRF under 2 ground motions scaled to the MCE. The largest residual drift obtained under the MCE ground motions is 0.18%, which is very small and so self centering behaviour is provided. The connections relative rotations under the MCE are higher than the MCE demands. Also significant yielding occurred on the beams flanges, up to 9 ε_y, however beam local buckling did not occur.

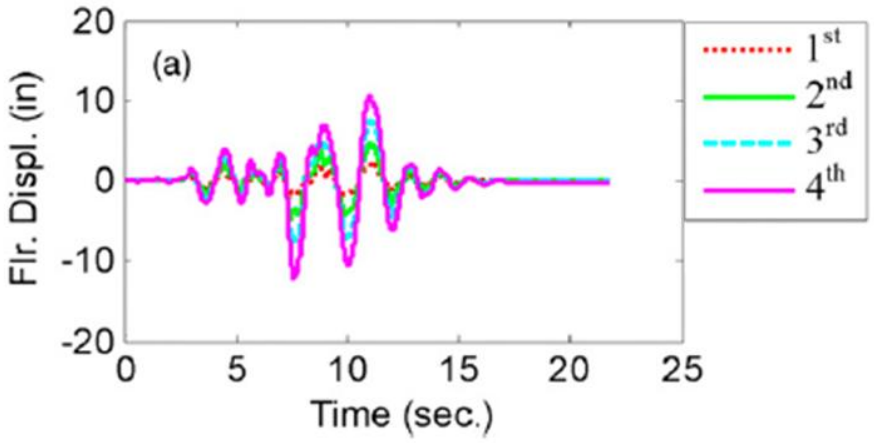

Figure 2.60 Floor displacement time histories from one ground motions scaled to MCE (Lin et al 2013b)

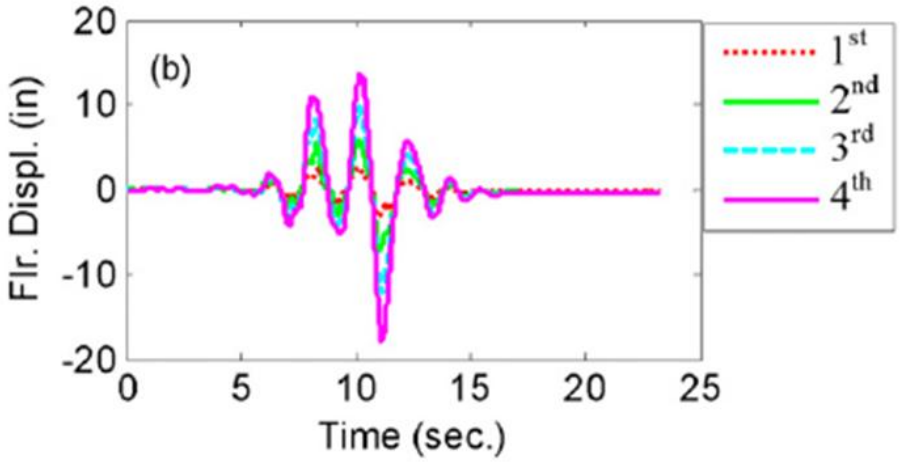

Figure 2.61 Floor displacement time histories from one ground motions scaled to MCE (Lin et al 2013b)

Also quasi static tests were performed up to higher interstorey drifts than those of the MCE, to examine the ultimate behaviour of the PT connections. Figure 2.62 shows local buckling on the bottom flange and bottom part of the web of the beam, occurred under roof drift higher than 1.8 times the MCE demand.

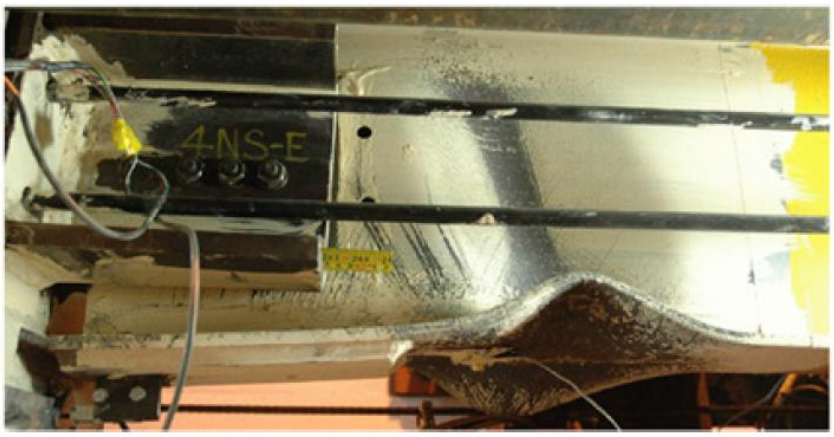

Figure 2.62 Buckling of beam bottom flange and web

To prevent PT strands yielding, (Lin et al 2013b) use a PT strand fuse, which yields at a specific load to limit the force developed in the PT strands. Quasi static tests indicate that the recommended fuses controlled the force developed in the PT strands and prevented the PT strands from yielding.

2.5 Preliminary assessment of SC-MRFs with PT connections using web hourglass shape pins

A new steel PT connection using web hourglass shape steel pins (WHPs) has been recently developed, modelled in ABAQUS and experimentally validated in Vasdravellis et al (2013a,b). The connection isolates inelastic deformations in WHPs, avoids damage in other connection parts as well as in beams and columns, and, eliminates residual drifts. WHPs do not interfere with the composite slab and are very easy-to-replace without bolting or welding, and so, the connection enables non-disruptive repair and rapid return to building occupancy in the aftermath of a strong earthquake.

Figure 2.63 shows a schematic representation of a SC-MRF incorporating PT connections with WHPs, and figure 2.64 shows the details of an exterior PT connection. Two high strength steel bars located at the mid-depth of the beam, one at each side of the web, pass through holes drilled on the column flanges. The bars are post-tensioned and anchored to the exterior column flange, and so, clamp the beam to the column. Four WHPs are inserted in aligned holes drilled on the web of the

beam and on strong supporting plates. The supporting plates are welded on the column flanges and have large thickness to provide fixed support boundary conditions to WHPs. Energy dissipation is provided by inelastic bending of the WHPs which are symmetrically placed (close to the top and bottom beam flange) to provide increased lever arm, and so, increased internal moment resistance. Both sides of the beam web are reinforced with steel plates to increase the contact surface of the WHPs with the web. So, possible ovalization of the holes drilled on the web and the reinforcing plates under the WHP bearing forces will be negligible and pronounced pinching behavior under cyclic deformations can be avoided. The connection includes beam flange reinforcing plates to avoid excessive early yielding in the beam flanges under the high PT bars forces. In addition, the panel zone is strengthened with doubler and continuity plates.

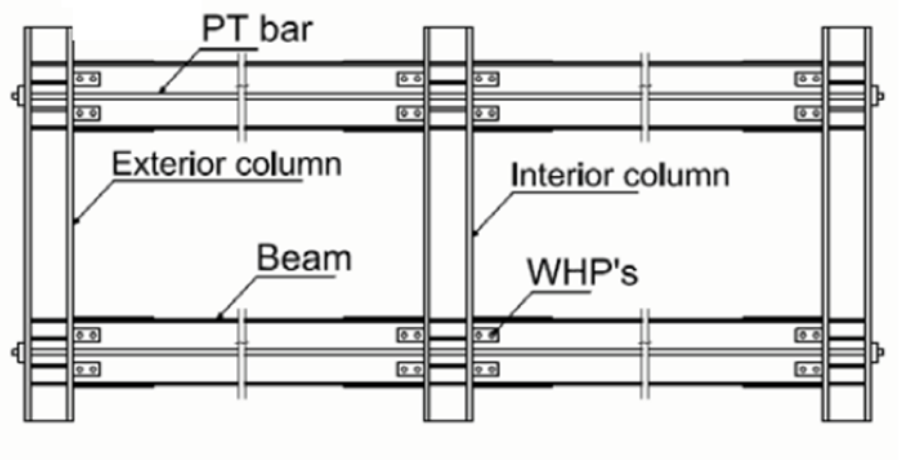

Figure 2.63 SC-MRF incorporating PT connections with WHPs (Vasdravellis et al 2013a,b)

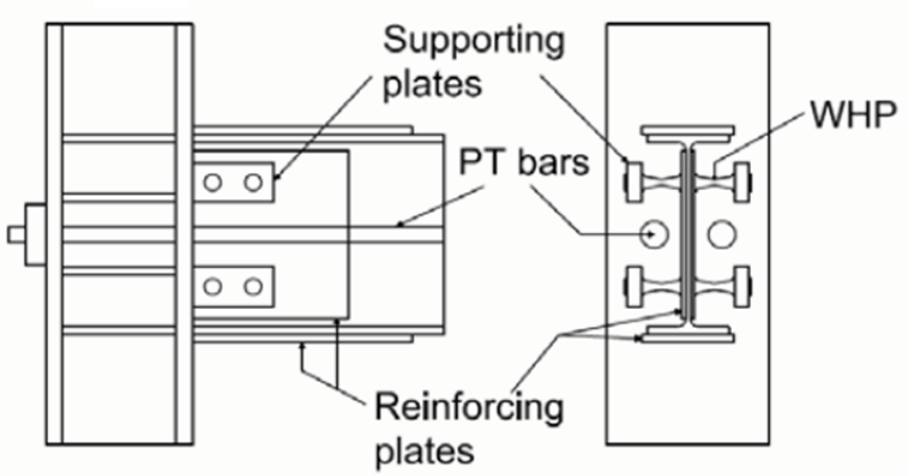

Figure 2.64 Exterior PT connection details (Vasdravellis et al 2013a,b)

Preliminary studies on SC-MRFs using PT connections with WHPs have been carried out as part of this PhD, and presented in (Dimopoulos et al 2013). In these studies a model for the PT connection with WHPs and the associated beams and columns was developed in OpenSees. This model consists of nonlinear beam-column elements, and hysteretic and contact zero-length spring elements appropriately placed in the beam-column interface. More details on the modelling procedure followed are provided in (Dimopoulos et al 2013) and in chapter 3 of this PhD thesis. The model was calibrated against experimental results and found to accurately simulate the connection behavior.

Figure 2.65 (a) shows the plan view of the 5-storey, 4-bay by 3-bay prototype office building used for the study. The building has four identical MRFs to resist lateral loads in the longitudinal plan direction. The design study focused on one of the interior MRFs shown in figure 2.65 (b). This MRF was designed either as a conventional steel MRF according to EC8 (Eurocode 8 2013) or as a steel SC-MRF using PT connections with WHPs according to Garlock et al (2007) to compare their seismic performance. Both the MRF and the SC-MRF have same beam and column cross sections, while WHPs and the required beam flange reinforcing plated of the SC-MRF have practical sizes.

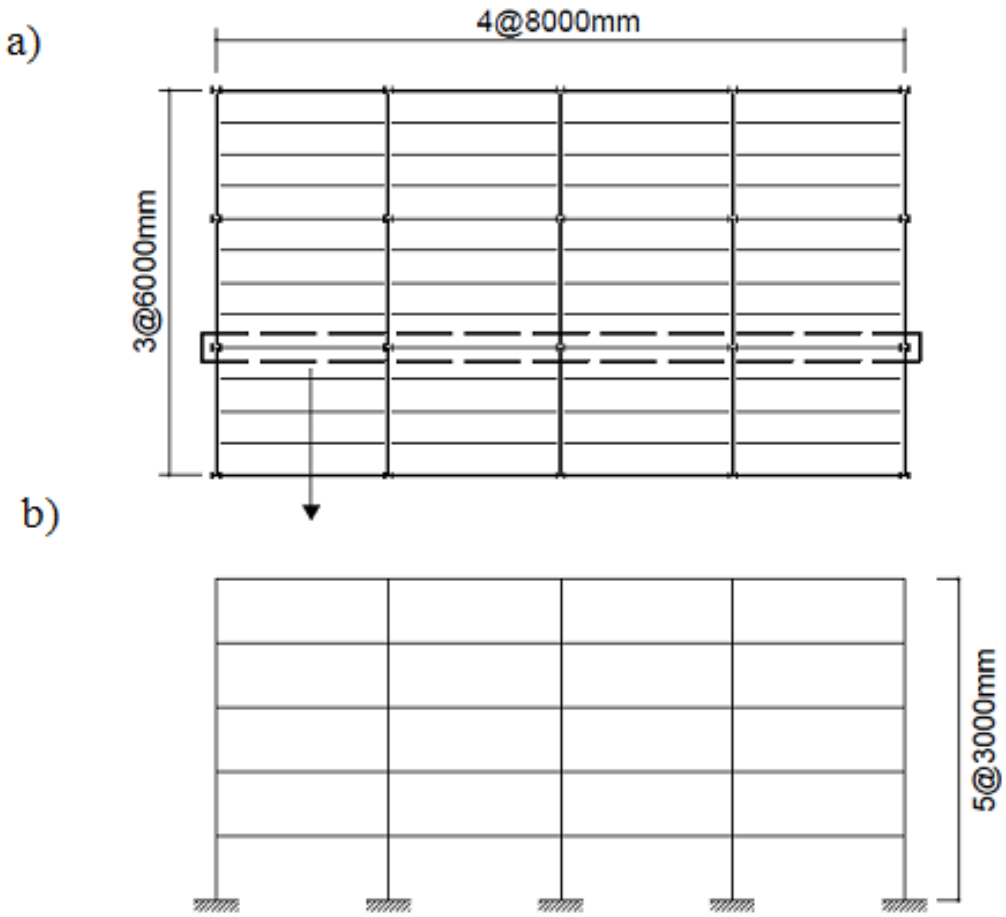

Figure 2.65 (a) Plan view of prototype building; (b) elevation of interior MRF (Dimopoulos et al 2013)

Figure 2.66-67 show the base shear coefficient (V/W) - roof drift (θ_r) behaviour of the conventional MRF and the SC-MRF from nonlinear monotonic (pushover) static analysis using nonlinear models of the MRF and the SC-MRF in OpenSees (Mazzoni et al. 2006). V is the base shear and W is the seismic weight. An inverted triangular force distribution along with roof displacement control was used in these analyses. The MRF and the SC-MRF have comparable base shear strengths and comparable initial stiffness. The pushover curves are plotted along with points associated with structural limit states and vertical lines corresponding to roof drifts expected under the FOE, DBE and MCE. The structural limit states for the conventional MRF are beam yielding and base column yielding and occur at θ_r equal to 0.82% and 0.92% respectively. The conventional MRF avoids damage under the FOE but experiences significant damage under the DBE. The structural limit states

for the SC-MRF are decompression in a PT connection, WHP yielding, base column yielding and beam yielding. Figure 2.67 shows that the beams of the SC-MRF are damage-free for θ_r equal or lower than 3%, i.e., drifts higher than the MCE. Damage in the SC-MRF is experienced at the column bases that yield at θ_r equal to 0.97%. No PT bar yielding is observed. The first decompression occurs at θ_r equal to 0.4% while WHPs yield at θ_r equal to 0.62% which is almost equal to the FOE drift. Decompression does not involve damage while yielding of the WHPs is acceptable under low drifts since WHPs can be easily replaced without bolting or welding. The conventional MRF experiences softening at θ_r equal to 1.25% while the SC-MRF shows a more gradual softening behaviour. In particular, the SC-MRF shows softening due to decompression in the PT connections at low drifts and further softening due to plastic deformations at the column bases and yielding of a large number of WHPs at θ_r equal to 1%.

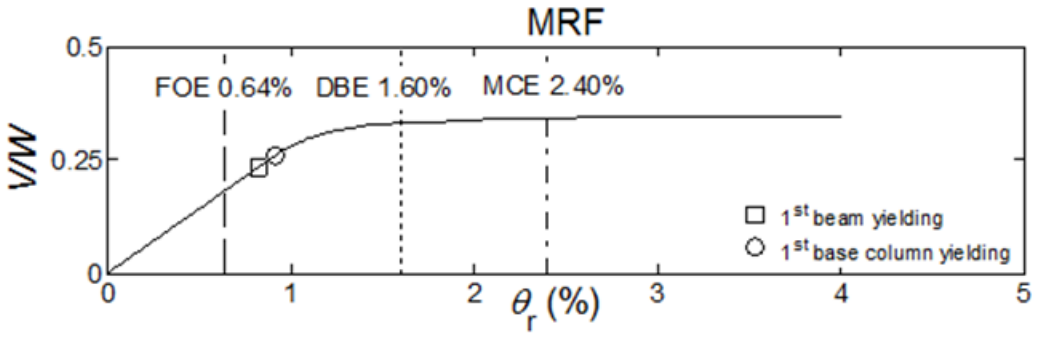

Figure 2.66 Base shear coefficient – roof drift behavior of MRF from nonlinear monotonic (pushover) static analysis (Dimopoulos et al 2013)

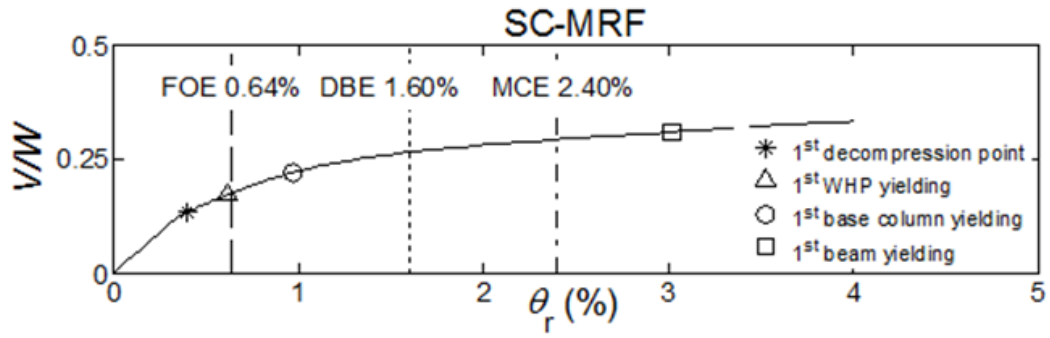

Figure 2.67 Base shear coefficient– roof drift behavior of SC-MRF from nonlinear monotonic (pushover) static analysis (Dimopoulos et al 2013)

Figures 2.68-69 show the V/W - θ_r behaviour of the MRF and the SC-MRF from nonlinear cyclic (push-pull) static analysis. The first cycle of the analysis is performed up to the DBE drift, while the next cycle up to the MCE drift. The SC-MRF shows full re-centering capability under the DBE, adequate energy dissipation and a small residual drift under the MCE due to plastic deformations at the column bases. The conventional MRF shows large energy dissipation capacity due to plastic deformations at the beam ends and at the column bases, and the possibility of experiencing large residual drifts under the DBE and MCE.

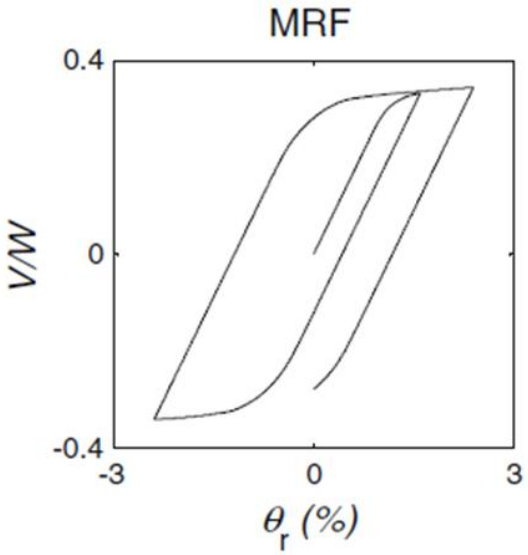

Figure 2.68 Base shear coefficient-roof drift behavior of MRF from nonlinear cyclic (push-pull) static analysis (Dimopoulos et al 2013)

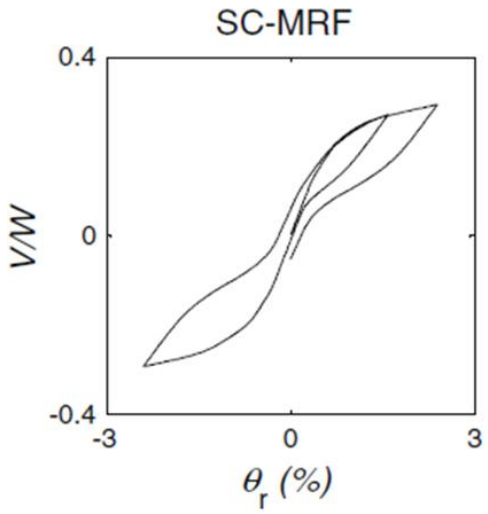

Figure 2.69 Base shear coefficient-roof drift behavior of SC-MRF from nonlinear cyclic (push-pull) static analysis (Dimopoulos et al 2013)

A set of 20 earthquake ground motions were selected, and scaled to the FOE, DBE and MCE level, according to the scaling procedure of Somerville (1997). These ground motions were used in 2D nonlinear dynamic time history analyses to evaluate the performance of the SC-MRF and the performance of the conventional MRF. More details on the selection and scaling of the ground motions can be found in Dimopoulos et al (2013).

Figures 2.70-71 show the comparison of the roof drift time histories for the conventional MRF and the SC-MRF under one of the 20 selected ground motions, scaled to the DBE and MCE. Near the end of the time histories the SC-MRF oscillates around the origin, indicating negligible residual drift, while the conventional MRF experiences residual drifts. The peak roof displacements of the MRF and the SC-MRF are similar.

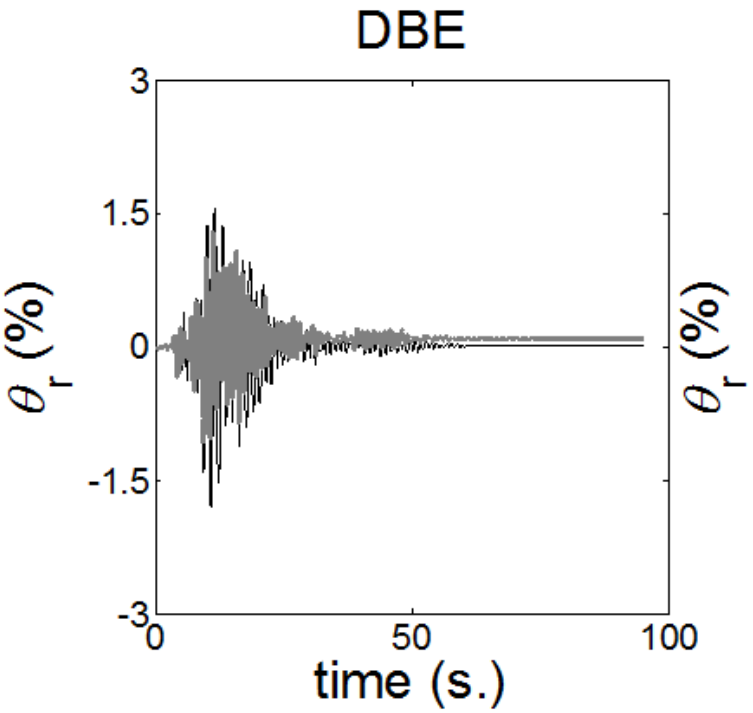

Figure 2.70 Comparison of the roof drift time histories under one of the 20 selected ground motions, scaled to the DBE (Dimopoulos et al 2013)

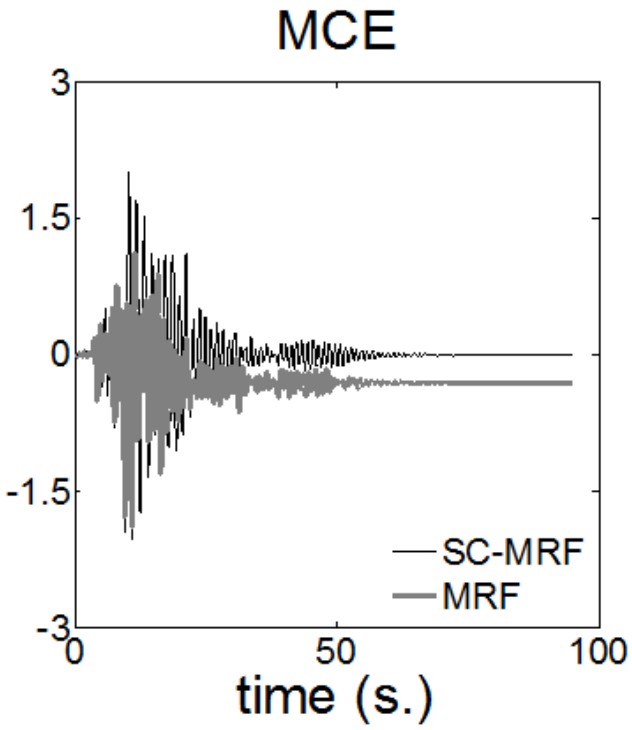

Figure 2.71 Comparison of the roof drift time histories under one of the 20 selected ground motions, scaled to the MCE (Dimopoulos et al 2013)

Figures 2.72-73 show the stress-strain hysteresis at points A and B (extreme column base flange fibers), and, C and D (extreme beam flange fibers) of the first storey of the conventional MRF under one of the 20 ground motions scaled to the DBE and MCE. Figures 2.78-79 show similar information for the SC-MRF. The stress-strain hysteresis immediately after the end of the beam flange reinforcing plate (points E and F) of the SC-MRF is also shown. The SC-MRF eliminates beam plastic deformations under both the DBE and MCE, while the conventional MRF experiences appreciable beam damage.

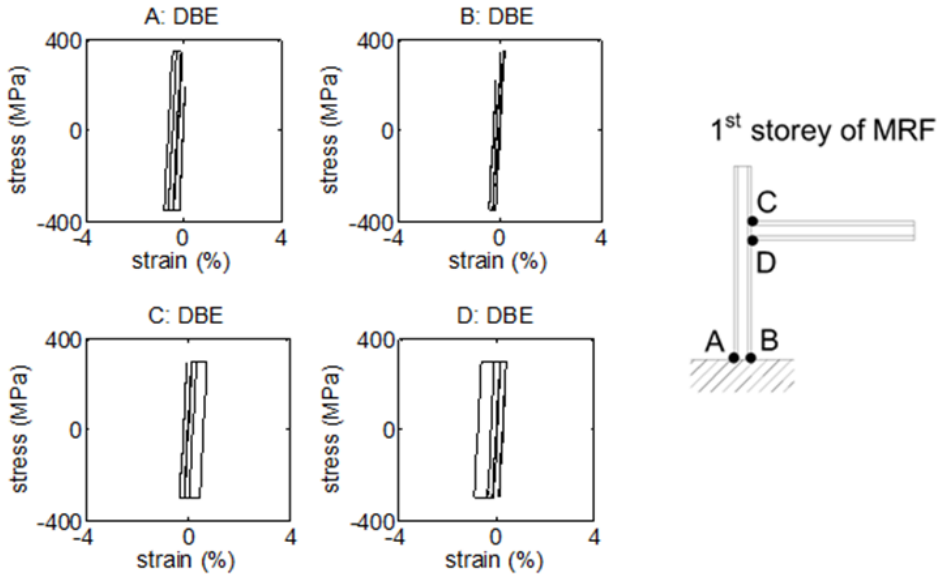

Figure 2.72 Stress-strain hysteresis at points A, B, C and D of the conventional MRF under one of the 20 ground motions scaled at the DBE (Dimopoulos et al 2013)

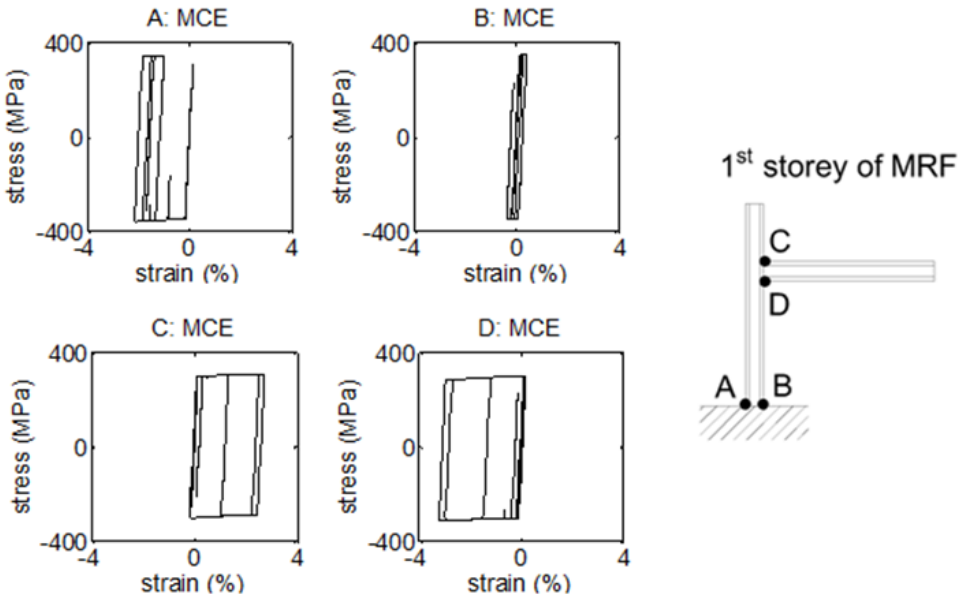

Figure 2.73 Stress-strain hysteresis at points A, B, C and D of the conventional MRF under one of the 20 ground motions scaled at the MCE (Dimopoulos et al 2013)

Figures 2.74-75 show that the column bases of the SC-MRF experience larger plastic deformations than those of the column bases of the conventional MRF.

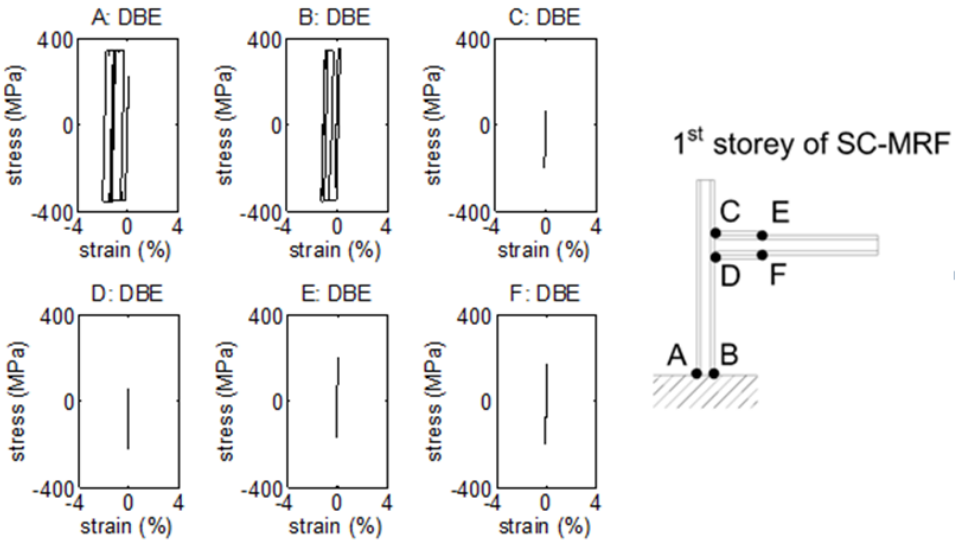

Figure 2.74 Stress-strain hysteresis at points A, B, C, D, E and F of the SC-MRF under one of the 20 ground motions scaled at the DBE

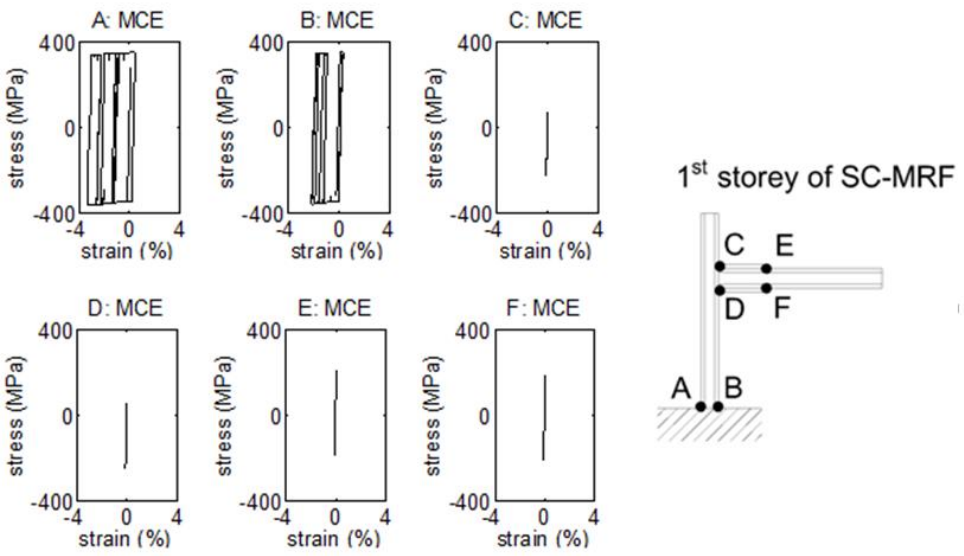

Figure 2.75 Stress-strain hysteresis at points A, B, C, D, E and F of the SC-MRF under one of the 20 ground motions scaled at the MCE

Figures 2.76-81 show the μ, μ + σ and median maximum interstorey drift ($\theta_{s\text{-}max}$) values of the MRF and SC-MRF under the 20 selected earthquake ground motions scaled to the FOE, DBE and MCE. The μ, μ + σ and median height-wise $\theta_{s\text{-}max}$ distributions show identical shapes. The MRF has the largest $\theta_{s\text{-}max}$ in the fourth storey with μ values equal to 0.75% under the FOE, 1.65% under the DBE and 2.2% under the MCE, i.e., close to the design values of 0.64% under the FOE and 1.6% under the DBE, and, smaller than the design value of 2.4% under the MCE. The SC-MRF has the largest $\theta_{s\text{-}max}$ in the fourth storey with mean values equal to 0.75% under the FOE, 1.8% under the DBE and 2.5% under the MCE, i.e., slightly larger than the DBE and MCE design ones.

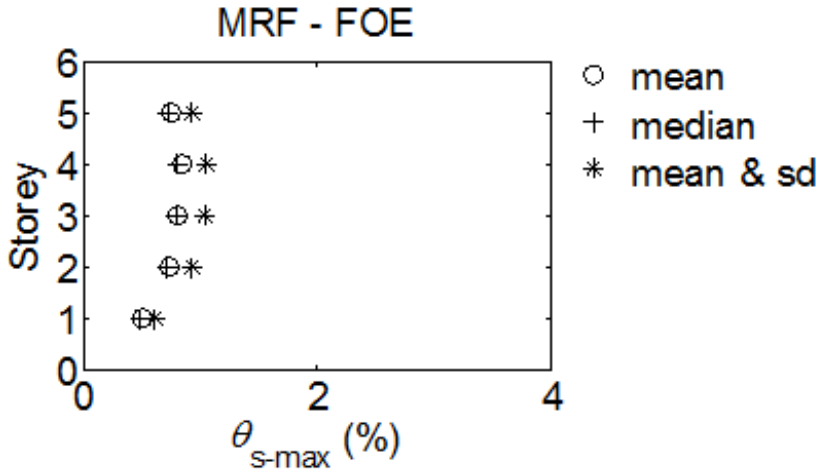

Figure 2.76 Statistics of peak storey drifts of the conventional MRF under 20 earthquake ground motions scaled to the FOE (Dimopoulos et al 2013)

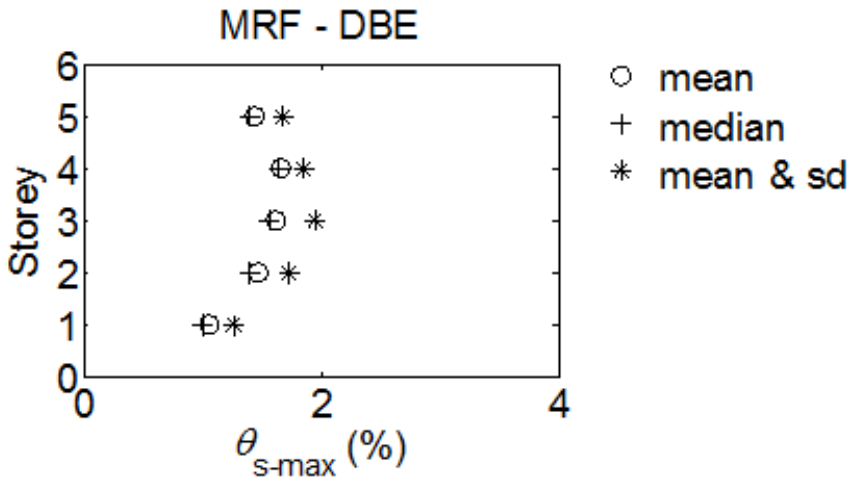

Figure 2.77 Statistics of peak storey drifts of the conventional MRF under 20 earthquake ground motions scaled to the DBE (Dimopoulos et al 2013)

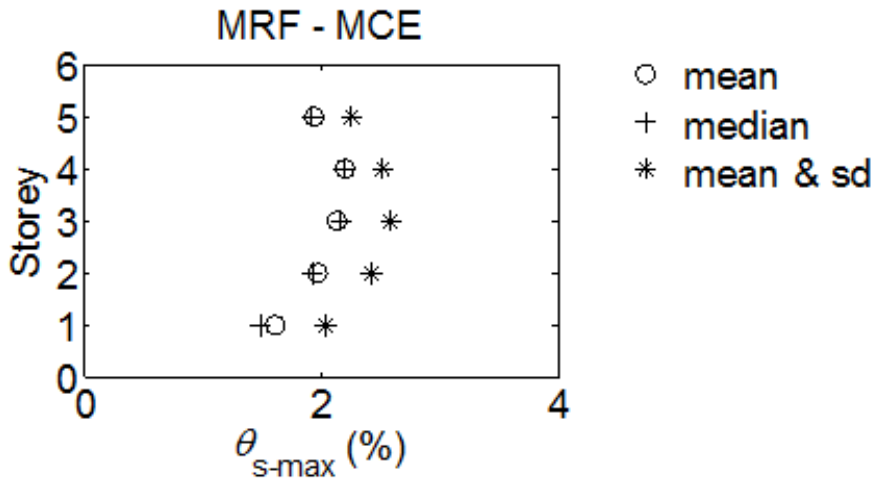

Figure 2.78 Statistics of peak storey drifts of the conventional MRF under 20 earthquake ground motions scaled to the MCE (Dimopoulos et al 2013)

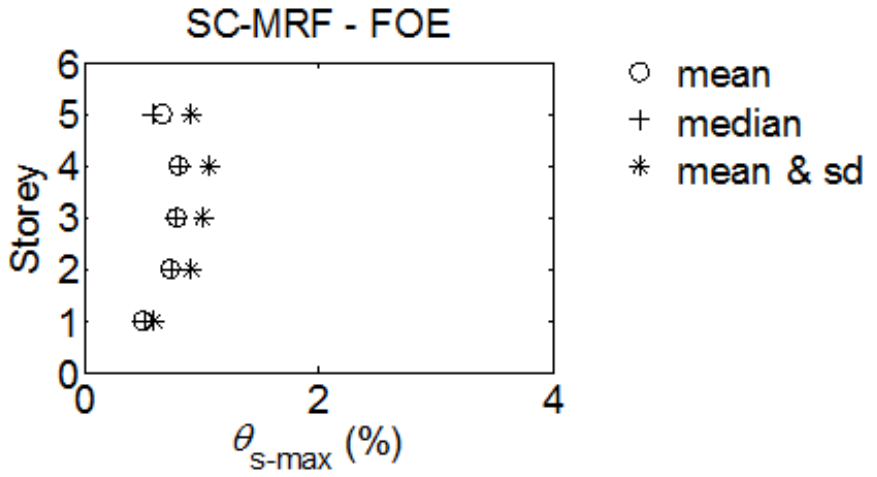

Figure 2.79 Statistics of peak storey drifts of the SC-MRF under 20 earthquake ground motions scaled to the FOE (Dimopoulos et al 2013)

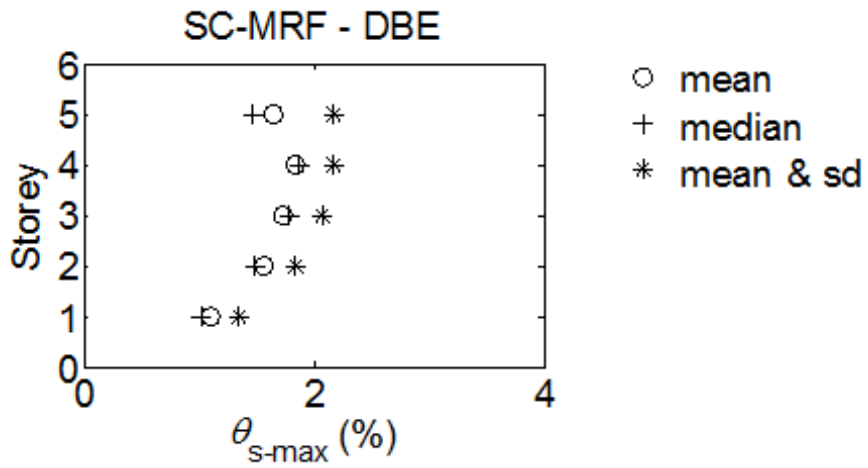

Figure 2.80 Statistics of peak storey drifts of the SC-MRF under 20 earthquake ground motions scaled to the DBE (Dimopoulos et al 2013)

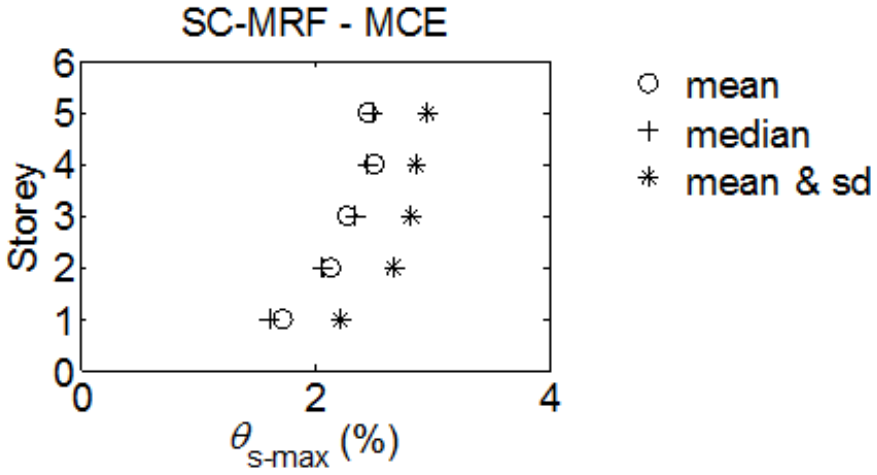

Figure 2.81 Statistics of peak storey drifts of the SC-MRF under 20 earthquake ground motions scaled to the MCE (Dimopoulos et al 2013)

Figures 2.82-87 show the μ, $\mu + \sigma$ and median values of the residual storey drift ($\theta_{s\text{-}res}$). $\theta_{s\text{-}res}$ show a uniform height-wise distribution for the conventional MRF and large dispersion compared to that of $\theta_{s\text{-}max}$. The largest $\theta_{s\text{-}res}$ of the conventional MRF occurs in the first storey with mean values equal to 0.1% under the DBE and 0.3% under the MCE. The associated $\mu + \sigma$ $\theta_{s\text{-}res}$ values are equal to 0.25% under the DBE and 0.6% under the MCE. The latter $\theta_{s\text{-}res}$ values indicate that repair of damage in the conventional MRF would be costly and disruptive after the DBE and not financially viable after the MCE (McCormick et al 2008). These results highlight the need for EC8 (Eurocode 8 2013) to include residual deformations as an additional seismic

performance parameter. The SC-MRF practically eliminates residual storey drifts apart from the first storey that has μ and $\mu + \sigma\ \theta_{s\text{-}res}$ values equal to 0.1% and 0.15% under both the DBE and MCE. The latter $\theta_{s\text{-}res}$ values are lower than the global sway imperfections defined in EC3 (Eurocode 3 2010) and so it can be assumed that there will be no need for these residual drifts to be straightened out. Figure 2.87 shows small $\mu + \sigma\ \theta_{s\text{-}res}$ values in the third storey of the SC-MRF due to modest yielding in the beam ends.

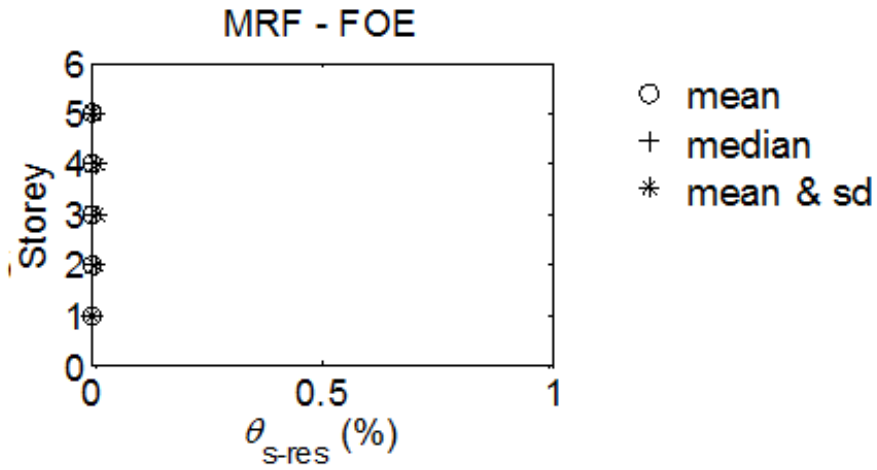

Figure 2.82 Statistics of residual storey drifts of the conventional MRF under 20 earthquake ground motions scaled to the FOE (Dimopoulos et al 2013)

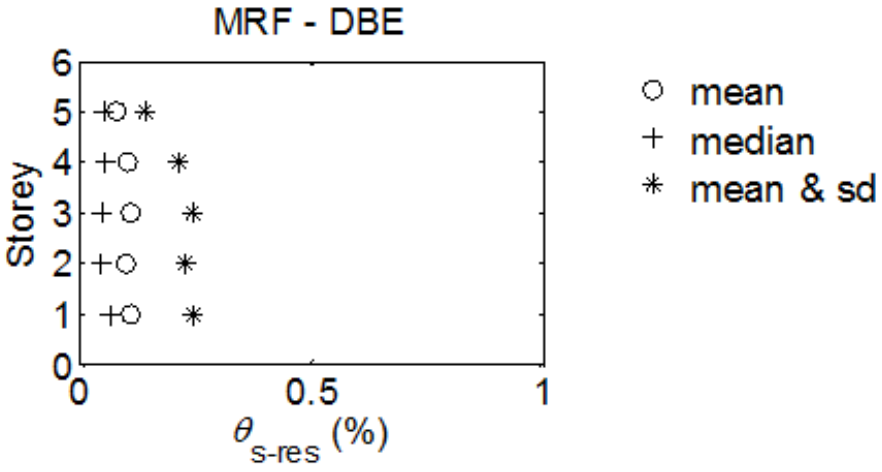

Figure 2.83 Statistics of residual storey drifts of the conventional MRF under 20 earthquake ground motions scaled to the DBE (Dimopoulos et al 2013)

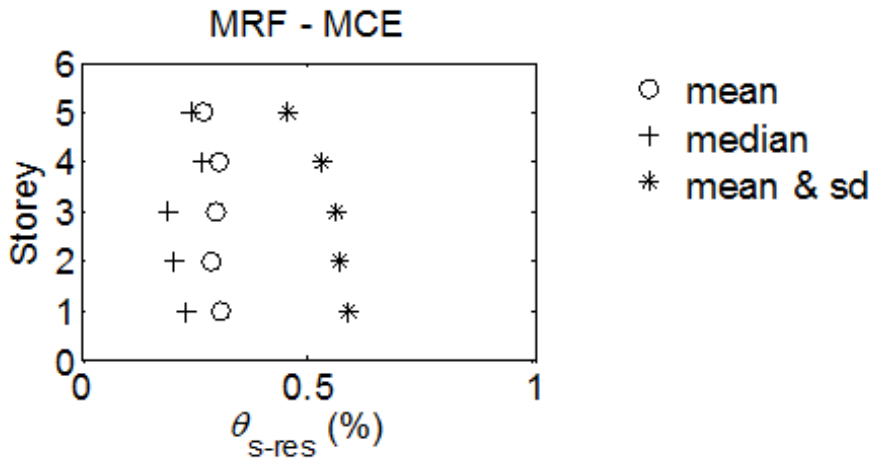

Figure 2.84 Statistics of residual storey drifts of the conventional MRF under 20 earthquake ground motions scaled to the MCE (Dimopoulos et al 2013)

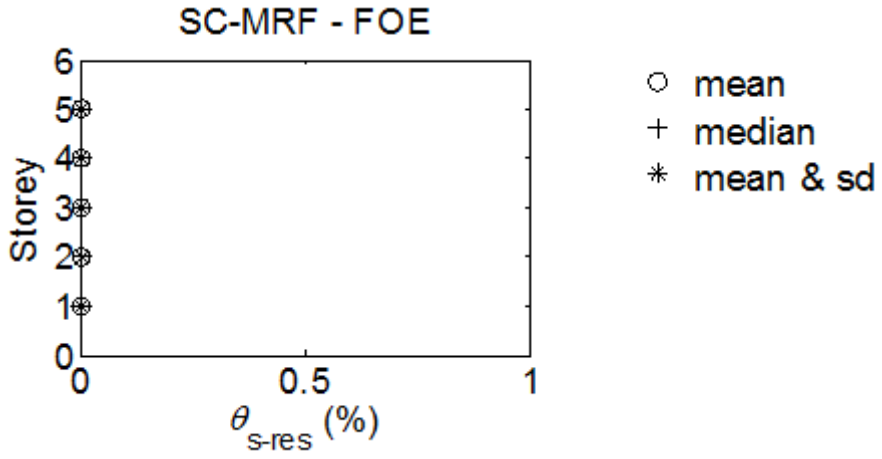

Figure 2.85 Statistics of residual storey drifts of the SC-MRF under 20 earthquake ground motions scaled to the FOE (Dimopoulos et al 2013)

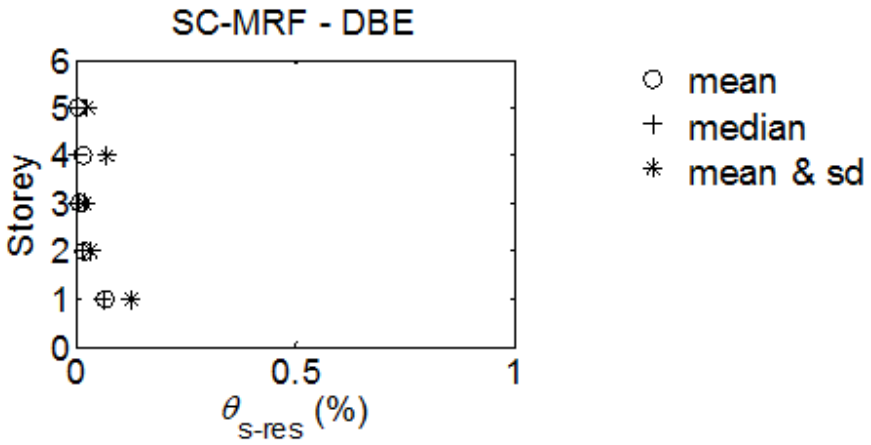

Figure 2.86 Statistics of residual storey drifts of the SC-MRF under 20 earthquake ground motions scaled to the DBE (Dimopoulos et al 2013)

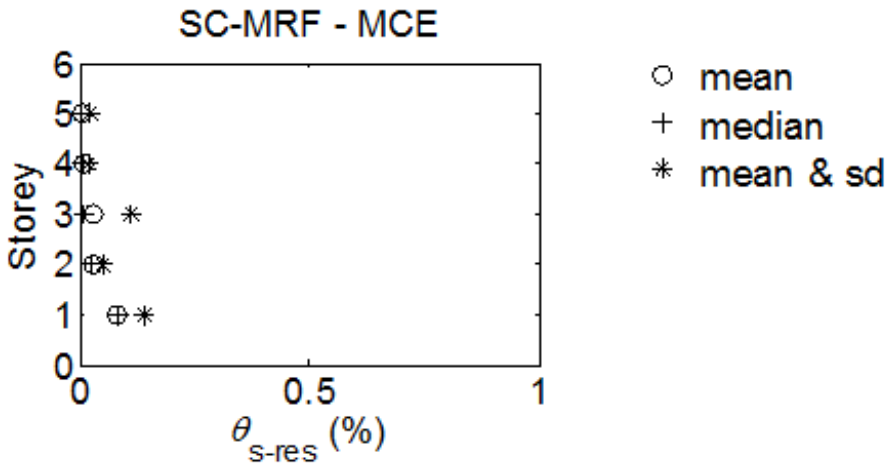

Figure 2.87 Statistics of residual storey drifts of the SC-MRF under 20 earthquake ground motions scaled to the MCE (Dimopoulos et al 2013)

2.6 Research needs

On the basis of the literature review in Sections 2.2 to 2.4, several research needs have been identified and discussed in the following paragraphs.

Research towards the standardization of steel SC-MRFs within the framework of EC8 (Eurocode 8 2013) is missing. In particular, there are no previous studies that focused on designing steel SC-MRFs according to the guidelines of EC8 (Eurocode 8 2013). Moreover, according to the existing design procedures for SC-MRFs (Garlock et al 2007, Kim and Christopoulos 2009b), PT connections rotation demands are estimated using approximate formulae. Hybrid simulation tests of SC-MRFs developed by (Lin et al 2013a,b) showed that these formulae result in underestimation of the rotations obtained both under the DBE and MCE. These results highlight the need of a more robust way to estimate the PT connections rotation demands. In addition, SC-MRFs have similar peak story drifts with conventional MRFs. Viscous dampers could be combined with SC-MRFs to control peak story drifts but an integrated design approach for SC-MRFs with viscous dampers has not been reported.

The ATC-63 (FEMA-P695 2008) project sets a limit on the permissible probability of collapse under the MCE equal to 10%. As this limit has been primarily set for conventional structural systems, lower probabilities of collapse should be offered by resilient structures. The behaviour under seismic intensities higher than MCE and the collapse resistance of SC-MRFs have not been examined in the existing literature. Nonlinear models of PT connections, able to capture the strength and stiffness deterioration due to local buckling should be developed in order to evaluate the seismic response of SC-MRFs up to collapse.

To properly assess the seismic resilience of SC-MRFs, the actual economic seismic losses should be rigorously estimated. The literature review shows that the potential of steel SC-MRFs to reduce economic seismic losses has not been assessed and quantified. In order to accurately estimate the seismic losses of SC-MRFs, the effect of the residual story drift value, beyond which is less expensive to rebuild a structure than to repair should be carefully studied. Moreover, the probability of collapse (i.e.

total loss of the building) should be considered during a seismic economic loss estimation study.

2.7 Research objectives

The objectives of this PhD thesis research are outlined below:

- To develop nonlinear models of PT connections, able to capture the strength and stiffness deterioration due to local buckling in order to evaluate the seismic response of SC-MRFs up to collapse.
- To develop a seismic design procedure of steel SC-MRFs with viscous dampers, within the framework of EC8 (Eurocode 8 2013), where a robust way to estimate the PT connections rotation demands will be implemented.
- To assess the accuracy of the proposed design procedure, and investigate different design scenarios of SC-MRFs with viscous dampers.
- To assess the behaviour of SC-MRFs with viscous dampers under seismic intensities higher than MCE, and their collapse resistance.
- To assess and quantify the potential of steel SC-MRFs with viscous dampers to reduce economic seismic losses.

2.8 Thesis structure

A modelling procedure in OpenSees (Mazzoni et al 2006) of PT connections able to capture the stiffness and strength deterioration due to local buckling is presented in chapter 3 of this PhD thesis. Experimental tests results and finite element models (FEM) in Abaqus of beams and PT connections, loaded up to the occurrence of local buckling have been used for the validation of the proposed OpenSees model.

A design procedure of steel SC-MRFs with viscous dampers, within the framework of EC8 (Eurocode 8 2013) is described in chapter 4 of this PhD thesis. SC-MRFs are using the recently developed PT connection with WHPs (Vasdravellis et al 2013a,b), presented in section 2.5 (see figures 2.63-64). Performance levels are defined with respect to drifts, residual drifts and limit states in the PT connections. A preliminary

pushover analysis is conducted at the early phase of the design process to estimate rotations and axial forces in PT connections instead of using approximate formulae.

The recommended seismic design procedure of SC-MRFs with viscous dampers presented in chapter 4 is evaluated in chapter 5 of this PhD thesis. A prototype building is designed as a SC-MRF with or without viscous dampers. Different designs of the SC-MRF with viscous dampers are considered to investigate all possible scenarios, i.e. use of dampers to achieve drifts significantly lower than the EC8 (Eurocode 8 2013) drift limit; to significantly reduce steel weight without exceeding the EC8 (Eurocode 8 2013) drift limit; or to reduce steel weight and achieve drifts lower than the EC8 (Eurocode 8 2013) drift limit. Nonlinear dynamic analyses in OpenSees using models capable of simulating all structural limit states up to collapse confirm the minimal-damage performance of the SC-MRFs, and the accuracy of the seismic design procedure.

The seismic behaviour of SC-MRFs with viscous dampers up to collapse is evaluated in chapter 6 of this PhD thesis by conducting incremental dynamic analysis (IDA) (Vamvatsikos and Cornell 2002), and their superior collapse resistance is confirmed. The economic seismic losses of steel buildings using SC-MRFs with viscous dampers are evaluated and compared with that of conventional MRFs in chapter 7 of this PhD thesis. For the economic seismic loss estimation the FEMA-P58 (FEMA P-58 2012) methodology is implemented. The probability of collapse and the probability of the building to be demolished due to high values of residual drifts are considered. Damage states of PT connections are defined based on nonlinear dynamic analysis results. A parametric study on the effect of the assumed residual story drift value beyond which is less expensive to rebuild a structure than to repair is conducted. Results show that the use of SC-MRFs with viscous dampers achieves significant repair cost reductions compared to the conventional MRF. The conclusions of this PhD thesis are presented in chapter 8.

3 Development of models for PT connections

3.1 Introduction

In this chapter, a modelling procedure of PT connections with WHPs and the associated beams and columns in OpenSees is developed and presented. The recommended model has been calibrated against results from large-scale experimental tests conducted by (Vasdravellis et al 2013a) and found to accurately simulate the connection behavior (see Figure 2.68) before the occurrence of local buckling. In PT connections, beam local buckling is expected just after the end of the reinforcing plates. The model of Lignos and Krawinkler (2007) is able to capture the stiffness and strength deterioration of steel beams, but has not been calibrated against beams, subjected to axial compressive forces like in PT connections.

For this reason, the validity of the proposed OpenSees model to capture stiffness and strength deterioration due to beam local buckling, using the model of Lignos and Krawinkler (2007) is examined. The OpenSees model is compared against finite elements models (FEM) in Abaqus, developed for the available experimental setups of PT connections (Kim and Christopoulos 2008a, Kim and Christopoulos 2008b) where the local buckling occurred in the beams. For the development of FEM models, able to reliably simulate the local buckling on the PT connections beams, a parametric study has been carried out. In this parametric study, FEM models for the experimental specimens of Elkady et al (2014) and D'Aniello et al (2012) in beam elements with and with no axial force respectively have been developed. The OpenSees model is validated against the FEM and it is concluded that the recommended OpenSees model is capable to accurately capture the stiffness and strength deterioration in the beams of the PT connections under high drifts.

3.2 FEM models for beams with no axial force.

In this section three beam elements with I cross section, that were tested by D'Aniello et al (2007) have been modelled in Abaqus and subjected to both monotonic and cyclic loading. The cross sections, yielding strength (f_y), and ultimate strength (f_u) of the beams are shown in Table 3.1. The height of the tested beams is

1875mm, and fixed conditions have been applied on their bases. The beams were modelled using C3D8R solid elements apart from 300mm over their fixed base that was modelled using solid elements with incompatible modes C3D8I. C3D8I are first order elements that are enhanced by incompatible modes to improve their bending behaviour (Abaqus 2010). The mesh was refined in regions where severe plastic deformations or buckling phenomena were expected to occur, i.e. 300 mm over the fixed base. For this part of the beam there are have 12 elements along the length of the beam web, and 10 elements along the length of the flanges, and 15 elements along the beam length of this part. A coarser mesh was used for regions that were expected to remain essentially elastic, i.e. the top 300mm of the column. At this part there are 4 elements along the length of the beam web, 8 elements along the length of the beam flanges and 3 elements along the beam length of this part. For the remaining beam part an approximate global size of 50mm is applied. All over the beam, there are 4 elements along the thickness of the flange and the web. Figure 3.1 shows the mesh of model for the IPE300. An elasto-plastic law with combined isotropic-kinematic hardening rule was specified for the steel material. The kinematic hard parameter and the γ value for the combined isotropic-kinematic hardening law were defined equal to 3500 and 15 respectively according to a preliminary parametric study on these parameters. A multi-point beam type constrain has been defined at the top surface of the beam. The control point of this constrain is a point along the top surface and slave nodes are all the nodes of this surface. The horizontal load was applied as an imposed displacement at the control point of the top surface. This loading configuration allows to the beam to rotate at the top. In order to capture local buckling phenomena, geometrical imperfections have been inserted into the analysis. To insert geometrical imperfections in the model, a modal analysis is first performed, and a number of eigenvalues are obtained. After the modal analysis a geometrical imperfection equal to the beam web length divided by 200 is applied over the mode that results in beam web and flange local buckling according to Eurocode 3 (EC3 part 1-5 2006). For the cyclic tests the AISC 2005 (AISC 341-05 2005) loading protocol was adopted.

Table 3.1 Steel properties of tested beams

Section	Location	f_y (MPa)	f_u (MPa)
HEB 160	Web	338	475
	Upper flange	328	456
	Lower flange	346	463
HEB 240	Web	318	351
	Upper flange	295	433
	Lower flange	273	448
IPE 300	Web	353	447
	Upper flange	317	438
	Lower flange	342	440

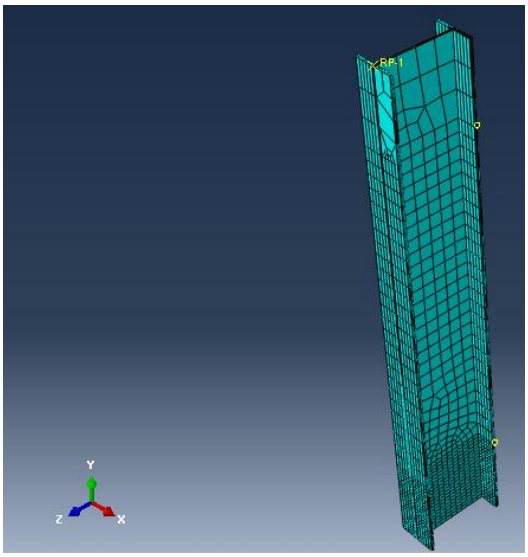

Figure 3.1 Mesh configuration of the model for the IPE300 specimen

3.2.1 IPE300

Figure 3.2 shows the drift – moment curve for the IPE300 beam under monotonic loading, and figure 3.3 shows the drift – moment curve for the IPE300 beam under cyclic loading respectively. It is observed that the FEM modelling is able to capture the stiffness and strength deterioration due to local buckling phenomena with sufficient accuracy at similar drifts with the experiments. Figure 3.4 shows the

failure mode observed in Abaqus and experiment for the IPE300 beam under monotonic and figure 3.5 shows the failure mode observed in Abaqus and experiment for the IPE300 beam under cyclic loading respectively. The failure modes in Abaqus coincide with the failure modes observed in the experiments.

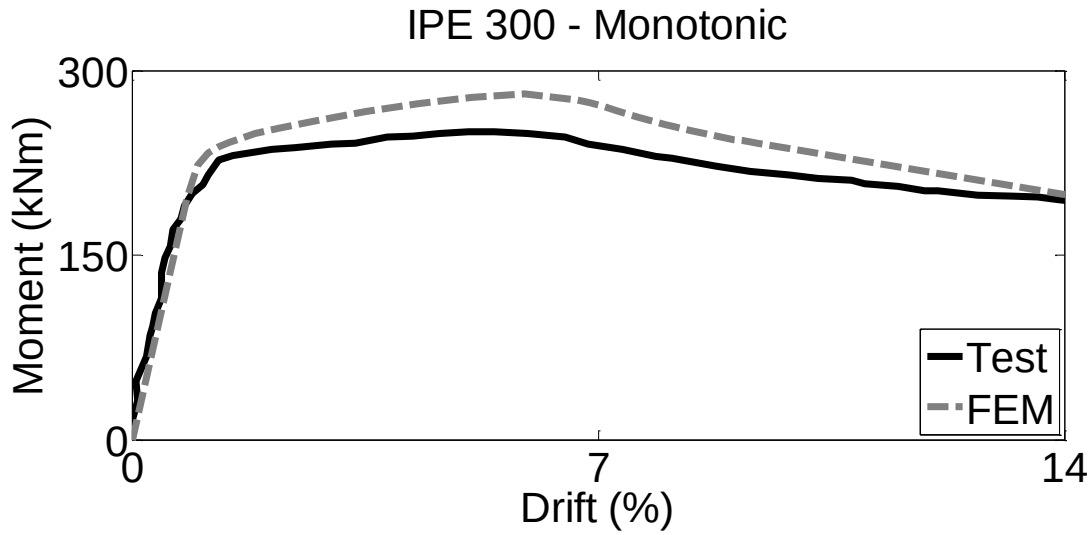

Figure 3.2 Experimental against tests results under monotonic loading for IPE300

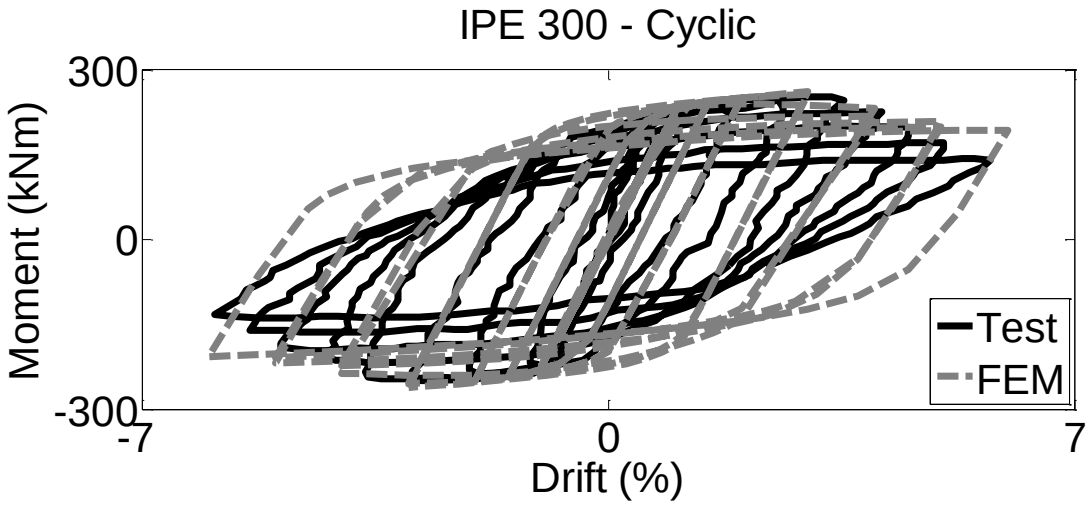

Figure 3.3 Experimental against tests results under cyclic loading for IPE300

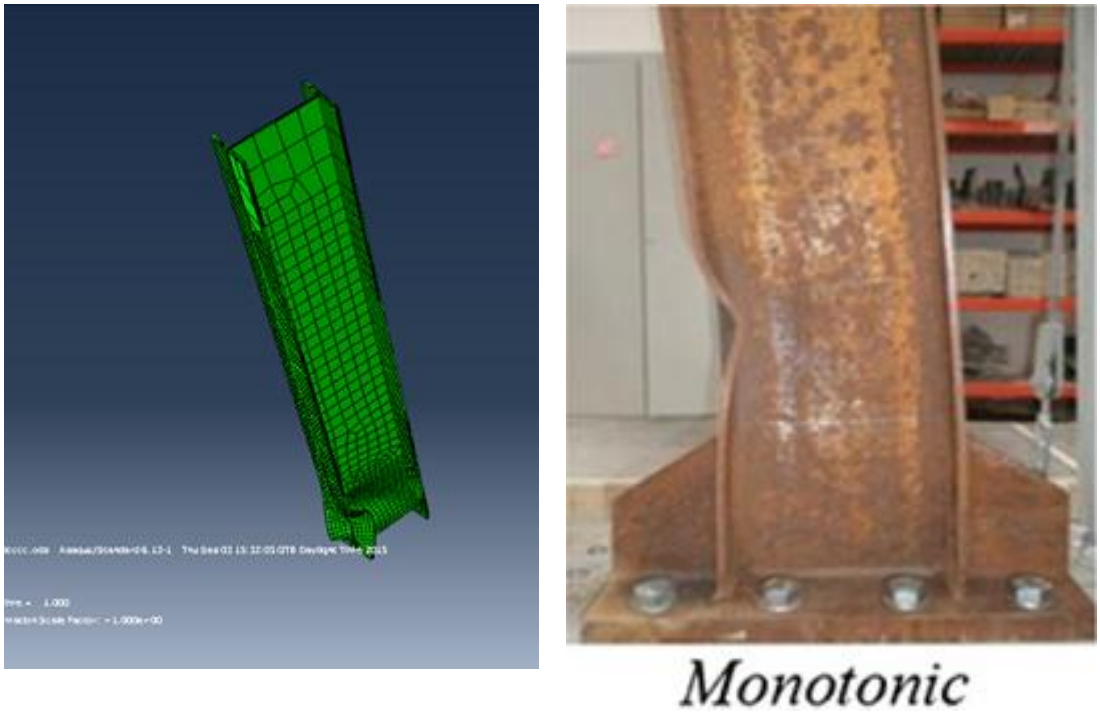

Figure 3.4 Failure mode of IPE300 under monotonic loading in (a) Abaqus; and (b) experiment of (D'Aniello et al 2007)

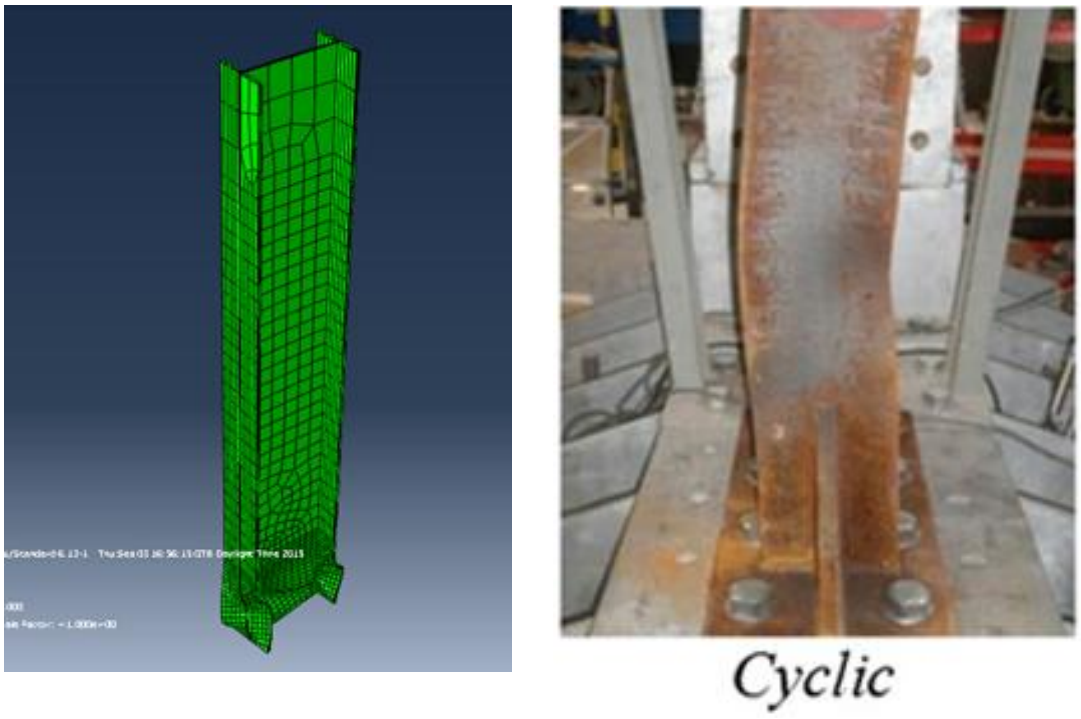

Figure 3.5 Failure mode of IPE300 under cyclic loading in (a) Abaqus and (b) experiment of (D'Aniello et al 2007)

3.2.2 HEA160

Figure 3.6 shows the drift – moment curve for the HEA160 beam under monotonic loading and figure 3.7 shows the drift – moment curve for the HEA160 beam under cyclic loading respectively. It is observed that the FEM modelling is able to capture the stiffness and strength deterioration due to local buckling phenomena with sufficient accuracy at similar drifts with the experiments. Figure 3.8 shows the failure mode observed in Abaqus and experiment for the HEA160 beam under monotonic and figure 3.9 shows the failure mode observed in Abaqus and experiment for the HEA160 beam under cyclic loading. The failure modes in Abaqus coincide with the failure modes observed in the experiments.

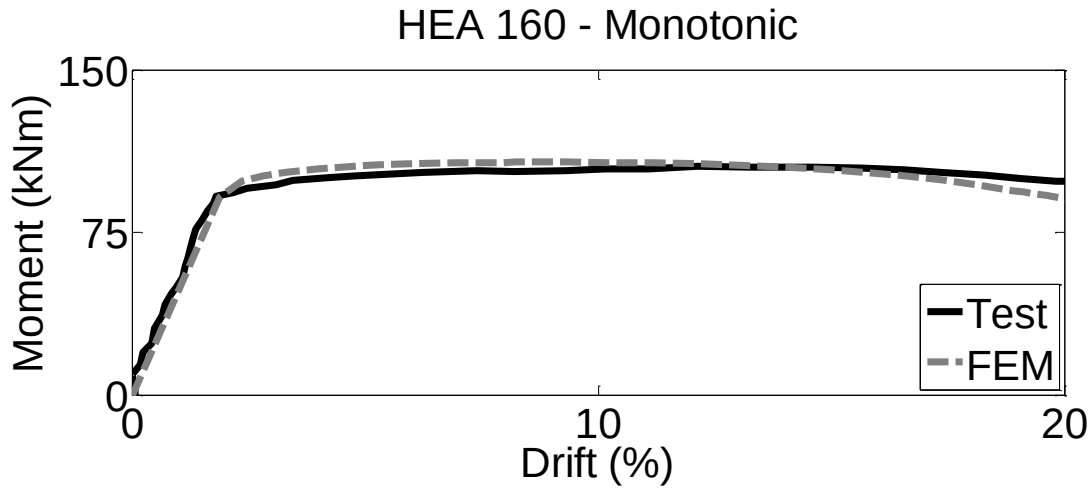

Figure 3.6 Experimental against test results under monotonic loading for HEA 160

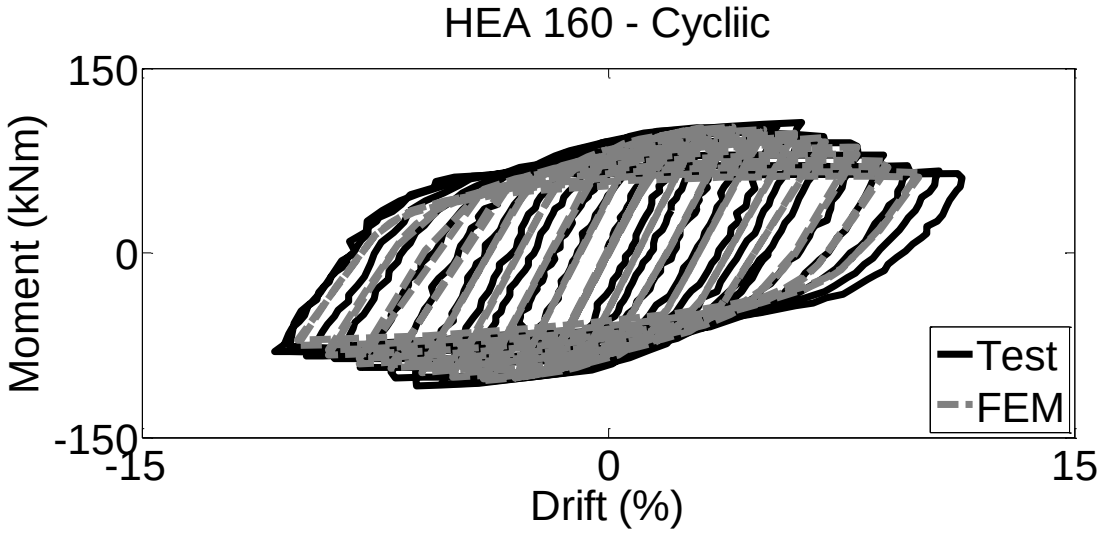

Figure 3.7 Experimental against test results under cyclic loading for HEA 160

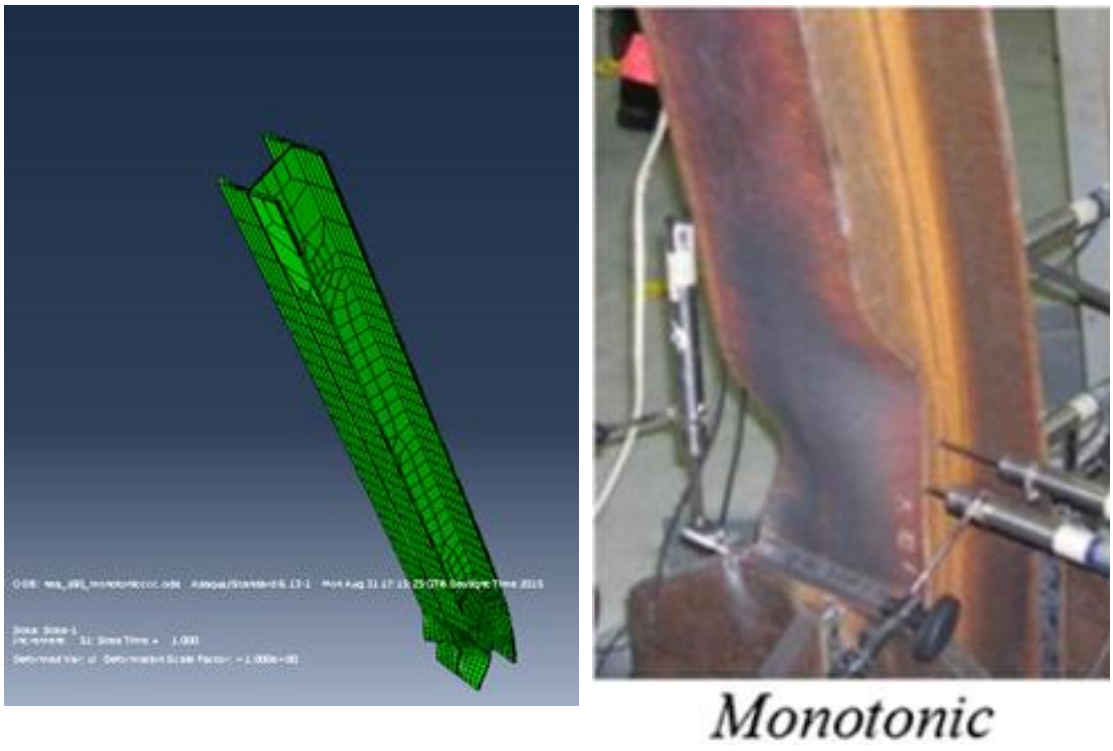

Figure 3.8 Failure mode of HEA160 under monotonic loading in (a) Abaqus and (b) experiment of (D'Aniello et al 2007)

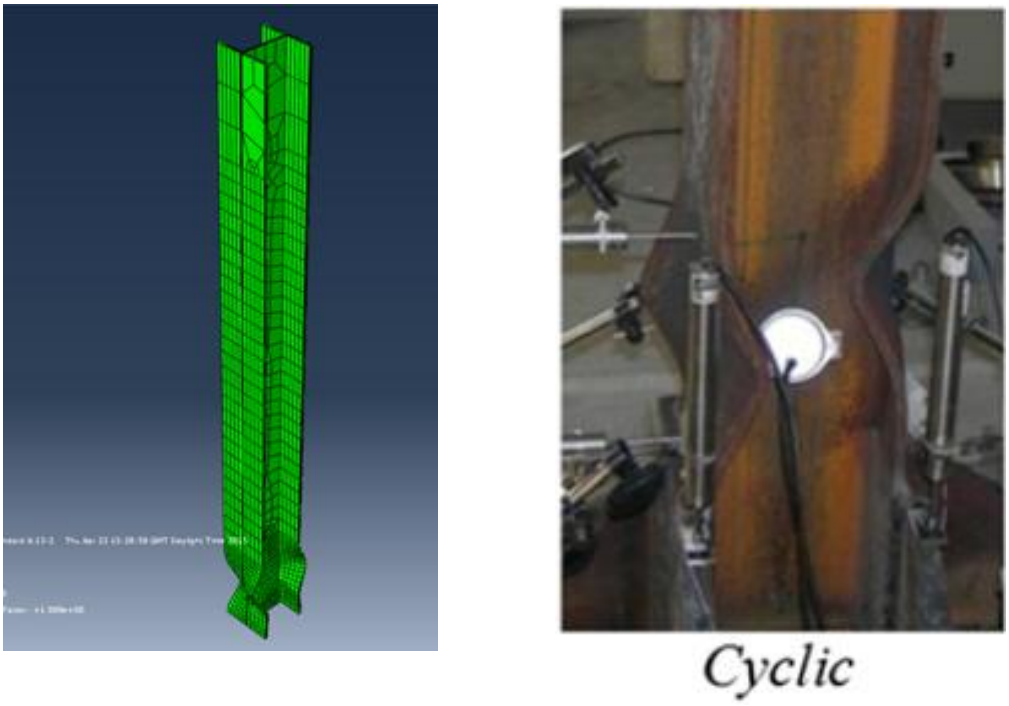

Figure 3.9 Failure mode of HEA160 under cyclic loading in (a) Abaqus and (b) experiment of (D'Aniello et al 2007)

3.2.3 HEB240

Figure 3.10 shows the drift – moment curve for the HEB240 beam under monotonic and loading and figure 3.11 shows the drift – moment curve for the HEB240 beam under cyclic loading respectively. It's observed that the FEM modelling is able to capture the stiffness and strength deterioration due to local buckling phenomena with sufficient accuracy at similar drifts with the experiments. Figure 3.12 shows the failure mode observed in Abaqus and the experiment for the HEB240 beam under monotonic loading. Figure 3.13 shows the failure mode observed in Abaqus and the experiment for the HEB240 beam under cyclic loading. The failure modes in Abaqus coincide with the failure modes observed in the experiments.

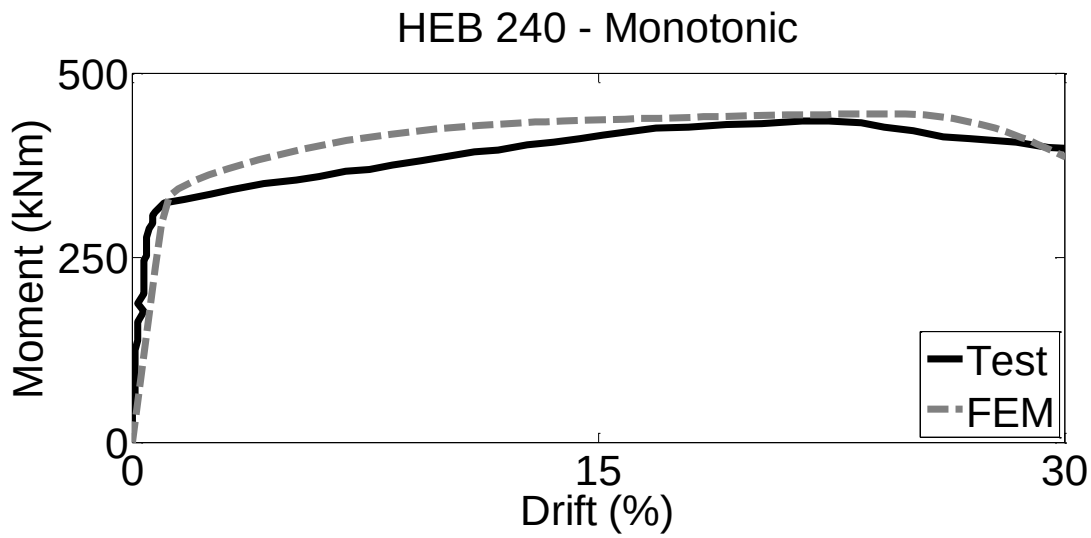

Figure 3.10 Experimental against tests results under monotonic loading for HEB240

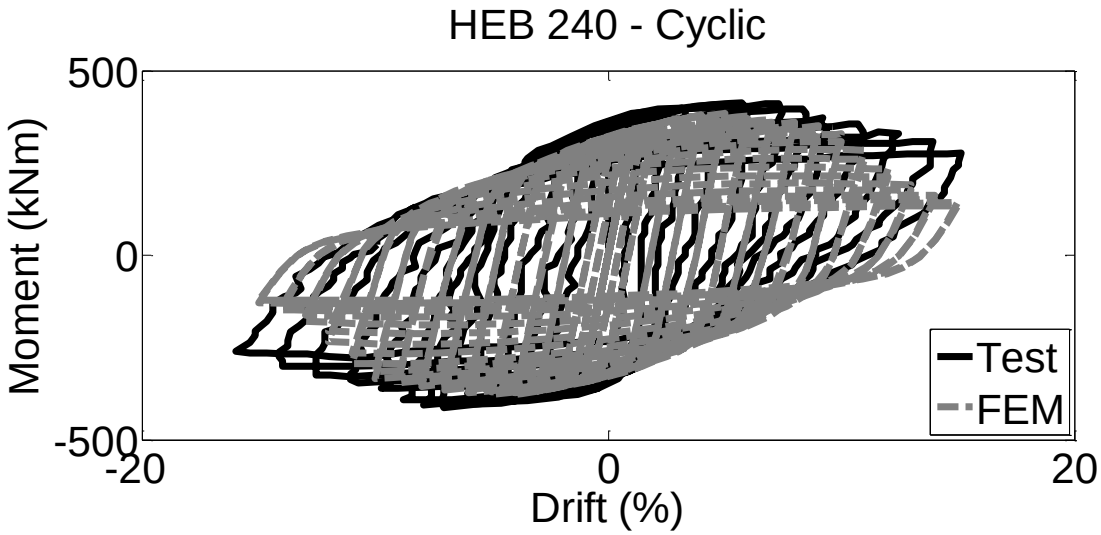

Figure 3.11 Experimental against tests results under cyclic loading for HEB240

(a)

(b)

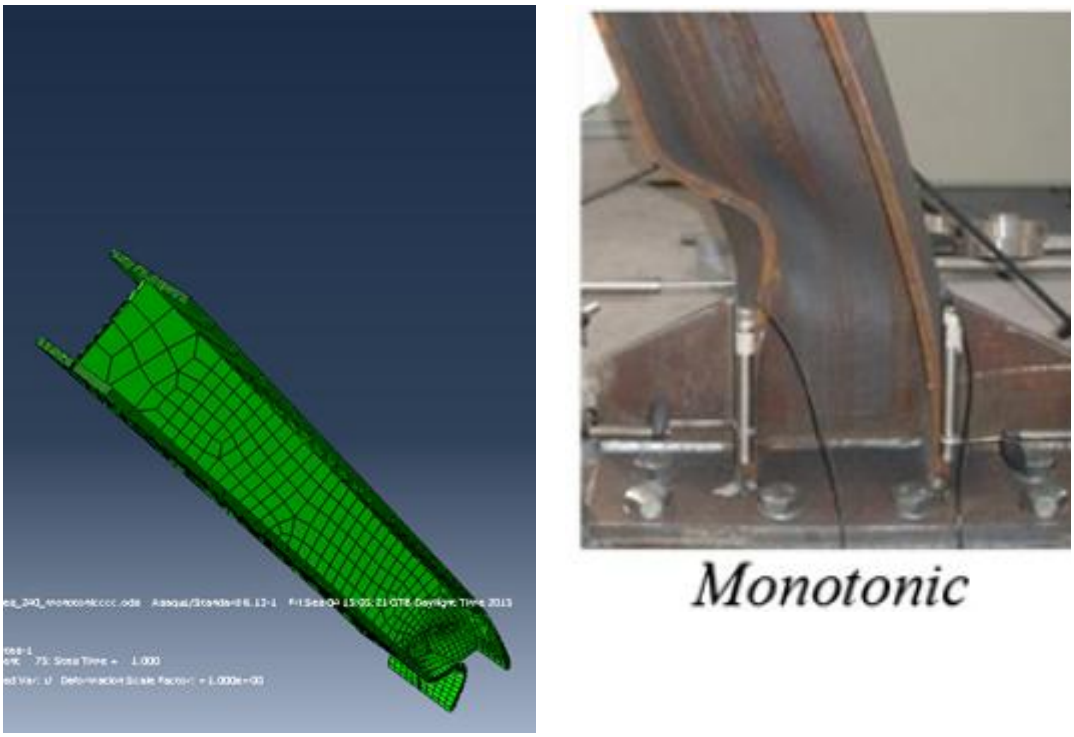

Figure 3.12 Failure mode of HEB240 under monotonic loading in (a) Abaqus and (b) experiment of D'Aniello et al (2007)

(a)

(b)

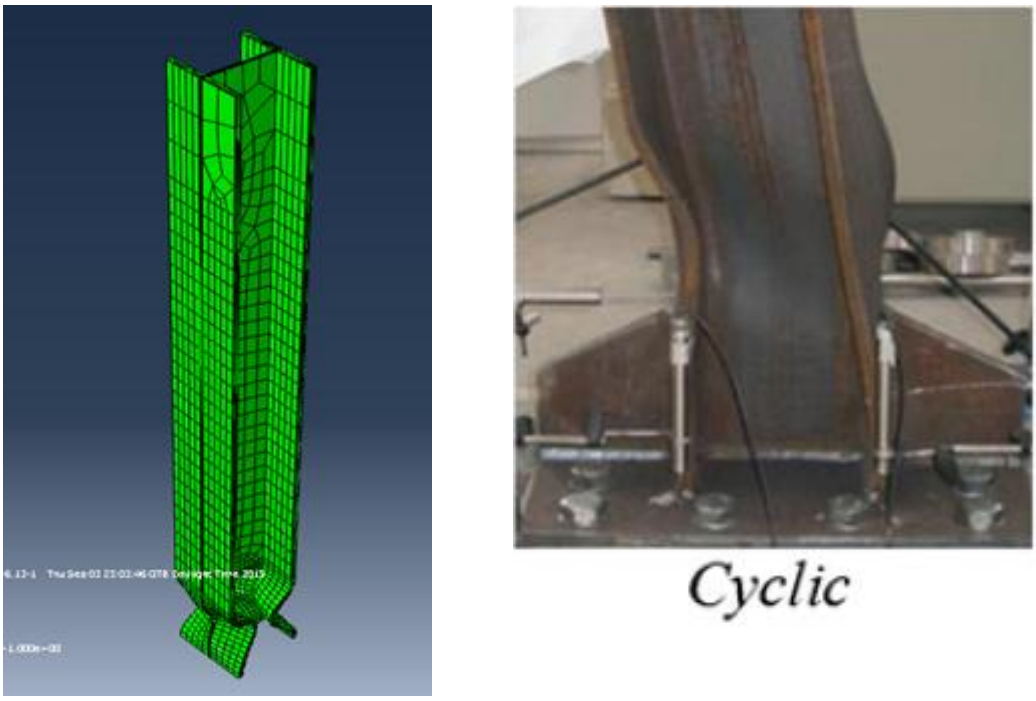

Figure 3.13 Failure mode of HEB240 under cyclic loading in (a) Abaqus and (b) experiment of (D'Aniello et al 2007)

3.3 FEM models for beams with axial force.

It has already been mentioned that beams in PT connections are subjected into compressive forces. The main scope of this chapter is to study the cyclic behaviour of a steel beam section subjected into compressive force. For this reason, test results from a specimen in Newell and Uang (2006) and Elkady et al (2014) representing typical first-story interior column have been collected, and FEM has been developed. The column has a length of 4600mm, which represents typical first story height in steel MRFs. Fully fixed boundary conditions are applied at the base of the column (i.e. fixed support), while partially fixed boundary conditions with flexible rotational stiffness are applied at the top of the column (i.e., flexible support) in order to consider the flexibility of the beam-to-column connection at the same location. The column cross section is W14x176 of steel grade A992. The material properties are for the top flange (f_y: 409MPa, f_u: 555MPa), for the bottom flange (f_y: 389MPa, f_u: 520MPa), and for the web (f_y: 402MPa, f_u: 550MPa). The column was modelled using C3D8R solid elements apart from 600mm over its fixed base and 600mm under the top flexible support, that were modelled using solid elements with incompatible modes C3D8I. The mesh was refined in regions where severe plastic deformations or buckling phenomena were expected to occur (600 mm over the fixed base and 600mm under the flexible support). In these parts there are 50 elements along the length of the beam part both in the beam web and flange. There are 10 elements along the flanges length and 12 elements along the beam web length. Also there are 4 elements along the thickness of the flanges and the web. A coarser mesh was used for regions that were expected to remain essentially elastic (the middle part of the column between the two refined meshed parts). At this part there are elements of approximate size equal to 50mm. Figure 3.14 shows the mesh of model for the W14x176.

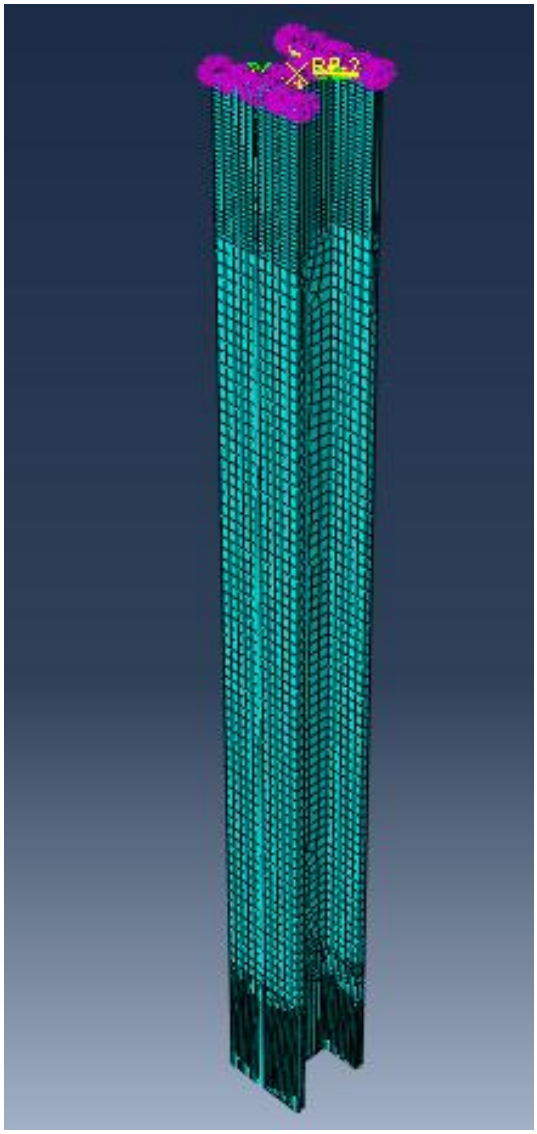

Figure 3.14 Mesh configuration and vertical springs at the top surface of the model for the W14x176 specimen

An elasto-plastic law with kinematic hardening rule was specified for the steel material. The partially fixed conditions at the column's top surface were modelled by defining vertical springs at the column's top surface (shown in figure 3.14). A multi-point beam type constrain as been defined at the top surface of the beam. The control point of this constrain is a point along the top surface and slave nodes are all the nodes of this surface. The horizontal load was applied as an imposed displacement at the control point of the top surface. This configuration allows to the column to rotate with a certain rotational stiffness developed by vertical springs at the top surface. In order to capture local buckling phenomena, geometrical imperfections have been inserted into the analysis as described in section 3.2. The

loading protocol is described in Newell and Uang (2006), where for the application of the axial force a bilinear "drift-axial force" diagram has been adopted. The inclination of the "drift - axial force" diagram has a constant value until 0.3% drift, and after that is reduced by 97%. The axial force equals to 35% of the cross section yielding axial force (P_y) at 0.6% drift. The axial force P is added to or subscribed from the gravity force, which is applied on its own at the first step. The axial force is applied at each analysis step as a vertical imposed displacement at the top of column. This imposed displacement comes through division of the axial force by the column's axial stiffness.

Figure 3.15 shows the drift– moment curve for the W14x176 beam under cyclic loading. It's observed that the FEM modelling is able to capture the stiffness and strength deterioration due to local buckling phenomena with sufficient accuracy at similar drifts with the experiment. Figure 3.16 shows the failure mode observed in Abaqus and the experiment of Newell and Uang (2006) for the W14x176 beam under cyclic loading. The failure mode in Abaqus coincides with the failure mode observed in the experiment.

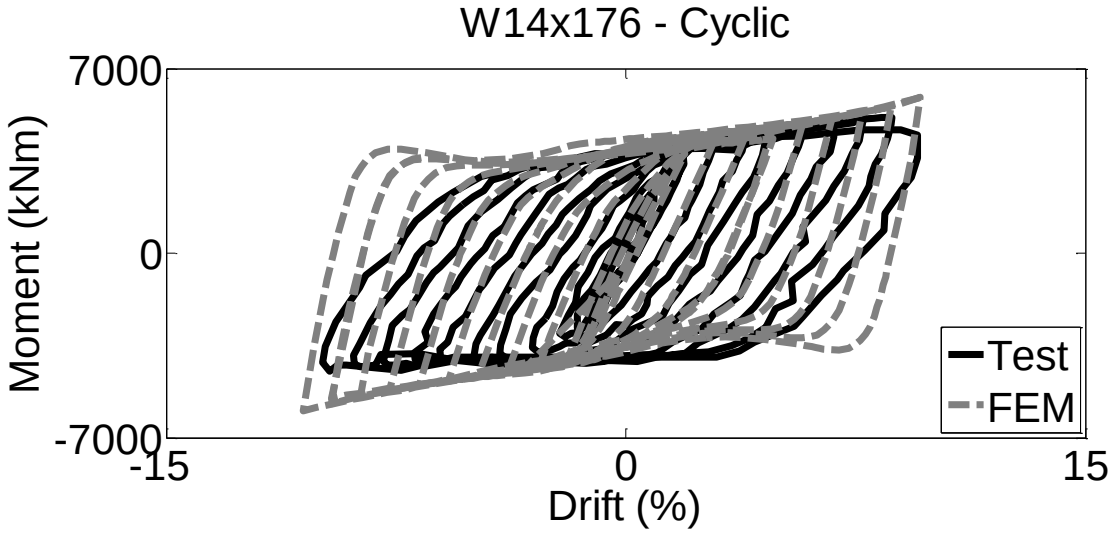

Figure 3.15 Experimental against tests results under cyclic loading for W14x176

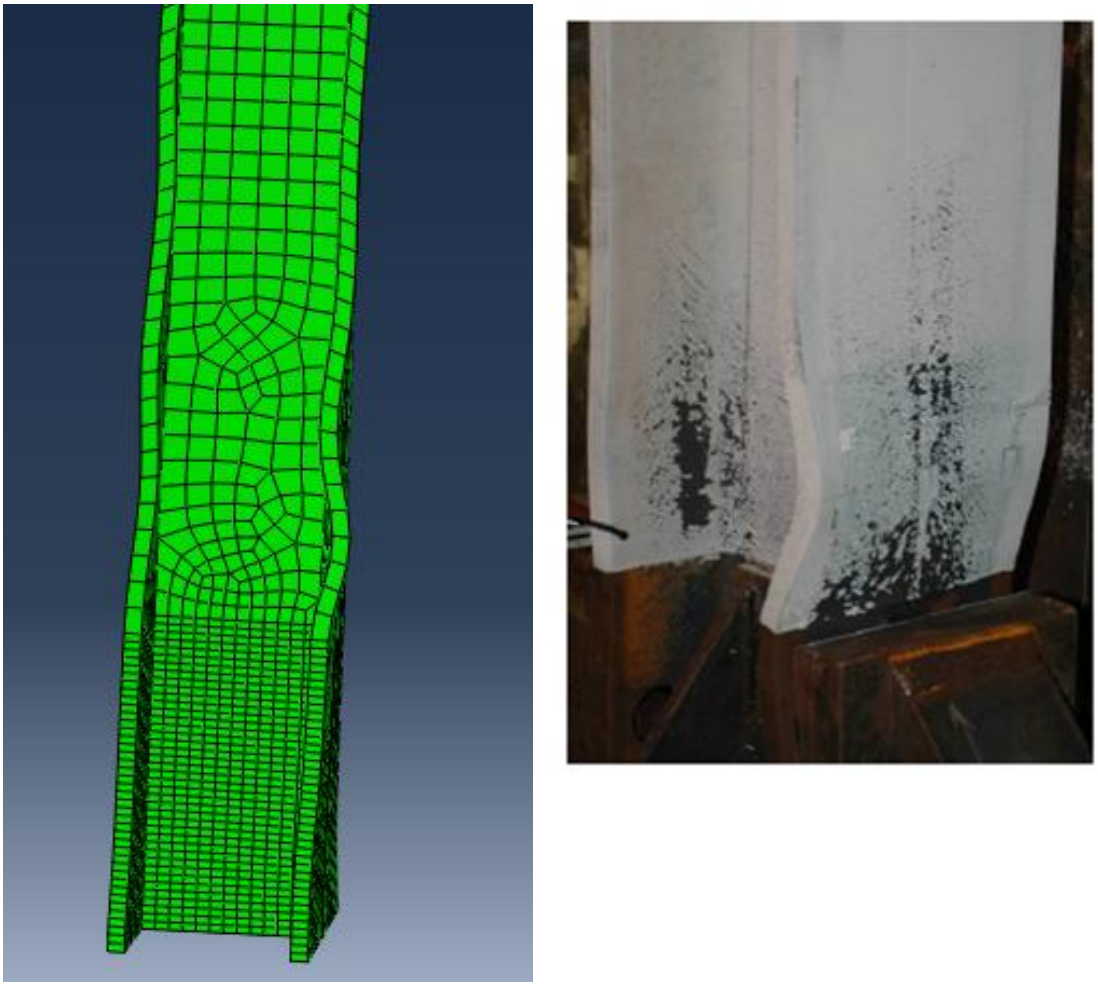

Figure 3.16 Failure mode of W14x176 under cyclic loading in (a) Abaqus and (b) experiment of (Newell and Uang 2006)

3.4 FEM models for PT connections

3.4.1 Experimental setup of PT connection

A steel PT connection is developed and experimentally validated in (Kim and Christopoulos 2008). The connection incorporates bolt-stressed FEDs consisting of stainless steel interfaces and new non asbestos (NAO) break lining pads as the energy dissipating mechanism. Figure 2.27 shows details of the FEDs. PT high strength steel bars are running parallel to the beam to provide self-centering capability to the system. Figure 3.17 shows a photo of the experimental setup in (Kim and Christopoulos 2008). Results from cyclic tests on the PT connection are presented in (Kim and Christopoulos 2008). The tests have been developed up to high drifts, where local buckling on the beam has been occurred.

The column and beams were W360x509 and W610x113 sections, respectively. Both members were 350W steel with nominal yield strength of 350MPa. Steel plates with 12mm thickness and nominal yield strength of 550MPa, were welded to the beam flanges and ended at 835mm from the column flange. Continuity plates, 20mm thick were welded to the inside of the column flanges and web to provide appropriate force flow from the beam to the column. Contact plates, 25mm thick (Grade 550) were placed between the beam and the column flange. Longitudinal stiffeners along the beam web have been inserted to prevent local buckling on the web. Roller supports have been inserted along the beams. Six 60-mm-diameter holes were introduced in the column flanges to accommodate the PT bars and the vertical movements expected during testing. Six 32-mm-diameter Dywidag high-strength bars with a nominal ultimate strength of 1,030 MPa were selected to provide the post-tensioning. Figure 3.18 shows a drawing depicting the experimental setup and Figure 2.19 shows the details of the PT connection. The initial tension of each PT bar was 200kN, which corresponded to 24% of their ultimate strength. The total friction developed by each FED was about 280kN. The loading protocol of AISC (2005) was applied on the specimen and the results are presented in (Kim and Christopoulos 2008).

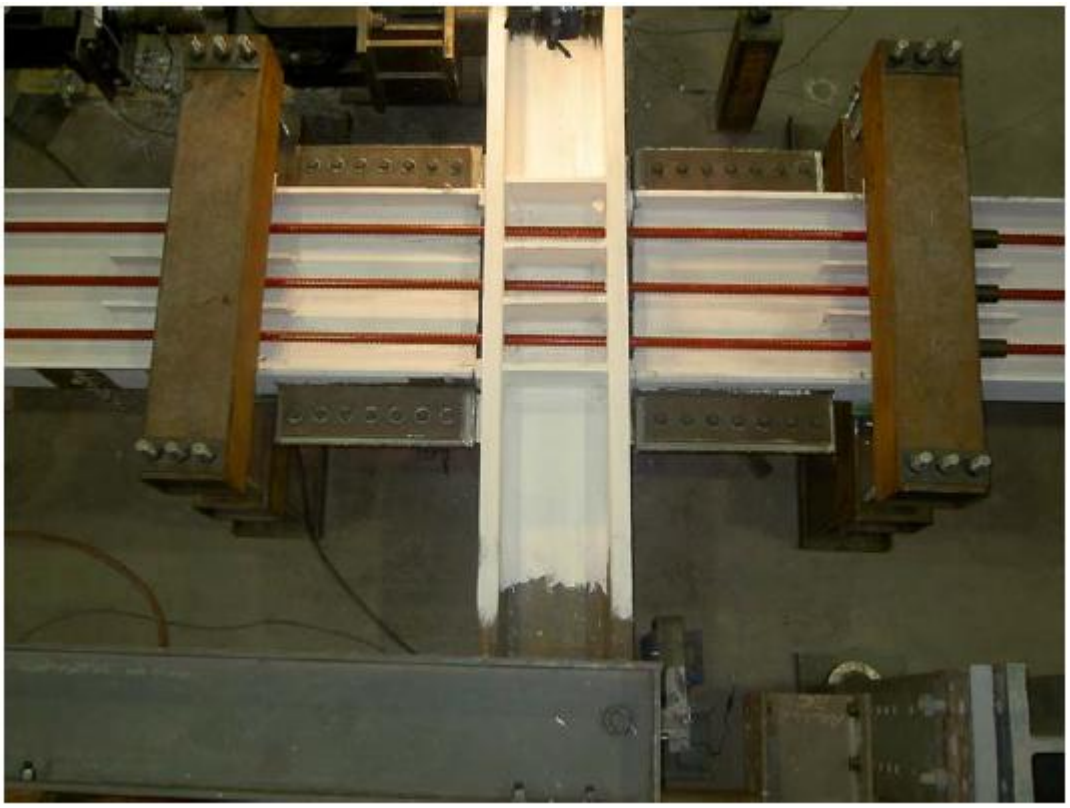

Figure 3.17 Photo from the experimental setup (Kim and Christopoulos 2008)

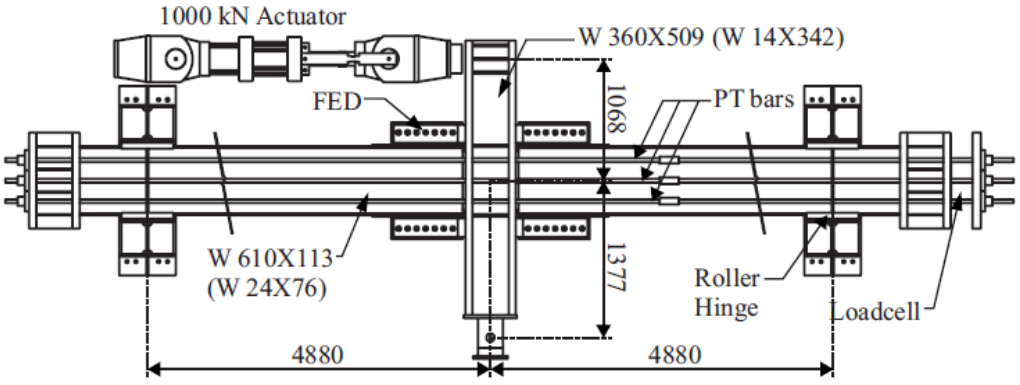

Figure 3.18 Experimental setup developed (Kim and Christopoulos 2008)

3.4.2 FEM in Abaqus of PT connection

FEM models have been developed in Abaqus, simulating the aforementioned experimental setup. Figure 3.19 shows the model in Abaqus for the PT connection. The column, the longitudinal stiffeners, the anchor block the continuity plates and the beam apart from the areas where local buckling phenomena are expected to occur are modeled using C3D8R solid elements. The part of the beams after beam reinforcing plates, where local buckling is expected to occur (300mm along the beam axis) are modeled using solid elements with incompatible modes C3D8I and with a refined mesh. There are 16 elements along the length of the beam web, and 4 elements along the flanges length. There is one element along the thickness of the web and 2 elements along the thickness of the flanges and the reinforcing plates. The approximate global size of the beams elements is 75mm. The approximate global size of the washers elements is 15mm. The approximate global size of the column's elements is 50mm, while there are 12 elements along the perimeter of the holes. Anchor blocks have elements of 25mm global size. The web reinforcing plates have elements of 30mm global size. Figure 3.20 shows the mesh of the model for the PT connection.

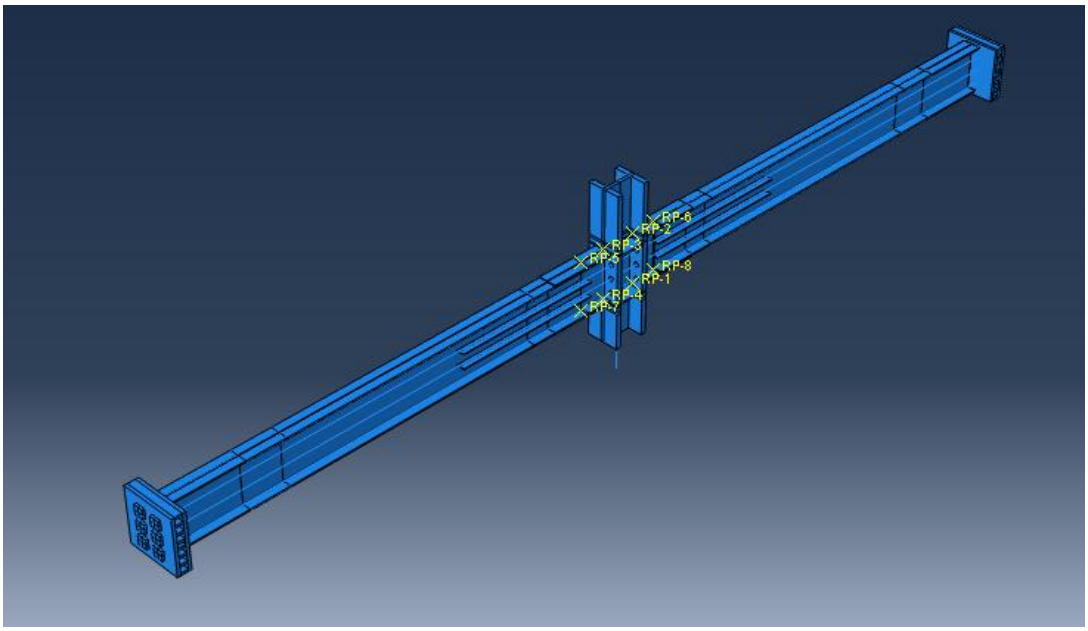

Figure 3.19 FEM of the PT connection developed in Kim and Christopoulos (2008)

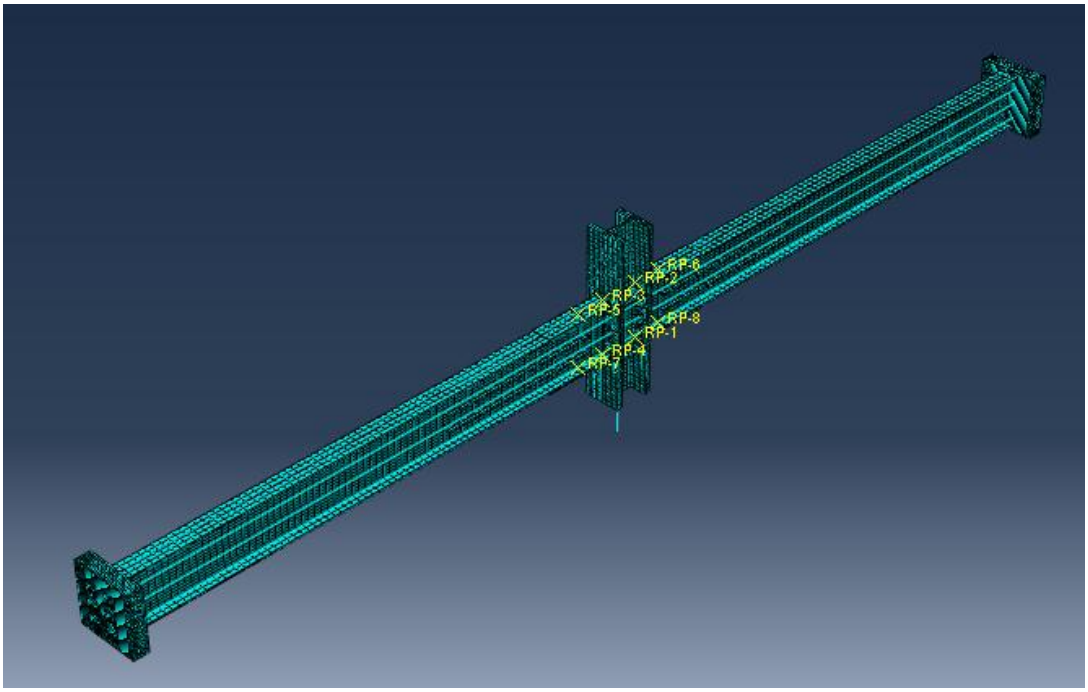

Figure 3.20 Mesh of the model for the PT connection developed in Kim and Christopoulos (2008)

An elasto-plastic law with isotropic hardening rule was specified for the steel material. PT bars were modeled using truss elements. The post tensioning was modeled using bolt load on the PT bars and by applying a certain shortening (Adjust length) on the truss elements in the first step of the analysis. The start and end points of the PT bars trusses are connected with the surfaces of the washers which are attached on the anchor blocks using tie constraints. The washers are connected to the anchor blocks using surface to surface contact with "hard contact" normal, and with friction coefficient 0.6 tangential behaviors. The beams are connected to the anchor blocks using tie constraints. Also, the beams are connected to the column using surface to surface contact with "hard contact" normal, and with friction coefficient 0.6 tangential behaviors. The FEDs were modeled using connector elements between the beams flanges and the column, where a perfectly plastic law was specified for the connector material. For the modelling of the column's support a beam element has been inserted under the column and has been restrained on the base in all the translational degrees of freedom but is free to rotate. The top point of the beam

element is constrained with the column's base using kinematic coupling constraint in all the degrees of freedom. The rollers supports on the beams have been modeled by applying restrains on the vertical translational degree of freedom in certain areas of the beams flanges.

3.5 Models of PT connections in OpenSees

3.5.1 Model of PT connection with WHPs in OpenSees

A model for the PT connection with WHPs and the associated beams and columns was developed in OpenSees. Figure 3.24 shows the proposed model, which was calibrated against experimental results and found capable to accurately simulate the PT connection behaviour. The columns and the reinforced lengths of the beams are modelled as nonlinear force-based beam-column fiber elements. Fibers have bilinear elastoplastic stress-strain behaviour (Steel01 in OpenSees) with post-yield stiffness ratio of 0.003. The assumption of stable hysteresis for the columns is fully justified as heavy columns with webs and flanges of low slenderness (e.g. compact HEB sections) do not show cyclic deterioration even under large drifts (Newell and Uang 2008). Beam local buckling is expected just after the end of the reinforcing plates.

Stiffness and strength deterioration due to beam local buckling just after the end of the beam flange reinforcing plates is captured using the Modified Ibarra-Medina-Krawinkler Deterioration Model (Lignos and Krawinkler 2007) with Bilinear Hysteretic Response (Bilin in OpenSees). This model provides the moment-rotation hysteresis of steel beams and has been calibrated with data from more than 350 experiments on steel beam-to-column connections. Figures 3.21-22 show the monotonic backbone curve and the cyclic curve of the model in (Lignos and Krawinkler 2007). Three strength parameters (M_y: Effective yield moment; M_{cap}: capping moment strength; and residual moment $Mr=\kappa \cdot M_y$) and four deformation parameters (θ_y: yield rotation; θ_p: pre-capping plastic rotation for monotonic loading; θ_{pc}: post-capping plastic rotation; and θ_u: ultimate rotation capacity) define the monotonic backbone curve (see figure 3.21). Regression formulas are provided in (Lignos and Krawinkler 2007) to estimate the moment rotation deterioration parameters in different connection types. So, the unreinfo1rced lengths of the beams

are modelled as elastic elements with zero length rotational springs at their ends that exhibit the model of (Lignos and Krawinkler 2007). This modelling procedure for the beams is shown in shown in section 5.3 (See figure 5.3).

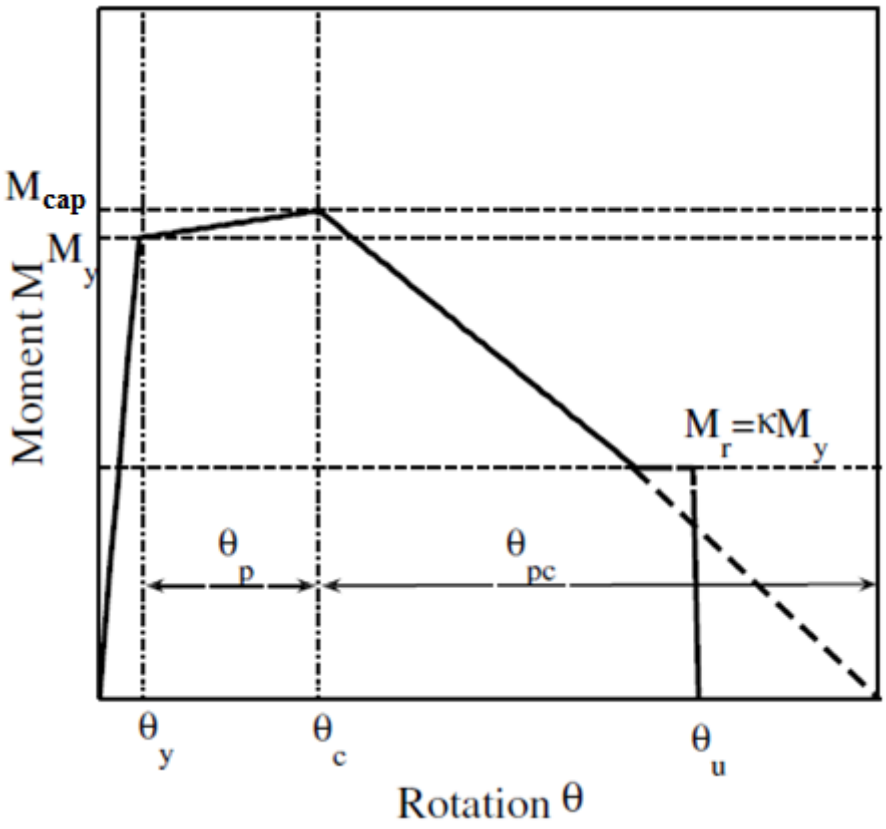

Figure 3.21 Monotonic backbone curve of model in Lignos and Krawinkler (2007)

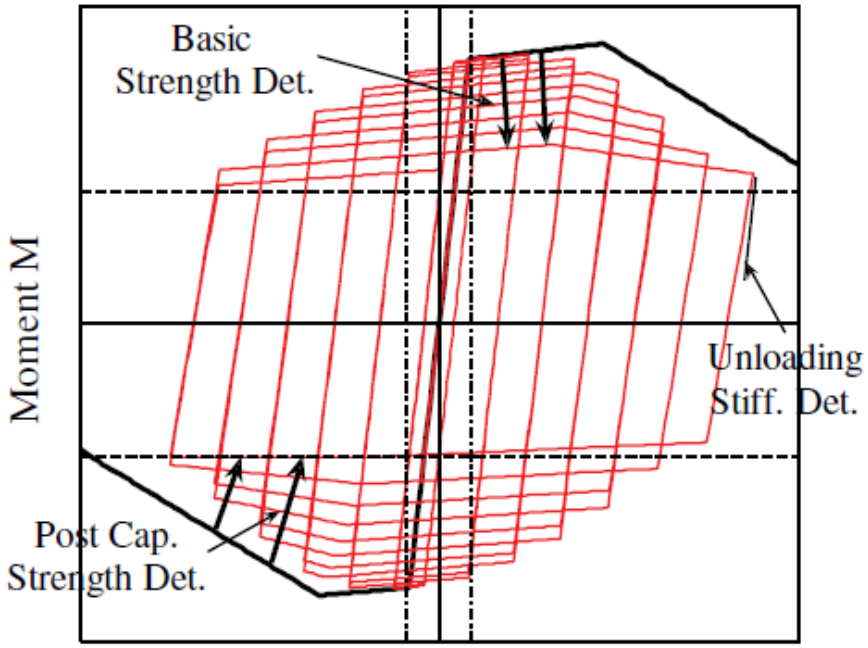

Figure 3.22 Cyclic curve of model in Lignos and Krawinkler (2007)

In this section, the unreinforced lengths of the beams are modelled using force-based beam-column fiber elements with end hinges (Scott and Fenves 2006). And the model in (Lignos and Krawinkler 2007) is used for the stress-strain cyclic behavior of the fibers using appropriate calibration (See figure 3.24). So, the stiffness and strength deterioration due to beam local buckling is captured. This modelling approach results in smoother hysteretic curves for flexural members similar to that observed in experiments (Hamidia et al 2014). For this higher smoothness in the hysteresis, this modelling approach is also preferable for analysis up to collapse because non-smooth hysteresis results in convergence problems. The same modelling approach is used in section 6.3 (see figure 6.2).

Rigid elastic beam-column elements are used to model the beam-column interface. To capture the gap opening mechanism in the beam-column interface, three zero-length contact spring elements are placed at equal spaces along the beam flange thickness. These contact springs have an elastic compression-no tension force-displacement behaviour (ENT material in OpenSees) with compression stiffness (E_{comp}) of 20 times the axial stiffness of the beam. Larger values for this stiffness were found to produce practically the same results but with more iterations to

achieve convergence in nonlinear analysis. Figure 3.23 shows the force-displacement curve of the model (ENT material in OpenSees).

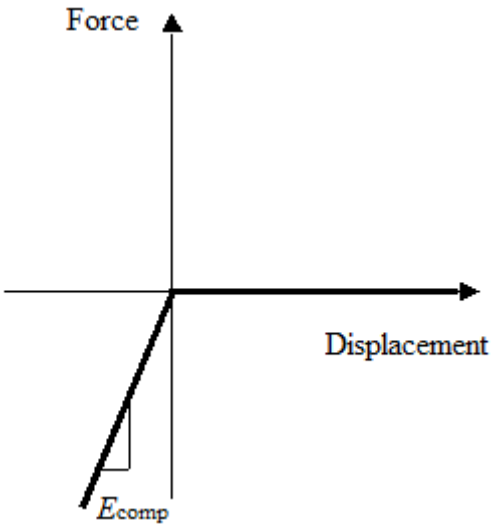

Figure 3.23 Force displacement curve of the model (ENT material in OpenSees)

Two zero-length hysteretic springs are placed at the exact locations of WHPs along the depth of the beam web. These springs are associated with a smooth Giuffre-Menegotto-Pinto model with isotropic hardening (Steel 02 material in OpenSees) (See model hysteresis in figure 3.27) as recent experimental studies show that WHPs have stable hysteresis and do not fracture under collapse loading protocols associated with storey drifts of more than 10% (Vasdravellis et al 2015).

Panel zones are modelled using the Scissors model (Charney and Downs 2004) which introduces four additional rigid elastic beam-column elements and two nodes in the panel zone centre connected with two zero-length rotational springs. These springs have bilinear elastoplastic hysteresis (Steel01 material in OpenSees) with properties that reflect the contribution of the column web (including doupler plates) and the column flanges in the force-deformation panel zone shear behaviour. PT bars were modelled using a truss element running parallel to beam center-line axis and connected to the exterior nodes of the panel zones of the exterior columns of the SC-MRF. The truss element has a cross-section area equal to A_{PT} and material with bilinear elastoplastic hysteresis. To account for post-tensioning, an initial strain equal to $T_0/(A_{PT} \cdot E_{PT})$ is imposed to the truss element, where T_0 is the initial PT force and E_{PT} is the modulus of elasticity of the PT bar material. Post-tensioning results in

axial shortening of beams and deflections of columns which decrease the PT force. To avoid this decrease, the initial strain in the truss element is increased to ensure that the post-tensioning force in the PT bars is equal to T_0 after beam shortening.

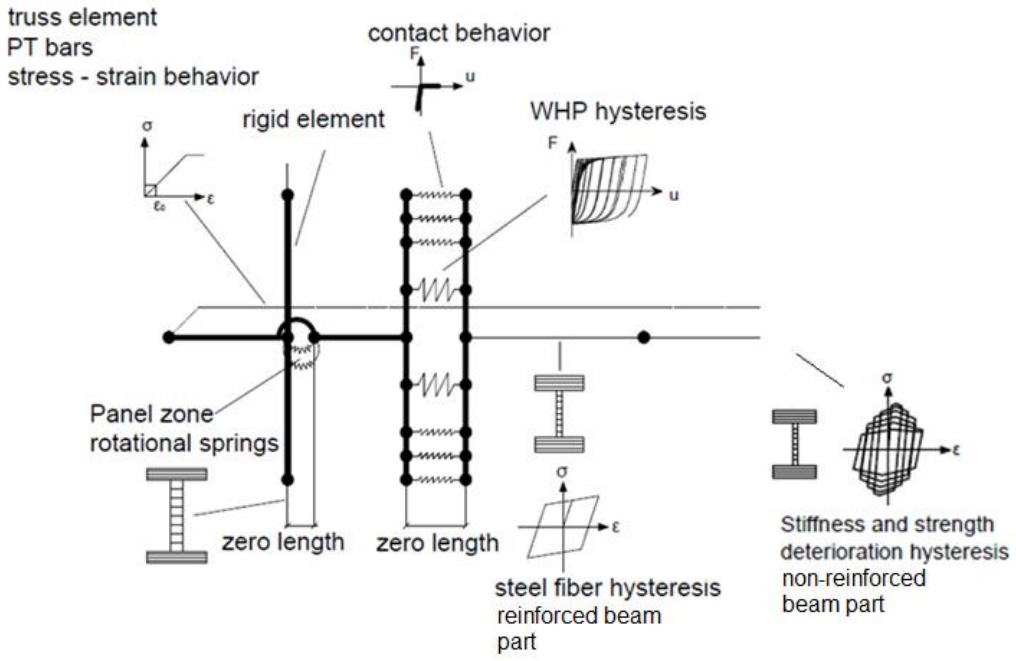

Figure 3.24 Model for a PT connection with WHPs and associated columns and beam

3.5.2 Assessment of OpenSees model for WHPs

WHPs are designed to have an hourglass shape to provide enhanced energy dissipation and fracture capacity (Kobori et al. 1992). Figure 3.25 shows the assumed static system for half a WHP. The yield strength, V_{WHP}, of half a WHP is controlled either by the plastic moment of resistance, M_{pl}, or the plastic shear resistance, V_{pl} EC3 (Eurocode 3 2010):

$$M_{\mathrm{pl}} = \frac{D_{\mathrm{e}}^3}{6} f_{\mathrm{y}} \tag{3.1}$$

$$V_{\mathrm{pl}} = 0.9 \frac{\pi D_{\mathrm{i}}^2}{4} f_{\mathrm{y}} / \sqrt{3} \tag{3.2}$$

Where f_y is the yield strength of the WHP material, D_e is the equivalent external diameter (to be defined later), and D_i is the diameter at the mid-length of half a WHP, as indicated in Figure 3.25. The factor 0.9 in equation 2 accounts for the relation between the average shear stress and the maximum shear stress in a circular section. The internal WHP part is connected to the external WHP part using a radius of 5 mm to avoid stress concentration and early fracture. It is assumed that D_e, which controls the WHP bending resistance, is equal to the diameter at the start of the round-shaped part with radius *r*. Plastic analysis assumes that the plastic moment of resistance should be reached at the ends before the plastic shear resistance is reached at the mid-length of half a WHP. By equilibrium, the aforementioned condition can be written as:

$$V_{WHP} = \frac{2M_{Pl}}{L_{WHP}} < V_{pl} \tag{3.3}$$

Where, L_{WHP} is the clear length of the bending parts of half a WHP. The yield force of a WHP, $F_{y,WHP}$, is then calculated as:

$$F_{y,WHP} = 2V_{WHP} \tag{3.4}$$

Based on the virtual work method along with analytical integration, the elastic stiffness K_{fe} of a WHP is calculated as:

$$K_{fe} = 2\frac{9\pi D_e^3 D_i EG}{(40ED_e^2 L_{WHP} + 48GL_{WHP}^3)} \tag{3.5}$$

Where, *E* is the modulus of elasticity and *G* the shear modulus of the WHPs material.

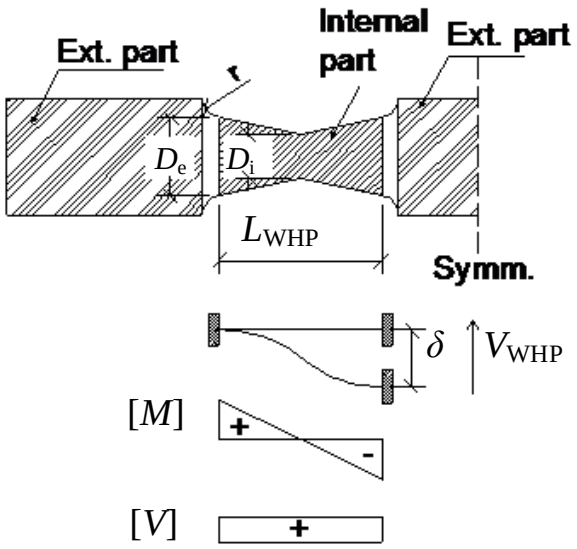

Figure 3.25 Geometry of half a WHP, assumed static system, and internal forces diagrams.

The Steel02 OpenSees hysteretic model used for the WHP force-displacement behaviour was calibrated against experimental results from WHPs component tests previously conducted by (Vasdravellis et al 2013a). Figure 3.26 shows the experimental setup for a pair of WHPs with the following properties. D_e=20 mm, D_i=14 mm, L_{WHP}=40 mm, f_y=560 MPa and E=200 GPa. Figure 3.27 shows a comparison between the experimental hysteresis and the Steel02 hysteretic model and confirms a good agreement. The Steel02 model has a yield strength equal to $2 \cdot F_{y,WHP}$; initial elastic stiffness equal to $0.6 \cdot (2 \cdot K_{fe})$; strain hardening ratio equal to 0.01; parameters controlling the transition from the elastic to inelastic regions of the hysteresis R_o=30, CR_1=0.925 and CR_2=0.15; and isotropic hardening parameters a_1=0.025, a_2=2.5, a_3=0.0 and a_4=1.0. The factor '2' for the calculation of the yield strength and stiffness reflects that a zero-length spring represents a pair of WHPs.

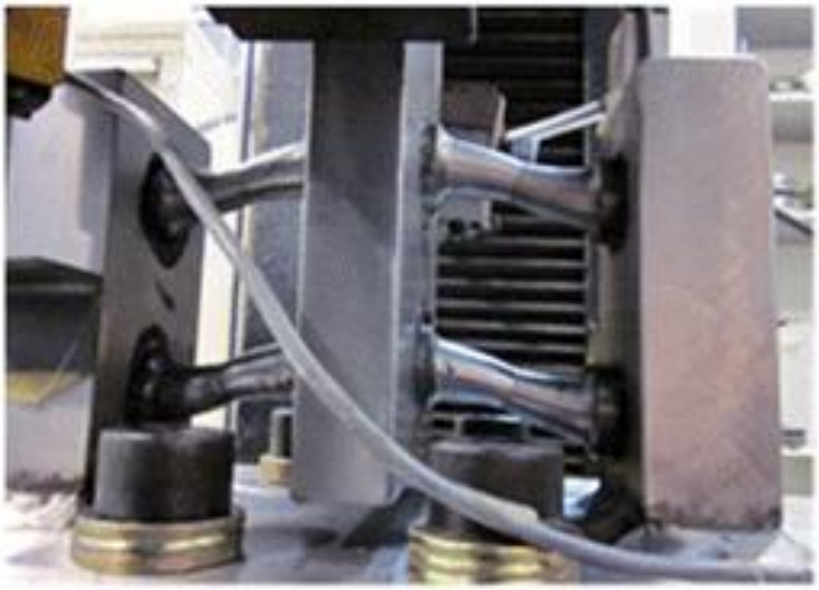

Figure 3.26 Setup for WHP component tests

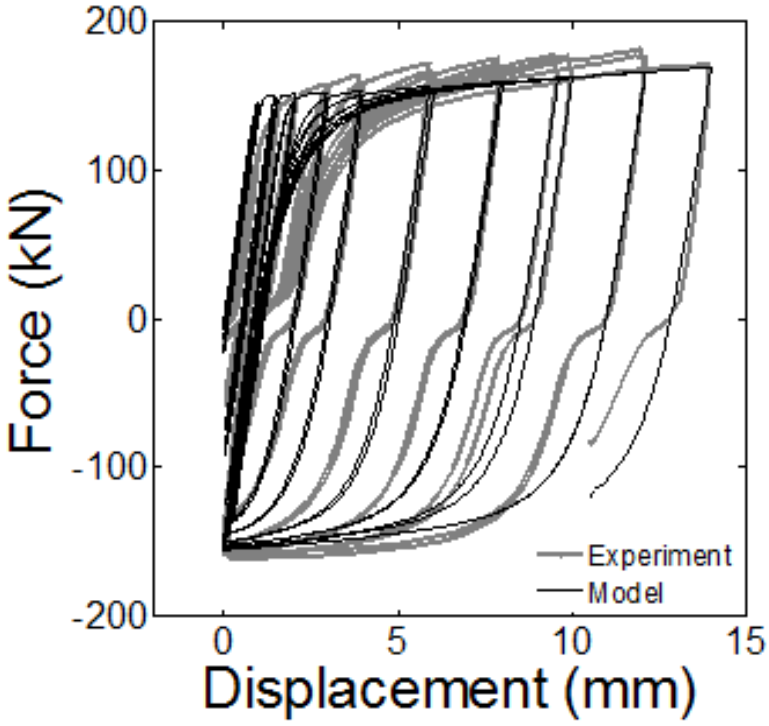

Figure 3.27 Comparison of experimental hysteresis and OpenSees hysteretic model of WHPs

3.5.3 Assessment of OpenSees model for PT connection with WHPs

The accuracy of the model for the PT connection with WHPs and the associated beams and columns (discussed in Section *3.5.1*) was assessed using results from large-scale experimental tests previously conducted by Vasdravellis et al (2013a). Figure 3.28 shows the experimental test setup. A strong 310UC158 column was used along with two additional steel members welded to the column to form a truss system which increases the horizontal stiffness of the test setup. The whole system was bolted on the strong floor. The beam had a 250UB37 cross-section. The length of the beam flange reinforcing plates was 0.7 m. The total post-tensioning force was 504 kN. The displacement history was applied vertically by a hydraulic actuator positioned at a distance of 1800mm from the inner face of the column. The beam sections, column sections and beam flange reinforcing plates were made of steel with yield strength equal to 300 MPa. The WHPs were made of steel with yield strength equal to 560 MPa. The material of the PT bars had nominal yield strength equal to 930 MPa, tensile stress 1050 MPa and elongation capacity 6%, according to the specifications of the supplier. The AISC (2005) loading protocol was used. This protocol consisted of three initial sets of six cycles at 6.75 mm, 9 mm, and 13.5 mm displacements, four subsequent cycles at 18 mm, and six sets of two cycles at 27, 36, and 54 mm. These displacements correspond to drifts equal to 0.00375, 0.005, 0.0075, 0.01, 0.015, 0.02, and 0.03. Figure 3.29 shows the experimental and analytical hysteresis for the PT connection and confirms a good agreement between the proposed model and the test results.

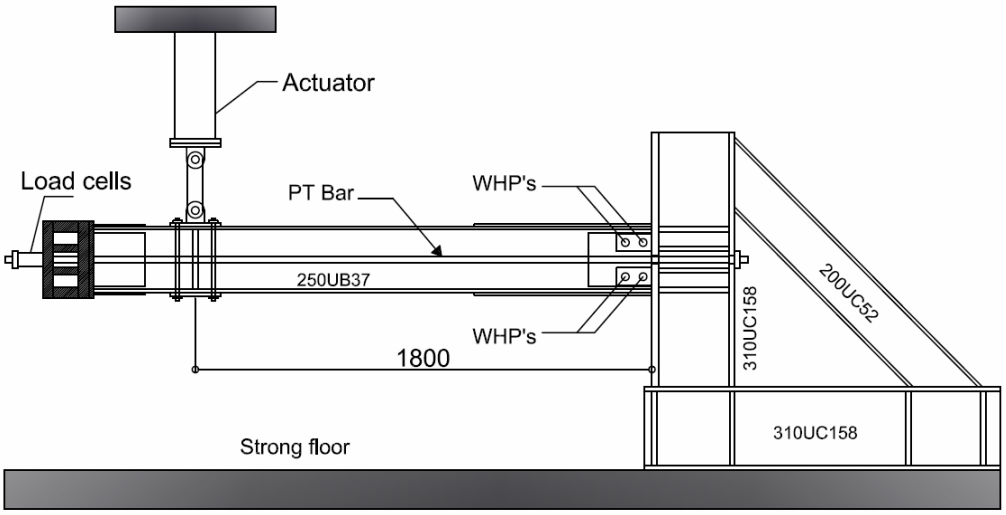

Figure 3.28 Setup for tests of PT connection with WHPs

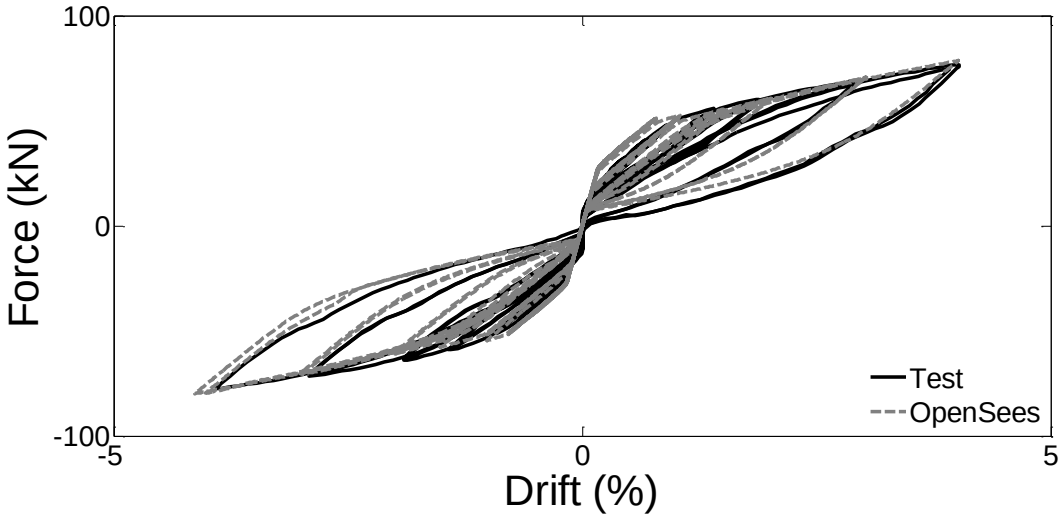

Figure 3.29 Comparison of experimental hysteresis and OpenSees model

3.6 Assessment of FEM and OpenSees model for PT connections under high drifts

In this chapter the FEM and the OpenSees model, will be compared against experiments conducted in Kim and Christopoulos (2008). The FEM is the one discussed in section 3.4.2. The OpenSees model has been developed following the procedure discussed in section 3.5.1. In this OpenSees model two zero-length hysteretic springs are placed at the exact locations of FEDs along the depth of the beam web. These springs have bilinear elastoplastic stress-strain behavior (Steel01 in OpenSees) instead of (Steel02 in OpenSees) used for WHPs. Very high elastic

stiffness and negligible post yield stiffness is use in (Steel01 in OpenSees) to provide perfectly plastic behavior.

Figure 3.30 shows the drift – force curve for the PT connection under monotonic loading. It is observed that both the FEM in Abaqus and the modelling in OpenSees are able to capture the deterioration due to local buckling phenomena with sufficient accuracy at similar drifts with the experiment.

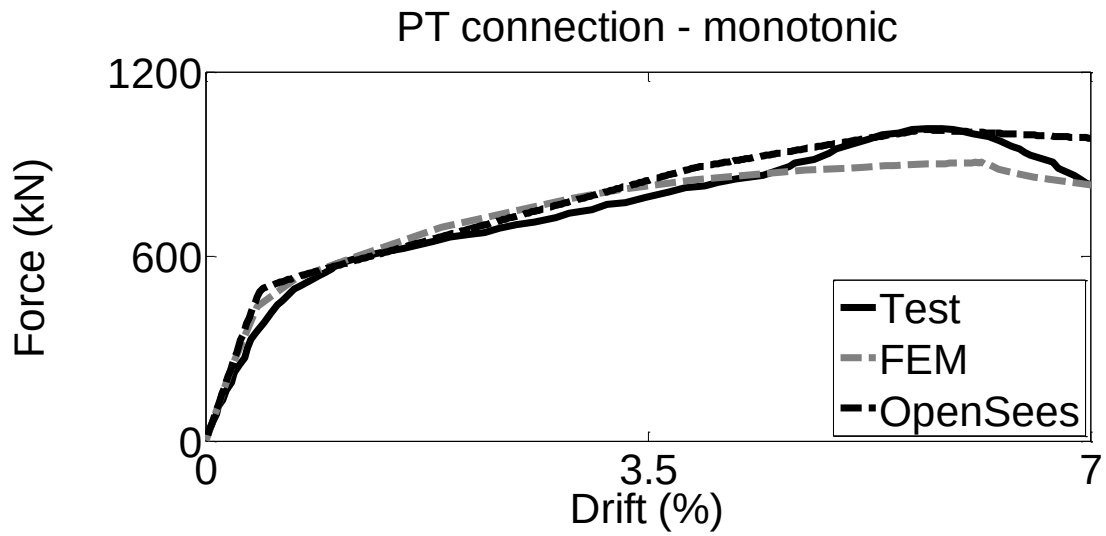

Figure 3.30 Experimental against modelling results under monotonic loading

Figure 3.31 shows the failure mode observed in Abaqus for the PT connection under cyclic loading. Figure 3.32 shows the failure mode observed in the experiment under cyclic loading, which coincides with the failure mode observed in Abaqus.

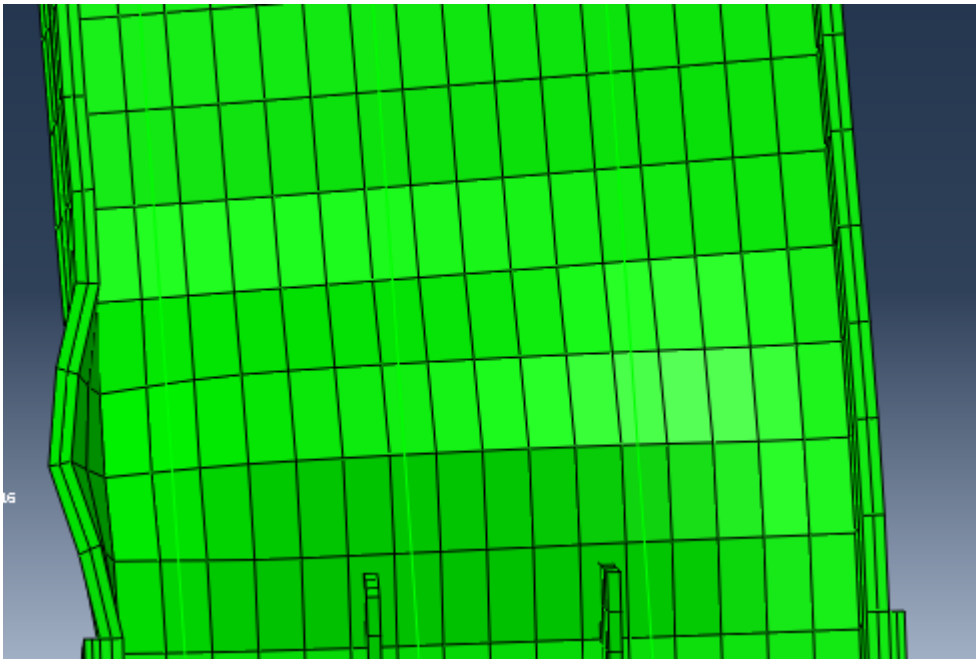

Figure 3.31 Failure mode of PT connection under monotonic loading in Abaqus

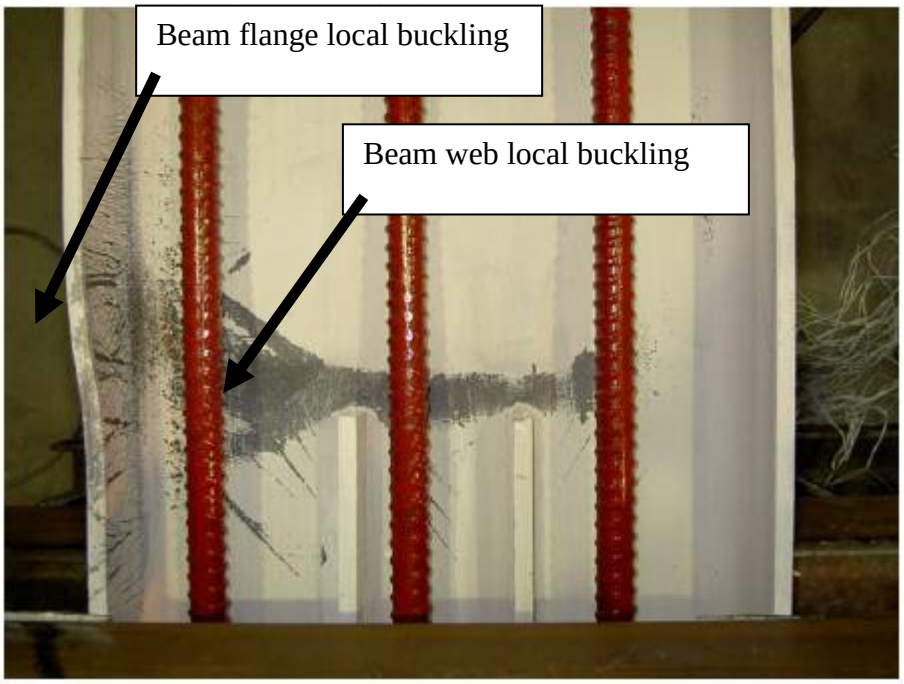

Figure 3.32 Experimental failure mode of PT connection under monotonic loading (Kim and Christopoulos 2008)

Figure 3.33 shows the drift – force curve, following (AISC 2005) for the PT connection under cyclic loading up to a drift equal to 3.5%. A good agreement between the FEM in Abaqus, the model in OpenSees and the tests results is confirmed.

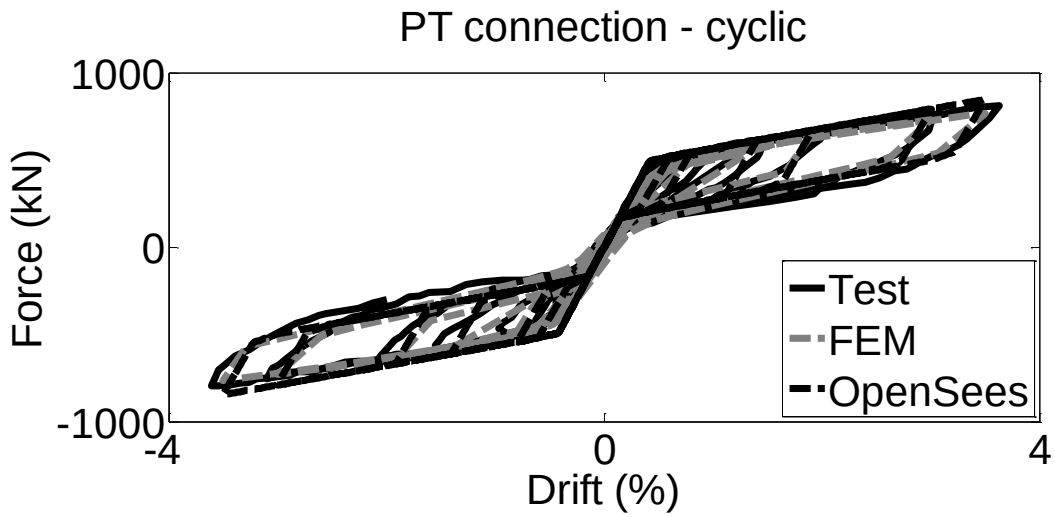

Figure 3.33 FEM & OpenSees model against experimental results under cyclic loading

Figure 3.34 shows the drift – force curve for the PT connection under cyclic loading for drift equal to 2%, 4%, 6% and 8%. It is shown that the OpenSees model is capable to capture the stiffness and strength deterioration due to local buckling phenomena with sufficient accuracy at similar drifts with the FEM.

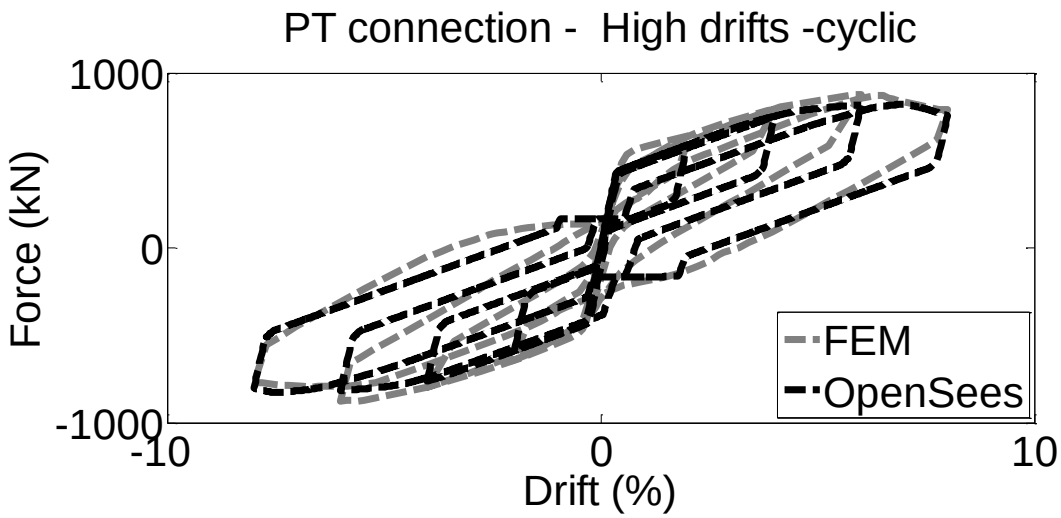

Figure 3.34 FEM & OpenSees model under high drifts cyclic loading

3.7 Summary

In this chapter, FEM of steel beams with or without axial force were developed in Abaqus and subjected into cyclic and monotonic loading. The FEM were compared against experimental results, and the comparison showed that the recommended modelling procedure is capable to simulate the beam local buckling. A FEM of a PT connection was developed according to the aforementioned procedure in Abaqus and validated against experimental results. This FEM was subjected into monotonic and cyclic loading under high drifts in order to develop beam flange and web local buckling. A modelling procedure for PT connections in OpenSees has been developed and compared against FEM and experimental results. The comparison showed that the PT connection model in OpenSees is able to accurately capture the connection behaviour and the stiffness and strength deterioration because of local buckling under high drifts. So the proposed model can be used in the modelling of SC-MRFs up to collapse.

4 Seismic design procedure for SC-MRFs with viscous dampers

4.1 Introduction

In this chapter a seismic design and assessment procedure of steel SC-MRFs with viscous dampers within the framework of EC8 (Eurocode 8 2013) is developed. Research towards the standardization of steel SC-MRFs within the framework of EC8 (Eurocode 8 2013) is missing. Moreover, the effectiveness of the seismic design strategy that combines steel SC-MRFs with viscous dampers to simultaneously control peak story drifts and residual story drifts has not been assessed. In this chapter the SC-MRFs are using the recently developed PT connection with WHPs (Vasdravellis et al 2013a,b; Dimopoulos et al 2013). Performance levels are defined with respect to drifts, residual drifts and limit states in the PT connections. A preliminary pushover analysis is conducted at the early phase of the design process to estimate rotations and axial forces in PT connections instead of using approximate formulae.

4.2 SC-MRF using PT connections with WHPs

4.2.1 Structural details

Figure 4.1 shows a SC-MRF using PT connections with WHPs, and figure 4.2 shows an exterior PT connection with WHPs (Vasdravellis et al 2013a). Two high strength steel bars located at the mid depth of the beam, one at each side of the beam web, pass through holes drilled on the column flanges. The bars are post-tensioned and anchored to the exterior columns. WHPs are inserted in aligned holes on the beam web and on supporting plates welded to the column flanges. Energy is dissipated through inelastic bending of the WHPs that have an optimized hourglass shape (Figure 4.3) with enhanced fracture capacity (Vasdravellis et al 2015). The beam web and the beam flanges are reinforced with steel plates. The panel zone is strengthened with doubler and continuity plates. A fin plate welded on the column flange and bolted on the beam web is used for easy erection and resistance against gravity loads before post-tensioning. Slotted holes on the beam web ensure negligible influence of the fin plate on the PT connection behaviour.

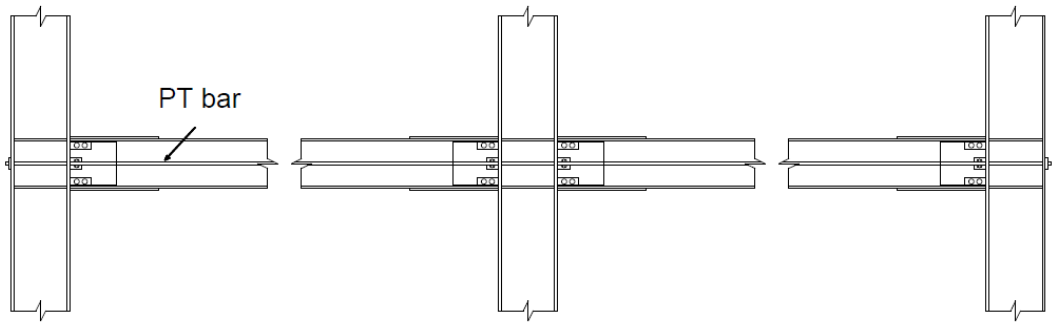

Figure 4.1 SC-MRF

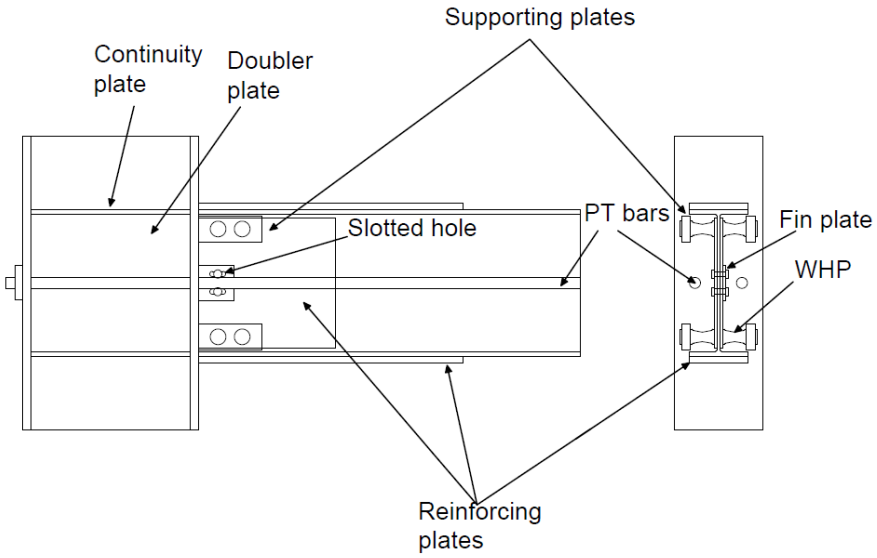

Figure 4.2 Exterior PT connections with WHPs

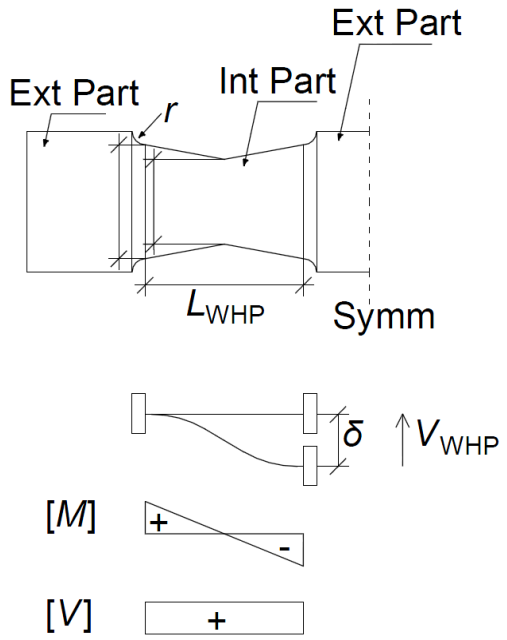

Figure 4.3 WHP geometry and assumed static system

A discontinuous steel-concrete composite slab (details shown in figures 4.4-5) is used to avoid damage in the slab as the gaps in the PT connections open and close (see figures 4.6-7), i.e. similar to the solutions proposed in (Chou et al 2009, Kim and Christopoulos 2008a,b Kim and Christopoulos 2009a). Shear studs for composite action are welded only on the secondary beams. The slab discontinuity is achieved by using two angle sections sliding on the beam framing perpendicularly to the SC-MRF columns. The slab reinforcing mesh is discontinued at the level of the angles. The secondary beams and the slab are placed after post-tensioning. The slab diaphragm eliminates beam shortening, and so, the internal axial forces in the beams remain constant and equal to those due to initial post-tensioning of the PT bars. Any further increase in the PT bars forces due to elongation under gap opening is transferred to the beam-column interfaces by the slab diaphragm.

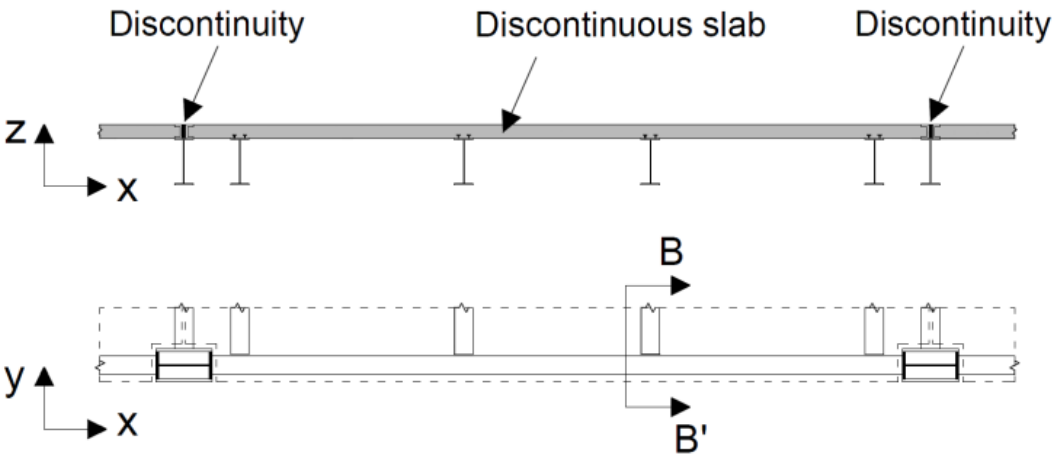

Figure 4.4 Discontinuous steel-concrete composite slab details

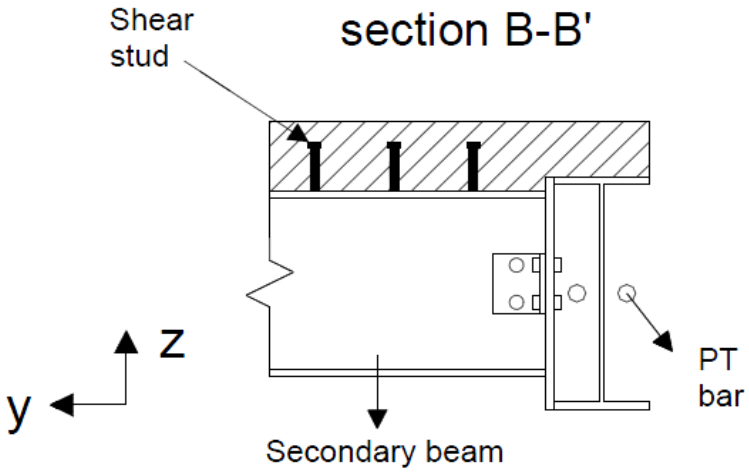

Figure 4.5 Discontinuous steel-concrete composite slab details (section B-B)

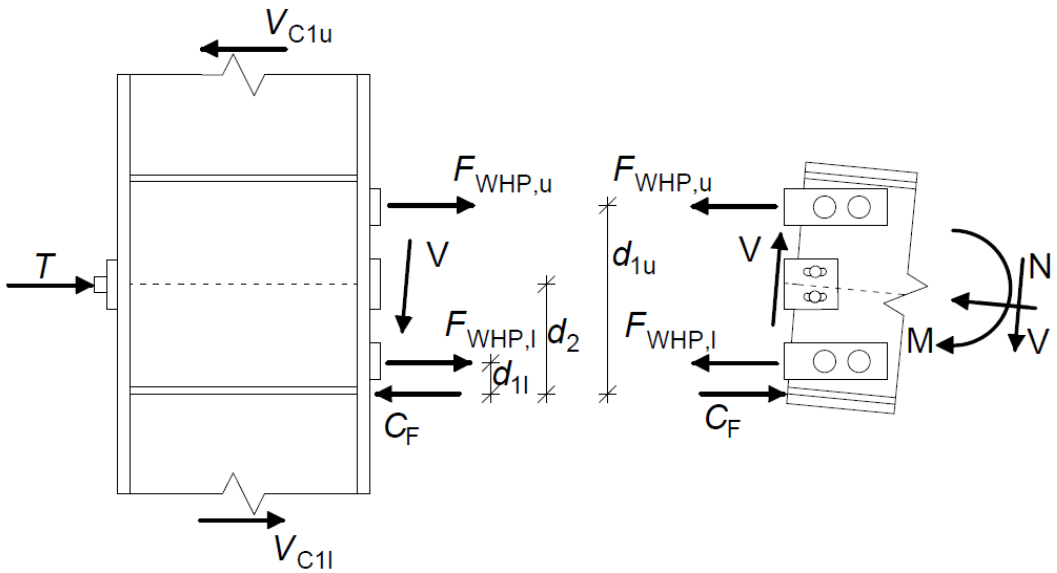

Figure 4.6 Free body diagram of an external PT connection

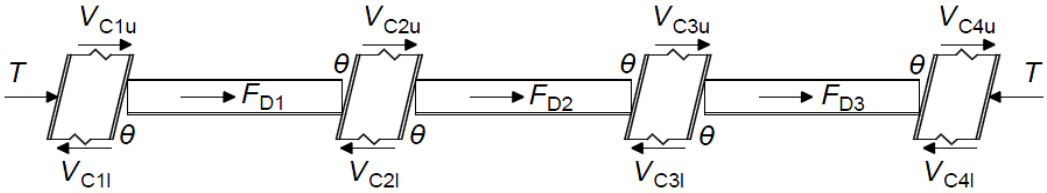

Figure 4.7 SC-MRF expansion and horizontal forces equilibrium

4.2.2 PT connection behavior

Figure 4.6 shows the free body diagram of an external PT connection where d_{1u} and d_{1l} are the distances of the upper and lower WHPs from the center of rotation that is assumed to be at the inner edge of the beam flange reinforcing plates; d_2 is the distance of the PT bars from the center of rotation; T is the total force in both PT bars; $F_{WHP,u}$ and $F_{WHP,l}$ are the forces in the upper and lower WHPs; C_F is the compressive force in the beam-column interface; V_{C1u} and V_{C1l} are the shear forces in the upper and lower column, M is the PT connection moment, V is the beam shear force; and N is the horizontal clamping force that is transferred to the beam-column interface through the slab diaphragm and the beam. Figure 4.7 shows the SC-MRF expansion due to rotations θ in the PT connections. N is given by

$$N = T + V_{C1u} - V_{C1l} \tag{4.1.a}$$

for the external connection of figure 4.6 and by

$$N = T + \sum (V_{Ciu} - V_{Cil}) + \sum F_{Dj} \tag{4.1.b}$$

for an internal connection of figure 4.7 where V_{Ciu} and V_{Cil} are the shear forces developed in all the columns i and F_{Dj} are the slab inertia forces transferred (by the secondary beams) to the mid-depth of all the beams j up to the point of the examined internal connection. Equations (4.1.a) and (4.1.b) are derived by horizontal equilibrium of the free body diagrams of figures 4.6 and 4.7.

Figure 4.8 shows the theoretical cyclic M-θ behaviour of the PT connection with WHPs. M is given by

$$M = M_{\mathrm{N}} + M_{\mathrm{WHP}} \tag{4.2}$$

where M_{N} is the moment contribution from N (shown in figure 4.9) and M_{WHP} is the moment contribution from the WHPs (shown in figure 4.10). Similar expressions can be found in the literature (Vasdravellis et al 2013a, Garlock et al 2007, Kim and Christopoulos 2008a, Kim and Christopoulos 2009a). After decompression of the PT connection (Point 1 in figure 4.8), gap opens and the behaviour becomes nonlinear elastic with rotational stiffness S_1. At point 2, the upper WHPs yield and M continues to increase with slope S_2. At point 3, the lower WHPs yield and M continues to increase with slope S_3. When loading is reversed, the connection begins to unload until the gap closes. Equations to calculate $S_{\mathrm{WHP},1}$ to $S_{\mathrm{WHP},3}$, S_{N}, S_1 to S_3 and θ_2 to θ_3 are provided in section 4.2.3.

The M_{WHP}-θ behaviour is multi-linear elastoplastic (see Figure 4.10). When loading is reversed and until the gap closes, the PT bars unload with their elastic stiffness. This explains why the M_{N}-θ curve fully unloads with its initial stiffness.

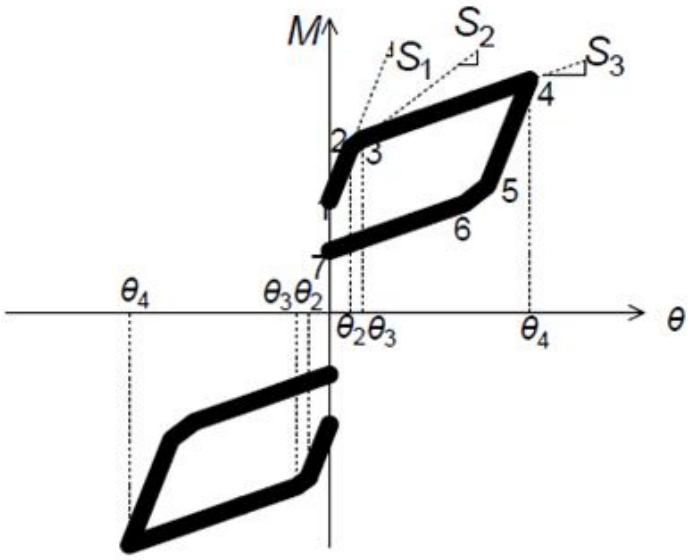

Figure 4.8 Theoretical cyclic behaviour of the PT connection with WHPs

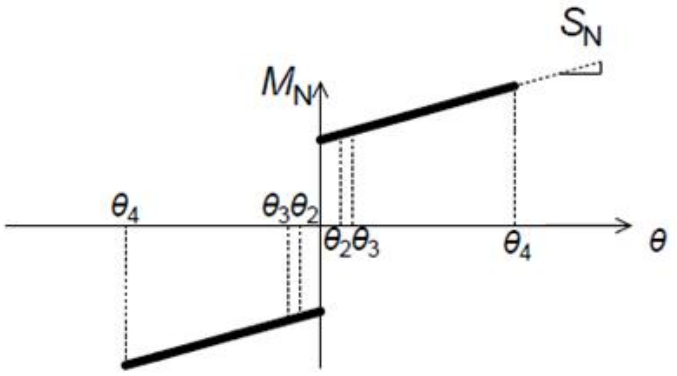

Figure 4.9 Moment contribution from *N*

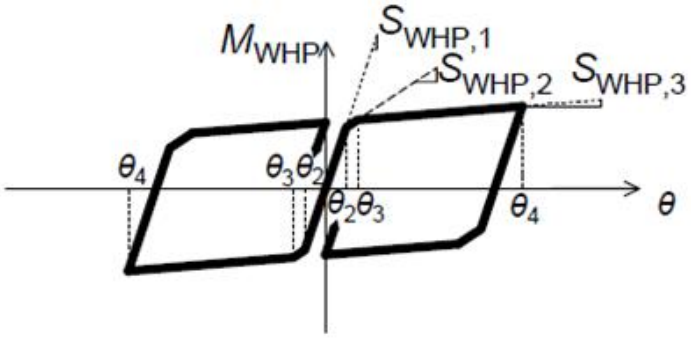

Figure 4.10 Moment contribution from the WHPs

4.2.3 Design procedure for the PT connection

Given the rotations of the PT connection under the DBE and MCE (i.e. θ_{DBE} and θ_{MCE}) and the corresponding forces V_{Ciu}, V_{Cil} and F_{Dj} from a preliminary pushover analysis of the SC-MRF that is discussed in Section 4.3, the design procedure

involves sizing of the connection components (e.g. PT bars, WHPs, fuse, reinforcing plates) to achieve a target connection performance, and has the following steps:

Step (1): Calculate the initial post-tensioning force. Select a value for the ratio $M_{IGO}/M_{pl,b}$ where M_{IGO} is the moment at point 2 in figure 4.8 and $M_{pl,b}$ is the plastic moment of resistance of the beam. $M_{IGO}/M_{pl,b}$ should be less than one for the SC-MRF to have base shear strength comparable to that of conventional MRFs. Select a value for the ratio M_d/M_{IGO} where M_d is the moment contribution from the total initial post-tensioning force T_0 in both PT bars. In past research, M_d is referred as decompression moment (Garlock et al 2007, Kim and Christopoulos 2008a, Kim and Christopoulos 2009a). M_d/M_{IGO} should be larger than 0.5 to approximately achieve self-centering behaviour of the PT connection (Rojas et al 2005, Garlock et al 2007) (the effectiveness of the selected M_d/M_{IGO} value is accurately evaluated in design Step 4). T_0 is given by

$$T_0 = \frac{M_d}{d_2} \tag{4.3}$$

Step (2): Design the PT bars. Assume an initial PT bar diameter d_{PT} and calculate the total yield force of both PT bars, T_y, by

$$T_y = 0.5 \cdot f_{y,PT} \cdot \pi \cdot d_{PT}^2 \tag{4.4}$$

where $f_{y,PT}$ is the yield strength of the PT bar material. Calculate T by

$$T(\theta) = T_0 + d_2 \cdot \theta \cdot K_{PT} \tag{4.5}$$

where K_{PT} is the total axial stiffness of both PT bars, calculated by

$$K_{PT} = \frac{E_{PT} \cdot A_{PT}}{L_{PT}} \cdot \frac{\sum_{i=1}^{n} \Delta_{gap,i}}{\Delta_{gap}} \tag{4.6}$$

where E_{PT} is the Young's moduli, A_{PT} is the total cross-section areas, and L_{PT} is the total length of the PT bars. $\Delta_{gap,i}$ is the gap opening at the mid-depth of the beam of a connection i, n is the total number of connections per floor, and Δ_{gap} is the gap opening of the specific connection to be designed. The gap opening of any connection can be calculated as

$$\Delta_{gap,i} = d_{2,i} \cdot \theta_i \tag{4.7}$$

Select the safety factor against PT bar yielding γ_{PT} (recommendations are given in chapter 5) and check if $T_y/T(\gamma_{PT} \cdot \theta_{MCE}) \geq 1.0$. If $T_y/T(\gamma_{PT} \cdot \theta_{MCE}) < 1.0$, design Step 2 should be repeated with a larger d_{PT}.

The difference of equation (4.5) with those proposed in (Garlock et al 2007, Kim and Christopoulos 2009b) is that beam shortening is not considered as this is eliminated by the slab diaphragm (see previous discussion in section 4.2.1).

Step (3): Design the WHPs. Select the number of upper and lower WHPs, n_{WHPs} (=2 in figure 4.2), and calculate the required yield force of one WHP, $F_{WHP,y}$, from

$$F_{WHP,y} = \frac{d_{1u}}{n_{WHPs}} \cdot \frac{M_{IGO} - M_N(\theta_2)}{d_{1u}^2 + d_{1l}^2} \tag{4.8}$$

by substituting M_d for $M_N(\theta_2)$ as $M_N(\theta_2)$ is still unknown. The required plastic moment of resistance of the WHPs cross-section, $M_{pl,WHP}$ is calculated by

$$M_{pl,WHP} = 0.25 \cdot F_{WHP,y} \cdot L_{WHP} \tag{4.9}$$

where L_{WHP} is the length of half a WHP (see figure 4.3). The external, D_e, and internal, D_i, diameters of the WHP (Figure 4.3) are designed by using

$$D_e = \left(\frac{6 \cdot M_{pl,WHP}}{f_{y,WHP}} \right)^{\frac{1}{3}} \tag{4.10}$$

$$D_{\mathrm{i}} \geq \sqrt{\frac{2 \cdot F_{\mathrm{y,WHP}} \cdot \sqrt{3}}{\pi \cdot f_{\mathrm{y,WHP}}}} \tag{4.11}$$

where $f_{\mathrm{y,WHP}}$ is the yield strength of the WHP material. The elastic stiffness of a WHP is calculated from (Vasdravellis et al 2013a)

$$K_{\mathrm{fe}} = \frac{18 \cdot \pi \cdot D_{\mathrm{e}}^3 \cdot D_{\mathrm{i}} \cdot E_{\mathrm{WHP}} \cdot G_{\mathrm{WHP}}}{40 \cdot E_{\mathrm{WHP}} \cdot D_{\mathrm{e}}^2 \cdot L_{\mathrm{WHP,i}} + 48 \cdot G_{\mathrm{WHP}} \cdot L_{\mathrm{WHP,i}}^3} \tag{4.12}$$

where E_{WHP} is the Young's modulus and G_{WHP} the shear modulus of the WHP material. θ_2 and θ_3 (Figure 4.10) are calculated by

$$\theta_2 = F_{\mathrm{WHP,y}} / (K_{\mathrm{fe}} \cdot d_{1\mathrm{u}}) \tag{4.13}$$

$$\theta_3 = F_{\mathrm{WHP,y}} / (K_{\mathrm{fe}} \cdot d_{1\mathrm{l}}) \tag{4.14}$$

With θ_2 known, $M_{\mathrm{N}}(\theta_2)$ is calculated by

$$M_{\mathrm{N}}(\theta_2) = M_{\mathrm{d}} + K_{\mathrm{PT}} \cdot d_2^2 \cdot \theta_2 + S_{\mathrm{F}} \cdot \theta_2 \tag{4.15}$$

where S_{F} is the additional rotational stiffness of the frame due to the columns restraint that opposes gap opening. S_{F} is calculated by

$$S_{\mathrm{F}} = \frac{N(\theta_2) - T(\theta_2)}{\theta_2} \cdot d_2 \tag{4.16}$$

where ($N(\theta_2)$-$T(\theta_2)$) is calculated from equation (4.1) by using values for V_{Cil}, V_{Ciu} and F_{Dj} from a preliminary pushover analysis (discussed in Section 4.3). The new value of $M_{\mathrm{N}}(\theta_2)$ is used in equation. (4.8) and the WHP design process (Equations (4.8)-(4.16)) is repeated.

(Step 4): Self-centering capability. To check whether the PT connection provides self-centering behaviour up to a desired rotation θ_{SC}, the following relation should be satisfied:

$$M_d \geq \theta_2 \cdot (S_1 - S_2) + \theta_3 \cdot (S_2 - S_3) \tag{4.17}$$

where S_1 to S_3 (see figure 4.8) are given by

$$S_1 = S_{N,1} + S_{WHP,1} + S_F(\theta) \approx K_{PT} \cdot d_2^2 + 2 \cdot K_{fe} \cdot (d_{1l}^2 + d_{1u}^2) \tag{4.18a}$$

$$S_2 = S_{N,1} + S_{WHP,2} + S_F(\theta) \approx K_{PT} \cdot d_2^2 + 2 \cdot (K_{fe} \cdot d_{1l}^2 + K_{fp} \cdot d_{1u}^2) \tag{4.18b}$$

$$S_3 = S_{N,1} + S_{WHP,3} + S_F(\theta) \approx K_{PT} \cdot d_2^2 + 2 \cdot K_{fp} \cdot (d_{1l}^2 + d_{1u}^2) \tag{4.18c}$$

and K_{fp} is the post-yield stiffness of a WHP that is assumed equal to 2% the initial stiffness. If equation (4.17) is not satisfied, return to design Step 1 and repeat the design procedure with a higher M_d/M_{IGO} ratio. Equation (4.17) was derived by following the procedure described in (Christopoulos et al 2002).

(Step 5): Design the reinforcing plates. Following the design procedure in (Garlock et al 2007), the length, L_{rp}, and the area, A_{rp}, of the beam flange reinforcing plate (Figure 4.2) are designed to control beam flange yielding at $\theta=\theta_{DBE}$. L_{rp} is given by

$$L_{rp} \geq \frac{L_b}{2} \cdot \frac{M - M_{rp}}{M} \tag{4.19}$$

where L_b is the beam clear length and M_{rp} is the moment at the end of the reinforcing plate. M_{rp} is calculated as a function of the beam internal axial force and a predefined target value of $\varepsilon_c/\varepsilon_y$ where ε_c the maximum compressive strain in the beam flange at the end of the reinforcing plate and ε_y the yield strain of the beam material (Garlock et al 2007). As was discussed, the beam internal axial force remains constant due to the slab diaphragm and can be conservatively assumed equal

to T_0 without considering the column restraint. M depends on the rotation θ, i.e. for $\theta_2<\theta<\theta_3$

$$M = d_{1u} \cdot n_{WHPs} \cdot \left[F_{WHP,y} + K_{fp} \cdot d_{1u} \cdot (\theta - \theta_2) \right] + d_{1l}{}^2 \cdot n_{WHPs} \cdot K_{fe} \cdot \theta + d_2 \cdot N(\theta) \quad (4.20a)$$

and for $\theta \geq \theta_3$

$$M = n_{WHPs} \cdot F_{WHP,y} \cdot d_{1u} + n_{WHPs} \cdot F_{WHP,y} \cdot d_{1l} + n_{WHPs} \cdot \left[d_{1u}{}^2 \cdot K_{fp} \cdot (\theta - \theta_2) + d_{1l}{}^2 \cdot K_{fp} \cdot (\theta - \theta_3) \right] + d_2 \cdot N(\theta) \quad (4.20b)$$

The minimum A_{rp} to avoid beam flange yielding at the beam-column interface is calculated by

$$A_{rp} = \frac{C_F - b_f \cdot t_f \cdot f_{y,b}}{f_{y,rp}} \quad (4.21)$$

where $f_{y,rp}$ is the yield strength of the reinforcing plate material and t_f and b_f are the thickness and width of the beam flange, respectively. For $\theta_2<\theta<\theta_3$, C_F (see figure 4.8) is obtained by

$$C_F = N(\theta) + n_{WHPs} \cdot \left[F_{WHP,y} + d_{1u} \cdot K_{fp} \cdot (\theta - \theta_2) + d_{1l} \cdot K_{fe} \cdot \theta \right] \quad (4.22a)$$

and for $\theta > \theta_3$ by

$$C_F = N(\theta) + 2 \cdot n_{WHPs} \cdot F_{WHP,y} + n_{WHPs} \cdot \left[d_{1u} \cdot K_{fp} \cdot (\theta - \theta_2) + d_{1l} \cdot K_{fp} \cdot (\theta - \theta_3) \right] \quad (4.22b)$$

Equations (4.19) – (4.22b) were derived following the design methodology described in (Garlock et al 2007). The beam web reinforcing plates and the supporting plates are designed to avoid yielding under the peak WHP bearing forces following the design procedure in (Vasdravellis et al 2015). The panel zones are designed according to EC8 (Eurocode 8 2013) and EC3 (Eurocode 3 2010) and are reinforced with doubler and continuity plates.

4.3 Performance-based seismic design procedure

The seismic design procedure for steel SC-MRFs with or without viscous dampers is based on the force based design method (e.g. EC8 (Eurocode 8 2013)) using multiple limit states. SC-MRFs reduce the structural damage, by avoiding the development of plastic deformations on the beams, while the use of viscous dampers results in reduce of buildings displacements and accelerations. So this way we achieve reduce in the damage of structural, non structural elements and contents. The proposed design procedure ensures a pre-defined structural and non-structural target building performance, and has the following steps:

(Step 1): Define target building performance. Structural limit states include limit states of the PT connections, yielding and plastic hinge formation at the column bases, and limit values for the maximum residual storey drift, $\theta_{s,res}$. Limit states of the PT connections include WHPs yielding (controlled by $M_{IGO}/M_{pl,b)}$, PT bar yielding (controlled by γ_{PT}), beam flange yielding at the end of the reinforcing plate (controlled by $\varepsilon_c/\varepsilon_y$), beam flange yielding at the beam-column interface (controlled by equation (4.21)), and self-centering behaviour (controlled by M_d/M_{IGO} and equation (4.17)). Non-structural limit states include limit values for the peak storey drift, $\theta_{s,max}$. For example, the following target building performance can be defined for a SC-MRF with viscous dampers and PT connections with WHPs by associating limit states with seismic intensities: *Operational* under the FOE: no yielding in beams and column bases; $\theta_{s,max}$ lower than the 'damage limitation' values of EC8; and PT connection decompression and modest yielding in WHPs. *Rapid Return to Occupancy* under the DBE: elimination of $\theta_{s,res}$; modest or no yielding in the beam flanges; modest or no yielding in base columns; low $\theta_{s,max}$ to ensure rapid repair of damaged drift-sensitive non-structural elements; and yielding and rapid replacement of WHPs. *Life Safety and Reparability* under the MCE: no beam plastic hinge formation; modest base column plastic hinge rotations; and $\theta_{s,res}$ lower than the global sway imperfections defined in EC3 (Eurocode 3 2010).

(Step 2): Select supplemental damping. The supplemental damping ratio ξ_s is added to the inherent damping ratio to provide a total damping ratio ξ_t which is then used to calculate the damping reduction factor B (Whittaker et al 2003) or η in EC8

(Eurocode 8 2013). This factor is used to scale down the elastic design spectrum of EC8.

(Step 3): Design beams and columns. The beam and column cross-sections are sized by designing the building as a conventional steel MRF on the basis of the modal response spectrum analysis (e.g. EC8 Eurocode 8 2013) and with respect to the highly damped spectrum of Step 2. A strength-based design for the DBE is first performed by reducing the highly damped spectrum with the behaviour factor q (i.e., 6.5 in EC8 (Eurocode 8 2013) for high ductility class MRFs). $\theta_{s,max}$ is then estimated on the basis of the equal displacement rule of EC8 (Eurocode 8 2013) to check the design against the FOE and DBE $\theta_{s,max}$ criteria of Step 1. The DBE ultimate limit state of EC8 (Eurocode 8 2013) is satisfied by enforcing the capacity design rule and the local ductility details for steel MRFs, and by taking into account second-order effects (P-Δ) through the storey drift sensitivity coefficient (Eurocode 8 2013).

(Step 4): Design fluid viscous dampers. Given ξ_s from Step 2 and the fundamental period of vibration T_1 from Step 3, nonlinear viscous dampers are designed by using the formula (Whittaker et al 2003):

$$\xi_s = \frac{\sum_j (2\pi)^a T^{2-a} \lambda_j f_j^{1+a} c_j u_r^{a-1} (\phi_j - \phi_{j-1})^{1+a}}{8\pi^3 \sum_j m_j \varphi_j^2} \tag{4.23}$$

where j denotes a specific storey, α is the velocity exponent of the nonlinear viscous dampers, λ_j a dimensionless parameter that depends on α, f_j the cosine of the angle of the damper centerline to the horizontal (e.g. f_j=1.0 for horizontal damper placement), c_j the damper constant, u_r the amplitude of the roof displacement, m_j the storey mass, and φ_j the modal coordinate of the first mode shape. Equation (4.23) assumes that viscous dampers are supported by braces stiff enough so that drift produces damper rather than brace deformation. Figures 4.11-12 show that dampers and supporting braces can be inserted in a gravity frame of the building. Equation (4.23) suggests that the required ξ_s can be provided by different combinations of c_j. A recent work showed small differences in the seismic performance of steel MRFs with viscous

dampers designed for the same ξ_s yet different methods (two advanced based on numerical optimization and three simplified of distributing c_j along the height of the building (Whittle et al 2012). Based on the latter finding and on recent research results presented in (Seo et al 2014), viscous dampers can be sized to satisfy a simple stiffness proportional distribution, i.e. $c_j=\varepsilon K_j$, where K_j is the horizontal storey stiffness of the SC-MRF and ε is a constant that is obtained by substituting $c_j=\varepsilon K_j$ into equation (4.23). The columns and braces of the gravity frame with dampers are designed to avoid buckling under the peak damper forces which are estimated using simplified procedures in (Whittaker et 2003). In case of large not practical c_j values, Steps 2 to 4 should be repeated by selecting a lower ξ_s value in Step 2.

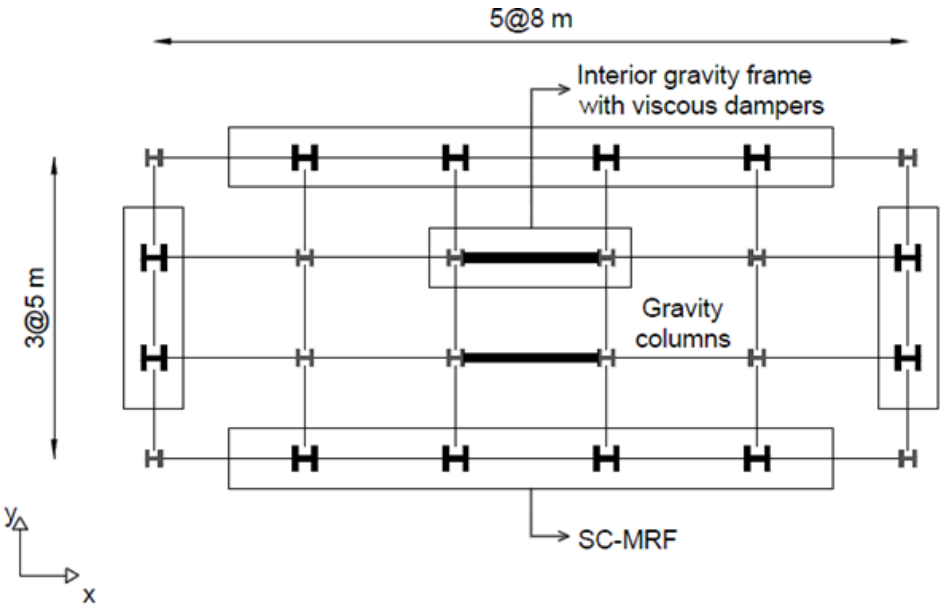

Figure 4.11 Plan view of a prototype building with SC-MRFs and viscous dampers

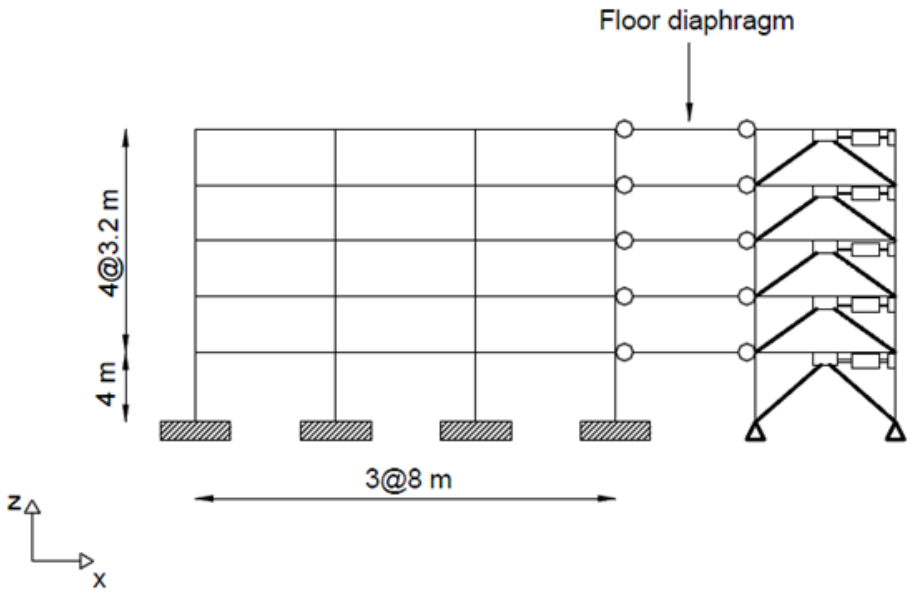

Figure 4.12 Elevation view of a prototype building with SC-MRFs and viscous dampers

(Step 5): Preliminary pushover analysis. A preliminary pushover analysis is performed using a simple model with nonlinear beam-column elements for the columns, elastic elements for the beams and nonlinear rotational springs at the ends of the beams to simulate the M-θ behaviour of the PT connections. The rotational springs should have a large initial stiffness (e.g. 60 times the beam flexural stiffness to provide stable and accurate results), a yield moment equal to M_{IGO} calculated from an appropriate $M_{IGO}/M_{pl,b}$ value as explained in section 4.2.3, and post-yield stiffness equal to $K_{PT} \cdot d_2^2$ where K_{PT} is estimated from equation (4.6). A_{PT} in equation (4.6) is calculated on the basis of an appropriate M_d/M_{IGO} value as explained in section 4.2.3. The required PT bar diameter can be estimated by assuming $T_0/T_y \approx 0.5$, which approximately ensures that PT bars avoid yielding under large rotations in the PT connections (Rojas et al 2004). At each step of the pushover analysis, the connection rotations and member forces are post-processed. PT connection rotations and member forces of a SC-MRF can be also estimated using approximate formulae, such as those presented in (Garlock et al 2007), instead of using pushover analysis. However, pushover analysis is now available in most commercial software packages and is also promoted by EC8 (Eurocode 8 2013) as an alternative to linear analysis methods. In addition, the limit states of Step 1 associated with base column yielding and plastic hinge formation are checked. Modest yielding at column bases, i.e. low rotation ductility values (e.g. less than 2 (FEMA-273 1997)), under the DBE and

MCE along with full self-centering capability of the PT connections will ensure satisfaction of the $\theta_{s,res}$ criteria of Step 1.

(Step 6): Design PT connections. Given the results of the preliminary pushover analysis of Step 5, PT connections are designed using the procedure in section 4.2.3 to achieve the target connection performance defined in Step 1.

4.4 Summary

This chapter focused on seismic design and assessment of steel SC-MRFs with viscous dampers within the framework of EC8 (Eurocode 8 2013). SC-MRFs are using the recently developed PT connection with WHPs (Vasdravellis et al 2013a,b). Performance levels are defined with respect to drifts, residual drifts and limit states in the PT connections. A preliminary pushover analysis is conducted at the early phase of the design process to estimate rotations and axial forces in PT connections instead of using approximate formulae. Strict design criteria for the PT connections along with a low peak storey drift target value should be enforced to genuinely achieve seismic resilience, e.g. rapid return to building occupancy after the DBE.

5 Design modelling and seismic assessment of SC-MRFs with viscous dampers

5.1 Introduction

In this chapter a prototype building is designed as a SC-MRF with or without viscous dampers according to the design procedure presented in chapter 4. Different designs of the SC-MRF with viscous dampers are considered to investigate all possible scenarios, i.e. use of dampers to achieve drifts significantly lower than the EC8 (Eurocode 8 2013) drift limit; to significantly reduce steel weight without exceeding the EC8 (Eurocode 8 2013) drift limit; or to reduce steel weight and achieve drifts lower than the EC8 (Eurocode 8 2013) drift limit. Nonlinear dynamic analyses in OpenSees (Mazzoni et al 2006) using models capable of simulating all structural limit states up to collapse confirm the minimal-damage performance of the SC-MRFs. It is shown that the use of the preliminary pushover analysis makes the design procedure very accurate in predicting structural and non-structural limit states. Supplemental damping along with strict design criteria for the PT connections are found to significantly improve the seismic performance of the SC-MRFs

5.2 SC-MRFs with viscous dampers

5.2.1 Prototype building

Figures 5.1-2 show the plan and elevation view respectively, of a 5-storey, 5-bay by 3-bay prototype building having two identical SC-MRFs in the 'x' plan direction. Viscous dampers are inserted in the interior gravity frames (with pinned beam-column and column base connections) that are coupled with the perimeter SC-MRFs through the floor diaphragm to form SC-MRFs with viscous dampers as shown in figure 5.2. This chapter focuses on one of the SC-MRFs with dampers. The building has ductile non-structural elements, and so, $\theta_{s,max}$ should be lower than 0.75% under the FOE according to EC8 (Eurocode 8 2013). The DBE is expressed by the Type 1 elastic response spectrum of EC8 (Eurocode 8 2013) with peak ground acceleration equal to 0.35g and ground type B. The FOE has intensity of 40% (reduction factor v=0.4 in EC8 (Eurocode 8 2013)) the intensity of the DBE. The MCE has intensity

of 150% the intensity of the DBE (FEMA-368 2000a). The model used for the design is based on the centerline dimensions of the SC-MRF without accounting for the finite panel zone dimensions. A 'lean-on' column is included in the model to account for the P-Δ effects of the vertical loads acting on the gravity columns in the tributary plan area (half of the total plan area) assigned to the SC-MRF. A rigid diaphragm constraint is imposed at the nodes of each floor level for the design. The steel yield strength is equal to 355 MPa for the columns, 275 MPa for the beams, 835 MPa for PT bars, 235 MPa for the WHPs, and 275 MPa for the beam reinforcing plates. Nonlinear viscous dampers are designed with a horizontal configuration (i.e. f_j =1) and a=0.5. The inherent damping ratio of the SC-MRF is equal to 3%.

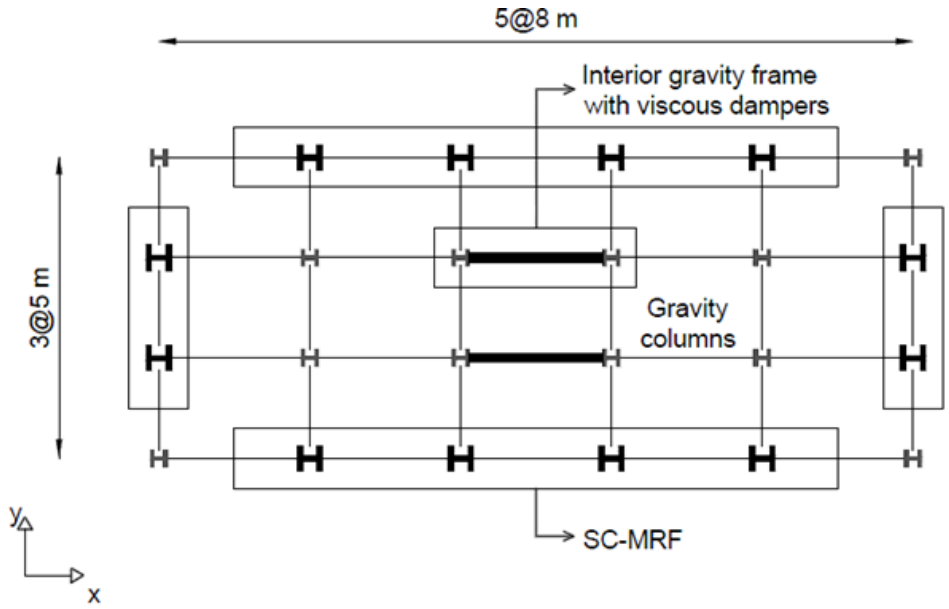

Figure 5.1 Plan view of a prototype building with SC-MRFs and viscous dampers

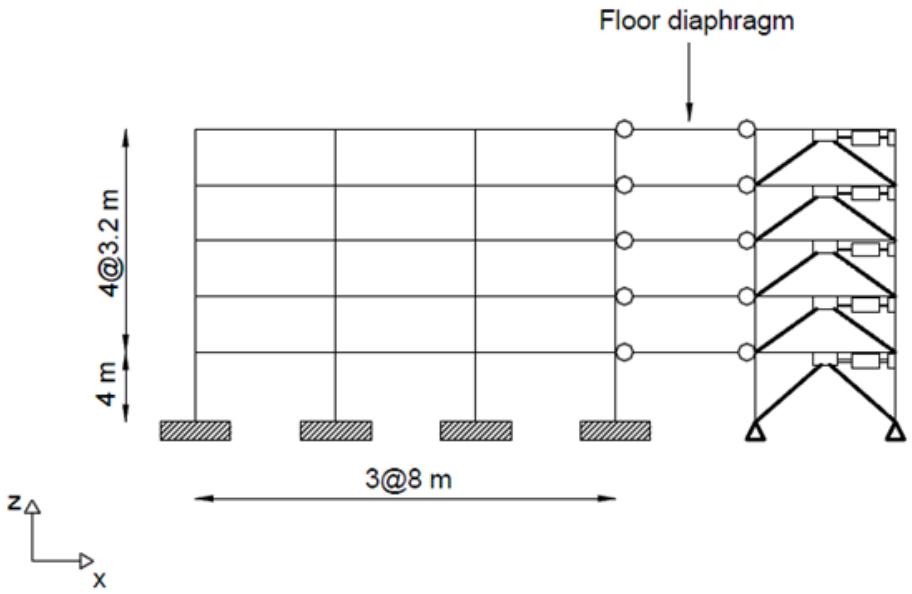

Figure 5.2 Elevation view of a prototype building with SC-MRFs and viscous dampers

5.2.2 Design cases

Different versions of the SC-MRF with viscous dampers (see figure 5.2) are designed to investigate different design scenarios. The PT connections are designed for $M_{IGO}/M_{pl,b}$=0.65 and M_d/M_{IGO}=0.6. A $\varepsilon_c/\varepsilon_y$ value equal to 2 under the DBE was used for conventional performance SC-MRFs, i.e. according to the recommendation in Garlock et al (2007). To achieve structural and non-structural damage harmonization, stricter design criteria ($\varepsilon_c/\varepsilon_y$ and γ_{PT}) are used for the PT connections of the SC-MRFs designed for lower $\theta_{s,max}$. Table 5.1 provides a comparison of the steel weight, T, ξ_t and design criteria of the SC-MRFs which are discussed below:

Table 5.1 Data and design criteria for the SC-MRFs with viscous dampers

SC-MRF	Steel Weight [a] (kN)	T (s.)	ξ_t (%)	$\theta_{s,max}$ FOE (%)	$\theta_{s,max}$ DBE (%)	$\theta_{s,max}$ MCE (%)	$\varepsilon_c/\varepsilon_y$ (DBE)	γ_{PT}
CP3D100W	268	1.27	3.00	0.72	1.80	2.70	2.0	2.1
HP20D100W	268	1.27	20.0	0.48	1.20	1.80	1.0	3.5
CP11D86W	230	1.63	11.0	0.72	1.80	2.70	2.0	2.1
HP19.5D86W	230	1.63	19.5	0.60	1.50	2.25	1.3	2.6
CP22D70W	190	2.22	22.0	0.72	1.80	2.70	2.0	2.1

[a] Beams and columns

CP3D100W: Conventional performance SC-MRF without viscous dampers (ξ_t =3%).

HP20D100W: High performance SC-MRF with viscous dampers (ξ_t =20%). It demonstrates the design scenario where viscous dampers are used to achieve $\theta_{s,max}$ significantly lower than the EC8 (Eurocode 8 2013) limit. It also demonstrates the design scenario where strict design criteria for the PT connections along with a low $\theta_{s,max}$ target value are enforced to genuinely achieve seismic resilience. Its target performance led to the same cross sections and PT connections details with those of CP3D100W.

CP11D86W: Conventional performance SC-MRF with viscous dampers (ξ_t =11%). Its steel weight is 86% the steel weight of CP3D100W. It represents the design scenario where viscous dampers are used to reduce steel weight without exceeding the EC8 (Eurocode 8 2013) $\theta_{s,max}$ limit.

HP19.5D86W: High performance SC-MRF with viscous dampers (ξ_t=19.5%). It represents the design scenario where viscous dampers are used to reduce steel weight and achieve $\theta_{s,max}$ lower than the EC8 (Eurocode 8 2013) limit. Its target performance led to the same cross sections and PT connections details with those of CP11D86W.

CP22D70W: Conventional performance SC-MRF with viscous dampers (ξ_t=22%). Its steel weight is 70% the steel weight of CP3D100W. It represents the design scenario where viscous dampers are used to significantly reduce steel weight without exceeding the EC8 (Eurocode 8 2013) $\theta_{s,max}$ limit.

Table 5.2 provides the θ_{DBE} and θ_{MCE} (from preliminary pushover analyses; Step 5 in chapter 4.3) used to design the PT connections of the SC-MRFs. Tables 5.3-5.5 provide the beams and columns cross-sections, d_{PT} and T_0, L_{rp} and A_{rp}, and c of the SC-MRFs.

Table 5.2 θ_{DBE} and θ_{MCE} (in rads) used to design the PT connections of the SC-MRFs

Storey	CP3D100W		HP20D100W		CP11D86W		HP19.5D86W		CP22D70W	
	θ_{DBE}	θ_{MCE}	θ_{DBE}	θ_{MCE}	θ_{DBE}	θ_{MCE}	θ_{DBE}	θ_{MCE}	θ_{DBE}	θ_{MCE}
1	0.013	0.023	0.008	0.013	0.011	0.020	0.009	0.015	0.012	0.018
2	0.015	0.024	0.009	0.015	0.014	0.023	0.012	0.019	0.015	0.022
3	0.015	0.024	0.009	0.015	0.016	0.025	0.013	0.020	0.017	0.025
4	0.013	0.021	0.007	0.013	0.015	0.024	0.012	0.019	0.017	0.025
5	0.010	0.018	0.004	0.010	0.013	0.022	0.010	0.018	0.015	0.023

Table 5.3 Design details for the CP3D100W and HP20D100W SC-MRFs

Storey	Cross sections			PT bars		WHPs			Reinforcing plates		Viscous dampers c (kN·(s./m)$^{0.5}$)	
	Beams	Columns	Gravity columns	T_0 (kN)	d_{PT} (mm)	D_e (mm)	D_i (mm)	L_{WHP} (mm)	L_{rp} (mm)	A_{rp} (mm)	CP3D100W	HP20D100W
1	IPE550	HEB650	HEB240	1087	43	43	33	70	1258	6720	-	1156
2	IPE600	HEB650	HEB240	1256	50	46	36	70	1461	8580	-	887
3	IPE550	HEB650	HEB240	1087	43	44	33	70	1311	6720	-	765
4	IPE500	HEB600	HEB220	941	37	41	30	70	1073	5200	-	596
5	IPE500	HEB600	HEB220	941	35	39	28	70	724	4200	-	438

Table 5.4 Design details for the CP11D86W and HP19.5D86W SC-MRFs

Storey	Cross sections			PT bars		WHPs			Reinforcing plates		Dampers c (kN·(s./m)$^{0.5}$)	
	Beams	Columns	Gravity columns	T_0 (kN)	d_{PT} (mm)	D_e (mm)	D_i (mm)	L_{WHP} (mm)	L_{rp} (mm)	A_{rp} (mm)	CP11D86W	HP19.5D86W
1	IPE450	HEB600	HEB240	811	33	40	29	70	942	3990	961	1812
2	IPE500	HEB600	HEB240	941	39	42	32	70	1150	5200	676	1275
3	IPE450	HEB600	HEB240	811	35	40	29	70	1129	4370	549	1035
4	IPE400	HEB550	HEB220	701	30	38	27	70	1065	3600	426	803
5	IPE400	HEB550	HEB220	701	30	36	25	70	829	3240	279	525

Table 5.5 Design details for the CP22D70W SC-MRF

Storey	Cross sections			PT bars			WHPs			Reinforcing plates		Dampers c (kN·(s./m)$^{0.5}$)
	Beams	Columns	Gravity columns	T_0 (kN)	d_{PT} (mm)	D_e (mm)	D_i (mm)	L_{WHP} (mm)	L_{rp} (mm)	A_{rp} (mm)	CP22D70W
1	IPE360	HEB500	HEB240	607	27	36	25	70	867	2890	1655
2	IPE400	HEB500	HEB240	701	30	39	28	70	961	3420	1094
3	IPE360	HEB500	HEB240	607	28	37	25	70	953	2890	877
4	IPE330	HEB450	HEB220	523	25	35	24	70	992	2560	666
5	IPE330	HEB450	HEB220	523	25	33	22	70	745	2240	435

A conventional steel MRF without dampers has been also designed for comparison with the SC-MRFs. This MRF has the same cross-sections and the same drift performance with the CP3D100W SC-MRF.

5.3 Nonlinear Models

Figure 5.3 shows the model developed in OpenSees for the SC-MRFs, based on the PT connection model, proposed in section 3.5.1. Annex A shows the OpenSees script for the conventional performance SC-MRF without viscous dampers (*CP3D100W*) for a monotonic pushover static analysis. The proposed model for PT connections and the associated beams and columns (see figure 3.28) was validated against FEM and experimental results and found capable to simulate accurately the PT connection behaviour. Also the proposed model is able to capture the stiffness and strength deterioration due to beam local buckling under high drifts. The assumption of stable hysteresis for the columns is fully justified as heavy columns with webs and flanges of low slenderness (e.g. compact HEB sections in Tables 5.3-5.5) do not show cyclic deterioration even under large drifts (Newell and Uang 2008). PT bars are modelled as a truss element running parallel to the beam center-line axis and connected to the exterior nodes of the panel zones of the left and right exterior columns.

To account for P-Δ effects, the gravity columns associated with one of the two lateral resisting frames of the plan in figure 5.2 are modelled as 3 lean-on columns, i.e. one for each bay of the frame. Diaphragm action is modelled with truss elements connecting the lean on columns nodes to nodes defined along the length of the beams at the points where secondary beams are placed. These trusses have stiffness of 100 times the axial beam stiffness.

Nonlinear viscous dampers are modelled with zero length elements (Viscous material of OpenSees). While their supporting braces are modelled with elastic braces as they are strong enough to avoid buckling. In the analytical model, the damper limit states caused by their stroke limit are not considered, i.e. it is assumed that dampers will be manufactured with enough stroke to avoid reaching their limit states even under very large storey drifts.

The connections of the conventional MRF are assumed to be rigid and have full strength, while beams are modeled as elastic elements with zero length rotational springs at their ends that exhibit strength and stiffness deterioration (Lignos and Krawinkler 2007). Columns and panel zones are modeled as described above for the SC-MRFs.

The OpenSees models for the SC-MRFs and the conventional MRF include the effect of the panel zone stiffness, and so, result in shorter *T* values than those shown in Table 5.1 that are based on the centerline models used for design. *T* from the OpenSees models is 1.00 s. for the CP3D100W and the HP20D100W, 1.35 s. for the CP11D86W and the HP19.5D86W, 1.95 s. for the CP22D70W, and 1.18 s. for the conventional MRF.

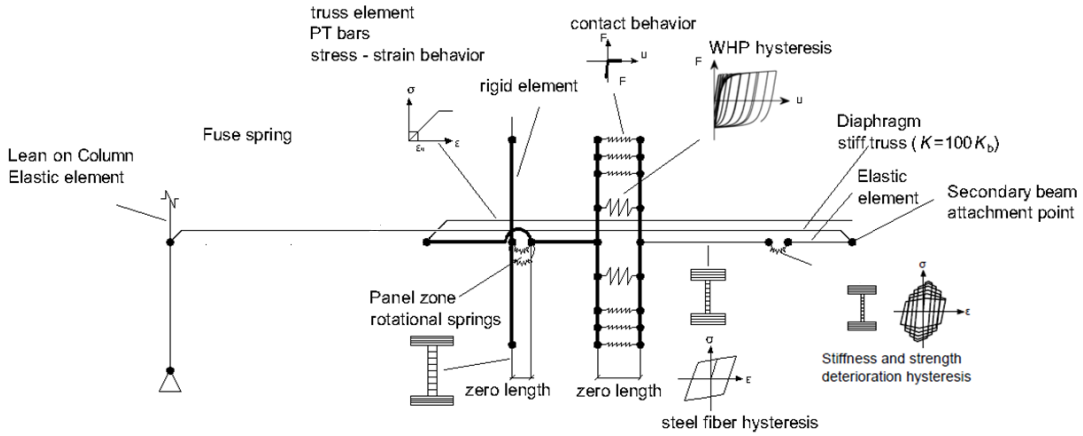

Figure 5.3 Model for an exterior PT connection and the associated beams and columns

5.4 Monotonic and cyclic base shear vs. roof drift behaviour

Figures 5.4-8 show the base shear coefficient (*V/W*; *V*:base shear and *W*:seismic weight) - roof drift (θ_r) behaviour of the SC-MRFs and the conventional MRF from nonlinear monotonic static (pushover) analysis under an inverted triangular force distribution, similar to that specified in EC8 (Eurocode 8 2013). A nonlinear force-controlled static analysis under gravity loads and the applied post-tensioning is first performed. The stiff truss elements that simulate diaphragm action are not included

in the SC-MRF models for this analysis to allow post tensioning and initial beam shortening without the slab presence. Then, the stiff truss elements are added into the model and a displacement-controlled pushover analysis is executed up to θ_r of 10%. Pushover curves are shown along with structural limit states and θ_r estimations under the FOE, DBE and MCE.

Figure 5.4 shows the pushover curve of CP3D100W. WHPs yield at θ_r lower than the FOE θ_r (0.6%) followed by column plastic hinge at θ_r equal to 1.0%. Plastic hinge at the end of the beam flange reinforcing plate occurs at θ_r equal to 2.5%. The strength of the CP3D100W continues to increase up to θ_r equal to 4.7% where beam local buckling occurs and strength deterioration initiates. The behaviour of CP3D100W is consistent with the target performance of minor beam yielding ($\varepsilon_c/\varepsilon_y$=2) under the DBE. PT bars do not yield even under very large drifts as the beam plastic hinge rotations drastically reduce gap opening and PT bar elongation. The peak *V/W* is 0.34. Viscous dampers do not affect the behaviour of the SC-MRFs under static loading, and so, HP20D100W has the same pushover curve (see figure 5.5) with CP3D100W apart from lower θ_r under the FOE, DBE and MCE. The behaviour of HP20D100W is consistent with the target performance of $\varepsilon_c/\varepsilon_y$=1 under the DBE. Column plastic hinge occurs at θ_r equal to 1%, while beam plastic hinge occurs at θ_r higher than the MCE θ_r.

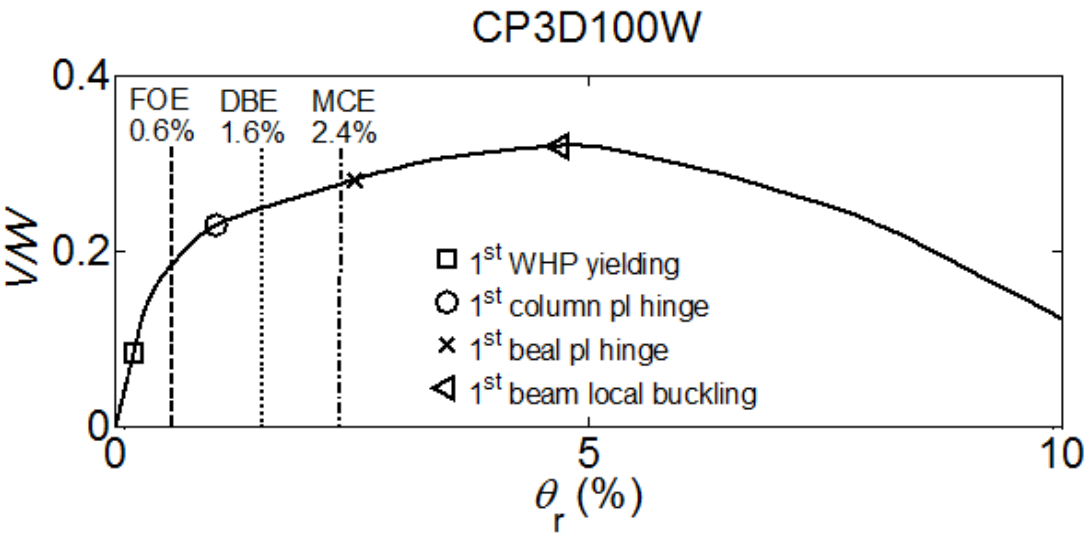

Figure 5.4 Base shear coefficient - roof drift behaviour from nonlinear monotonic (pushover) static analysis of CP3D100W

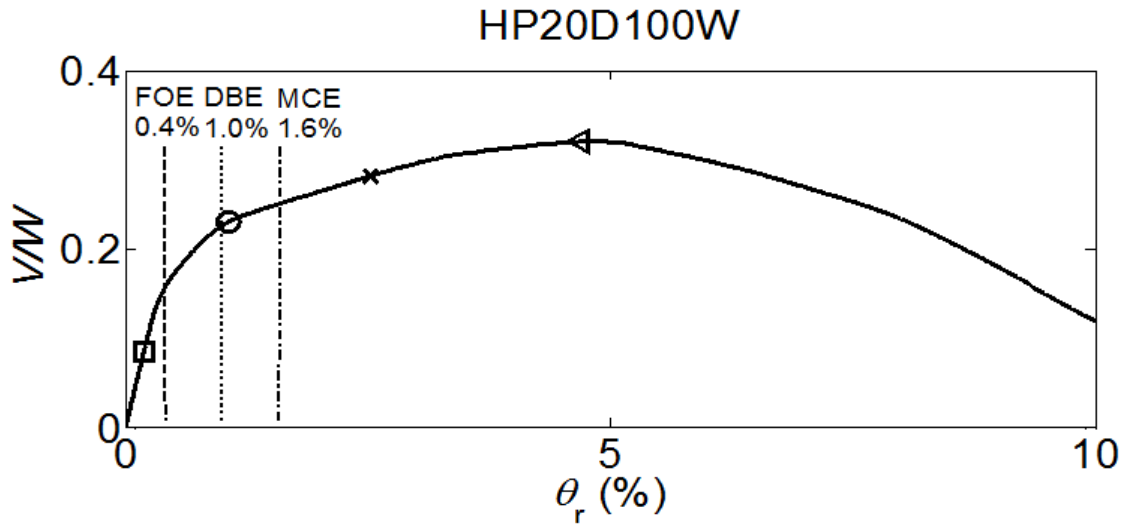

Figure 5.5 Base shear coefficient - roof drift behaviour from nonlinear monotonic (pushover) static analysis of HP20D100W

Figure 5.6 shows the pushover curve of CP11D86W. WHPs yield at θ_r lower than the FOE θ_r (0.59%). Column and beam plastic hinge occurs at the MCE θ_r (2.40%). The beam plastic hinge rotation capacity is reached at 6% θ_r. The behaviour of CP11D86W is consistent with the target performance of minor beam yielding ($\varepsilon_c/\varepsilon_y$=2). The peak *V/W* is 0.16. HP19.5D86W has the same pushover curve (see figure 5.7) with CP11D86W apart from lower θ_r under the FOE, DBE and MCE. The behaviour of CP11D86W is consistent with the target performance of $\varepsilon_c/\varepsilon_y$=1.3 under the DBE and. Column plastic hinge and beam plastic hinge occur at θ_r higher than the MCE θ_r (1.95%).

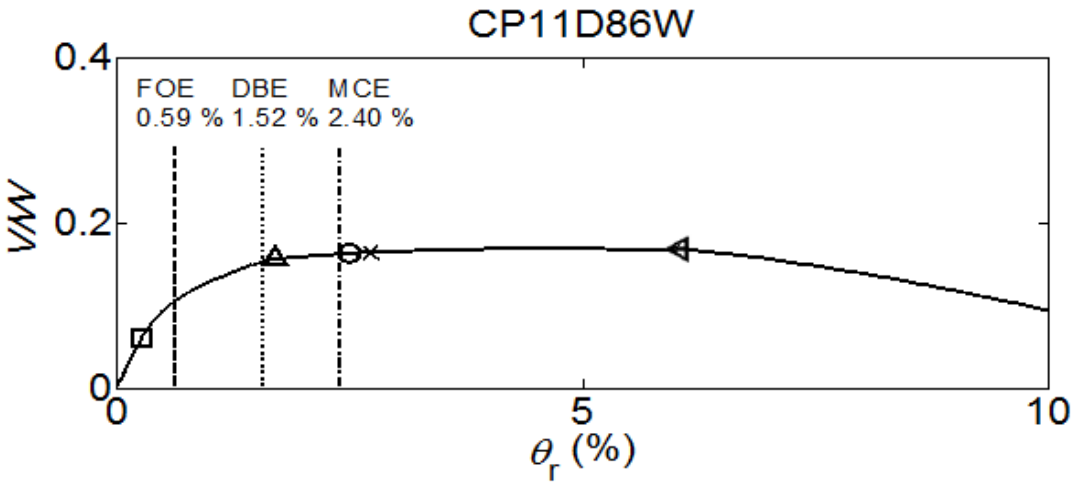

Figure 5.6 Base shear coefficient - roof drift behaviour from nonlinear monotonic (pushover) static analysis of CP11D86W

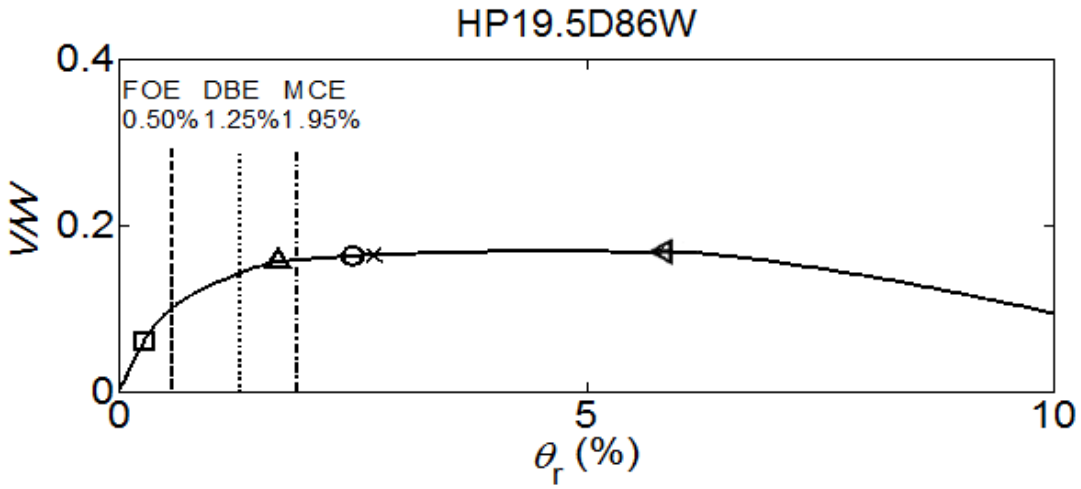

Figure 5.7 Base shear coefficient - roof drift behaviour from nonlinear monotonic (pushover) static analysis of HP19.5D86W

Figure 5.8 shows the pushover curve of CP22D70W. WHPs yield at θ_r lower than the FOE θ_r (0.61%) followed by beam plastic hinge after the DBE θ_r (1.50%). The descending branch of the pushover curve initiates at the MCE θ_r (2.23%) solely due to excessive P-Δ effects. Column plastic hinge occurs at 7.1% θ_r followed by beam local buckling at 8.2% θ_r. The behaviour of CP22D70W is consistent with the target performance of minor beam yielding ($\varepsilon_c/\varepsilon_y$=2). The peak *V/W* is 0.11.

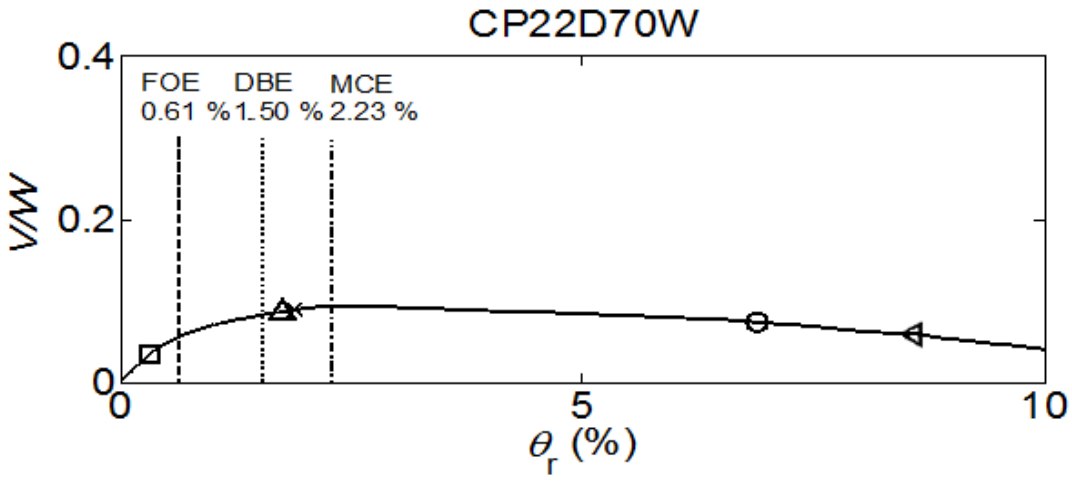

Figure 5.8 Base shear coefficient - roof drift behaviour from nonlinear monotonic (pushover) static analysis of CP22D70W

Figure 5.9 shows the pushover curve of the conventional MRF. Column plastic hinge occurs at 0.55% θ_r followed by beam plastic hinge formation at 1.03% θ_r and beam local buckling at 3.0% θ_r. The behaviour of the conventional MRF is worse than the behaviour of the CP3D100W SC-MRF with the same cross-sections as all structural limit states are reached at lower θ_r. The peak *V/W* is 0.26.

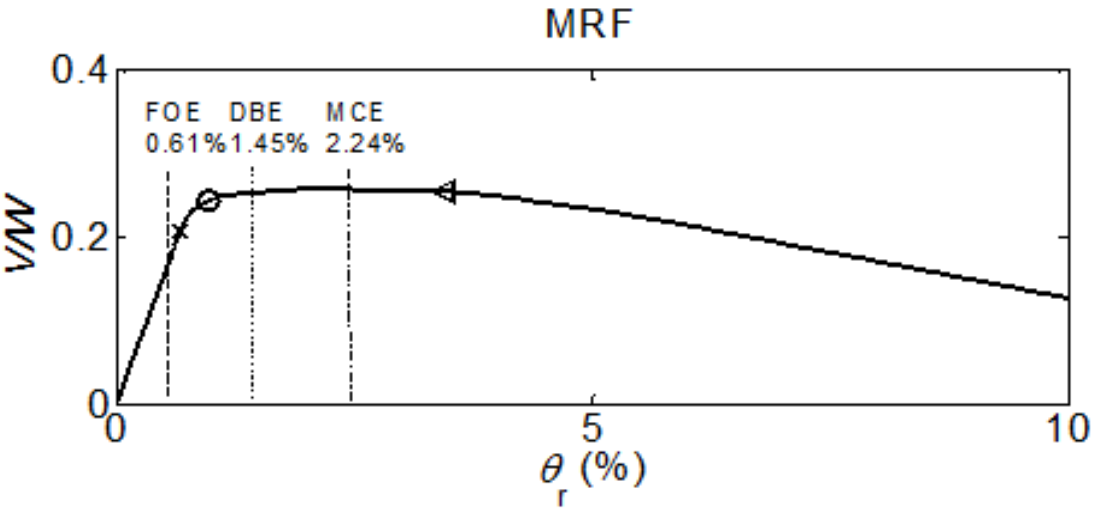

Figure 5.9 Base shear coefficient - roof drift behaviour from nonlinear monotonic (pushover) static analysis of conventional MRF

Figures 5.10-15 show the *V/W*-θ_r behaviour of the SC-MRFs and the conventional MRF from nonlinear cyclic (push-pull) static analysis up to the DBE θ_r. All SC-MRFs have good energy dissipation capacity and self-centering capability.

CP3D100W has a small residual θ_r due to modest column base yielding. The conventional MRF shows higher energy dissipation capacity but has significant residual θ_r compared to all SC-MRFs.

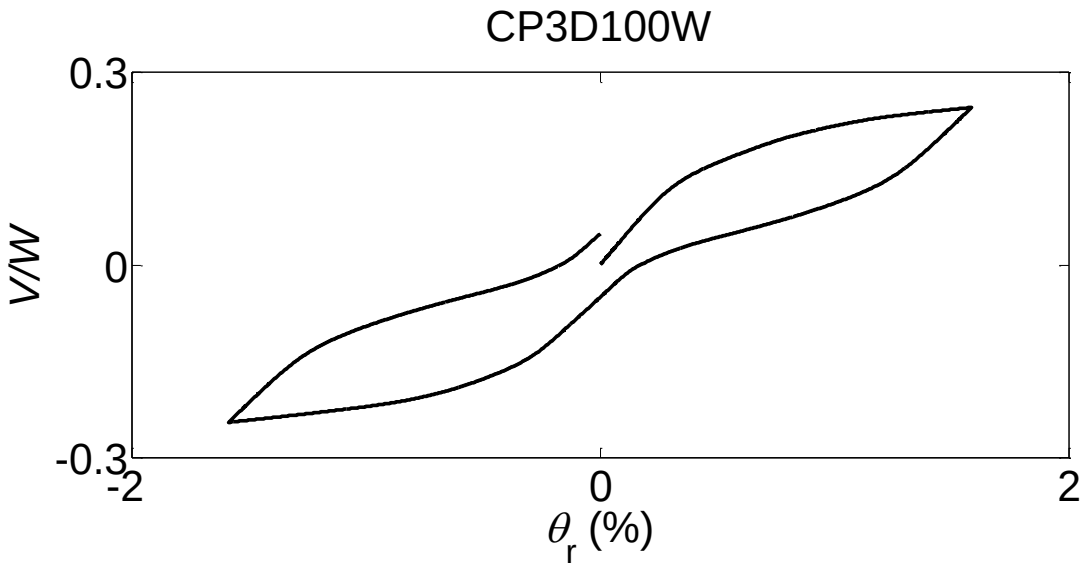

Figure 5.10 Base shear coefficient - roof drift behaviour from nonlinear cyclic (push-pull) static analysis up to DBE roof drift for CP3D100W

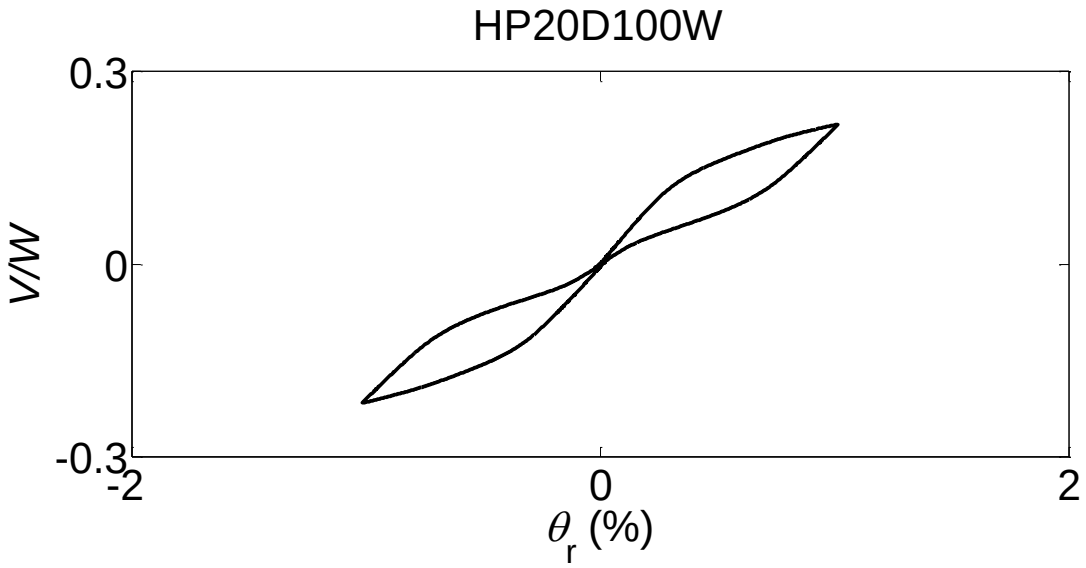

Figure 5.11 Base shear coefficient - roof drift behaviour from nonlinear cyclic (push-pull) static analysis up to DBE roof drift for HP20D100W

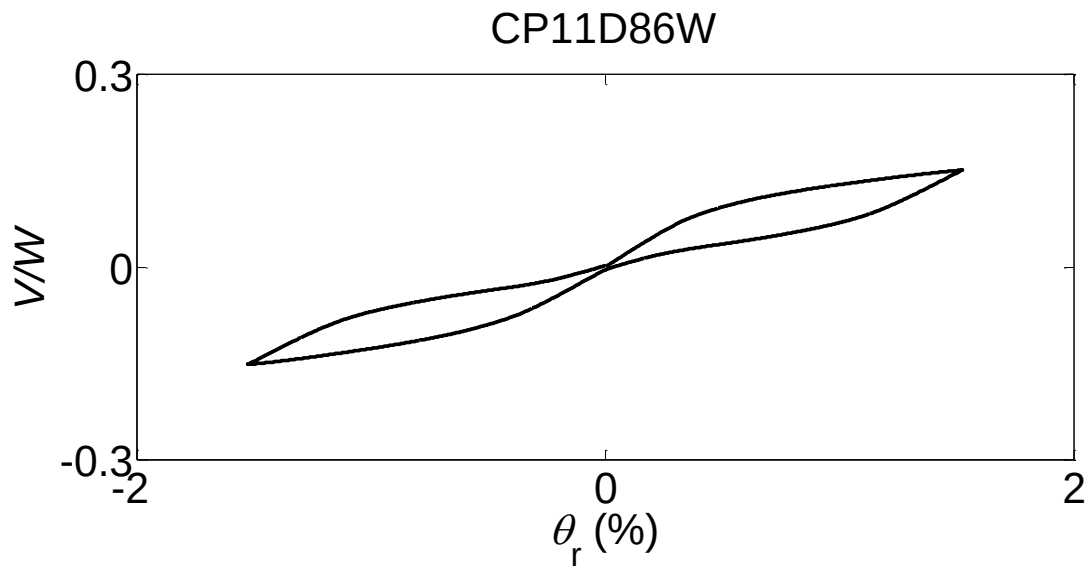

Figure 5.12 Base shear coefficient - roof drift behaviour from nonlinear cyclic (push-pull) static analysis up to DBE roof drift for CP11D86W

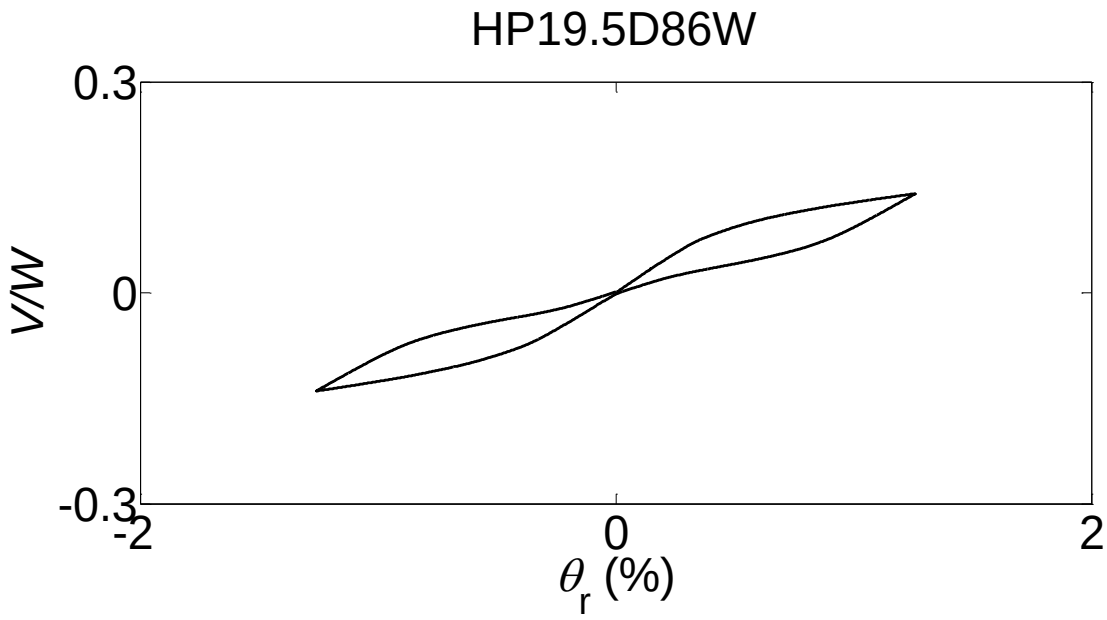

Figure 5.13 Base shear coefficient - roof drift behaviour from nonlinear cyclic (push-pull) static analysis up to DBE roof drift for HP19.5D86W

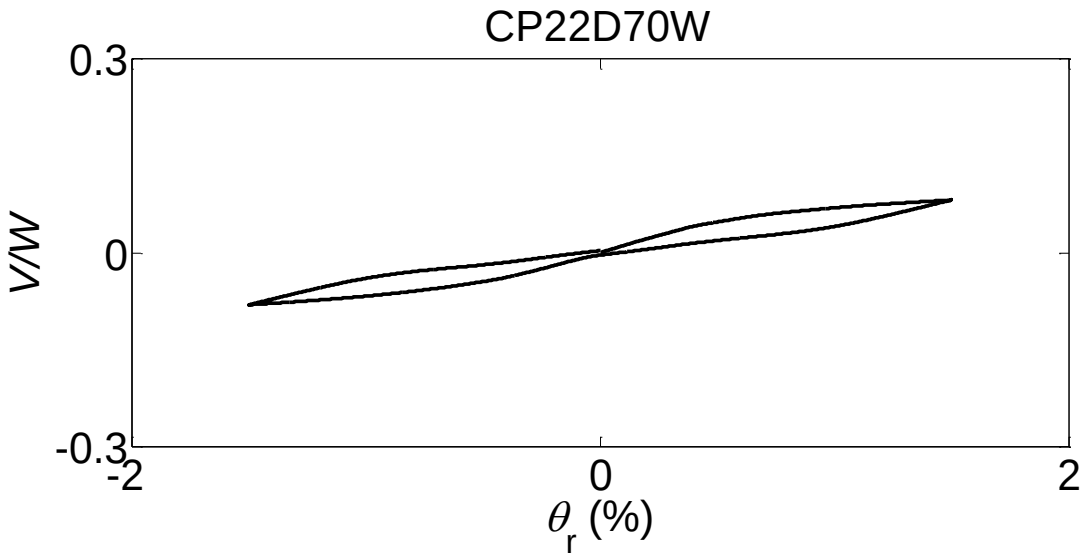

Figure 5.14 Base shear coefficient - roof drift behaviour from nonlinear cyclic (push-pull) static analysis up to DBE roof drift for CP22D70W

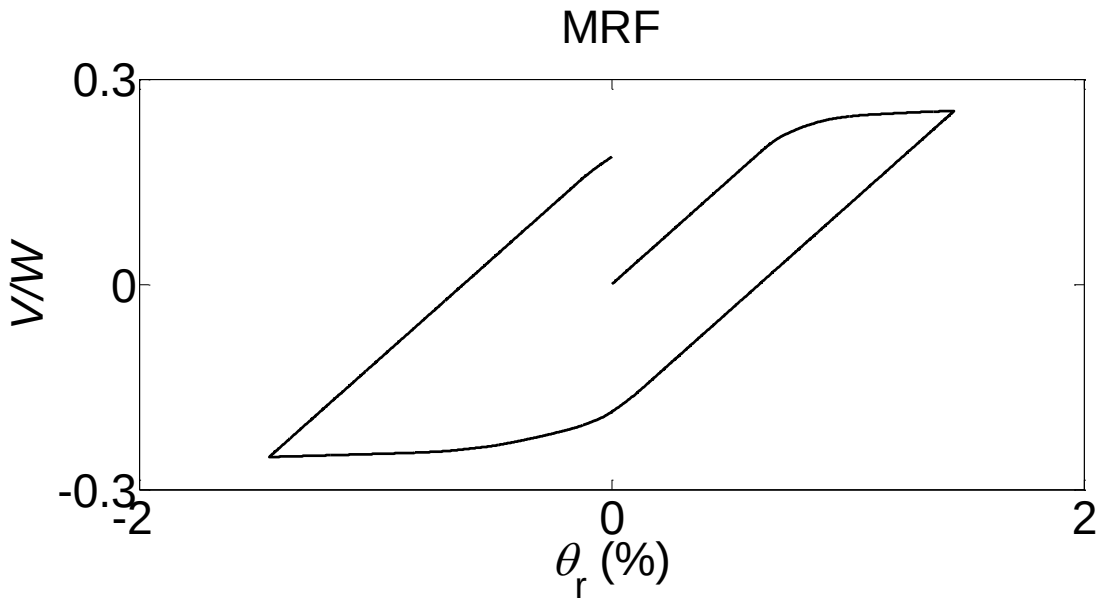

Figure 5.15 Base shear coefficient - roof drift behaviour from nonlinear cyclic (push-pull) static analysis up to DBE roof drift for conventional MRF

5.5 Fragilities under the DBE and MCE

5.5.1 Ground motions

A set of 22 recorded far-field ground motion pairs (i.e. 44 time histories) developed by the ATC-63 project (FEMA P695 2008) are used for nonlinear time history analyses. Ground motions were recorded on stiff soil, do not exhibit pulse-type near-fault characteristics, and were scaled at the DBE and MCE where seismic intensity is represented by the 5% spectral acceleration, S_a, at T from the OpenSees models in Section 5.3.

5.5.2 Nonlinear dynamic analysis

The Newmark method with constant acceleration is used to integrate the equations of motion. The Newton method with tangent stiffness is used to minimize the unbalanced forces within each integration time step. A Rayleigh damping matrix is used to model the inherent 3% critical damping at the first two modes of vibration. A nonlinear force-controlled static analysis under gravity loads and the applied post-tensioning is first performed. The stiff truss elements that simulate diaphragm action are not included in the SC-MRF model for this analysis to allow post tensioning and initial beam shortening without the slab presence. Then, the stiff truss elements are added into the model and the nonlinear dynamic analysis is executed. Each dynamic analysis is extended well beyond the actual earthquake time to allow for damped free vibration decay and accurate $\theta_{s,res}$ calculation.

5.5.3 Fragilities

Having $\theta_{s,max}$ and $\theta_{s,res}$ for a SC-MRF from nonlinear dynamic analyses using the 44 ground motions of Section 5.5.1 scaled at a specific seismic intensity, a fragility curve is constructed by fitting a lognormal cumulative distribution function to the ranked probabilities of non-exceedance, as shown in figure 5.16 for the CP3D100W under the DBE.

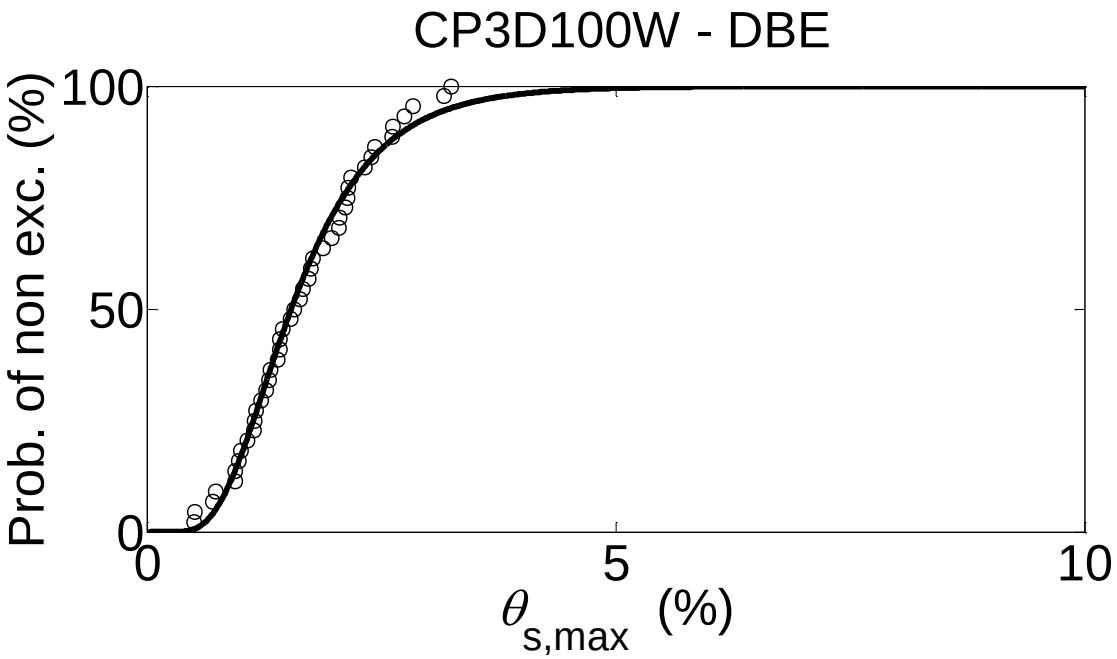

Figure 5.16 Fitted $\theta_{s,max}$ lognormal cumulative distribution function for the CP3D100W under the DBE;

Figure 5.17 shows the $\theta_{s,max}$ fragility curves of the SC-MRFs and the conventional MRF under the DBE. The $\theta_{s,max}$ at 50% probability of non-exceedance is 1.54% for the CP3D100W, 1.01% for the HP20D100W, 1.44% for the CP11D86W, 1.07% for the HP19.5D86W, 1.47% for the CP22D70W and 1.74% for the conventional MRF. These values are smaller than the design DBE $\theta_{s,max}$ values in Table 5.1 because the centerline models used for design are more flexible than the OpenSees models used in seismic analyses (see last paragraph of section 5.3). HP20D100W and HP19.5D86W have significantly better performance with fragility curves clearly shifted to the left of those of the other SC-MRFs. This demonstrates the effectiveness of supplemental damping to improve the structural and non-structural seismic performance of steel SC-MRFs. Although designed for different $\theta_{s,max}$ (1.2% vs. 1.5%), HP20D100W and HP19.5D86W have almost identical performance with no evident differences among their fragility curves. The other SC-MRFs, CP3D100W, CP11D86W CP22D70W (all designed for 1.8% $\theta_{s,max}$) have almost identical performance apart from probabilities of non-exceedance higher than 70% for which CP22D70W has a worse performance. This demonstrates that steel SC-MRFs with viscous dampers can be designed for less steel weight without compromising their

DBE performance. For probabilities of non-exceedance lower than 70%, the conventional MRF has worse performance compared to the SC-MRFs.

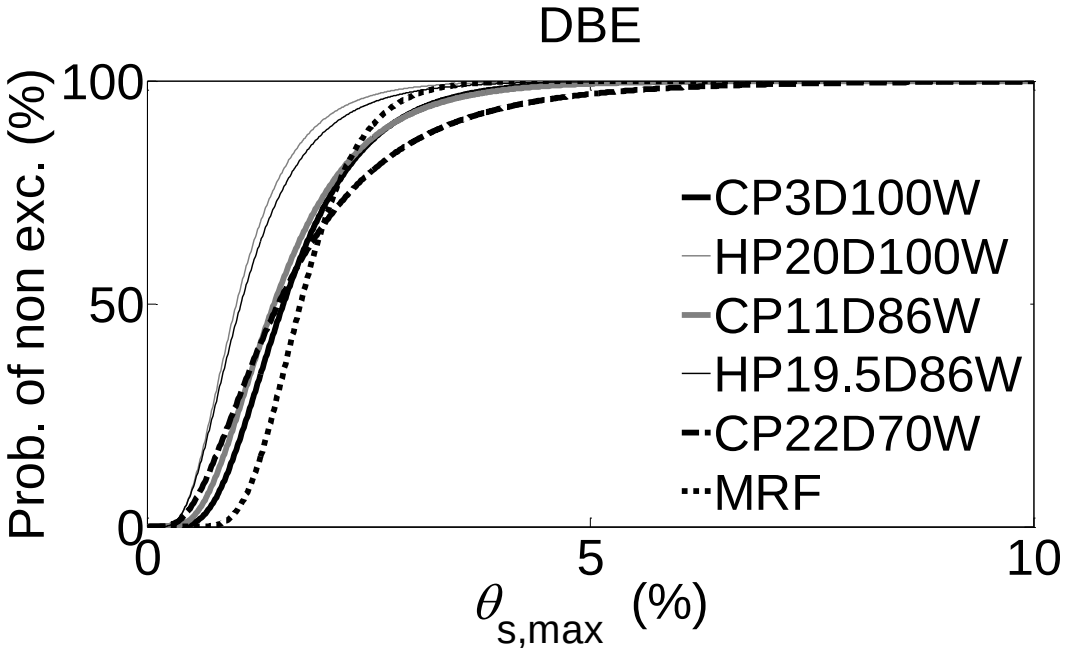

Figure 5.17 $\theta_{s,max}$ fragility curves under the DBE

Figure 5.18 shows the $\theta_{s,max}$ fragility curves of the SC-MRFs and the conventional MRF under the MCE. The $\theta_{s,max}$ at 50% probability of non-exceedance is 2.32% for the CP3D100W, 1.54% for the HP20D100W, 2.36% for the CP11D86W, 1.85% for the HP19.5D86W, 2.56% for the CP22D70W and 2.3% for the conventional MRF. These values are lower than the design MCE $\theta_{s,max}$ values in Table 5.1 for the reason explained in the previous paragraph. Similar to the DBE case, HP20D100W and HP19.5D86W have significantly better performance with fragility curves shifted to the left with respect to those of the other SC-MRFs. Contrary to the DBE case, HP20D100W has clearly better MCE performance than that of HP19.5D86W. CP3D100W, CP11D86W and the MRF have almost identical performance. Contrary to the DBE case, CP22D70W has worse MCE performance than that of CP3D100W and CP11D86W. These results demonstrate that steel SC-MRFs with viscous dampers can be generally designed for less steel weight without compromising their MCE performance; yet a restriction on the strength reduction may need to be established.

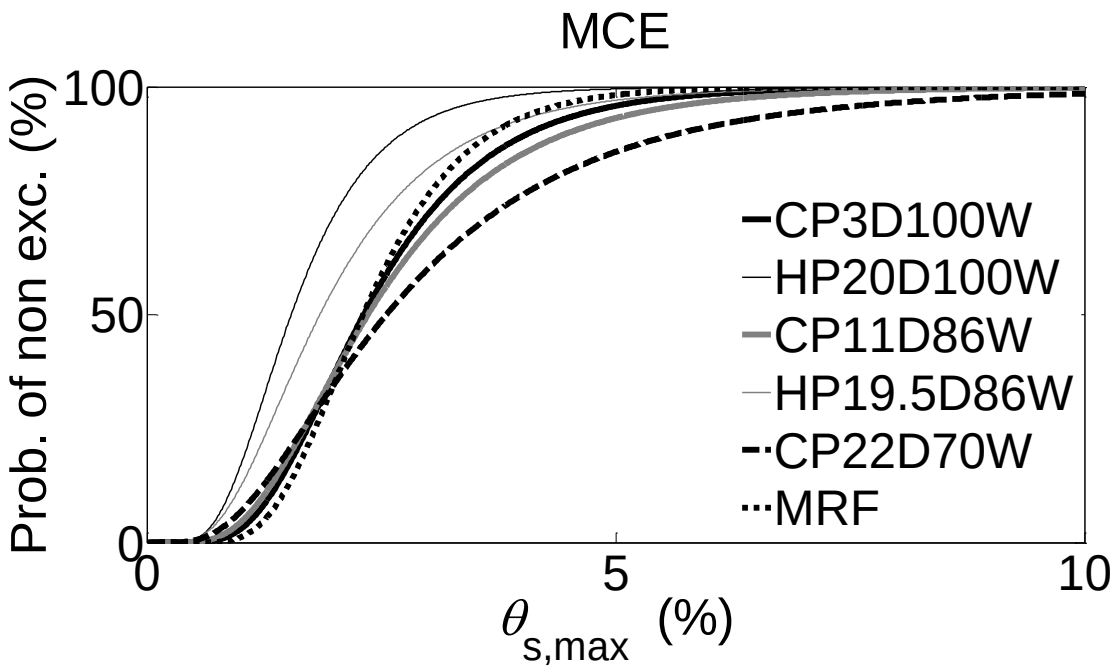

Figure 5.18 $\theta_{s,max}$ fragility curves under the MCE

Figure 5.19 shows the $\theta_{s,res}$ fragility curves of the SC-MRFs and the conventional MRF under the DBE. CP3D100W (that experiences larger plastic deformations at the column bases compared to the other SC-MRFs; see section 5.4) has the largest $\theta_{s,res}$ among the SC-MRFs with a value of 0.1% at 50% probability of non-exceedance. This $\theta_{s,res}$ value is lower than the global sway imperfections defined in EC3 (Eurocode 3 2010), and so, is considered very small. HP20D100W eliminates $\theta_{s,res}$. This demonstrates the effectiveness of supplemental damping to improve the $\theta_{s,res}$ performance of SC-MRFs. In general, figure 5.19 shows that the proposed design procedure results in SC-MRFs that eliminate $\theta_{s,res}$ under the DBE, whereas the conventional MRF has high $\theta_{s,res}$ with a value of 0.49% at 50% probability of non-exceedance.

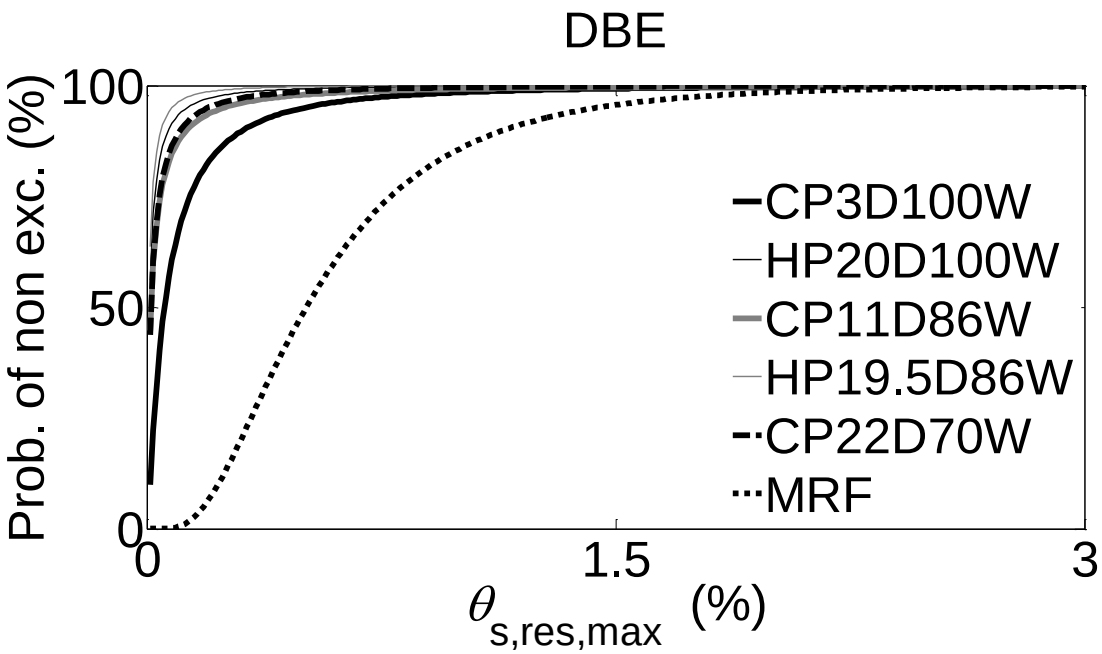

Figure 5.19 $\theta_{s,res}$ fragility curves under the DBE

Figure 5.20 shows the $\theta_{s,res}$ fragility curves of the SC-MRFs and the conventional MRF under the MCE. CP3D100W has the largest $\theta_{s,res}$ among the SC-MRFs with a value of 0.17% at 50% probability of non-exceedance. This $\theta_{s,res}$ value is lower than the global sway imperfections defined in EC3 (Eurocode 3 2010), and so, is considered very small. All the other SC-MRFs have $\theta_{s,res}$ lower or equal than 0.1% at 50% probability of non-exceedance. Similar to the DBE case, figure 5.20 shows the effectiveness of supplemental damping to improve the $\theta_{s,res}$ performance and that the proposed design procedure results in SC-MRFs with very low $\theta_{s,res}$ under the MCE. The conventional MRF has significant $\theta_{s,res}$ with a value of 0.75% at 50% probability of non-exceedance. It should be noted that a building may have to be demolished if the $\theta_{s,res}$ is higher than 0.5% (McCormick et al 2008).

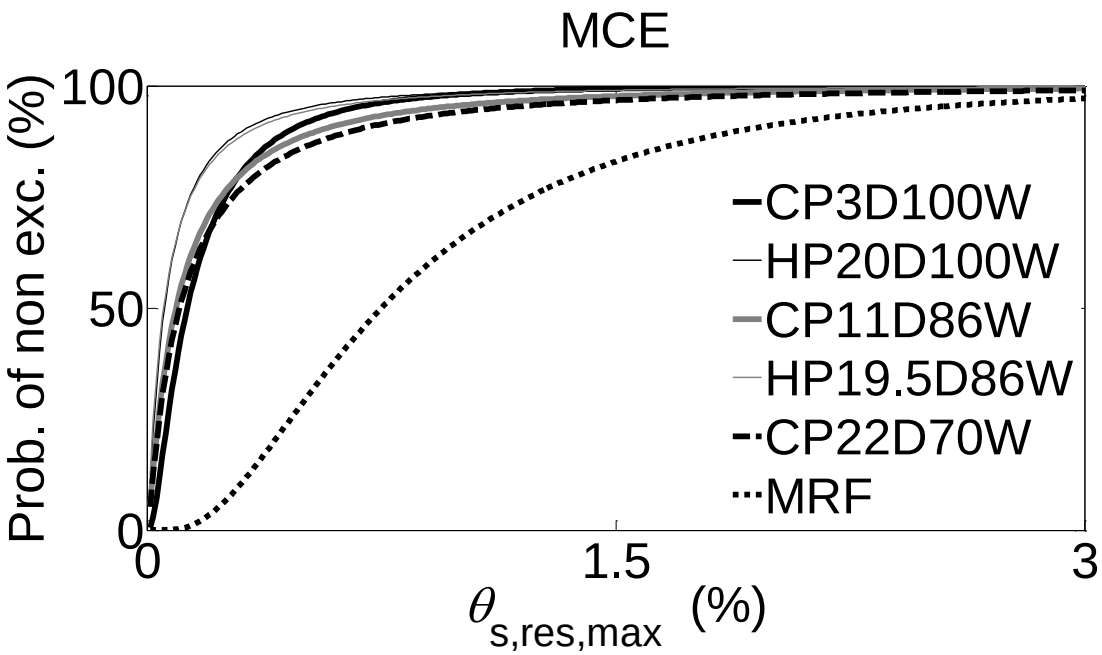

Figure 5.20 $\theta_{s,res}$ fragility curves under MCE

5.6 Summary

In this chapter a prototype building was designed as an SC-MRF with or without viscous dampers according to the design procedure presented in chapter 4. SC-MRF designs with different base shear strength and supplemental damping were investigated. Pushover and seismic analyses were conducted in OpenSees using models capable to capture all structural limit states up to collapse. Based on the results presented in this chapter, the following conclusions are drawn:

1. The preliminary pushover analysis makes the design procedure very accurate in predicting structural limit states.

2. The SC-MRFs designed in this chapter avoid beam and column base plastic hinge formation under the MCE and experience strength deterioration at roof drifts higher than 5%.

3. SC-MRFs with viscous dampers can be designed for less steel weight (resulting in less strength) without compromising their DBE drift performance. The

same is generally true for the MCE drift performance; yet a restriction on the strength reduction should be established.

4. Supplemental damping is very effective in improving the residual drift performance of SC-MRFs.

6 Collapse assessment of SC-MRFS with viscous dampers

6.1 Introduction

In this chapter, the potential of SC-MRFs and viscous dampers to improve the collapse resistance against that of MRFs is evaluated. The evaluation is based on the prototype steel building, presented in section 5.2.1 (see figures 5.1-2), designed using four different seismic resistant frames: (a) conventional MRFs; (b) MRFs with viscous dampers; (c) SC-MRFs; or (d) SC-MRFs with viscous dampers. All frames, are designed according to EC8 (Eurocode 8 2013), and have the same column/beam cross-sections and similar periods of vibration. Viscous dampers are designed to reduce the peak story drift under DBE from 1.8% to 1.2%. IDAs are conducted for all frames using models capable to simulate all limit states up to collapse. It is shown that the SC-MRF has higher collapse resistance than that of the MRF, while the use of viscous dampers results in higher collapse for both the MRF and the SC-MRF.

6.2 Design cases

This study focuses on one perimeter seismic resistant frame of the prototype building, presented in section 5.2.1 (see figures 5.1-2). This frame is designed as conventional MRF, MRF with viscous dampers, SC-MRF, or SC-MRF with viscous dampers using the seismic design procedures of chapter 4. The SC-MRF and the SC-MRF with viscous dampers have been presented in section 5.2.2 as CP3D100W and HP20D100W respectively. The conventional MRF has been also presented in section 5.2.2 while the MRF with viscous dampers has the same cross sections with the conventional MRF and the same viscous dampers with the SC-MRF with viscous dampers (see Table 5.3). Figures 5.4-5 and 5.9 show the V/W-θ_r behavior of the SC-MRF, the SC-MRF with viscous dampers and the conventional MRF from monotonic pushover analysis. Figure 6.1 shows the V/W-θ_r behavior of the MRF with viscous dampers from monotonic pushover analysis. The MRF with viscous dampers has the same pushover curve (see figure 6.1) with the MRF (see figure 5.9) but its performance is better because of the reduction in θ_r estimates under the FOE, DBE and MCE

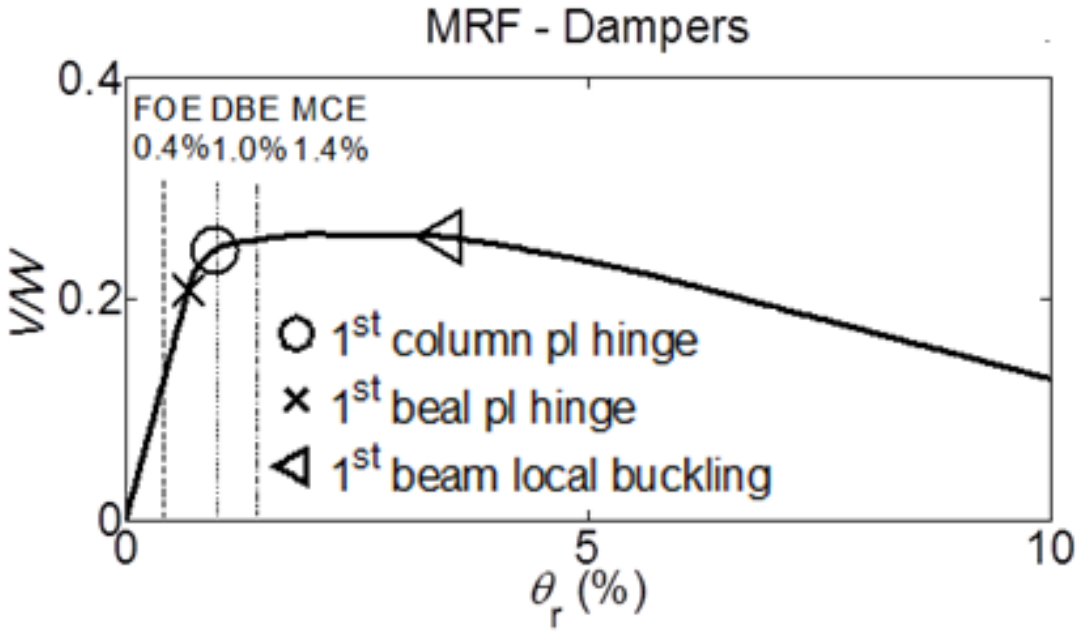

Figure 6.1 Base shear coefficient - roof drift behavior from nonlinear monotonic (pushover) static analysis of the conventional MRF with viscous dampers

6.3 Models for nonlinear analysis

Due to the high computational cost of IDAs (Vamvatsikos and Cornell 2002), conducted for the SC-MRFs, a simplified OpenSees model for the PT connections with WPHs has been adopted. In this simplified model, the *M-θ* behavior of the PT connection is simulated by inserting 2 parallel rotational springs at the beams ends. These rotational springs simulate the contribution of the WHPs and the PT bars on the overall rotational behavior of the PT connection. The accuracy of this simplified model has been evaluated against the PT connection model of sections 3.5.1 and 5.3, which is based on contact and hysteretic springs at the beam-column interface.

The stiffness and strength deterioration due to local buckling at the unreinforced lengths of the beams is modelled using force-based beam-column fiber elements with end hinges (Scott and Fenves 2006), where the model in Lignos and Krawinkler (2007) is used for the stress-strain cyclic behavior of the fibers. This modeling

approach results in smoother hysteretic curves and so, less convergence problems in high seismic intensity analysis as discussed in section 3.5.1.

Panel zones are modelled using the Krawinkler model (Krawinkler 1978). Krawinkler model introduces four additional rigid elastic beam column elements, which are connected at the upper left and lower right corners with rotational springs to represent panel zone shear resistance and column-flange bending resistance respectively. The lower left and upper right corners act like true hinges (see Figure 6.2). Figure 6.2 shows the model developed in OpenSees (Mazzoni et al 2006) for the SC-MRFs, based on the simplified PT connection model, discussed above. P-Δ effects and nonlinear viscous dampers are modelled based on section 5.3.

Figure 6.3 compares the base shear coefficient (V/W; V: base shear and W: seismic weight) - roof drift (θ_r) behaviors from nonlinear monotonic static (pushover) analysis, while Figure 6.4 compares the V/W-θ_r behaviors from nonlinear cyclic static (push-pull) analysis of the SC-MRF using either the simplified or the detailed PT connection model.

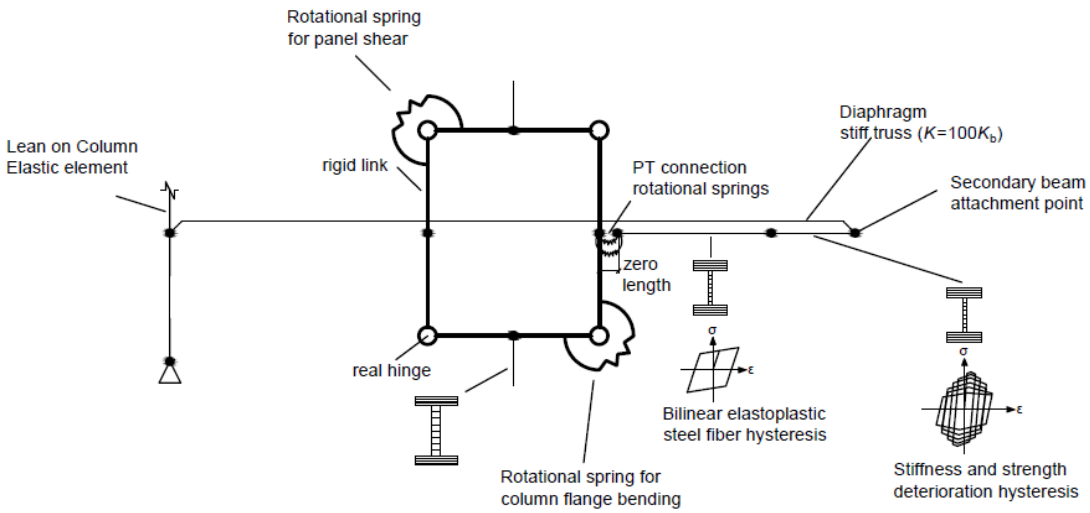

Figure 6.2 Simplified model for an exterior PT connection and the associated beams and columns

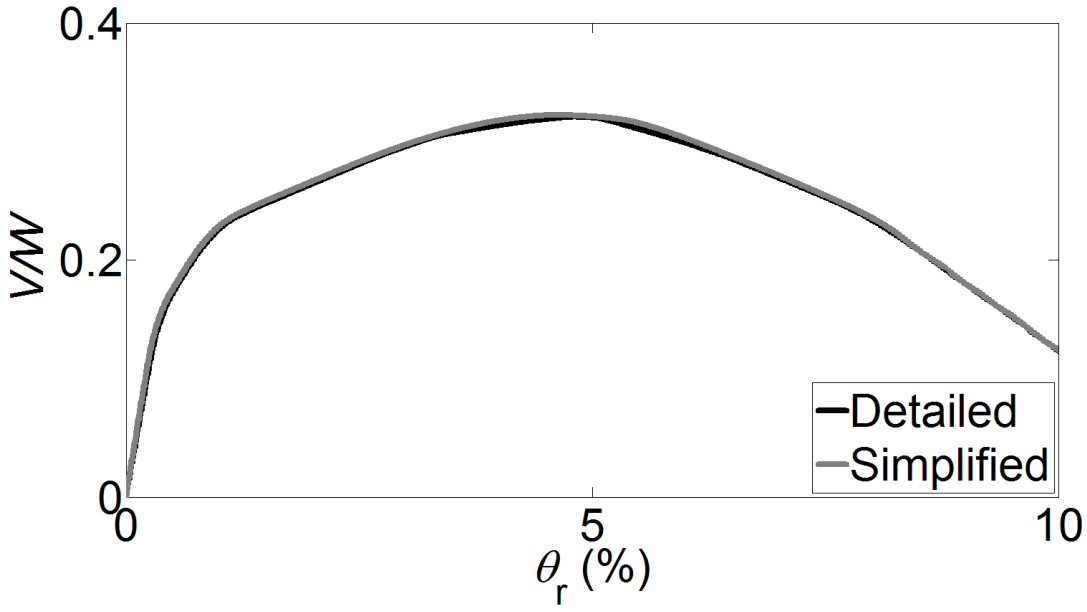

Figure 6.3 Comparison of the monotonic static (pushover) behaviors of the SC-MRF using either the simplified PT connection model in section 6.3 or the model in 5.3 for the PT connections.

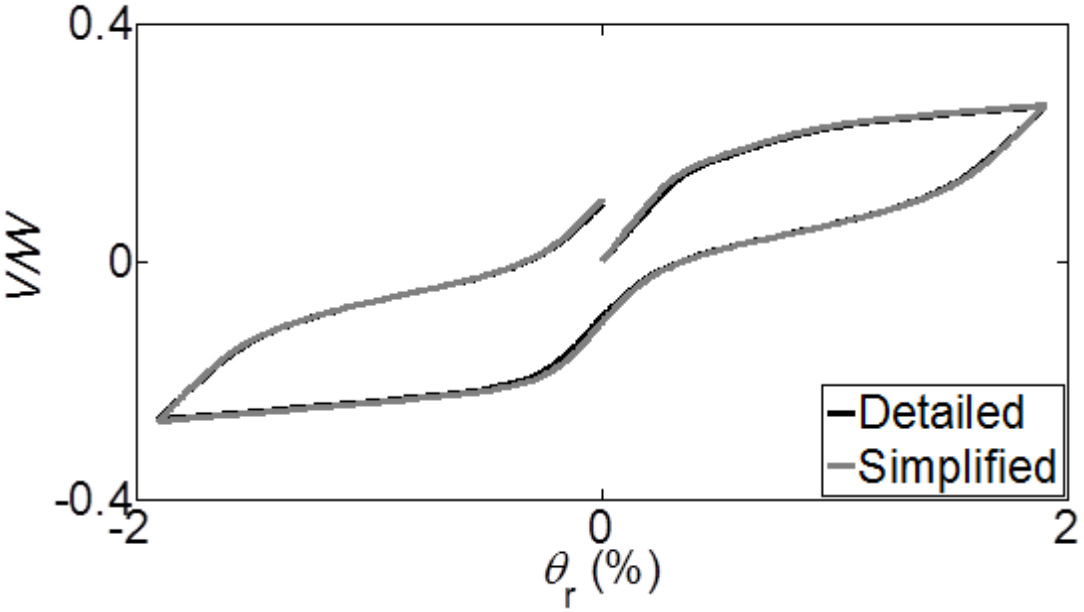

Figure 6.4 Comparison of the cyclic static (push-pull) behaviors of the SC-MRF using either the simplified PT connection model in section 6.3 or the model in 5.3 for the PT connections.

The connections of the conventional MRF are assumed to be rigid and have full strength, while beams are modeled as elastic elements with zero length rotational springs at their ends that exhibit strength and stiffness deterioration (Lignos and Krawinkler 2007). Columns and panel zones are modeled as described above for the SC-MRF.

6.4 Incremental dynamic analysis and collapse prediction

A single IDA of a frame under an earthquake ground motion consists of a dynamic analysis sequence of this frame under scaled images of the ground motion accelerogram. The accelerogram scaling is applied to cover the whole range from elastic to non-linear behaviour and finally to collapse of the structure. Collapse is defined as the point, on which deformations increase in an infinite way (without bound). An IDA curve is a plot of an engineering demand parameter (EDP) (e.g. $\theta_{s,max}$) recorded in an IDA study versus one or more intensity measure (IM) (e.g. The spectral acceleration at the fundamental period of vibration, $S_a(T_1)$). At the collapse point the IDA curve flattens out in a plateau (flatline).

For all the design cases of this chapter, IDA (Vamvatsikos and Cornell 2002) was performed up to collapse under a set of 22 far-field ground motions pairs (i.e. 44 time histories) used in the FEMA P695 project (FEMA P695 2008). For each design case and ground motion, the $S_a(T_1)$ collapse value at which $\theta_{s,max}$ increases without bound was obtained.

For the IDA implementation of a MRF under 44 time histories, the Matlab code presented in Annex B was developed. According to this code, a scale factor is progressively applied in every time history, corresponding to $S_a(T_1)$ values from 0.02g with an incremental step equal to 0.02g.

When a scale factor is applied into the time history, a dynamic analysis is performed for the frame under the scaled time history. If the analysis cannot be completed due to in-convergence, the analysis time step is progressively divided by 1, 10, 20, 50, 100, 500, and 1000, until convergence is achieved. If the analysis cannot be

completed even after this procedure, we assume that for this scale factor, structural collapse has been occurred.

If the analysis was completed for this scale factor, the floor displacements and accelerations are collected, so $\theta_{s,max}$ and peak floor accelerations (PFA) are known. In order to examine if structural collapse has been occurred, even if the analysis was complete, two collapse conditions are inserted. The first condition is that structural collapse occurs if $\theta_{s,max}$ is more than 10% (Vamvatsikos and Cornell 2002). The second condition is that structural collapse occurs if the inclination of the IDA curve for an earthquake between the last two IDA points is less than 20% of the initial IDA inclination (Vamvatsikos and Cornell 2002).

A Rayleigh damping matrix was used to model the inherent 3% critical damping at the first two modes of vibration. Each dynamic analysis was extended well beyond the actual earthquake time to allow for damped free vibration decay and accurate $\theta_{s,res}$ calculation. Figures 6.5-6.8 show the IDA curves of all design cases.

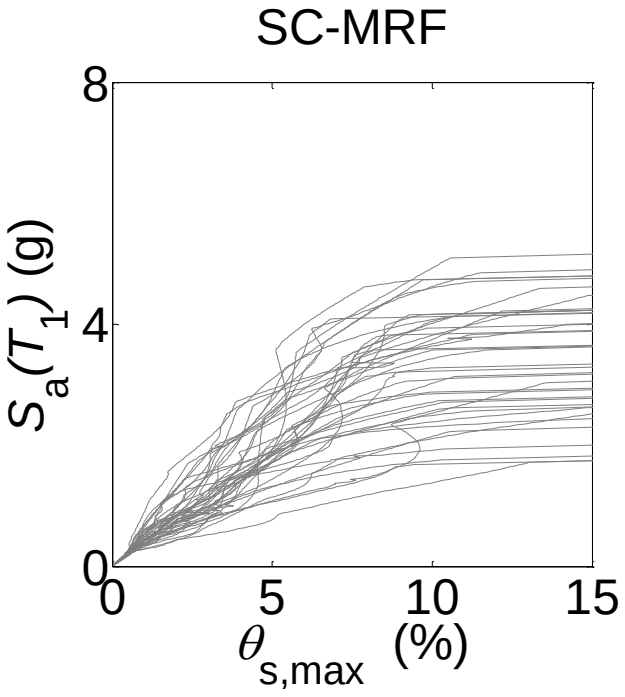

Figure 6.5 IDA curves of the SC-MRF

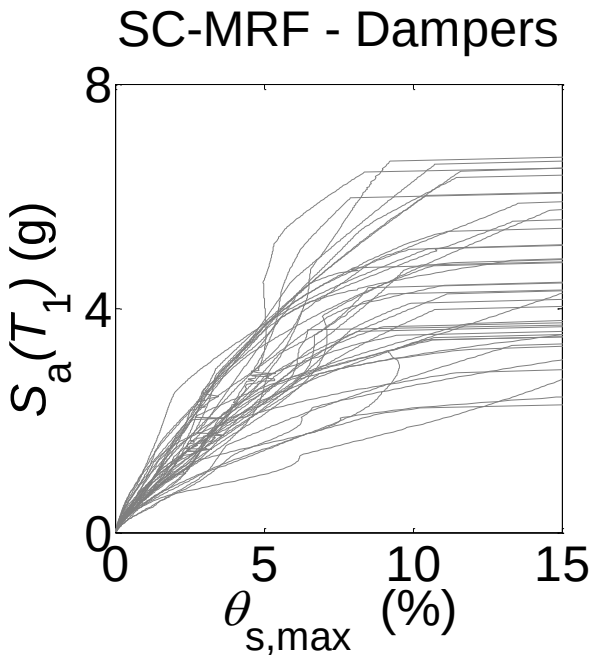

Figure 6.6 IDA curves of the SC-MRF with viscous dampers

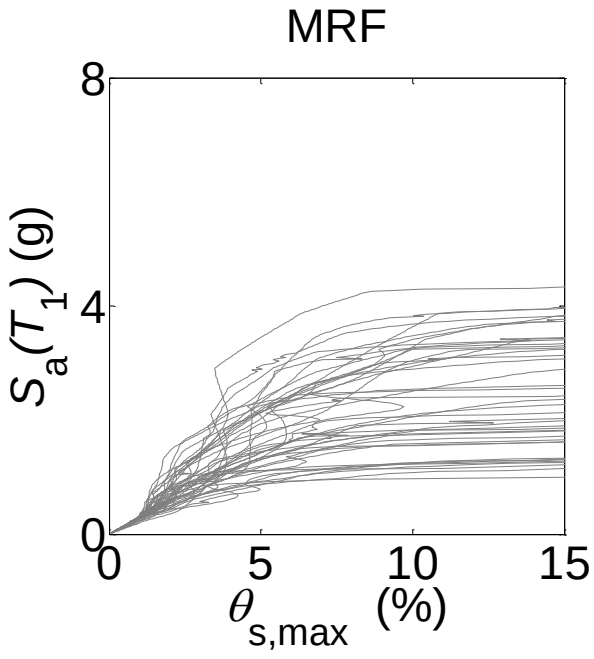

Figure 6.7 IDA curves of the conventional MRF

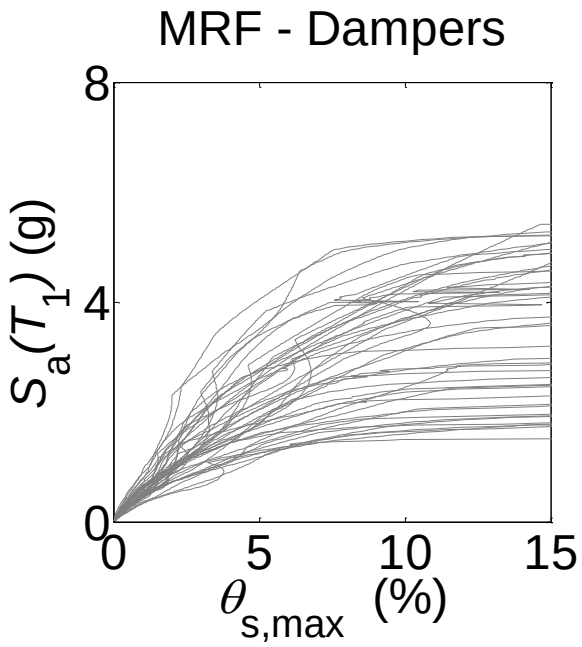

Figure 6.8 IDA curves of the MRF with viscous dampers

Figure 6.9 shows a collapse fragility curve, constructed by fitting a lognormal cumulative distribution function to the $S_a(T_1)$ collapse values for the SC-MRF. Figure 6.10 shows the collapse fragility curves of all design cases, where $S_a(T_1)$ is normalized by $S_{a,MCE}$, i.e. the MCE spectral acceleration at T_1. Beyond just simplifying the discussion to follow, this normalization will also simplify the comparison of structures having (mildly, in this case) different fundamental periods. Thus, the $S_a(T_1)$ at 50% probability of collapse is $5.5 \cdot S_{a,MCE}$ for the SC-MRF with viscous dampers, $5.0 \cdot S_{a,MCE}$ for the MRF with viscous dampers, $4.5 \cdot S_{a,MCE}$ for the SC-MRF and $3.6 \cdot S_{a,MCE}$ for the MRF. The results show that the SC-MRFs have collapse resistance higher than that of the MRFs. It is also evident that supplemental viscous damping significantly improves the collapse resistance of both the MRF and the SC-MRF.

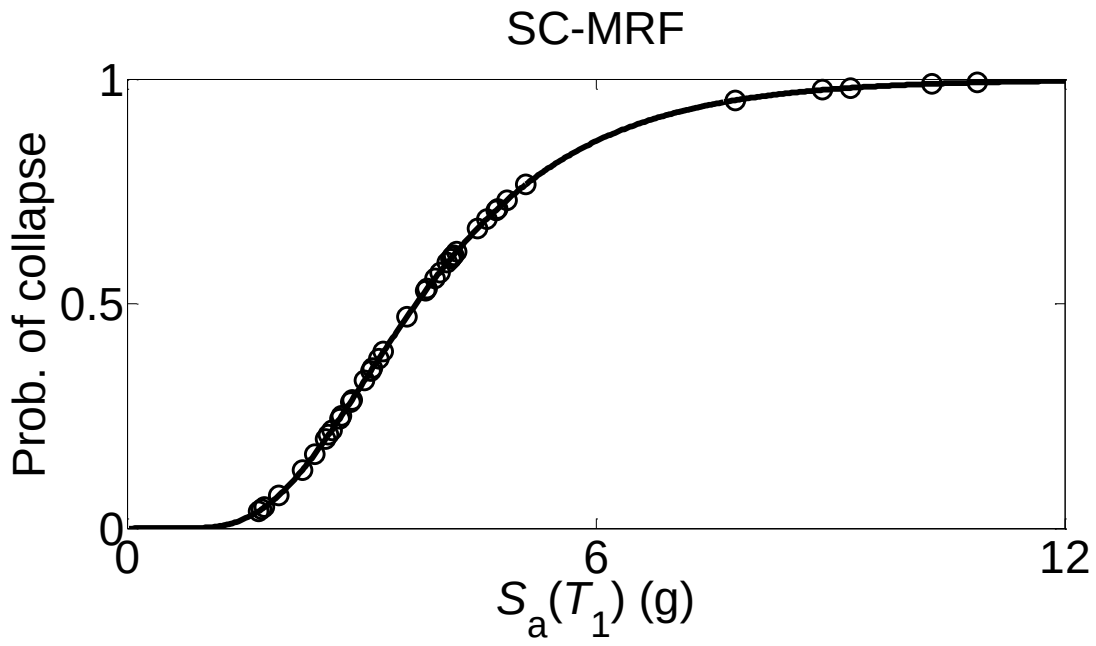

Figure 6.9 Collapse fragility curve of to SC-MRF fitted to the $S_a(T_1)$ collapse values

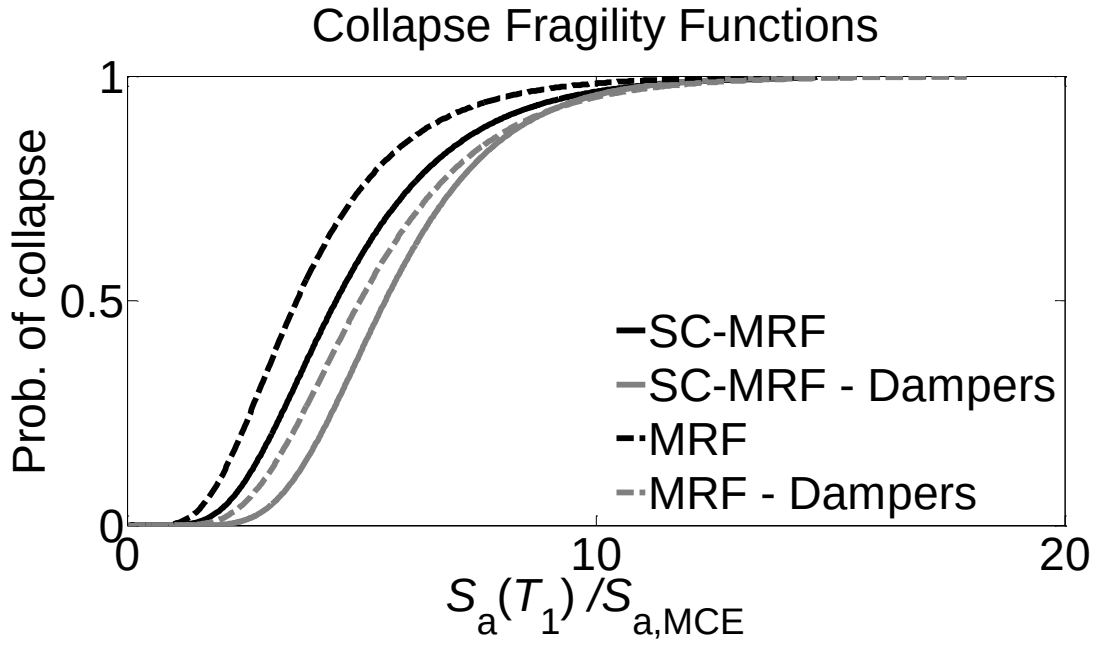

Figure 6.10 Collapse fragility curves of all design cases ($S_a(T_1)$ is normalized by $S_{a,MCE}$)

6.5 Summary

In this chapter the potential of SC-MRFs and viscous dampers to improve the collapse resistance against that of MRFs has been evaluated. The evaluation is based on a 5-story prototype steel building designed to use different seismic-resistant frames, i.e.: conventional MRFs; MRFs with viscous dampers; SC-MRFs; or SC-MRFs with viscous dampers. These frames were designed according to EC8 (Eurocode 8 2013), and have the same beam/column cross-sections and similar periods of vibration. Viscous dampers are designed to achieve a total damping ratio of 20% at the fundamental period of vibration. The estimated peak story drift under the design earthquake for the frames with and without dampers is 1.2% and 1.8%, respectively. IDAs have been conducted using models capable of simulating all structural limit states up to collapse.

Based on the results presented in this chapter The SC-MRF has higher collapse resistance than that of the MRF, while the use of viscous dampers results in higher collapse resistance for both the MRF and the SC-MRF. The 50% probability of collapse is associated with seismic intensities of 5.5·MCE for the SC-MRF with viscous dampers; 5.0·MCE for the MRF with viscous dampers; 4.5·MCE for the SC-MRF; and 3.6·MCE for the MRF.

7 Probabilistic economic seismic loss estimation in steel buildings using SC-MRFs and viscous dampers

7.1 Introduction

In this chapter, the potential of SC-MRFs and viscous dampers to reduce the economic seismic losses in steel buildings is evaluated. The evaluation is based on the prototype steel building, presented in section 5.2.1 (see figures 5.1-2), and the four design cases of seismic resistant frames presented in section 6.2: (a) conventional MRFs; (b) MRFs with viscous dampers; (c) SC-MRFs; or (d) SC-MRFs with viscous dampers. All frames are designed according to EC8 (Eurocode 8 2013), and have the same column/beam cross-sections and similar periods of vibration. Viscous dampers are designed to reduce the peak story drift under the DBE from 1.8% to 1.2%. Losses are estimated by developing vulnerability functions according to the FEMA P-58 (FEMA P-58 2012) methodology, which considers uncertainties in earthquake ground motion, structural response, and repair costs. Both the probability of collapse and the probability of demolition due to excessive residual story drifts are taken into account. A parametric study on the effect of the residual story drift threshold beyond which is less expensive to rebuild a structure than to repair is also conducted. It is shown that viscous dampers reduce the repair cost for seismic intensities up to three times the MCE. On the other hand, post-tensioning reduces the repair cost only for seismic intensities higher than the DBE. Viscous dampers are more effective than post-tensioning for seismic intensities equal or lower than the MCE, while the opposite is true for seismic intensities higher than 2·MCE. This chapter also highlights the effectiveness of combining post-tensioning and supplemental viscous damping by showing that the SC-MRF with viscous dampers achieves repair cost reductions between 70% and 100% compared to the repair cost of the conventional MRF under both the DBE and MCE.

7.2 Literature review on economic seismic losses

To properly assess the seismic resilience of a structural system, the actual economic seismic losses should be rigorously estimated. This can be accomplished using procedures that quantify and propagate uncertainties such as the early one developed

by Porter et al (2001), which uses nonlinear dynamic analyses, predicts damage at the component level using fragility functions, and finally estimates the total building repair cost. This procedure was further developed to become the PEER (Pacific Earthquake Engineering Research) methodology that is now known as the 2nd generation performance based earthquake engineering (PBEE-2) (Cornell and Krawinkler 2000). Early studies on PBEE-2 showed that component damageability and ground motion time histories have strong influence on loss uncertainty, while material properties and other uncertainties in the structural model may have relatively little influence (Porter et al 2002 and Aslani and Miranda 2005). Ramirez and Miranda [Ramirez and Miranda 2012] showed how the probability of having to demolish a building as the result of excessive residual story drifts influences seismic loss estimation. Furthermore, they conducted sensitivity analysis to show that the estimate of loss is more sensitive to the median residual drift threshold for demolition rather than its dispersion. A critical review of PBEE-2 and examination of its limitations has been conducted by Gunay and Mosalam (Gunay and Mosalam 2013). The state-of-art in economic seismic loss estimation is described by the FEMA P-58 methodology that adopts PBEE-2 along with a database of structural and non-structural component fragility functions and repair cost estimates (FEMA P-58 2012).

7.3 Economic seismic loss estimation framework

7.3.1 Loss estimation framework

According to FEMA P-58 (FEMA P-58 2012), the seismic losses for a building are split into: (a) structural loss due to damage in load-carrying structural members; (b) non-structural loss due to damage in non-load carrying components such as partitions, piping systems, etc.; and (c) building contents loss. These losses are assessed using detailed component fragility functions, i.e., functions of relevant EDPs, such as $\theta_{s,max}$ or PFA occurred during an earthquake, that determine the probability of violating a certain damage state (DS). Thus, for a given value of the chosen seismic IM, each component is assigned with the corresponding probability of being in any DS, which is then associated with a probabilistic cost function. This function defines the cumulative distribution of the repair cost of the component for the given DS. Summing up all component costs over the entire building yields the total economic seismic loss (see Section 7.3.4 for more details).

7.3.2 Probability of collapse and probability of demolition

The probability of collapse can be explicitly incorporated in the loss estimation framework following the methodology in Aslani and Miranda (2005), i.e. collapse is assumed to cause instant loss of the entire building and its contents. The probability of demolition can be also explicitly incorporated following the methodology in (Ramirez and Miranda 2012), i.e. by recognising that the building will be demolished when a critical value of the maximum residual story drift between all stories ($\theta_{s,res}$) is exceeded. For example, McCormick et al (2008) concluded that in Japan is generally less expensive to rebuild a structure than to repair it when $\theta_{s,res}$ is higher than 0.5%. In this work, the probability of having to demolish the structure conditioned on $\theta_{s,res}$, $P(D|\theta_{s,res})$, is assumed to follow a lognormal distribution with log-standard deviation (standard deviation of the logarithm of the data) equal to 0.3 (Ramirez and Miranda 2012) and a median value equal to 0.5%, 1.0% and 1.5% to allow a parametric study to be conducted.

7.3.3 Vulnerability functions

The mean annual frequency (MAF) of exceeding values of a decision variable (DV), such as the repair cost or the loss ratio (i.e. repair cost over the building replacement cost), is estimated as (Cornell and Krawinkler 2000):

$$\lambda_{DV}(DV \geq dv) = \int_{IM}\int_{DM}\int_{EDP} G(dv|DM)\left|dG(DM|EDP)\right|\left|dG(EDP|IM)\right|\left|\frac{d\lambda(IM)}{dIM}\right| dIM \qquad (7.1)$$

where $\lambda_{DV}(DV \geq dv)$ is the MAF of exceeding loss level *dv* for the given site and building. *G(dv|DM)* is the probability of exceedance of dv given a damage measure DM. This continuous DM was employed by Cornell and Krawinkler (2000) for theoretical simplicity and it is typically discretized in practice into two or more discrete damage states (DSs) to simplify the assignment of associated repair costs. Thus *G*(*DM*|*EDP*), i.e., the probability of exceedance of DM given an EDP, becomes *G*(*DS*|*EDP*), the familiar component fragility function. Finally, *G*(*EDP*|*IM*) is the probability of exceedance of EDP given an IM and λ(*IM*) is the MAF of exceedance of the IM.

In this chapter, only a part of Equation (7.1) is used to assess the performance of a building in an objective manner that does not depend on the site, i.e. using only the integrals of loss over EDP and DM (or DS) without the final convolution with λ(*IM*). The result is known as vulnerability function, formally written as:

$$G(DV|IM) = \int_{DM}\int_{EDP} G(dv|DM)\left|dG(DM|EDP)\right|\left|dG(EDP|IM)\right| \qquad (7.2)$$

Vulnerability functions essentially represent entire distributions of the building loss at each level of the IM. Thus, they can be visualized as continuous curves of any desired distribution statistic given the IM, such as their 16%, 50% and 84% fractile values. Monte Carlo Simulation (MCS) is used to evaluate the integrals in Equation (7.2). The MCS procedure involves seven steps (see Section 7.3.4) and simulates all

random variables in Equation (2) (i.e. DV, EDP, DS) to finally compute DV for a wide range of IMs.

7.3.4 Steps of MCS procedure

Step (1): EDPs prediction. IDA is conducted up to global collapse for a large enough suite of ground motions (44 used in this study), while appropriate interpolation (Vamvatsikos and Cornell 2002) of the analysis results is employed to extract the distribution of the EDPs ($\theta_{s,max}$, PFA and $\theta_{s,res}$) at any level of the IM. $S_a(T_1)$ is chosen as IM following FEMA P-58 (FEMA P-58 2012) guidelines. As no scaling limit is employed, nor are the records carefully selected for a given site and intensity level, this approach may be questionable for high levels of intensity, since sufficiency is not assured (Luco and Bazzurro 2007). Still, this is only an issue when convolution with seismic hazard is attempted (Equation. (7.1)). When using $S_a(T_1)$ solely for comparing the response or vulnerability of buildings with close periods, similar levels of bias will creep in, thus cancelling each other out when taking ratios, as attested, for example, by the spectral-shape correction formula of (FEMA P695 2008). Thus, although the absolute values of loss estimated may become conservative at high IM levels, their relevant sizes will remain valid for comparison.

Step (2): Estimate the total replacement cost of the building. The distribution of the replacement cost of the building itself, considering only structural and non-structural components, is estimated using data for new steel construction from (www.SteelConstruction.info). This is augmented by the distribution of the replacement cost for the building contents, as obtained from the corresponding content repair cost functions at their most severe DS (FEMA P-58 2012), indicative of replacement. To combine them, Monte Carlo simulation is employed using uncorrelated stratified sampling. Since we are not interested in the extreme values, but mainly in the first few moments of the uncertain cost, the efficiency of stratified sampling (McKay et al 979) allows us to use only (N_c= 40) samples from each constituent distribution to accurately capture the distribution of the total building replacement cost (cost replacement new).

Step (3): Three-dimensional (3D) table 'C'. A 3D table 'C' is created. The number of rows of the table is equal to the IM values (60 $S_a(T_1)$ values from 0 to 4.0g)

considered in the loss estimation framework. The number of columns is equal to the number of ground motions (N_{rec}) used to conduct the IDA in Step (1) ($N_{rec} = 44$ in this study), and the third dimension is equal to N. The following steps describe how table 'C' is filled with cost values.

Step (4): Incorporate the probability of collapse. If collapse has occurred for the i^{th} value of IM and the j^{th} ground motion, the C(i, j, 1:N_c) cells are filled by randomly permuting the N_c total building replacement cost values from Step (2).

Step (5): Incorporate the probability of demolition given no collapse. $\theta_{s,res}$ is obtained for the i^{th} value of IM and the j^{th} ground motion to allow calculation of $P(D|\theta_{s,res})$. If collapse has not already occurred (step 4), N_{dem} (where $N_{dem} = P(D|\theta_{s,res}) \cdot N_c$) out of the N_c cells C(i, j, 1:N_c) are randomly filled by using stratified sampling on the total building replacement cost distribution.

Step (6): Estimate the total repair cost of the building given no collapse or demolition. A number of DSs and corresponding fragility curves are defined for each structural, non-structural and content component of the building using data available in FEMA P-58 (FEMA P-58 2012). For a specific value of an EDP (i.e. EDP_k) corresponding to the i^{th} value of IM and the j^{th} ground motion, the component fragility curve defines the probability $G(DS|EDP_k)$ that the component will experience damage equal or higher than that associated with a specific DS (see Figures 7.1-2). Subtracting these probabilities for two sequential DSs provides the probability $\Delta G(DS|EDP_k)$ of the component to experience damage equal to that associated with a DS (see Figure 7.3). This probability is multiplied by ($N_c - N_{dem}$) to calculate the number of repair cost values associated with the DS. Repair cost values are obtained from the cost function of the specific DS and component. Repeating this procedure for all DSs results in N-N_{dem} repair cost values for the component. Repair costs for all components are calculated using the aforementioned procedure and are added to provide the total repair cost values used to fill the remaining N-N_{dem} empty cells of the C(i, j, 1: N_c) matrix, respecting the desired correlation structure. Any of these total repair cost values should be lower than the total building replacement cost, otherwise the former is replaced with the latter on a case-by-case basis.

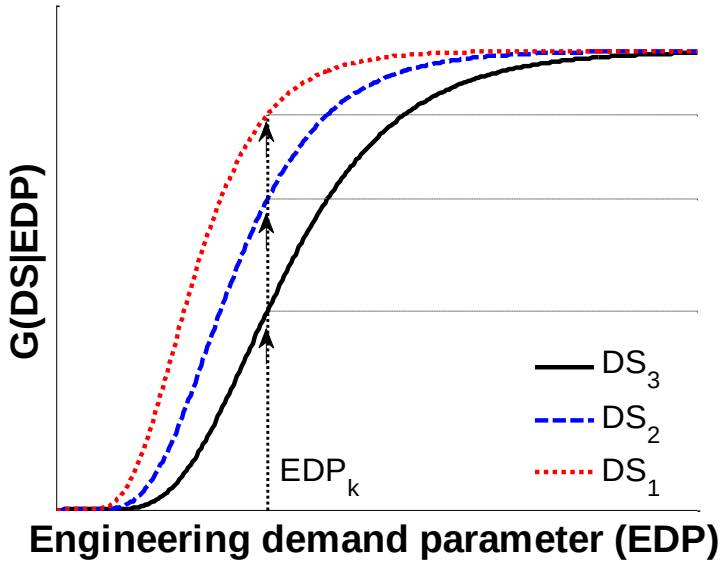

Figure 7.1 Component fragility curve

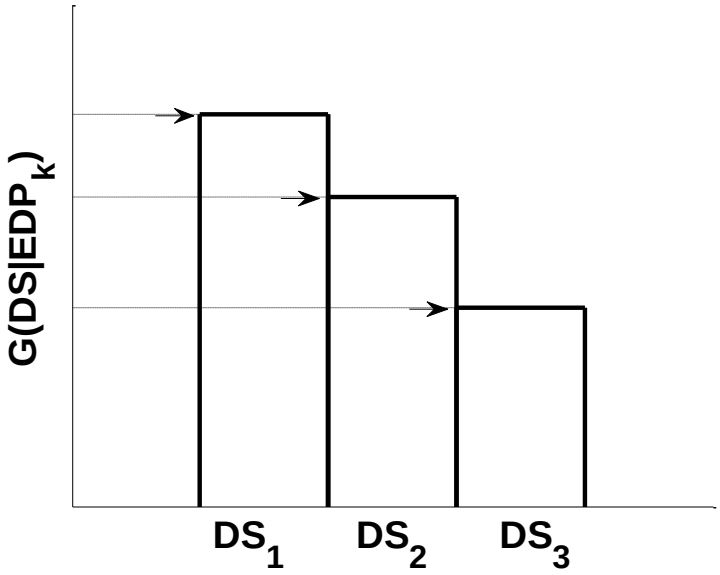

Figure 7.2 Probability $G(DS|EDP_k)$ that the component will experience damage equal or higher than that associated with a specific DS

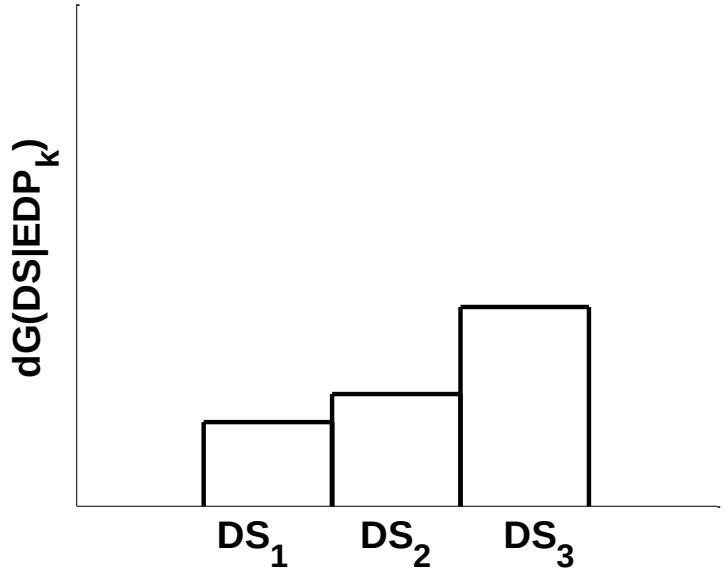

Figure 7.3 Probability $\Delta G(DS|EDP_k)$ of the component to experience damage equal to that associated with a DS

Step (7): Quantile cost values at each IM. For all $N \cdot N_{rec}$ cost values at the same IM level, quantile values at 16%, 50% and 84% (or any desired distribution statistic) are estimated and plotted.

7.4 Prototype building

This study is based on the prototype steel building, presented in section 5.2.1 (see figures 5.1-2), and the four design cases of seismic resistant frames presented in section 6.2: (a) conventional MRFs; (b) MRFs with viscous dampers; (c) SC-MRFs; or (d) SC-MRFs with viscous dampers. All frames are designed according to EC8 (Eurocode 8 2013), and have the same column/beam cross-sections and similar periods of vibration. Viscous dampers are designed to reduce the peak story drift under the DBE from 1.8% to 1.2%.

Table 7.1 Prototype building components per story

MRF components	FEMA P-58 (ID)	SC-MRF components	units	EDP
Steel column base plate	B1031.011b	-//-	8	$\theta_{s,max}$
Post-Northridge welded steel moment connection beam, one side	B1035.021 / None	PT connection, beam one side	4	$\theta_{s,max}$
Post-Northridge welded steel moment connection, beams both sides	B1035.031 / None	PT connection, beams both sides	4	$\theta_{s,max}$
Bolted shear tab gravity connections	B1031.001	-//-	28	$\theta_{s,max}$
Curtain walls	B2022.001	-//-	54	$\theta_{s,max}$
Suspended ceiling	C3032.003a	-//-	26	PFA
Cold water piping	D2021.011a	-//-	1	PFA
Hot water piping	D2022.012b	-//-	1	PFA
HVAC	D3041.001a	-//-	3	PFA
Modular office work stations	E2022.001	-//-	90	PFA
Unsecured fragile objects on shelves	E2022.010	-//-	90	PFA
Electronic equipment on wall	E2022.021	-//-	1	PFA
Desktop electronics	E2022.022	-//-	90	PFA
Book case	E2022.102a	-//-	90	PFA

It is assumed that the prototype building includes the structural components, non-structural components and contents listed in Table 7.1. Table 7.1 lists the type of component, the associated FEMA P-58 (FEMA P-58 2012) identification (ID), the component units that the building includes per story, and the associated EDP used to assess the component DS. Table 7.2 lists the components and total buildings costs.

Table 7.2 Components and total building costs ($\$\cdot 10^6$)

Components cost					
	MRF	SC-MRF	Gravity frames	Braces and dampers	Non-structural elements
Cost	2.586	2.609	1.522	0.060	1.473

Total building cost				
	MRF	MRF with dampers	SC-MRF	SC-MRF with dampers
Cost	5.581	5.641	5.604	5.664

Market research and engineering judgment are used to determine fragility and cost functions for the PT connections, which are not provided by FEMA P-58 (FEMA P-58 2012). The DSs in the PT connections are associated with the replacement of WHPs and the plastic hinge rotation, θ_p, at the end of the beam flange reinforcing plate. θ_p is associated to $\theta_{s,max}$ on the basis of pushover analysis. Replacement of WHPs corresponds to only one DS associated with $\theta_{s,max}$ equal to 1.8%. The cost functions related to θ_p at the end of the beam flange reinforcing plate were determined using mean and dispersion values from conventional welded moment resisting connections. The labour and material cost of the WHPs, which is negligible compared to the cost of other building components, has been used to determine the cost function related with WHPs replacement. The contents cost functions have been developed based on USA market prices. The cost of the dampers is based on their stroke and force capacities and results in a 2% of the building cost.

7.5 Economic seismic losses

7.5.1 Vulnerability functions

Figures 7.4-7.6 show the vulnerability functions of the repair cost and figures 7.7-7.9 show the vulnerability functions of the loss ratio at 16%, 50% and 84% probability of exceedance for all frames. These results are obtained for median and lognormal standard deviation values of the $P(D|\theta_{s,res})$ distribution equal to 0.5% (McCormick et al 2008) and 0.3 (Ramirez and Miranda 2012) respectively. Figure 7.5 shows that at 50% probability of exceedance, the repair cost of the MRF, the MRF with viscous dampers, the SC-MRF, and the SC-MRF with viscous dampers significantly increases after a seismic intensity of 0.9·MCE, 1.2·MCE, 1.9·MCE, and 2.8·MCE, respectively. The results clearly show three different regions of loss given IM. First is the low-intensity gradually ascending part that is dominated by non-structural and contents loss plus some early structural damage (mainly due to yielding). Second is the horizontal plateau that appears when demolition (or collapse) starts becoming influential, quickly accelerating losses to reach the total replacement cost. Finally, a near-vertical segment indicates where the building has practically lost all value at high intensities, needing replacement regardless of the specific value of the IM. In all cases, the introduction of dampers clearly pushes the plateau to appear at higher IMs,

thus delaying the need for demolition. Post-tensioning seems to have a similar and actually additive beneficial effect.

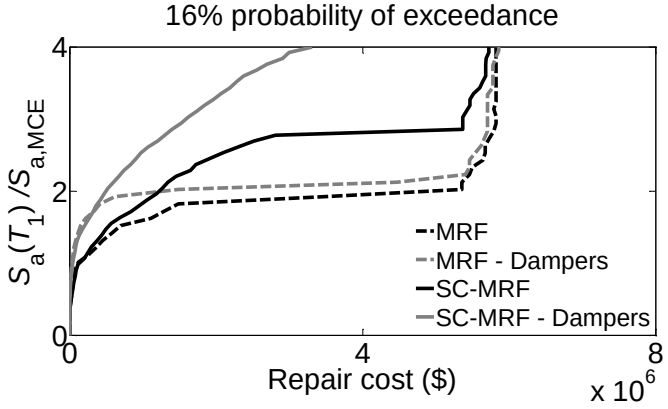

Figure 7.4 Vulnerability functions of the repair cost at 16% probability of exceedance (the $P(D|\theta_{s.res})$ distribution has median value equal to 0.5%).

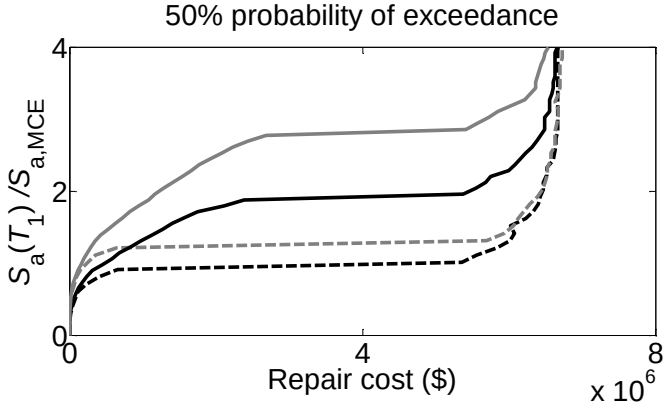

Figure 7.5 Vulnerability functions of the repair cost at 50% probability of exceedance (the $P(D|\theta_{s.res})$ distribution has median value equal to 0.5%).

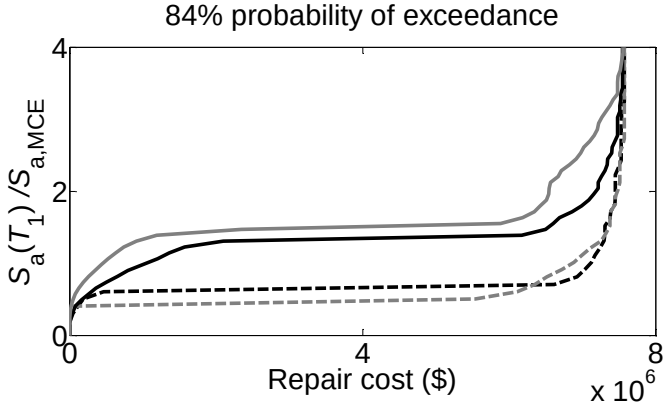

Figure 7.6 Vulnerability functions of the repair cost at 84% probability of exceedance (the $P(D|\theta_{s.res})$ distribution has median value equal to 0.5%).

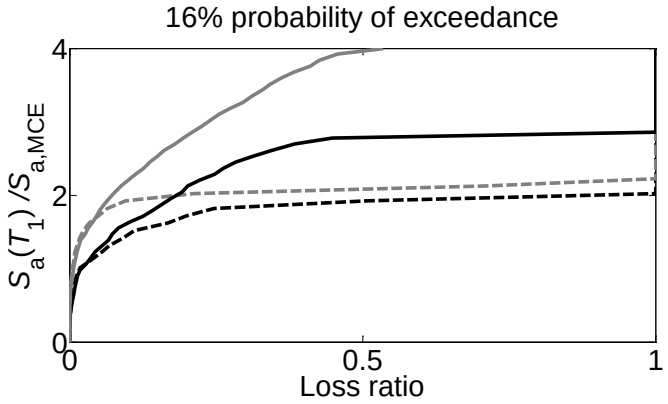

Figure 7.7 Vulnerability functions of the loss ratio at 16% probability of exceedance (the $P(D|\theta_{s.res})$ distribution has median value equal to 0.5%).

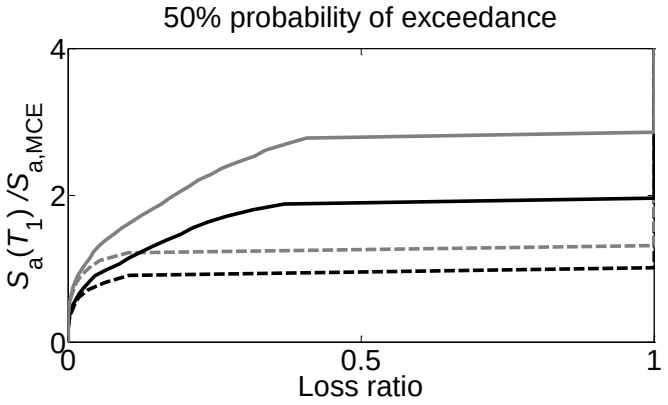

Figure 7.8 Vulnerability functions of the loss ratio at 50% probability of exceedance (the $P(D|\theta_{s.res})$ distribution has median value equal to 0.5%).

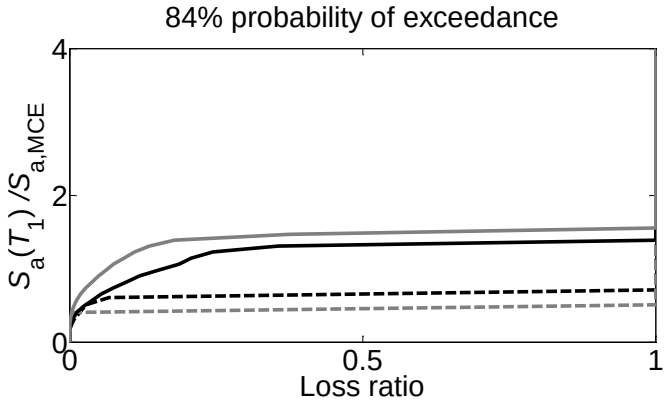

Figure 7.9 Vulnerability functions of the loss ratio at 84% probability of exceedance (the $P(D|\theta_{s.res})$ distribution has median value equal to 0.5%).

Table 7.3 presents repair cost values at 50% probability of exceedance for all design cases and for different seismic intensities. Under the FOE and DBE, the SC-MRF has repair costs similar to those of the MRF. Under the MCE and 2·MCE, the repair costs of the SC-MRF are 92% and 14% less than the repair costs of the MRF, respectively. For higher seismic intensities, the SC-MRF and the MRF have similar repair costs. These results demonstrate that for a median value of the $P(D|\theta_{s,res})$ distribution equal to 0.5%, post-tensioning is effective in reducing the repair cost for seismic intensities between the DBE and 2·MCE. Under the FOE, DBE and MCE, the MRF with viscous dampers has 100%, 57% and 95% less repair costs than those of the MRF. For seismic intensities equal or higher than the 2·MCE, the MRF and the MRF with viscous dampers have similar repair costs. These results demonstrate that for a median value of the $P(D|\theta_{s,res})$ distribution equal to 0.5%, supplemental viscous damping is effective in reducing the repair cost for seismic intensities lower than 2·MCE. Moreover, Table 7.3 shows that the SC-MRF with viscous dampers has the best performance with repair costs significantly lower than those of the MRF for seismic intensities lower than 3·MCE.

Table 7.3 Repair cost (in \$ (10^6)) at 50% probability of exceedance for different seismic intensities (the $P(D|\theta_{s.res})$ distribution has median value equal to 0.5%).

Design cases	FOE	DBE	MCE	2·MCE	3·MCE	4·MCE
MRF	0.01	0.14	5.36	6.46	6.67	6.68
MRF - Dampers	0.00	0.06	0.25	6.46	6.67	6.73
SC-MRF	0.01	0.13	0.45	5.54	6.49	6.66
SC-MRF - Dampers	0.00	0.04	0.16	1.28	5.72	6.54

7.5.2 Sensitivity of loss estimates to changes in the probability of demolition

To examine the sensitivity of the economic seismic loss to the probability of demolition, additional loss analyses are conducted using median vales of the $P(D|\theta_{s,res})$ distribution equal to 1.0% and 1.5%, while holding the dispersion constant at 0.3. Figures 7.10-7.11 show vulnerability functions of the repair cost and loss ratio at 50% probability of exceedance for median values of the $P(D|\theta_{s,res})$ equal to 1.0%. Figures 7.12-7.13 show vulnerability functions of the repair cost and loss ratio at 50% probability of exceedance for median values of the $P(D|\theta_{s,res})$ equal to 1.5%. Figure 7.10 shows that at 50% probability of exceedance, the repair costs of the MRF, the MRF with viscous dampers, the SC-MRF, and the SC-MRF with viscous dampers significantly increase after a seismic intensity of 1.5·MCE, 1.6·MCE, 2.5·MCE, and 3.3·MCE, respectively. The corresponding seismic intensities in Figure 7.12 are equal to 1.7·MCE, 1.9·MCE, 3.0·MCE, and 3.7·MCE, respectively.

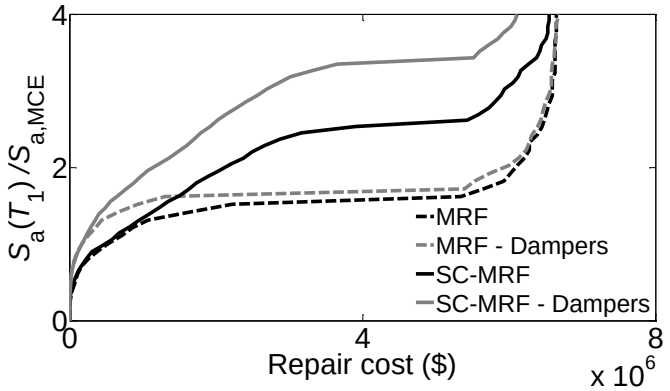

Figure 7.10 Vulnerability function of the repair cost at 50% probability of exceedance (the $P(D|\theta_{s.res})$ distribution has median value equal to 1.0%).

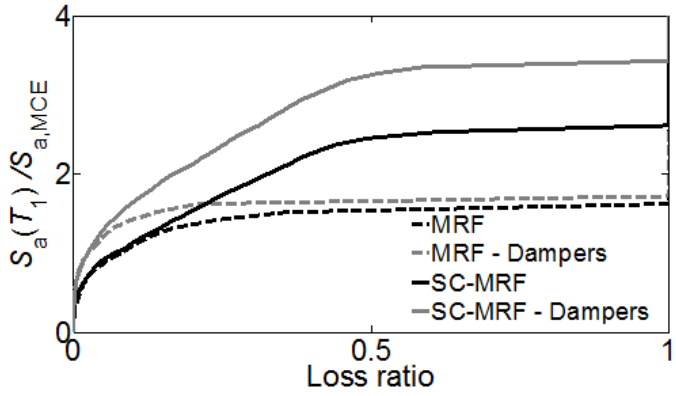

Figure 7.11 Vulnerability function of the loss ratio at 50% probability of exceedance (the $P(D|\theta_{s.res})$ distribution has median value equal to 1.0%).

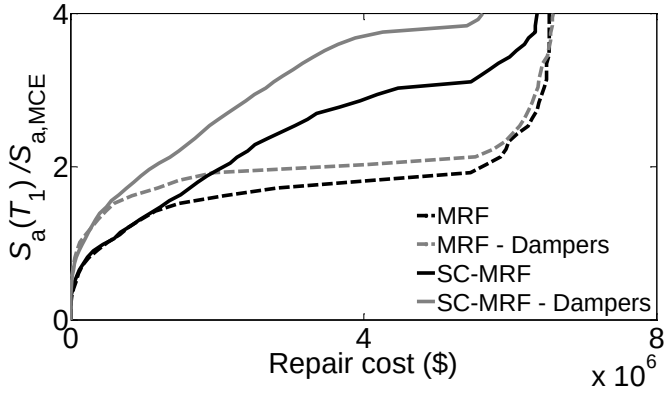

Figure 7.12 Vulnerability function of the repair cost at 50% probability of exceedance (the $P(D|\theta_{s.res})$ distribution has median value equal to 1.5%).

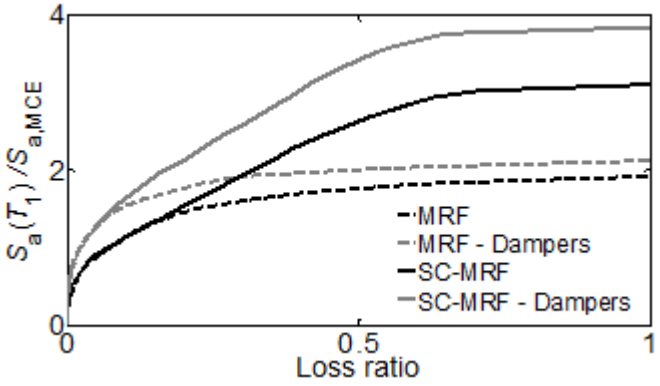

Figure 7.13 Vulnerability function of the loss ratio at 50% probability of exceedance (the $P(D|\theta_{s.res})$ distribution has median value equal to 1.5%).

Table 7.4 presents repair cost values at 50% probability of exceedance for all design cases and for a median value of the $P(D|\theta_{s,res})$ distribution equal to 1.0%. Under the FOE, DBE and MCE, the SC-MRF has similar repair costs with those of the MRF. Under the 2·MCE, the SC-MRF has 64% less repair costs than those of the MRF. For seismic intensities higher than 3·MCE, the SC-MRF and the MRF have similar repair costs. These results demonstrate that for a median value of the $P(D|\theta_{s,res})$ distribution equal to 1.0%, post-tensioning is effective in reducing the repair cost for seismic intensities between the MCE and 3·MCE. Under the FOE, DBE and MCE, the MRF with viscous dampers has 100%, 73% and 67% less repair costs than those of the MRF. For seismic intensities higher than 2·MCE, the MRF with viscous dampers and the MRF have similar repair costs. These results demonstrate that for a median value of the $P(D|\theta_{s,res})$ distribution equal to 1.0%, supplemental viscous damping is effective in reducing the repair cost for seismic intensities lower than 2·MCE. Table 7.4 also shows that the SC-MRF with viscous dampers has the best performance with significantly lower repair costs than those of the MRF for seismic intensities lower than 4·MCE.

Table 7.4 Repair cost (in \$ (10^6)) at 50% probability of exceedance for different seismic intensities (the $P(D|\theta_{s.res})$ distribution has median value equal to 1.0%).

Design cases	$S_{a,FOE}$	$S_{a,DBE}$	$S_{a,MCE}$	$2\cdot S_{a,MCE}$	$3\cdot S_{a,MCE}$	$4\cdot S_{a,MCE}$
MRF	0.01	0.15	0.54	6.11	6.59	6.65
MRF - Dampers	0.00	0.04	0.18	6.00	6.57	6.68
SC-MRF	0.01	0.12	0.45	2.20	5.94	6.54
SC-MRF - Dampers	0.00	0.04	0.16	1.22	2.70	6.11

The results in Table 7.5 show that under the FOE, DBE and MCE, the SC-MRF has repair costs similar to those of the MRF. Under the 2·MCE, 3·MCE and 4·MCE, the SC-MRF has 74%, 55% and 12% less repair costs than those of the MRF. These results demonstrate that for a median value of the $P(D|\theta_{s,res})$ distribution equal to 1.5%, post-tensioning is effective in reducing the repair cost for seismic intensities between the MCE and 4·MCE. Under the FOE, DBE, MCE and 2·MCE, the MRF with viscous dampers has 100%, 75%, 75% and 29% less repair costs than those of the MRF. For seismic intensities higher than 3·MCE, the MRF with viscous dampers and the MRF have similar repair costs. These results demonstrate that for a median value of the $P(D|\theta_{s,res})$ distribution equal to 1.5%, supplemental viscous damping is effective in reducing the repair cost for seismic intensities lower than 3·MCE. Table 7.5 also shows that the SC-MRF with viscous dampers has the best performance with significantly lower repair costs than those of the MRF for seismic intensities equal or lower than 4·MCE.

Table 7.5 Repair cost (in \$ (10^6)) at 50% probability of exceedance for different seismic intensities (the $P(D|\theta_{s.res})$ distribution has median value equal to 1.5%).

Design cases	$S_{a,FOE}$	$S_{a,DBE}$	$S_{a,MCE}$	$2\cdot S_{a,MCE}$	$3\cdot S_{a,MCE}$	$4\cdot S_{a,MCE}$
MRF	0.01	0.16	0.51	5.67	6.46	6.53
MRF - Dampers	0.00	0.04	0.13	4.05	6.38	6.60
SC-MRF	0.01	0.12	0.44	1.50	2.88	5.72
SC-MRF - Dampers	0.00	0.04	0.15	0.66	1.79	3.04

A careful comparison among the results of Tables 7.3, 7.4, and 7.5 shows that supplemental viscous damping is more effective than post-tensioning in reducing the repair cost for seismic intensities equal or lower than the MCE. The opposite is true for seismic intensities higher than 2·MCE. The effectiveness of post-tensioning increases as the median of the $P(D|\theta_{s,res})$ distribution increases for seismic intensities equal or higher than the 2·MCE. Moreover, the effectiveness of viscous damping is not clearly affected by the median of the $P(D|\theta_{s,res})$ distribution. In addition, the repair cost of the MRF under the MCE is significantly increased with a decrease of the median of the $P(D|\theta_{s,res})$ distribution from 1.0% to 0.5%. It should be highlighted that seismic intensities higher than MCE have low probability of occurrence, yet this chapter examines such high seismic intensities to identify the intensity level after which the repair cost of the low damage SC-MRF with viscous dampers quickly accelerates,

7.6 Summary

In this chapter the potential of SC-MRFs and viscous dampers to reduce the economic seismic losses in steel buildings has been evaluated. The evaluation is based on a 5-story prototype steel building designed to use different seismic-resistant frames, i.e.: conventional MRFs; MRFs with viscous dampers; SC-MRFs; or SC-MRFs with viscous dampers. These frames were designed according to EC8 (Eurocode 8 2013), and have the same beam/column cross-sections and similar periods of vibration. The SC-MRF has similar initial stiffness but higher post-yield stiffness and peak base shear coefficient than the conventional. Viscous dampers are designed to achieve a total damping ratio of 20% at the fundamental period of vibration. The estimated peak story drift under the design earthquake for the frames with and without dampers is 1.2% and 1.8%, respectively. The economic losses are estimated by developing vulnerability functions according to the FEMA P-58 (FEMA P-58 2012) methodology, which considers uncertainties in earthquake ground motion, structural response, and repair costs. Both the probability of sidesway collapse and the probability of demolition due to excessive residual story drifts are taken into account. Moreover, a parametric study on the effect of the assumed residual story drift value beyond which is less expensive to rebuild a structure than to repair has been conducted. In particular, the probability of having to demolish the building conditioned to residual story drift, i.e. $P(D|\theta_{s,res})$, was assumed to follow a lognormal distribution with median values of 0.5%, 1.0% and 1.5%.

Based on the results presented in this paper and given the properties of the steel frames and ground motions as well as the assumptions used in loss analyses, the following conclusions are drawn:

1. The repair cost of the MRF under the MCE significantly increases with a decrease of the median value of the $P(D|\theta_{s,res})$ distribution from 1.0% to 0.5%.

2. For a median value of the $P(D|\theta_{s,res})$ distribution equal to 0.5%, viscous dampers are effective in reducing the repair cost for seismic intensities lower than 2·MCE. On the other hand, post-tensioning is effective only for seismic intensities between the DBE and 2·MCE.

3. For a median value of the $P(D|\theta_{s,res})$ distribution equal to 1.0%, viscous dampers are effective in reducing the repair cost for seismic intensities lower than 2·MCE. On the other hand, post-tensioning is effective only for seismic intensities between the MCE and 3·MCE.

4. For a median value of the $P(D|\theta_{s,res})$ distribution equal to 1.5%, viscous dampers are effective in reducing the repair cost for seismic intensities lower than 3·MCE. On the other hand, post-tensioning is effective only for seismic intensities between the MCE and 4·MCE.

5. Supplemental viscous damping is more effective than post-tensioning in reducing the repair cost for seismic intensities equal or lower than the MCE. The opposite is true for seismic intensities higher than 2·MCE.

6. The effectiveness of post-tensioning to reduce repair costs increases as the median value of the $P(D|\theta_{s,res})$ distribution increases for seismic intensities equal or higher than the 2·MCE. The effectiveness of supplemental viscous damping is not clearly affected by the median value of the $P(D|\theta_{s,res})$ distribution.

7. For seismic intensities lower or equal to 3·MCE, the SC-MRF with viscous dampers has superior seismic performance. For example, under both the DBE and MCE and for all the median values of the $P(D|\theta_{s,res})$ distribution, the SC-

MRF achieves repair cost reductions between 70% and 100% compared to the repair cost of the conventional MRF.

8 Conclusions and recommendations for further work

8.1 Conclusions

In this PhD thesis, conventional seismic-resistant steel frames and the associated seismic design methodology according to EC8 (Eurocode 8 2013) are first discussed. Several types of resilient structural systems like SC-MRFs, passive dampers, and combined systems, which can minimize structural and non-structural damage, are also discussed. An extensive literature review of all the existing PT connections is presented. In this literature review, all the existing numerical models and experiments for PT connections and SC-MRFs are presented, and, all the available seismic assessment studies on SC-MRFs are discussed. Based on the literature review, research needs are identified.

A modelling procedure of PT connections with WHPs and the associated beams and columns in OpenSees is developed. The recommended model has been calibrated against experimental results and found to accurately simulate the connection behavior. The ability of the recommended model to capture the stiffness and strength deterioration due to beam local buckling is also validated. The OpenSees model is compared against FEM models in Abaqus, which were developed and calibrated against experimental setups of PT connections where local buckling occurs in the beams. It is concluded that the recommended model of PT connections in OpenSees is able to accurately capture the connection behaviour, including the stiffness and strength deterioration due to local buckling in the beam flange and web. Therefore, the proposed model can be used in collapse simulations of SC-MRFs.

A seismic design and assessment procedure of steel SC-MRFs with viscous dampers within the framework of EC8 (Eurocode 8 2013) was developed. This design strategy combines steel SC-MRFs with viscous dampers to simultaneously control peak story drifts and residual story drifts. The SC-MRFs are using a recently developed PT connection with WHPs (Vasdravellis et al 2013a,b). In the proposed design procedure, performance levels are defined with respect to drifts, residual drifts and limit states in the PT connections. Also, a preliminary pushover analysis is

conducted at the early phase of the design process to estimate rotations and axial forces in PT connections instead of using approximate formulae.

A 5-story prototype steel building was designed using MRFs or SC-MRFs with different base shear strengths and viscous dampers. Different designs of the SC-MRFs with viscous dampers are considered to investigate all possible scenarios, i.e. use of dampers to achieve drifts significantly lower than the EC8 (Eurocode 8 2013) drift limit; to significantly reduce steel weight without exceeding the EC8 (Eurocode 8 2013) drift limit; or to reduce steel weight and achieve drifts lower than the EC8 (Eurocode 8 2013) drift limit. All the design cases were evaluated under the FOE, DBE and MCE seismic intensities through nonlinear dynamic analysis. Moreover, IDAs were conducted to evaluate the potential of SC-MRFs and viscous dampers to improve the collapse resistance in comparison to MRFs. For all the analysis, models capable of simulating all structural limit states up to collapse were used.

Based on the IDAs results, the potential of SC-MRFs and viscous dampers to reduce the economic seismic losses has been also evaluated. The economic losses are estimated by developing vulnerability functions according to the FEMA P-58 (FEMA P-58 2012) methodology, which considers uncertainties in earthquake ground motion, structural response, and repair costs. The probability of collapse and the probability of demolition due to excessive residual story drifts have been taken into account. Moreover, a parametric study on the effect of the residual story drift threshold beyond which is less expensive to rebuild a structure than to repair is also conducted. In particular, the probability of having to demolish the building conditioned to residual story drift, i.e. $P(D|\theta_{s,res})$, was assumed to follow a lognormal distribution with median values of 0.5%, 1.0% and 1.5%.

Based on the PhD research work briefly described above, the following conclusions are drawn.

- 3D FEM models in ABAQUS are capable to simulate the complex inelastic buckling that occurs either in the beam web or the beam flanges of PT connections under high axial forces and large drifts.

- Models for PT connections in OpenSees, which incorporate fiber beam-column elements along with zero-length nonlinear springs simulating contact/friction, are capable to simulate the complex hysteretic behaviour of PT connections under large cyclic drifts.
- The preliminary pushover analysis recommended as a major step of the proposed design procedure results in very accurate prediction of structural limit states in the PT connections.

- The SC-MRFs avoid beam and column base plastic hinge formation under the MCE and experience strength deterioration at roof drifts higher than 5%.

- The SC-MRFs with viscous dampers can be designed for less steel weight (resulting in less strength) without compromising their DBE drift performance. The same is generally true for the MCE drift performance, but a restriction on the strength reduction should be established.

- Viscous dampers are very effective in improving the residual drift performance of SC-MRFs.

- The SC-MRFs have higher collapse resistance than that of the MRFs, while the use of viscous dampers results in higher collapse resistance for both the MRFs and the SC-MRFs. The 50% probability of collapse is associated with seismic intensities of 5.5·MCE for the SC-MRF with viscous dampers; 5.0·MCE for the MRF with viscous dampers; 4.5·MCE for the SC-MRF; and 3.6·MCE for the MRF.

- The repair cost of the MRF under the MCE significantly increases with a decrease of the median value of the $P(D|\theta_{s,res})$ distribution from 1.0% to 0.5%.

- For a median value of the $P(D|\theta_{s,res})$ distribution equal to 0.5%, viscous dampers are effective in reducing the repair cost for seismic intensities lower than 2·MCE. On the other hand, post-tensioning is effective only for seismic intensities between the DBE and 2·MCE.

- For a median value of the $P(D|\theta_{s,res})$ distribution equal to 1.0%, viscous dampers are effective in reducing the repair cost for seismic intensities lower than 2·MCE. On the other hand, post-tensioning is effective only for seismic intensities between the MCE and 3·MCE.

- For a median value of the $P(D|\theta_{s,res})$ distribution equal to 1.5%, viscous dampers are effective in reducing the repair cost for seismic intensities lower than 3·MCE. On the other hand, post-tensioning is effective only for seismic intensities between the MCE and 4·MCE.

- Supplemental viscous damping is more effective than post-tensioning in reducing the repair cost for seismic intensities equal or lower than the MCE. The opposite is true for seismic intensities higher than 2·MCE.

- The effectiveness of post-tensioning to reduce repair costs increases as the median value of the $P(D|\theta_{s,res})$ distribution increases for seismic intensities equal or higher than the 2·MCE. The effectiveness of supplemental viscous damping is not clearly affected by the median value of the $P(D|\theta_{s,res})$ distribution.

- For seismic intensities lower or equal to 3·MCE, the SC-MRF with viscous dampers has superior seismic performance. For example, under both the DBE and MCE and for all the median values of the $P(D|\theta_{s,res})$ distribution, the SC-MRF achieves repair cost reductions between 70% and 100% compared to the repair cost of the conventional MRF.

8.2 Recommendations for further research

- Evaluation of the behaviour of steel SC-MRFs under progressive collapse conditions in a column loss scenario. A finite element model can be developed in Abaqus, simulating a building with SC-MRFs and a loss of column scenario analysis can be implemented.

- The fire resistance of SC-MRFs can be evaluated. Premature failure of the connections could be cause due to relaxation of the post-tensioning force in the PT bars or reduction of the strength and stiffness of the WHPs under temperature increase. PT bars could be protected with fire coating and WHPs could be made of fire resistant steel. Additionally, premature failure could be caused by local buckling in the beams as a result of bending moment and high compressive forces due to thermal expansion. Both experimental tests and numerical modelling will be needed to study the fire behaviour of SC-MRFs under fire.

- Experimental cyclic tests of PT connections with WHPs up to high drifts, after the occurrence of beams local buckling at the end of the reinforcing plates. Such tests will be carried out in the structures laboratory of University of Warwick, where cyclic tests will be implemented up to the structural collapse of a PT connection.

- Development of component fragility curves and cost functions for PT connections based on large data of experimental and FEM results. Finite elements of several PT connections from the existing literature can be developed. The finite element results can be combined with available experimental tests of PT connections from the existing literature. The analytical and the experimental results can be used to define damage states of PT connections and so to develop component fragility curves. Also in combination with experience of industrial market prices, cost functions of PT connections can be developed.

References

Abaqus user's manual. Version 6.10. Providence, RI, USA; 2010.

AISC 341-05. *Seismic provisions for structural steel buildings*; 2005.

All structure engineering LLC webpage

ASCE. *Minimum design loads for buildings and other structures*. ASCE 7, Reston, VA; 2005

Aslani H, Miranda E. *Probabilistic earthquake loss estimation and loss disaggregation in buildings*, Report No. 157, John A. Blume Earthquake Engineering Research Center, Stanford, CA, 2005.

Carr AJ. *RUAUMOKO—Inelastic Dynamic Analysis Program*. Department of Civil Engineering, University of Canterbury, Christchurch, New Zealand, 2005.

Charney FA, Downs WM. Connections in steel structures V. ESSC/AISC Workshop. Amsterdam; June 3-4 2004.

Chou CC, Chen JH, Chen YC and Tsai KC. Evaluating performance of post-tensioned steel connections with strands and reduced flange plates. *Earthquake Engineering and Structural Dynamics* 2006; 35(9): 1167-1185.

Chou C-C, Tsai K-C, Yang W-C. Self-centering steel connections with steel bars and a discontinuous composite slab. *Earthquake Engineering and Structural Dynamics* 2009; 38: 403-422.

Chou CC, Lai YJ. Post-tensioned self-centering moment connections with beam bottom flange energy dissipators. *Journal of Constructional Steel Research* 2009; 65(10-11): 1931-1941.

Christopoulos C, Filiatrault A, Uang CM, Folz B. Posttensioned energy dissipating connections for moment-resisting steel frames. *Journal of Structural Engineering (ASCE)* 2002a; 128(9): 1111-1120.

Christopoulos C, Filiatrault A, and Folz B. Seismic response of self-centering hysteretic SDOF systems. *Earthquake engineering and structural dynamics* 2002b; 31: 1131-1150.

Christopoulos C, Pampanin S, Priestley MJN. New damage index for framed systems based on residual deformations. *Journal of earthquake engineering* 2003; 7(1), 97-118.

Christopoulos C, Filiatrault A. Principles of passive supplemental damping and seismic isolation, Italy; 2006.

Constantinou MC, Symans MD, Experimental and analytical investigation of seismic response of structures with supplemental fluid viscous dampers. Technical report NCEER-92-0032, NCER1992. National center for earthquake research, Buffalo, New York; 1992.

Cornell CA, Krawinkler H. Progress and challenges in seismic performance assessment. *PEER Center News* 2000; 3(2):1–4.

D'Aniello M, Landolfo R, Piluso V, Rizzano G. Ultimate behavior of steel beams under non uniform bending. *Journal of Constructional Steel Research* 2012; 78: 144-158

Dimopoulos AI, Karavasilis TL, Vasdravellis G, Uy B. Seismic design, modelling and assessment of self-centering steel frames using post-tensioned connections with web hourglass shape pins. *Bulletin of Earthquake Engineering* 2013; 11:1797–1816.

Dimopoulos AI, Tzimas AS, Karavasilis TL, and Vamvatsikos D. Probabilistic economic seismic loss estimation in steel buildings using post-tensioned moment

resisting frames and viscous dampers. *Earthquake engineering and structural dynamics* 2016; DOI: 10.1002/eqe.2722.

Dolce M, Manfredi G. Research needs in earthquake engineering highlighted by the 2009 L'Aquila earthquake. The ReLUIS-DPC Project Report; 2009.

Elghazouli AY. Assessment of European seismic design procedures for steel framed structures. *Bulletin of Earthquake Engineering* 2010; 8:65–89.

Elkady A, Lignos DG. Analytical investigation of the cyclic behavior and plastic hinge formation in deep wide-flange steel beam-columns. *Bulletin of Earthquake Engineering* 2014; DOI 10.1007/s10518-014-9640-y.

EC3. Eurocode 3: Design of steel structures - Part 1-1: General rules and rules for steel buildings; 2010.

EC3. Eurocode 3: Design of steel structures - Part 1-5: Plated structural elements; 2006.

EC8. Eurocode 8: Design of structures for earthquake resistance; 2013.

Federal Emergency Management Agency, FEMA. NEHRP guidelines for the seismic rehabilitation of buildings. Report FEMA-273. Washington (DC); 1997.

Federal Emergency Management Agency (FEMA). NEHRP recommended provisions for seismic regulations for new buildings and other structures, Part 1 - provisions. Report FEMA-368, Washington (D.C); 2000a

FEMA P695. Quantification of building seismic performance factors. ATC-63 Project. Applied Technology Council. CA. USA; 2008.

FEMA P58. Seismic Performance Assessment of Buildings. ATC. Applied Technology Council. CA. USA; 2012.

Garlock M, Ricles JM, Sause R. Experimental studies of full-scale posttensioned steel connections. *Journal of Structural Engineering* 2005; 131(3): 438-448.

Garlock M, Sause R, Ricles JM. Behavior and design of posttensioned steel frame systems. *Journal of Structural Engineering* 2007; 133(3): 389-399.

Gunay S, Mosalam KM. PEER Performance-Based Earthquake Engineering Methodology, Revisited. *Journal of Earthquake Engineering* 2013; 17:829-858.

Housner GW. Limit design of structures to resist earthquakes. 1st World Conference on Earthquake Engineering, Berkeley, CA, 5.1-5.13; 1956.

Hamidia M, Filiatrault A, Aref A. Simplified seismic sidesway collapse analysis of frame buildings. *Earthquake engineering and structural dynamics* 2014; 43:429-448.

Kam WY, Pampanin S, Carr AJ, Palermo A. Design procedure and behaviour of advanced flag-shape (AFS) MDOF systems. NZSEE Conference; 2008.

Kam WY, Pampanin S, Palermo A, Car AJ. Self-centering structural systems with combination of hysteretic and viscous energy dissipations. *Earthquake Engineering and Structural Dynamics* 2010; 39(10): 1083-1108.

Karavasilis TL, Ricles JM, Sause R, Chen C. Experimental evaluation of the seismic performance of steel MRFs with compressed elastomer dampers using large-scale real-time hybrid simulation. *Engineering Structures* 2011; 33(6):1859-1869.

Karavasilis TL, Kerawala S, Hale E. Model for hysteretic behaviour of steel energy dissipation devices and evaluation of a minimal-damage seismic design approach for steel frames. *Journal of Constructional Steel Research* 2012; 70:358-367.

Karavasilis TL, Seo C-Y. Seismic structural and non-structural performance evaluation of highly damped self-centering and conventional systems. *Engineering Structures* 2011; 33: 2248-2258.

Kelly JM, Skinner RI, and Heine AJ. Mechanisms of energy absorption in special devices for use in earthquake resistant structures. *Bulletin of the New York Zealand Society for earthquake engineering* 1972; 5(3), 63-88.

Kim HJ, Christopoulos C. Friction damped posttensioned self-centering steel moment-resisting frames. *Journal of Structural Engineering* 2008a; 134(11): 1768-1779.

Kim HJ and Christopoulos C. Numerical models and ductile ultimate deformation response of post-tensioned self-centering moment connections. *Earthquake engineering and structural dynamics* 2009a; 38: 1-21.

Kim HJ, Christopoulos C. Seismic design procedure and seismic response of post-tensioned self-centering steel frames. *Earthquake Engineering and Structural Dynamics* 2009b; 38: 355-376.

Kobori T, Miura Y, Fukuzawa E, Yamada T, Arita T, Takenaka Y, Miyagawa N, Tanaka N, Fukumoto T. Development and application of hysteresis steel dampers. Earthquake Engineering, 10th World Conference. Rotterdam: Balkema; 1992;

Krawinkler H. Shear in Beam-Column joints in Seismic Design of Frames. *Engineering Journal* 1978; 15(2) AISC, Chicago, Illinois.

Kurama YC. Seismic design of unbonded post-tensioned precast concrete walls with supplementary viscous damping. *ACI Structural Journal* 2000; 97(3):648–658.

Lignos DG, Krawinkler H. A database in support of modelling of component deterioration for collapse prediction of steel frame structures. ASCE Structures Congress, SEI institute, Long Beach CA; 2007.

Lin YC, Sause R, and Ricles JM. Seismic performance of a self-centering steel moment resisting frame system with beam web friction devices: Hybrid simulations under the DBE. *Journal of structural engineering* 2013a 139(11), 1823–1832.

Lin YC, Sause R, and Ricles JM. Seismic performance of a large-scale steel self-centering moment resisting frame: MCE hybrid simulations and quasi-static pushover tests. *Journal of structural engineering* 2013b; 139(7), 1227–1236.

Luco N, Bazzurro P. Does amplitude scaling of ground motion records result in biased nonlinear structural drift responses? *Earthquake Engineering and Structural Dynamics* 2007; 36(13): 1813-1835.

Mazzoni S, McKenna F, Scott M, Fenves G. Open system for earthquake engineering simulation (OpenSees). User Command Language Manual, Pacific Earthquake Engineering Research Center, University of California, Berkeley; 2006.

McCormick J, Aburano H, Ikenaga M, Nakashima M. Permissible residual deformation levels for building structures considering both safety and human elements. 14th Word Conference of Earthquake Engineering, Beijing, China; 2008.

McKay MD, Beckman RJ, Conover WJ. A comparison of three methods for selecting values of input variables in the analysis of output from a computer code. *Technometrics* 1979; 21(2): 239-245.

Muto K. Earthquake resistant design of 36-storied Kasamigaseki building. 4th world conference on earthquake engineering, 3, J-4, 16-33; 1969.

Newell J, Uang C-M. Cyclic behaviour of steel columns with combined high axial load and drift demand. Report No. SSRP-06/22. Department of Structural Engineering, University of California, San Diego, La Jolla; 2006.

Newell J, Uang C-M. Cyclic behavior of steel wide-flange columns subjected to large drift. *Journal of Structural Engineering* 2008; 134:1334-1342.

Ogreen engineering web page.

Pall AS, Marsh C, Fazio P. Friction joints for seismic control of large panel structures. *Journal of prestressed concrete institute* 1980; 25(6), 38-61.

Porter KA, Kiremidjian AS, LeGrue JS. Assembly-based vulnerability of buildings and its use in performance evaluation. *Earthquake Spectra* 2001; 17(2):291-312.

Porter, KA, Beck, JL, Shaikhutdinov, RV. Sensitivity of building loss estimates to major uncertain variables. *Earthquake Spectra* 2002; 18 (4): 719-743.

Prakash V, Powell G, and Campbell S. 'DRAIN-2DX base program description and user guide, version 1.10. Report No UCB/ SEMM-93/17&18. Structural Engineering Mechanics and Materials. Department of Civil Engineering. University of California, Berkeley, Calif; 1993.

Ramirez CM, Miranda E. Significance of residual drifts in building earthquake loss estimation. *Earthquake Engineering and Structural Dynamics* 2012; 41:1477-1493.

Ricles J, Sause R, Garlock M, and Zhao C. Posttensioned seismic-resistant connections for steel frames. *Journal of structural engineering* 2001; 127(2): 113–121.

Ricles J, Sause R, Peng SW, and Lu LW. Experimental evaluation of earthquake resistant posttensioned steel connections. *Journal of structural engineering* 2002; 128(7): 850–859.

Rojas P. Seismic analysis, design, and evaluation of posttensioned friction damped connections for steel moment resisting frames. PhD dissertation in Civil and Environmental Engineering Department. Lehigh University, Bethlehem, Pa; 2003.

Rojas P, Ricles JM, Sause R. Seismic performance of post-tensioned steel moment resisting frames with friction devices. *Journal of Structural Engineering* 2005; 131(4): 529-540.

Sanchez-Ricart L, Plumier A. Parametric study of ductile moment-resisting steel frames: A first step towards Eurocode 8 calibration. Earthquake Engineering and Structural Dynamics 2008; 37(7): 1135–1155.

Scott MH, Fenves GL. Plastic hinge integration methods for force –based beam-column elements. *Journal of Structural Engineering* 2006; 132(2): 244-252.

Skinner RI, Kelly KM, Heine AJ. Optimal seismic response control with dampers. *Earthquake engineering and structural dynamics* 1975; 3: 287-296.

Tsai KC, Chou CC, Lin CL, Chen PC, Jhang SJ. Seismic self-centering steel beam-to-column moment connections using bolted friction devices. Earthquake Engineering and Structural Dynamics 2008; 37: 627-645.

Tyler RG. Damping in Building structures by Means of PTFE sliding joints. *Bulletin of the New Zealand society for earthquake engineering* 1977; 10(3): 139-142.

Tzimas AS, Karavasilis TL, Bazeos N, Beskos DE. A hybrid force/displacement seismic design method for steel building frames. Engineering Structures 2013; 56: 1452-1463.

Tzimas AS, Dimopoulos AI, Karavasilis TL. EC8-based seismic design and assessment of self-centering post-tensioned steel frames with viscous dampers. *Journal of Constructional Steel Research* 2015; 105:60-73.

Vamvatsikos D, Cornell CA. Incremental dynamic analysis. *Earthquake Engineering and Structural Dynamics* 2002; 31(3): 491-514.

Vasdravellis G, Karavasilis TL, Uy B. Large-scale experimental validation of steel post-tensioned connections with web hourglass pins. *Journal of Structural Engineering* 2013a; 139(6):1033-1042.

Vasdravellis G, Karavasilis TL, Uy B. Finite element models and cyclic behaviour of self-centering post-tensioned connections with web hourglass pins. *Engineering Structure*s 2013b; 52:1-16.

Vasdravellis G, Karavasilis TL, Uy B. Design rules, experimental evaluation, and fracture models for high-strength and stainless steel hourglass shape energy dissipation devices. *Journal of Structural Engineering* 2015; 140(11):04014087

Whittaker AS, Constantinou MC, Ramirez OM, Johnson MW, Chrysostomou CZ. Equivalent lateral force and modal analysis procedures of the 2000 NEHRP Provisions for buildings with damping systems. *Earthquake Spectra* 2003; 19(4):959–80.

Wolski M, Ricles JM, Sause R. Experimental study of a self-centering beam-column connection with bottom flange friction device. *Journal of Structural Engineering* 2009; 135(5): 479-488.

Annex A. OpenSees script for a 5 storeys - 3 bays SC-MRF using PT connections with WHPs

```
#--------------------------------------------------------------------------------------------------
# OpenSees script for a 5 storeys - 3 bays SC-MRF using PT connection with WHPs
# Written by: Athanasios Dimopoulos
#--------------------------------------------------------------------------------------------------

# Clear database

wipe


# Units: KN, m

# Define the model builder

model BasicBuilder -ndm 2 -ndf 3;

# Define basic grid lines

# x: hoizontal axis

# y: vertical axis

# Define lean on columns x coordinates

set xL1 -24.0;
set xL2 -16.0;
set xL3 -8.00;

# Define columns vertical x coordinates

set x1 0.0;
set x2 8.0;
set x3 16.00;
set x4 24.00;

# Define floors horizontal y coordinates

set y1 0.0;
set y2 4.0;
set y3 7.2;
set y4 10.4;
set y5 13.6;
set y6 16.8;

# Define beam section geometrical properties

# R: for sections of beam elements with reinforcing plates on the flanges)

# 1, 2, 3, 4, 5 stands for storey

# d: section height; tw: web thickness; bf: flange width; tf: flange thickness; As: shear area

# b stands for beams and c for columns

# IPE500R1
set     dbr1    0.614   ;
set     twbr1   0.0111  ;
set     bfbr1   0.21    ;
set     tfbr1   0.0492  ;
set     Asbr1   0.006815 ;

# IPE500R3
set     dbr3    0.614   ;
set     twbr3   0.0111  ;
set     bfbr3   0.21    ;
set     tfbr3   0.0492  ;
set     Asbr3   0.006815 ;

# IPE550R2
```

```
set     dbr2    0.678     ;
set     twbr2   0.012     ;
set     bfbr2   0.22      ;
set     tfbr2   0.058     ;
set     Asbr2   0.008136  ;

# IPE450R4
set     dbr4    0.552     ;
set     twbr4   0.0102    ;
set     bfbr4   0.2       ;
set     tfbr4   0.042     ;
set     Asbr4   0.00563   ;

# IPE450R5
set     dbr5    0.542     ;
set     twbr5   0.0102    ;
set     bfbr5   0.2       ;
set     tfbr5   0.037     ;
set     Asbr5   0.005528  ;

# Define Column sections

# HEB600
set     dc2     0.6       ;
set     twc2    0.0155    ;
set     bfc2    0.3       ;
set     tfc2    0.03      ;
set     Asc2    0.0093    ;

# HEB650
set     dc1     0.65      ;
set     twc1    0.016     ;
set     bfc1    0.3       ;
set     tfc1    0.031     ;
set     Asc1    0.0104    ;

# Define Additional grids for the rigid components of the panel zones (scissor model), simulating the sc connections' interface

CGrid points in x direction for the simulation of the rigid components (first 3 floors)

# C stands for column; B stands for beams; L stands for left; R stands for right; T stands for top of the beam; B stands for bottom of the beam;

# 1 stands for the y coordinate of the exterior fiber of the beam reinforcing plate

# 2 stands for the y coordinate of the interior fiber of the beam reinforcing plate

# 3 stands for the y coordinate of the interior fiber of the beam flange

set x11CL [expr $x1-0.5*$dc1];
set x11CR [expr $x1+0.5*$dc1];

set x12CL [expr $x2-0.5*$dc1];
set x12CR [expr $x2+0.5*$dc1];

set x13CL [expr $x3-0.5*$dc1];
set x13CR [expr $x3+0.5*$dc1];

set x14CL [expr $x4-0.5*$dc1];
set x14CR [expr $x4+0.5*$dc1];


# Grid points in x direction for the simulation of the rigid components (4 & 5 floors)

set x21CL [expr $x1-0.5*$dc2];
set x21CR [expr $x1+0.5*$dc2];

set x22CL [expr $x2-0.5*$dc2];
set x22CR [expr $x2+0.5*$dc2];

set x23CL [expr $x3-0.5*$dc2];
set x23CR [expr $x3+0.5*$dc2];

set x24CL [expr $x4-0.5*$dc2];
set x24CR [expr $x4+0.5*$dc2];
```

```
# Grid points in y direction for the simulation of the rigid components (1 & 2 floors)

set y2BT  [expr $y2+0.5*$dbr1];
set y2BT1 [expr $y2BT-($tfbr1-$tfb13)];
set y2BT2 [expr $y2BT1-$tfb13];
set y2BT3 [expr $y2BT2-0.05];

set y2BB  [expr $y2-0.5*$dbr1];
set y2BB1 [expr $y2BB+($tfbr1-$tfb13)];
set y2BB2 [expr $y2BB1+$tfb13];
set y2BB3 [expr $y2BB2+0.05];

set y3BT  [expr $y3+0.5*$dbr2];
set y3BT1 [expr $y3BT-($tfbr2-$tfb2)];
set y3BT2 [expr $y3BT1-$tfb2];
set y3BT3 [expr $y3BT2-0.05];

set y3BB  [expr $y3-0.5*$dbr2];
set y3BB1 [expr $y3BB+($tfbr2-$tfb2)];
set y3BB2 [expr $y3BB1+$tfb2];
set y3BB3 [expr $y3BB2+0.05];

# Grid points in y direction for the simulation of the rigid components (3 & 4 floors)

set y4BT  [expr $y4+0.5*$dbr3];
set y4BT1 [expr $y4BT-($tfbr3-$tfb13)];
set y4BT2 [expr $y4BT1-$tfb13];
set y4BT3 [expr $y4BT2-0.05];

set y4BB  [expr $y4-0.5*$dbr3];
set y4BB1 [expr $y4BB+($tfbr3-$tfb13)];
set y4BB2 [expr $y4BB1+$tfb13];
set y4BB3 [expr $y4BB2+0.05];

set y5BT  [expr $y5+0.5*$dbr4];
set y5BT1 [expr $y5BT-($tfbr4-$tfb45)];
set y5BT2 [expr $y5BT1-$tfb45];
set y5BT3 [expr $y5BT2-0.05];

set y5BB  [expr $y5-0.5*$dbr4];
set y5BB1 [expr $y5BB+($tfbr4-$tfb45)];
set y5BB2 [expr $y5BB1+$tfb45];
set y5BB3 [expr $y5BB2+0.05];

# Grid points in y direction for the simulation of the rigid components (5 floor)

set y6BT  [expr $y6+0.5*$dbr5];
set y6BT1 [expr $y6BT-($tfbr5-$tfb45)];
set y6BT2 [expr $y6BT1-$tfb45];
set y6BT3 [expr $y6BT2-0.05];

set y6BB  [expr $y6-0.5*$dbr5];
set y6BB1 [expr $y6BB+($tfbr5-$tfb45)];
set y6BB2 [expr $y6BB1+$tfb45];
set y6BB3 [expr $y6BB2+0.05];

# Define x coordinates for for the beams discretization (reinforcing plates at the supports)

# Floors 1

# RLength stands for reinforcing plate length and the number stands for the floor

set RLength1 1.258;

# bay 1
set xA1 [expr $x11CR+$RLength1];
set xA2 [expr $x12CL-$RLength1];
# bay 2
set xA3 [expr $x12CR+$RLength1];
set xA4 [expr $x13CL-$RLength1];
# bay 3
set xA5 [expr $x13CR+$RLength1];
set xA6 [expr $x14CL-$RLength1];
```

```
# Floor 2
set RLength2 1.461;

# bay 1
set xB1 [expr $x11CR+$RLength2];
set xB2 [expr $x12CL-$RLength2];
# bay 2
set xB3 [expr $x12CR+$RLength2];
set xB4 [expr $x13CL-$RLength2];
# bay 3
set xB5 [expr $x13CR+$RLength2];
set xB6 [expr $x14CL-$RLength2];


# Floor 3

set RLength3 1.311;

# bay 1
set xC1 [expr $x11CR+$RLength3];
set xC2 [expr $x12CL-$RLength3];
# bay 2
set xC3 [expr $x12CR+$RLength3];
set xC4 [expr $x13CL-$RLength3];
# bay 3
set xC5 [expr $x13CR+$RLength3];
set xC6 [expr $x14CL-$RLength3];

# Floor 4

set RLength4 1.073;

# bay 1
set xD1 [expr $x21CR+$RLength4];
set xD2 [expr $x22CL-$RLength4];
# bay 2
set xD3 [expr $x22CR+$RLength4];
set xD4 [expr $x23CL-$RLength4];
# bay 3
set xD5 [expr $x23CR+$RLength4];
set xD6 [expr $x24CL-$RLength4];

# Floor 5

set RLength5 0.724;

# bay 1
set xE1 [expr $x21CR+$RLength5];
set xE2 [expr $x22CL-$RLength5];
# bay 2
set xE3 [expr $x22CR+$RLength5];
set xE4 [expr $x23CL-$RLength5];
# bay 3
set xE5 [expr $x23CR+$RLength5];
set xE6 [expr $x24CL-$RLength5];

# Define nodes coordinates

# Column's nodes

# Col1
node 1  $x1 $y1;
node 2  $x1 $y2BB;
node 3  $x1 $y2BT;
node 4  $x1 $y3BB;
node 5  $x1 $y3BT;
node 6  $x1 $y4BB;
node 7  $x1 $y4BT;
node 8  $x1 $y5BB;
node 9  $x1 $y5BT;
node 10 $x1 $y6BB;
# Col2
node 11 $x2 $y1;
node 12 $x2 $y2BB;
node 13 $x2 $y2BT;
```

```
node 14 $x2 $y3BB;
node 15 $x2 $y3BT;
node 16 $x2 $y4BB;
node 17 $x2 $y4BT;
node 18 $x2 $y5BB;
node 19 $x2 $y5BT;
node 20 $x2 $y6BB;
# Col3
node 21 $x3 $y1;
node 22 $x3 $y2BB;
node 23 $x3 $y2BT;
node 24 $x3 $y3BB;
node 25 $x3 $y3BT;
node 26 $x3 $y4BB;
node 27 $x3 $y4BT;
node 28 $x3 $y5BB;
node 29 $x3 $y5BT;
node 30 $x3 $y6BB;
# Col4
node 31 $x4 $y1;
node 32 $x4 $y2BB;
node 33 $x4 $y2BT;
node 34 $x4 $y3BB;
node 35 $x4 $y3BT;
node 36 $x4 $y4BB;
node 37 $x4 $y4BT;
node 38 $x4 $y5BB;
node 39 $x4 $y5BT;
node 40 $x4 $y6BB;

#beam's nodes

#1st floor
#1st bay
node 41 $x11CR $y2;
node 42 $xA1  $y2;
node 43 $xA2  $y2;
node 44 $x12CL $y2;
#2nd bay
node 45 $x12CR $y2;
node 46 $xA3  $y2;
node 47 $xA4  $y2;
node 48 $x13CL $y2;
#3rd bay
node 49 $x13CR $y2;
node 50 $xA5  $y2;
node 51 $xA6  $y2;
node 52 $x14CL $y2;


#2nd floor
#1st bay
node 53 $x11CR $y3;
node 54 $xB1  $y3;
node 55 $xB2  $y3;
node 56 $x12CL $y3;
#2nd bay
node 57 $x12CR $y3;
node 58 $xB3  $y3;
node 59 $xB4  $y3;
node 60 $x13CL $y3;
#3rd bay
node 61 $x13CR $y3;
node 62 $xB5  $y3;
node 63 $xB6  $y3;
node 64 $x14CL $y3;


#3rd floor
#1st bay
node 65 $x11CR $y4;
node 66 $xC1  $y4;
node 67 $xC2  $y4;
node 68 $x12CL $y4;
#2nd bay
```

```
node 69 $x12CR $y4;
node 70 $xC3  $y4;
node 71 $xC4  $y4;
node 72 $x13CL $y4;
#3rd bay
node 73 $x13CR $y4;
node 74 $xC5  $y4;
node 75 $xC6  $y4;
node 76 $x14CL $y4;


#4rth floor
#1st bay
node 77 $x21CR $y5;
node 78 $xD1  $y5;
node 79 $xD2  $y5;
node 80 $x22CL $y5;
#2nd bay
node 81 $x22CR $y5;
node 82 $xD3  $y5;
node 83 $xD4  $y5;
node 84 $x23CL $y5;
#3rd bay
node 85 $x23CR $y5;
node 86 $xD5  $y5;
node 87 $xD6  $y5;
node 88 $x24CL $y5;

#5th floor
#1st bay
node 89 $x21CR $y6;
node 90 $xE1  $y6;
node 91 $xE2  $y6;
node 92 $x22CL $y6;
#2nd bay
node 93 $x22CR $y6;
node 94 $xE3  $y6;
node 95 $xE4  $y6;
node 96 $x23CL $y6;
#3rd bay
node 97 $x23CR $y6;
node 98 $xE5  $y6;
node 99 $xE6  $y6;
node 100 $x24CL $y6;

# Nodes of Horizontal rigid Panel zones (scissors model) components

#       1st     floor

node    101     $x11CL  $y2;
node    102     $x1     $y2;
node    103     $x11CR  $y2;
node    104     $x12CL  $y2;
node    105     $x2     $y2;
node    106     $x12CR  $y2;
node    107     $x13CL  $y2;
node    108     $x3     $y2;
node    109     $x13CR  $y2;
node    110     $x14CL  $y2;
node    111     $x4     $y2;
node    112     $x14CR  $y2;


#       2nd     floor

node    113     $x11CL  $y3;
node    114     $x1     $y3;
node    115     $x11CR  $y3;
node    116     $x12CL  $y3;
node    117     $x2     $y3;
node    118     $x12CR  $y3;
node    119     $x13CL  $y3;
node    120     $x3     $y3;
node    121     $x13CR  $y3;
node    122     $x14CL  $y3;
```

```
node    123     $x4     $y3;
node    124     $x14CR  $y3;

#       3rd     floor

node    125     $x11CL  $y4;
node    126     $x1     $y4;
node    127     $x11CR  $y4;
node    128     $x12CL  $y4;
node    129     $x2     $y4;
node    130     $x12CR  $y4;
node    131     $x13CL  $y4;
node    132     $x3     $y4;
node    133     $x13CR  $y4;
node    134     $x14CL  $y4;
node    135     $x4     $y4;
node    136     $x14CR  $y4;

#       4rth    floor

node    137     $x21CL  $y5;
node    138     $x1     $y5;
node    139     $x21CR  $y5;
node    140     $x22CL  $y5;
node    141     $x2     $y5;
node    142     $x22CR  $y5;
node    143     $x23CL  $y5;
node    144     $x3     $y5;
node    145     $x23CR  $y5;
node    146     $x24CL  $y5;
node    147     $x4     $y5;
node    148     $x24CR  $y5;

#       5th     floor

node    149     $x21CL  $y6;
node    150     $x1     $y6;
node    151     $x21CR  $y6;
node    152     $x22CL  $y6;
node    153     $x2     $y6;
node    154     $x22CR  $y6;
node    155     $x23CL  $y6;
node    156     $x3     $y6;
node    157     $x23CR  $y6;
node    158     $x24CL  $y6;
node    159     $x4     $y6;
node    160     $x24CR  $y6;

# Nodes of vertical rigid Panel zones (scissors model) components

# 1st floor
node 161 $x1 $y2;
node 162 $x2 $y2;
node 163 $x3 $y2;
node 164 $x4 $y2;

# 2nd floor
node 165 $x1 $y3;
node 166 $x2 $y3;
node 167 $x3 $y3;
node 168 $x4 $y3;


# 3rd floor
node 169 $x1 $y4;
node 170 $x2 $y4;
node 171 $x3 $y4;
node 172 $x4 $y4;


# 4rth floor
```

```
node 173 $x1 $y5;
node 174 $x2 $y5;
node 175 $x3 $y5;
node 176 $x4 $y5;


# 5th floor
node 177 $x1 $y6;
node 178 $x2 $y6;
node 179 $x3 $y6;
node 180 $x4 $y6;

# Nodes for the rigid plates simulating beam column interface

#       x coordinate: x1CR

#       y coordinate: y2

#       Upper part of plate

node    181     $x11CR  $y2BT3;
node    182     $x11CR  $y2BT2;
node    183     $x11CR  $y2BT1;
node    184     $x11CR  $y2BT;

node    185     $x11CR  $y2BT3;
node    186     $x11CR  $y2BT2;
node    187     $x11CR  $y2BT1;
node    188     $x11CR  $y2BT;

#       Bottom part of plate

node    189     $x11CR  $y2BB3;
node    190     $x11CR  $y2BB2;
node    191     $x11CR  $y2BB1;
node    192     $x11CR  $y2BB;

node    193     $x11CR  $y2BB3;
node    194     $x11CR  $y2BB2;
node    195     $x11CR  $y2BB1;
node    196     $x11CR  $y2BB;

#       y coordinate: y3

#       Upper part of plate

node    197     $x11CR  $y3BT3;
node    198     $x11CR  $y3BT2;
node    199     $x11CR  $y3BT1;
node    200     $x11CR  $y3BT;

node    201     $x11CR  $y3BT3;
node    202     $x11CR  $y3BT2;
node    203     $x11CR  $y3BT1;
node    204     $x11CR  $y3BT;

#       Bottom part of plate

node    205     $x11CR  $y3BB3;
node    206     $x11CR  $y3BB2;
node    207     $x11CR  $y3BB1;
node    208     $x11CR  $y3BB;

node    209     $x11CR  $y3BB3;
node    210     $x11CR  $y3BB2;
node    211     $x11CR  $y3BB1;
node    212     $x11CR  $y3BB;

#       y coordinate: y4

#       Upper part of plate

node    213     $x11CR  $y4BT3;
node    214     $x11CR  $y4BT2;
node    215     $x11CR  $y4BT1;
```

```
node    216     $x11CR  $y4BT;

node    217     $x11CR  $y4BT3;
node    218     $x11CR  $y4BT2;
node    219     $x11CR  $y4BT1;
node    220     $x11CR  $y4BT;

#       Bottom part of plate

node    221     $x11CR  $y4BB3;
node    222     $x11CR  $y4BB2;
node    223     $x11CR  $y4BB1;
node    224     $x11CR  $y4BB;

node    225     $x11CR  $y4BB3;
node    226     $x11CR  $y4BB2;
node    227     $x11CR  $y4BB1;
node    228     $x11CR  $y4BB;

#       y: coordinate y5

#       Upper part of plate

node    229     $x21CR  $y5BT3;
node    230     $x21CR  $y5BT2;
node    231     $x21CR  $y5BT1;
node    232     $x21CR  $y5BT;

node    233     $x21CR  $y5BT3;
node    234     $x21CR  $y5BT2;
node    235     $x21CR  $y5BT1;
node    236     $x21CR  $y5BT;

#       Bottom part of plate

node    237     $x21CR  $y5BB3;
node    238     $x21CR  $y5BB2;
node    239     $x21CR  $y5BB1;
node    240     $x21CR  $y5BB;

node    241     $x21CR  $y5BB3;
node    242     $x21CR  $y5BB2;
node    243     $x21CR  $y5BB1;
node    244     $x21CR  $y5BB;

#       y: coordinate y6

#       Upper part of plate

node    245     $x21CR  $y6BT3;
node    246     $x21CR  $y6BT2;
node    247     $x21CR  $y6BT1;
node    248     $x21CR  $y6BT;

node    249     $x21CR  $y6BT3;
node    250     $x21CR  $y6BT2;
node    251     $x21CR  $y6BT1;
node    252     $x21CR  $y6BT;

#       Bottom part of plate

node    253     $x21CR  $y6BB3;
node    254     $x21CR  $y6BB2;
node    255     $x21CR  $y6BB1;
node    256     $x21CR  $y6BB;

node    257     $x21CR  $y6BB3;
node    258     $x21CR  $y6BB2;
node    259     $x21CR  $y6BB1;
node    260     $x21CR  $y6BB;

#       x coordinate: x2CL

#       y coordinate: y2
```

```
#       Upper part of plate

node    261     $x12CL  $y2BT3;
node    262     $x12CL  $y2BT2;
node    263     $x12CL  $y2BT1;
node    264     $x12CL  $y2BT;

node    265     $x12CL  $y2BT3;
node    266     $x12CL  $y2BT2;
node    267     $x12CL  $y2BT1;
node    268     $x12CL  $y2BT;

#       Bottom

node    269     $x12CL  $y2BB3;
node    270     $x12CL  $y2BB2;
node    271     $x12CL  $y2BB1;
node    272     $x12CL  $y2BB;

node    273     $x12CL  $y2BB3;
node    274     $x12CL  $y2BB2;
node    275     $x12CL  $y2BB1;
node    276     $x12CL  $y2BB;

#       y coordinate: y3

#       Upper part of plate

node    277     $x12CL  $y3BT3;
node    278     $x12CL  $y3BT2;
node    279     $x12CL  $y3BT1;
node    280     $x12CL  $y3BT;

node    281     $x12CL  $y3BT3;
node    282     $x12CL  $y3BT2;
node    283     $x12CL  $y3BT1;
node    284     $x12CL  $y3BT;

#       Bottom part of plate

node    285     $x12CL  $y3BB3;
node    286     $x12CL  $y3BB2;
node    287     $x12CL  $y3BB1;
node    288     $x12CL  $y3BB;

node    289     $x12CL  $y3BB3;
node    290     $x12CL  $y3BB2;
node    291     $x12CL  $y3BB1;
node    292     $x12CL  $y3BB;

#       y coordinate: y4

#       Upper part of plate

node    293     $x12CL  $y4BT3;
node    294     $x12CL  $y4BT2;
node    295     $x12CL  $y4BT1;
node    296     $x12CL  $y4BT;

node    297     $x12CL  $y4BT3;
node    298     $x12CL  $y4BT2;
node    299     $x12CL  $y4BT1;
node    300     $x12CL  $y4BT;

#       Bottom part of plate

node    301     $x12CL  $y4BB3;
node    302     $x12CL  $y4BB2;
node    303     $x12CL  $y4BB1;
node    304     $x12CL  $y4BB;

node    305     $x12CL  $y4BB3;
node    306     $x12CL  $y4BB2;
node    307     $x12CL  $y4BB1;
node    308     $x12CL  $y4BB;
```

```
#       y: coordinate y5

#       Upper part of plate

node    309     $x22CL  $y5BT3;
node    310     $x22CL  $y5BT2;
node    311     $x22CL  $y5BT1;
node    312     $x22CL  $y5BT;

node    313     $x22CL  $y5BT3;
node    314     $x22CL  $y5BT2;
node    315     $x22CL  $y5BT1;
node    316     $x22CL  $y5BT;

#       Bottom part of plate

node    317     $x22CL  $y5BB3;
node    318     $x22CL  $y5BB2;
node    319     $x22CL  $y5BB1;
node    320     $x22CL  $y5BB;

node    321     $x22CL  $y5BB3;
node    322     $x22CL  $y5BB2;
node    323     $x22CL  $y5BB1;
node    324     $x22CL  $y5BB;

#       y: coordinate y6

#       Upper part of plate

node    325     $x22CL  $y6BT3;
node    326     $x22CL  $y6BT2;
node    327     $x22CL  $y6BT1;
node    328     $x22CL  $y6BT;

node    329     $x22CL  $y6BT3;
node    330     $x22CL  $y6BT2;
node    331     $x22CL  $y6BT1;
node    332     $x22CL  $y6BT;

#       Bottom part of plate

node    333     $x22CL  $y6BB3;
node    334     $x22CL  $y6BB2;
node    335     $x22CL  $y6BB1;
node    336     $x22CL  $y6BB;

node    337     $x22CL  $y6BB3;
node    338     $x22CL  $y6BB2;
node    339     $x22CL  $y6BB1;
node    340     $x22CL  $y6BB;

#       x coordinate: x2CR

#       y coordinate: y2

#       Upper part of plate

node    341     $x12CR  $y2BT3;
node    342     $x12CR  $y2BT2;
node    343     $x12CR  $y2BT1;
node    344     $x12CR  $y2BT;

node    345     $x12CR  $y2BT3;
node    346     $x12CR  $y2BT2;
node    347     $x12CR  $y2BT1;
node    348     $x12CR  $y2BT;

#       Bottom

node    349     $x12CR  $y2BB3;
node    350     $x12CR  $y2BB2;
node    351     $x12CR  $y2BB1;
node    352     $x12CR  $y2BB;
```

```
node    353     $x12CR  $y2BB3;
node    354     $x12CR  $y2BB2;
node    355     $x12CR  $y2BB1;
node    356     $x12CR  $y2BB;

#       y coordinate: y3

#       Upper part of plate

node    357     $x12CR  $y3BT3;
node    358     $x12CR  $y3BT2;
node    359     $x12CR  $y3BT1;
node    360     $x12CR  $y3BT;

node    361     $x12CR  $y3BT3;
node    362     $x12CR  $y3BT2;
node    363     $x12CR  $y3BT1;
node    364     $x12CR  $y3BT;

#       Bottom part of plate

node    365     $x12CR  $y3BB3;
node    366     $x12CR  $y3BB2;
node    367     $x12CR  $y3BB1;
node    368     $x12CR  $y3BB;

node    369     $x12CR  $y3BB3;
node    370     $x12CR  $y3BB2;
node    371     $x12CR  $y3BB1;
node    372     $x12CR  $y3BB;

#       y coordinate: y4

#       Upper part of plate

node    373     $x12CR  $y4BT3;
node    374     $x12CR  $y4BT2;
node    375     $x12CR  $y4BT1;
node    376     $x12CR  $y4BT;

node    377     $x12CR  $y4BT3;
node    378     $x12CR  $y4BT2;
node    379     $x12CR  $y4BT1;
node    380     $x12CR  $y4BT;

#       Bottom part of plate

node    381     $x12CR  $y4BB3;
node    382     $x12CR  $y4BB2;
node    383     $x12CR  $y4BB1;
node    384     $x12CR  $y4BB;

node    385     $x12CR  $y4BB3;
node    386     $x12CR  $y4BB2;
node    387     $x12CR  $y4BB1;
node    388     $x12CR  $y4BB;

#       y: coordinate y5

#       Upper part of plate

node    389     $x22CR  $y5BT3;
node    390     $x22CR  $y5BT2;
node    391     $x22CR  $y5BT1;
node    392     $x22CR  $y5BT;

node    393     $x22CR  $y5BT3;
node    394     $x22CR  $y5BT2;
node    395     $x22CR  $y5BT1;
node    396     $x22CR  $y5BT;

#       Bottom part of plate

node    397     $x22CR  $y5BB3;
```

```
node    398     $x22CR  $y5BB2;
node    399     $x22CR  $y5BB1;
node    400     $x22CR  $y5BB;

node    401     $x22CR  $y5BB3;
node    402     $x22CR  $y5BB2;
node    403     $x22CR  $y5BB1;
node    404     $x22CR  $y5BB;

#       y: coordinate y6

#       Upper part of plate

node    405     $x22CR  $y6BT3;
node    406     $x22CR  $y6BT2;
node    407     $x22CR  $y6BT1;
node    408     $x22CR  $y6BT;

node    409     $x22CR  $y6BT3;
node    410     $x22CR  $y6BT2;
node    411     $x22CR  $y6BT1;
node    412     $x22CR  $y6BT;

#       Bottom part of plate

node    413     $x22CR  $y6BB3;
node    414     $x22CR  $y6BB2;
node    415     $x22CR  $y6BB1;
node    416     $x22CR  $y6BB;

node    417     $x22CR  $y6BB3;
node    418     $x22CR  $y6BB2;
node    419     $x22CR  $y6BB1;
node    420     $x22CR  $y6BB;

#       x coordinate: x3CL

#       y coordinate: y2

#       Upper part of plate

node    421     $x13CL  $y2BT3;
node    422     $x13CL  $y2BT2;
node    423     $x13CL  $y2BT1;
node    424     $x13CL  $y2BT;

node    425     $x13CL  $y2BT3;
node    426     $x13CL  $y2BT2;
node    427     $x13CL  $y2BT1;
node    428     $x13CL  $y2BT;

#       Bottom part of plate

node    429     $x13CL  $y2BB3;
node    430     $x13CL  $y2BB2;
node    431     $x13CL  $y2BB1;
node    432     $x13CL  $y2BB;

node    433     $x13CL  $y2BB3;
node    434     $x13CL  $y2BB2;
node    435     $x13CL  $y2BB1;
node    436     $x13CL  $y2BB;

#       y coordinate: y3

#       Upper part of plate

node    437     $x13CL  $y3BT3;
node    438     $x13CL  $y3BT2;
node    439     $x13CL  $y3BT1;
node    440     $x13CL  $y3BT;

node    441     $x13CL  $y3BT3;
node    442     $x13CL  $y3BT2;
node    443     $x13CL  $y3BT1;
```

```
node    444     $x13CL  $y3BT;

#       Bottom part of plate

node    445     $x13CL  $y3BB3;
node    446     $x13CL  $y3BB2;
node    447     $x13CL  $y3BB1;
node    448     $x13CL  $y3BB;

node    449     $x13CL  $y3BB3;
node    450     $x13CL  $y3BB2;
node    451     $x13CL  $y3BB1;
node    452     $x13CL  $y3BB;

#       y coordinate: y4

#       Upper part of plate

node    453     $x13CL  $y4BT3;
node    454     $x13CL  $y4BT2;
node    455     $x13CL  $y4BT1;
node    456     $x13CL  $y4BT;

node    457     $x13CL  $y4BT3;
node    458     $x13CL  $y4BT2;
node    459     $x13CL  $y4BT1;
node    460     $x13CL  $y4BT;

#       Bottom part of plate

node    461     $x13CL  $y4BB3;
node    462     $x13CL  $y4BB2;
node    463     $x13CL  $y4BB1;
node    464     $x13CL  $y4BB;

node    465     $x13CL  $y4BB3;
node    466     $x13CL  $y4BB2;
node    467     $x13CL  $y4BB1;
node    468     $x13CL  $y4BB;

#       y: coordinate y5

#       Upper part of plate

node    469     $x23CL  $y5BT3;
node    470     $x23CL  $y5BT2;
node    471     $x23CL  $y5BT1;
node    472     $x23CL  $y5BT;

node    473     $x23CL  $y5BT3;
node    474     $x23CL  $y5BT2;
node    475     $x23CL  $y5BT1;
node    476     $x23CL  $y5BT;

#       Bottom part of plate

node    477     $x23CL  $y5BB3;
node    478     $x23CL  $y5BB2;
node    479     $x23CL  $y5BB1;
node    480     $x23CL  $y5BB;

node    481     $x23CL  $y5BB3;
node    482     $x23CL  $y5BB2;
node    483     $x23CL  $y5BB1;
node    484     $x23CL  $y5BB;

#       y: coordinate y6

#       Upper part of plate

node    485     $x23CL  $y6BT3;
node    486     $x23CL  $y6BT2;
node    487     $x23CL  $y6BT1;
node    488     $x23CL  $y6BT;
```

```
node    489     $x23CL  $y6BT3;
node    490     $x23CL  $y6BT2;
node    491     $x23CL  $y6BT1;
node    492     $x23CL  $y6BT;

#       Bottom part of plate

node    493     $x23CL  $y6BB3;
node    494     $x23CL  $y6BB2;
node    495     $x23CL  $y6BB1;
node    496     $x23CL  $y6BB;

node    497     $x23CL  $y6BB3;
node    498     $x23CL  $y6BB2;
node    499     $x23CL  $y6BB1;
node    500     $x23CL  $y6BB;

#       x coordinate: x3CR

#       y coordinate: y2

#       Upper part of plate

node    501     $x13CR  $y2BT3;
node    502     $x13CR  $y2BT2;
node    503     $x13CR  $y2BT1;
node    504     $x13CR  $y2BT;

node    505     $x13CR  $y2BT3;
node    506     $x13CR  $y2BT2;
node    507     $x13CR  $y2BT1;
node    508     $x13CR  $y2BT;

#       Bottom part of plate

node    509     $x13CR  $y2BB3;
node    510     $x13CR  $y2BB2;
node    511     $x13CR  $y2BB1;
node    512     $x13CR  $y2BB;

node    513     $x13CR  $y2BB3;
node    514     $x13CR  $y2BB2;
node    515     $x13CR  $y2BB1;
node    516     $x13CR  $y2BB;

#       y coordinate: y3

#       Upper part of plate

node    517     $x13CR  $y3BT3;
node    518     $x13CR  $y3BT2;
node    519     $x13CR  $y3BT1;
node    520     $x13CR  $y3BT;

node    521     $x13CR  $y3BT3;
node    522     $x13CR  $y3BT2;
node    523     $x13CR  $y3BT1;
node    524     $x13CR  $y3BT;

#       Bottom part of plate

node    525     $x13CR  $y3BB3;
node    526     $x13CR  $y3BB2;
node    527     $x13CR  $y3BB1;
node    528     $x13CR  $y3BB;

node    529     $x13CR  $y3BB3;
node    530     $x13CR  $y3BB2;
node    531     $x13CR  $y3BB1;
node    532     $x13CR  $y3BB;

#       y coordinate: y4

#       Upper part of plate
```

```
node    533     $x13CR  $y4BT3;
node    534     $x13CR  $y4BT2;
node    535     $x13CR  $y4BT1;
node    536     $x13CR  $y4BT;

node    537     $x13CR  $y4BT3;
node    538     $x13CR  $y4BT2;
node    539     $x13CR  $y4BT1;
node    540     $x13CR  $y4BT;

#       Bottom part of plate

node    541     $x13CR  $y4BB3;
node    542     $x13CR  $y4BB2;
node    543     $x13CR  $y4BB1;
node    544     $x13CR  $y4BB;

node    545     $x13CR  $y4BB3;
node    546     $x13CR  $y4BB2;
node    547     $x13CR  $y4BB1;
node    548     $x13CR  $y4BB;

#       y: coordinate y5

#       Upper part of plate

node    549     $x23CR  $y5BT3;
node    550     $x23CR  $y5BT2;
node    551     $x23CR  $y5BT1;
node    552     $x23CR  $y5BT;

node    553     $x23CR  $y5BT3;
node    554     $x23CR  $y5BT2;
node    555     $x23CR  $y5BT1;
node    556     $x23CR  $y5BT;

#       Bottom part of plate

node    557     $x23CR  $y5BB3;
node    558     $x23CR  $y5BB2;
node    559     $x23CR  $y5BB1;
node    560     $x23CR  $y5BB;

node    561     $x23CR  $y5BB3;
node    562     $x23CR  $y5BB2;
node    563     $x23CR  $y5BB1;
node    564     $x23CR  $y5BB;

#       y: coordinate y6

#       Upper part of plate

node    565     $x23CR  $y6BT3;
node    566     $x23CR  $y6BT2;
node    567     $x23CR  $y6BT1;
node    568     $x23CR  $y6BT;

node    569     $x23CR  $y6BT3;
node    570     $x23CR  $y6BT2;
node    571     $x23CR  $y6BT1;
node    572     $x23CR  $y6BT;

#       Bottom part of plate

node    573     $x23CR  $y6BB3;
node    574     $x23CR  $y6BB2;
node    575     $x23CR  $y6BB1;
node    576     $x23CR  $y6BB;

node    577     $x23CR  $y6BB3;
node    578     $x23CR  $y6BB2;
node    579     $x23CR  $y6BB1;
node    580     $x23CR  $y6BB;

#       x coordinate: x4CL
```

```
#       y coordinate: y2

#       Upper part of plate

node    581     $x14CL    $y2BT3;
node    582     $x14CL    $y2BT2;
node    583     $x14CL    $y2BT1;
node    584     $x14CL    $y2BT;

node    585     $x14CL    $y2BT3;
node    586     $x14CL    $y2BT2;
node    587     $x14CL    $y2BT1;
node    588     $x14CL    $y2BT;

#       Bottom part of plate

node    589     $x14CL    $y2BB3;
node    590     $x14CL    $y2BB2;
node    591     $x14CL    $y2BB1;
node    592     $x14CL    $y2BB;

node    593     $x14CL    $y2BB3;
node    594     $x14CL    $y2BB2;
node    595     $x14CL    $y2BB1;
node    596     $x14CL    $y2BB;

#       y coordinate: y3

#       Upper part of plate

node    597     $x14CL    $y3BT3;
node    598     $x14CL    $y3BT2;
node    599     $x14CL    $y3BT1;
node    600     $x14CL    $y3BT;

node    601     $x14CL    $y3BT3;
node    602     $x14CL    $y3BT2;
node    603     $x14CL    $y3BT1;
node    604     $x14CL    $y3BT;

#       Bottom part of plate

node    605     $x14CL    $y3BB3;
node    606     $x14CL    $y3BB2;
node    607     $x14CL    $y3BB1;
node    608     $x14CL    $y3BB;

node    609     $x14CL    $y3BB3;
node    610     $x14CL    $y3BB2;
node    611     $x14CL    $y3BB1;
node    612     $x14CL    $y3BB;

#       y coordinate: y4

#       Upper part of plate

node    613     $x14CL    $y4BT3;
node    614     $x14CL    $y4BT2;
node    615     $x14CL    $y4BT1;
node    616     $x14CL    $y4BT;

node    617     $x14CL    $y4BT3;
node    618     $x14CL    $y4BT2;
node    619     $x14CL    $y4BT1;
node    620     $x14CL    $y4BT;

#       Bottom part of plate

node    621     $x14CL    $y4BB3;
node    622     $x14CL    $y4BB2;
node    623     $x14CL    $y4BB1;
node    624     $x14CL    $y4BB;

node    625     $x14CL    $y4BB3;
```

```
node    626     $x14CL  $y4BB2;
node    627     $x14CL  $y4BB1;
node    628     $x14CL  $y4BB;

#       y: coordinate y5

#       Upper part of plate

node    629     $x24CL  $y5BT3;
node    630     $x24CL  $y5BT2;
node    631     $x24CL  $y5BT1;
node    632     $x24CL  $y5BT;

node    633     $x24CL  $y5BT3;
node    634     $x24CL  $y5BT2;
node    635     $x24CL  $y5BT1;
node    636     $x24CL  $y5BT;

#       Bottom part of plate

node    637     $x24CL  $y5BB3;
node    638     $x24CL  $y5BB2;
node    639     $x24CL  $y5BB1;
node    640     $x24CL  $y5BB;

node    641     $x24CL  $y5BB3;
node    642     $x24CL  $y5BB2;
node    643     $x24CL  $y5BB1;
node    644     $x24CL  $y5BB;

#       y: coordinate y6

#       Upper part of plate

node    645     $x24CL  $y6BT3;
node    646     $x24CL  $y6BT2;
node    647     $x24CL  $y6BT1;
node    648     $x24CL  $y6BT;

node    649     $x24CL  $y6BT3;
node    650     $x24CL  $y6BT2;
node    651     $x24CL  $y6BT1;
node    652     $x24CL  $y6BT;

#       Bottom part of plate

node    653     $x24CL  $y6BB3;
node    654     $x24CL  $y6BB2;
node    655     $x24CL  $y6BB1;
node    656     $x24CL  $y6BB;

node    657     $x24CL  $y6BB3;
node    658     $x24CL  $y6BB2;
node    659     $x24CL  $y6BB1;
node    660     $x24CL  $y6BB;


# Nodes of Lean on columns

node 661 $xL1 $y1;
node 662 $xL1 $y2;
node 663 $xL1 $y3;
node 664 $xL1 $y4;
node 665 $xL1 $y5;
node 666 $xL1 $y6;

node 667 $xL2 $y1;
node 668 $xL2 $y2;
node 669 $xL2 $y3;
node 670 $xL2 $y4;
node 671 $xL2 $y5;
node 672 $xL2 $y6;

node 673 $xL3 $y1;
node 674 $xL3 $y2;
```

```
node 675 $xL3 $y3;
node 676 $xL3 $y4;
node 677 $xL3 $y5;
node 678 $xL3 $y6;

# Additional nodes for flexural deterioration rotational springs (Lignos and Krawinkler 2007) definition

node 684 $xA1  $y2;
node 685 $xA2  $y2;
node 686 $xA3  $y2;
node 687 $xA4  $y2;
node 688 $xA5  $y2;
node 689 $xA6  $y2;
node 690 $xB1  $y3;
node 691 $xB2  $y3;
node 692 $xB3  $y3;
node 693 $xB4  $y3;
node 694 $xB5  $y3;
node 695 $xB6  $y3;
node 696 $xC1  $y4;
node 697 $xC2  $y4;
node 698 $xC3  $y4;
node 699 $xC4  $y4;
node 700 $xC5  $y4;
node 701 $xC6  $y4;
node 702 $xD1  $y5;
node 703 $xD2  $y5;
node 704 $xD3  $y5;
node 705 $xD4  $y5;
node 706 $xD5  $y5;
node 707 $xD6  $y5;
node 708 $xE1  $y6;
node 709 $xE2  $y6;
node 710 $xE3  $y6;
node 711 $xE4  $y6;
node 712 $xE5  $y6;
node 713 $xE6  $y6;

# Restrains (Boundary conditions)

fix 1  1 1 1;
fix 11 1 1 1;
fix 21 1 1 1;
fix 31 1 1 1;

fix 661 1 1 0;
fix 667 1 1 0;
fix 673 1 1 0;

fix 679 0 1 1;
fix 680 0 1 1;
fix 681 0 1 1;
fix 682 0 1 1;
fix 683 0 1 1;

# Constrains (Nodes with equal degrees of freedom)

# For the panel zones (scissors model), where the rotational springs are located (constrained in vertical and horizontal direction)

equalDOF        102     161     1 2 ;
equalDOF        105     162     1 2 ;
equalDOF        108     163     1 2 ;
equalDOF        111     164     1 2 ;
equalDOF        114     165     1 2 ;
equalDOF        117     166     1 2 ;
equalDOF        120     167     1 2 ;
equalDOF        123     168     1 2 ;
equalDOF        126     169     1 2 ;
equalDOF        129     170     1 2 ;
equalDOF        132     171     1 2 ;
equalDOF        135     172     1 2 ;
equalDOF        138     173     1 2 ;
equalDOF        141     174     1 2 ;
equalDOF        144     175     1 2 ;
equalDOF        147     176     1 2 ;
```

```
equalDOF        150     177     1 2 ;
equalDOF        153     178     1 2 ;
equalDOF        156     179     1 2 ;
equalDOF        159     180     1 2 ;
```

For the nodes between the beam and the panel zones (constraint in vertical direction)

1st bay

```
equalDOF        151     89      2;
equalDOF        152     92      2;
equalDOF        139     77      2;
equalDOF        140     80      2;
equalDOF        127     65      2;
equalDOF        128     68      2;
equalDOF        115     53      2;
equalDOF        116     56      2;
equalDOF        103     41      2;
equalDOF        104     44      2;
```

2nd bay

```
equalDOF        154     93      2;
equalDOF        155     96      2;
equalDOF        142     81      2;
equalDOF        143     84      2;
equalDOF        130     69      2;
equalDOF        131     72      2;
equalDOF        118     57      2;
equalDOF        119     60      2;
equalDOF        106     45      2;
equalDOF        107     48      2;
```

3rd bay

```
equalDOF        157     97      2;
equalDOF        158     100     2;
equalDOF        145     85      2;
equalDOF        146     88      2;
equalDOF        133     73      2;
equalDOF        134     76      2;
equalDOF        121     61      2;
equalDOF        122     64      2;
equalDOF        109     49      2;
equalDOF        110     52      2;
```

For the nodes between the reinfored and unreinforced parts of the beams, where the rotational springs of (Lignos and Krawinkler 2007) are located

```
equalDOF        42      684     1       2 ;
equalDOF        685     43      1       2 ;
equalDOF        46      686     1       2 ;
equalDOF        687     47      1       2 ;
equalDOF        50      688     1       2 ;
equalDOF        689     51      1       2 ;
equalDOF        54      690     1       2 ;
equalDOF        691     55      1       2 ;
equalDOF        58      692     1       2 ;
equalDOF        693     59      1       2 ;
equalDOF        62      694     1       2 ;
equalDOF        695     63      1       2 ;
equalDOF        66      696     1       2 ;
equalDOF        697     67      1       2 ;
equalDOF        70      698     1       2 ;
equalDOF        699     71      1       2 ;
equalDOF        74      700     1       2 ;
equalDOF        701     75      1       2 ;
equalDOF        78      702     1       2 ;
equalDOF        703     79      1       2 ;
equalDOF        82      704     1       2 ;
equalDOF        705     83      1       2 ;
equalDOF        86      706     1       2 ;
equalDOF        707     87      1       2 ;
equalDOF        90      708     1       2 ;
```

```
equalDOF        709     91      1       2 ;
equalDOF        94      710     1       2 ;
equalDOF        711     95      1       2 ;
equalDOF        98      712     1       2 ;
equalDOF        713     99      1       2 ;


# Materials IDs

# Steel hysteresis S275, S235

set S275 1;
set S355 2;

# Rigid hysteresis

set Srigid 3;


# Shear on columns material

set shearc1 20;
set shearc2 21;

# contact translational sptings materials

set ctTag1 22;
set ctTag2 23;
set ctTag3 24;
set ctTag4 25;
set ctTag5 26;

# PT bars trusses materials

set PT1 27;
set PT2 28;
set PT3 29;
set PT4 30;
set PT5 31;
set PTm 32;

# Panel zones rotational springs materials

set Spanel1  33;
set Sflange1 34;

set Spanel2  35;
set Sflange2 36;

set Spanel3  37;
set Sflange3 38;

set Spanel4  39;
set Sflange4 40;

set Spanel5 41;
set Sflange5 42;

# WHPs translational springs materials

set whpTag1 43;
set whpTag2 44;
set whpTag3 45;
set whpTag4 46;
set whpTag5 47;

# Diaphragm truss materias

set Diaph 59;

# deterioration (Lignos and Krawinkler 2007) translational springs materials

set lignos1 60;
set lignos2 61;
set lignos3 62;
```

```
set lignos4 63;
set lignos5 64;

# Materials properties

# Frame members' hysteretic behaviour

set E0       2.1e+08;
set nu       0.3;
set G        [expr $E0/(2.+2.*$nu)];
set FyS275   275000.0;
set FyS355   355000.0;
set p        0.002;

# Define S275 materials
uniaxialMaterial Steel01 $S275 $FyS275 $E0 $p  ;
uniaxialMaterial Steel01 $S355 $FyS355 $E0 $p  ;

# Rigid members hysteretic behaviour (elastic material with high modulus of elasticity x 1000)

uniaxial Material Elastic $Srigid [expr 1000*$E0];

# CONTACT translational spring behaviour

#define properties of the contact elements

set E1 [expr (20*$E0*0.0112)/8.0]; # compression stiffness 20 x Ebeam x Abeam (IPE450) / Lbeam (Christopoulos et al 2009)
set E2 [expr (20*$E0*0.0129)/8.0];
set E3 [expr (20*$E0*0.0112)/8.0];
set E4 [expr (20*$E0*0.009504)/8.0];
set E5 [expr (20*$E0*0.009504)/8.0];

# Define force-deformation relationship for CT spring (material)

uniaxialMaterial ENT $ctTag1 $E1
uniaxialMaterial ENT $ctTag2 $E2
uniaxialMaterial ENT $ctTag3 $E3
uniaxialMaterial ENT $ctTag4 $E4
uniaxialMaterial ENT $ctTag5 $E5

# PT bars hysteretic behaviour

uniaxialMaterial Steel01 $PTm 850000 2.1e+08 0.002 ;

# Insert initial strain to apply post tensioning

uniaxialMaterial InitStrainMaterial $PT1 $PTm [expr (1.14*1086.93/(2*3.14*0.043*0.043/4))/(2.1e+08)];
uniaxialMaterial InitStrainMaterial $PT2 $PTm [expr (1.195*1255.54/(2*3.14*0.050*0.050/4))/(2.1e+08)];
uniaxialMaterial InitStrainMaterial $PT3 $PTm [expr (1.17*1086.93/(2*3.14*0.043*0.043/4))/(2.1e+08)];
uniaxialMaterial InitStrainMaterial $PT4 $PTm [expr (1.155*941.226/(2*3.14*0.037*0.037/4))/(2.1e+08)];
uniaxialMaterial InitStrainMaterial $PT5 $PTm [expr (1.15*941.226/(2*3.14*0.035*0.035/4))/(2.1e+08)];

# Panel zones rotational springs' hysteretic behaviour

# spring behaviour due to panel

uniaxialMaterial Steel01 $Spanel1   3966.649016    1924876.259    [expr 0.001/1924876.259];
uniaxialMaterial Steel01 $Spanel2   4635.338218    2411541.372    [expr 0.001/2411541.372];
uniaxialMaterial Steel01 $Spanel3   4154.315573    2111320.843    [expr 0.001/2111320.843];
uniaxialMaterial Steel01 $Spanel4   3253.374804    1603475.660    [expr 0.001/1603475.660];
uniaxialMaterial Steel01 $Spanel5   3246.781017    1596982.548    [expr 0.001/1596982.548];

# spring behaviour due to flange

uniaxialMaterial Steel01 $Sflange1 235.7535272 28600.73867  [expr 0.001/28600.73867];
uniaxialMaterial Steel01 $Sflange2 252.7507460 32873.48474  [expr 0.001/32873.48474];
uniaxialMaterial Steel01 $Sflange3 246.9072877 31371.02210  [expr 0.001/31371.02210];
uniaxialMaterial Steel01 $Sflange4 224.2469537 27630.88745  [expr 0.001/27630.88745];
uniaxialMaterial Steel01 $Sflange5 223.7924605 27518.99897  [expr 0.001/27518.99897];

# WHPs translational spring hysteretic behaviour

set factor1 1.0;

set Fy1 [expr $factor1*355.89]; #yield strength
```

```
set Fy2 [expr $factor1*435.69];
set Fy3 [expr $factor1*381.30];
set Fy4 [expr $factor1*308.50];
set Fy5 [expr $factor1*265.52];

set factor2 0.3;

set E01 [expr 2*1041.19*1000]; #initial elastic tangent multipliedx1000 (kN,m) and x 0.6 due to calibration purposes
set E02 [expr 2*1305.74*1000];
set E03 [expr 2*930.670*1000];
set E04 [expr 2*855.470*1000];
set E05 [expr 2*716.270*1000];

set b 0.01; #strain-hardening ratio (ratio between post-yield tangent and initial elastic tangent)

#parameters to control the transition from elastic to plastic branches.

#The following values have been extracted from callibration process

set R0 30;
set CR1 0.925;
set CR2 0.15;
set a1 0.025;
set a2 2.5;
set a3 0;
set a4 1;

uniaxialMaterial Steel02 $whpTag1 $Fy1 $E01 $b $R0 $CR1 $CR2 $a1 $a2 $a3 $a4;
uniaxialMaterial Steel02 $whpTag2 $Fy2 $E02 $b $R0 $CR1 $CR2 $a1 $a2 $a3 $a4;
uniaxialMaterial Steel02 $whpTag3 $Fy3 $E03 $b $R0 $CR1 $CR2 $a1 $a2 $a3 $a4;
uniaxialMaterial Steel02 $whpTag4 $Fy4 $E04 $b $R0 $CR1 $CR2 $a1 $a2 $a3 $a4;
uniaxialMaterial Steel02 $whpTag5 $Fy5 $E05 $b $R0 $CR1 $CR2 $a1 $a2 $a3 $a4;

# Deterioarion (Lignos and Krawinkler 2007) rotational springs

uniaxialMaterial Bilin $lignos1 1833855.192 0.001376415 0.001376415 716.0645075
-716.0645075 1.079674696 1.079674696 1.079674696 1.079674696 1
1 1 1 0.028368595 0.028368595 0.167493363 0.167493363
0.4 0.4 0.3 0.3 1 1 ;
uniaxialMaterial Bilin $lignos2 2764800.813 0.00146471 0.00146471 1021.24 -
1021.24 1.102081185 1.102081185 1.102081185 1.102081185 1 1 1
1 0.025218094 0.025218094 0.16975396 0.16975396 0.4 0.4
0.3 0.3 1 1 ;
uniaxialMaterial Bilin $lignos3 1874969.543 0.001356419 0.001356419 716.0645075
-716.0645075 1.079674696 1.079674696 1.079674696 1.079674696 1
1 1 1 0.028155543 0.028155543 0.167493363 0.167493363
0.4 0.4 0.3 0.3 1 1 ;
uniaxialMaterial Bilin $lignos4 1219015.226 0.001429396 0.001429396 563.2996023
-563.2996023 1.082365181 1.082365181 1.082365181 1.082365181 1
1 1 1 0.032327923 0.032327923 0.169993268 0.169993268
0.4 0.4 0.3 0.3 1 1 ;
uniaxialMaterial Bilin $lignos5 1076059.476 0.001552053 0.001552053 563.2996023
-563.2996023 1.082365181 1.082365181 1.082365181 1.082365181 1
1 1 1 0.033728465 0.033728465 0.169993268 0.169993268
0.4 0.4 0.3 0.3 1 1 ;

# Diaphragm trusses material

uniaxialMaterial Elastic $Diaph $E0;

# Define Elements

# Define section IDs

set IPE500R1V 114 ;
set IPE500R3V 116 ;
set IPE550R2V 120 ;
set IPE450R4V 124 ;
set IPE450R5V 126 ;

set HEB500 127 ;
set HEB500V 128 ;
set HEB450 129 ;
set HEB450V 130 ;
```

```
# Define transformation IDs

set    PDTrans  1;
set    LNTrans  2;

# Define transformation

geomTransf PDelta $PDTrans;
geomTransf Linear $LNTrans;

# Include subroutine for WF sections

source WFSection.tcl

# Define Sections for reinforced lengths of beams

WFSection $IPE500R1V  $S275 $dbr1 $twbr1 $bfbr1 $tfbr1 8 4;
WFSection $IPE500R3V  $S275 $dbr3 $twbr3 $bfbr3 $tfbr3 8 4;
WFSection $IPE550R2V  $S275 $dbr2 $twbr2 $bfbr2 $tfbr2 8 4;
WFSection $IPE450R4V  $S275 $dbr4 $twbr4 $bfbr4 $tfbr4 8 4;
WFSection $IPE450R5V  $S275 $dbr5 $twbr5 $bfbr5 $tfbr5 8 4;

# Define Sections for columns

uniaxialMaterial Elastic $shearc1 [expr $G*$Asc1];
WFSection $HEB500 $S355 $dc1 $twc1 $bfc1 $tfc1 8 4;
section Aggregator $HEB500V $shearc1 Vy -section $HEB500;

uniaxialMaterial Elastic $shearc2 [expr $G*$Asc2];
WFSection $HEB450 $S355 $dc2 $twc2 $bfc2 $tfc2 8 4;
section Aggregator $HEB450V $shearc2 Vy -section $HEB450;

# Define number of integration points

set nI6 6;

# column's elements

# col1
element nonlinearBeamColumn     1     1 2     $nI6    $HEB500V     $PDTrans;
element nonlinearBeamColumn     2     3 4     $nI6    $HEB500V     $PDTrans;
element nonlinearBeamColumn     3     5 6     $nI6    $HEB500V     $PDTrans;
element nonlinearBeamColumn     4     7 8     $nI6    $HEB450V     $PDTrans;
element nonlinearBeamColumn     5     9 10     $nI6    $HEB450V     $PDTrans;

# col2
element nonlinearBeamColumn     6     11 12    $nI6    $HEB500V     $PDTrans;
element nonlinearBeamColumn     7     13 14    $nI6    $HEB500V     $PDTrans;
element nonlinearBeamColumn     8     15 16    $nI6    $HEB500V     $PDTrans;
element nonlinearBeamColumn     9     17 18    $nI6    $HEB450V     $PDTrans;
element nonlinearBeamColumn     10     19 20    $nI6    $HEB450V     $PDTrans;

# col3
element nonlinearBeamColumn     11     21 22    $nI6    $HEB500V     $PDTrans;
element nonlinearBeamColumn     12     23 24    $nI6    $HEB500V     $PDTrans;
element nonlinearBeamColumn     13     25 26    $nI6    $HEB500V     $PDTrans;
element nonlinearBeamColumn     14     27 28    $nI6    $HEB450V     $PDTrans;
element nonlinearBeamColumn     15     29 30    $nI6    $HEB450V     $PDTrans;

# col4
element nonlinearBeamColumn     16     31 32    $nI6    $HEB500V     $PDTrans;
element nonlinearBeamColumn     17     33 34    $nI6    $HEB500V     $PDTrans;
element nonlinearBeamColumn     18     35 36    $nI6    $HEB500V     $PDTrans;
element nonlinearBeamColumn     19     37 38    $nI6    $HEB450V     $PDTrans;
element nonlinearBeamColumn     20     39 40    $nI6    $HEB450V     $PDTrans;


# Beams elements

#          1st          floor          beams

element  nonlinearBeamColumn          21          41          42          $nI6          $IPE500R1V          $PDTrans;
element  elasticBeamColumn   22          684          685          0.0129          $E0          0.00070356          $PDTrans;
element  nonlinearBeamColumn          23          43          44          $nI6          $IPE500R1V          $PDTrans;
```

```
element nonlinearBeamColumn 24 45 46 $nI6 $IPE500R1V $PDTrans;
element elasticBeamColumn 25 686 687 0.0129 $E0 0.00070356 $PDTrans;
element nonlinearBeamColumn 26 47 48 $nI6 $IPE500R1V $PDTrans;

element nonlinearBeamColumn 27 49 50 $nI6 $IPE500R1V $PDTrans;
element elasticBeamColumn 28 688 689 0.0129 $E0 0.00070356 $PDTrans;
element nonlinearBeamColumn 29 51 52 $nI6 $IPE500R1V $PDTrans;

# 2nd floor beams

element nonlinearBeamColumn 30 53 54 $nI6 $IPE550R2V $PDTrans;
element elasticBeamColumn 31 690 691 0.0151 $E0 0.00097163 $PDTrans;
element nonlinearBeamColumn 32 55 56 $nI6 $IPE550R2V $PDTrans;

element nonlinearBeamColumn 33 57 58 $nI6 $IPE550R2V $PDTrans;
element elasticBeamColumn 34 692 693 0.0151 $E0 0.00097163 $PDTrans;
element nonlinearBeamColumn 35 59 60 $nI6 $IPE550R2V $PDTrans;

element nonlinearBeamColumn 36 61 62 $nI6 $IPE550R2V $PDTrans;
element elasticBeamColumn 37 694 695 0.0151 $E0 0.00097163 $PDTrans;
element nonlinearBeamColumn 38 63 64 $nI6 $IPE550R2V $PDTrans;

# 3rd floor beams

element nonlinearBeamColumn 39 65 66 $nI6 $IPE500R3V $PDTrans;
element elasticBeamColumn 40 696 697 0.0129 $E0 0.00070356 $PDTrans;
element nonlinearBeamColumn 41 67 68 $nI6 $IPE500R3V $PDTrans;

element nonlinearBeamColumn 42 69 70 $nI6 $IPE500R3V $PDTrans;
element elasticBeamColumn 43 698 699 0.0129 $E0 0.00070356 $PDTrans;
element nonlinearBeamColumn 44 71 72 $nI6 $IPE500R3V $PDTrans;

element nonlinearBeamColumn 45 73 74 $nI6 $IPE500R3V $PDTrans;
element elasticBeamColumn 46 700 701 0.0129 $E0 0.00070356 $PDTrans;
element nonlinearBeamColumn 47 75 76 $nI6 $IPE500R3V $PDTrans;

# 4rth floor beams

element nonlinearBeamColumn 48 77 78 $nI6 $IPE450R4V $PDTrans;
element elasticBeamColumn 49 702 703 0.0112 $E0 0.00050831 $PDTrans;
element nonlinearBeamColumn 50 79 80 $nI6 $IPE450R4V $PDTrans;

element nonlinearBeamColumn 51 81 82 $nI6 $IPE450R4V $PDTrans;
element elasticBeamColumn 52 704 705 0.0112 $E0 0.00050831 $PDTrans;
element nonlinearBeamColumn 53 83 84 $nI6 $IPE450R4V $PDTrans;

element nonlinearBeamColumn 54 85 86 $nI6 $IPE450R4V $PDTrans;
element elasticBeamColumn 55 706 707 0.0112 $E0 0.00050831 $PDTrans;
element nonlinearBeamColumn 56 87 88 $nI6 $IPE450R4V $PDTrans;

# 5th floor beams

element nonlinearBeamColumn 57 89 90 $nI6 $IPE450R5V $PDTrans;
element elasticBeamColumn 58 708 709 0.0112 $E0 0.00050831 $PDTrans;
element nonlinearBeamColumn 59 91 92 $nI6 $IPE450R5V $PDTrans;

element nonlinearBeamColumn 60 93 94 $nI6 $IPE450R5V $PDTrans;
element elasticBeamColumn 61 710 711 0.0112 $E0 0.00050831 $PDTrans;
element nonlinearBeamColumn 62 95 96 $nI6 $IPE450R5V $PDTrans;

element nonlinearBeamColumn 63 97 98 $nI6 $IPE450R5V $PDTrans;
element elasticBeamColumn 64 712 713 0.0112 $E0 0.00050831 $PDTrans;
element nonlinearBeamColumn 65 99 100 $nI6 $IPE450R5V $PDTrans;

# Define rigid elements

set HEB450rigid 321;

# DEfine rigid sections
```

WFSection $HEB450rigid $Srigid $dc2 $twc2 $bfc2 $tfc2 8 4;

Define vertical panel zones elements

element elasticBeamColumn 66 2 161 0.0218 2.10E+11 7.99E-04 $LNTrans;
element elasticBeamColumn 67 161 3 0.0218 2.10E+11 7.99E-04 $LNTrans;
element elasticBeamColumn 68 4 165 0.0218 2.10E+11 7.99E-04 $LNTrans;
element elasticBeamColumn 69 165 5 0.0218 2.10E+11 7.99E-04 $LNTrans;
element elasticBeamColumn 70 6 169 0.0218 2.10E+11 7.99E-04 $LNTrans;
element elasticBeamColumn 71 169 7 0.0218 2.10E+11 7.99E-04 $LNTrans;
element elasticBeamColumn 72 8 173 0.0218 2.10E+11 7.99E-04 $LNTrans;
element elasticBeamColumn 73 173 9 0.0218 2.10E+11 7.99E-04 $LNTrans;
element elasticBeamColumn 74 10 177 0.0218 2.10E+11 7.99E-04 $LNTrans;

element elasticBeamColumn 75 12 162 0.0218 2.10E+11 7.99E-04 $LNTrans;
element elasticBeamColumn 76 162 13 0.0218 2.10E+11 7.99E-04 $LNTrans;
element elasticBeamColumn 77 14 166 0.0218 2.10E+11 7.99E-04 $LNTrans;
element elasticBeamColumn 78 166 15 0.0218 2.10E+11 7.99E-04 $LNTrans;
element elasticBeamColumn 79 16 170 0.0218 2.10E+11 7.99E-04 $LNTrans;
element elasticBeamColumn 80 170 17 0.0218 2.10E+11 7.99E-04 $LNTrans;
element elasticBeamColumn 81 18 174 0.0218 2.10E+11 7.99E-04 $LNTrans;
element elasticBeamColumn 82 174 19 0.0218 2.10E+11 7.99E-04 $LNTrans;
element elasticBeamColumn 83 20 178 0.0218 2.10E+11 7.99E-04 $LNTrans;

element elasticBeamColumn 84 22 163 0.0218 2.10E+11 7.99E-04 $LNTrans;
element elasticBeamColumn 85 163 23 0.0218 2.10E+11 7.99E-04 $LNTrans;
element elasticBeamColumn 86 24 167 0.0218 2.10E+11 7.99E-04 $LNTrans;
element elasticBeamColumn 87 167 25 0.0218 2.10E+11 7.99E-04 $LNTrans;
element elasticBeamColumn 88 26 171 0.0218 2.10E+11 7.99E-04 $LNTrans;
element elasticBeamColumn 89 171 27 0.0218 2.10E+11 7.99E-04 $LNTrans;
element elasticBeamColumn 90 28 175 0.0218 2.10E+11 7.99E-04 $LNTrans;
element elasticBeamColumn 91 175 29 0.0218 2.10E+11 7.99E-04 $LNTrans;
element elasticBeamColumn 92 30 179 0.0218 2.10E+11 7.99E-04 $LNTrans;

element elasticBeamColumn 93 32 164 0.0218 2.10E+11 7.99E-04 $LNTrans;
element elasticBeamColumn 94 164 33 0.0218 2.10E+11 7.99E-04 $LNTrans;
element elasticBeamColumn 95 34 168 0.0218 2.10E+11 7.99E-04 $LNTrans;
element elasticBeamColumn 96 168 35 0.0218 2.10E+11 7.99E-04 $LNTrans;
element elasticBeamColumn 97 36 172 0.0218 2.10E+11 7.99E-04 $LNTrans;
element elasticBeamColumn 98 172 37 0.0218 2.10E+11 7.99E-04 $LNTrans;
element elasticBeamColumn 99 38 176 0.0218 2.10E+11 7.99E-04 $LNTrans;
element elasticBeamColumn 100 176 39 0.0218 2.10E+11 7.99E-04 $LNTrans;
element elasticBeamColumn 101 40 180 0.0218 2.10E+11 7.99E-04 $LNTrans;

Define horizontal panel zones elements

1st floor
element elasticBeamColumn 102 101 102 0.0218 2.10E+11 7.99E-04 $LNTrans;
element elasticBeamColumn 103 102 103 0.0218 2.10E+11 7.99E-04 $LNTrans;
element elasticBeamColumn 104 104 105 0.0218 2.10E+11 7.99E-04 $LNTrans;
element elasticBeamColumn 105 105 106 0.0218 2.10E+11 7.99E-04 $LNTrans;
element elasticBeamColumn 106 107 108 0.0218 2.10E+11 7.99E-04 $LNTrans;
element elasticBeamColumn 107 108 109 0.0218 2.10E+11 7.99E-04 $LNTrans;
element elasticBeamColumn 108 110 111 0.0218 2.10E+11 7.99E-04 $LNTrans;
element elasticBeamColumn 109 111 112 0.0218 2.10E+11 7.99E-04 $LNTrans;

2nd floor
element elasticBeamColumn 110 113 114 0.0218 2.10E+11 7.99E-04 $LNTrans;
element elasticBeamColumn 111 114 115 0.0218 2.10E+11 7.99E-04 $LNTrans;
element elasticBeamColumn 112 116 117 0.0218 2.10E+11 7.99E-04 $LNTrans;
element elasticBeamColumn 113 117 118 0.0218 2.10E+11 7.99E-04 $LNTrans;
element elasticBeamColumn 114 119 120 0.0218 2.10E+11 7.99E-04 $LNTrans;
element elasticBeamColumn 115 120 121 0.0218 2.10E+11 7.99E-04 $LNTrans;
element elasticBeamColumn 116 122 123 0.0218 2.10E+11 7.99E-04 $LNTrans;
element elasticBeamColumn 117 123 124 0.0218 2.10E+11 7.99E-04 $LNTrans;

3rd floor
element elasticBeamColumn 118 125 126 0.0218 2.10E+11 7.99E-04 $LNTrans;
element elasticBeamColumn 119 126 127 0.0218 2.10E+11 7.99E-04 $LNTrans;
element elasticBeamColumn 120 128 129 0.0218 2.10E+11 7.99E-04 $LNTrans;
element elasticBeamColumn 121 129 130 0.0218 2.10E+11 7.99E-04 $LNTrans;
element elasticBeamColumn 122 131 132 0.0218 2.10E+11 7.99E-04 $LNTrans;
element elasticBeamColumn 123 132 133 0.0218 2.10E+11 7.99E-04 $LNTrans;
element elasticBeamColumn 124 134 135 0.0218 2.10E+11 7.99E-04 $LNTrans;

```
element elasticBeamColumn 125 135 136 0.0218 2.10E+11 7.99E-04 $LNTrans;

#	4rth	floor
element elasticBeamColumn 126 137 138 0.0218 2.10E+11 7.99E-04 $LNTrans;
element elasticBeamColumn 127 138 139 0.0218 2.10E+11 7.99E-04 $LNTrans;
element elasticBeamColumn 128 140 141 0.0218 2.10E+11 7.99E-04 $LNTrans;
element elasticBeamColumn 129 141 142 0.0218 2.10E+11 7.99E-04 $LNTrans;
element elasticBeamColumn 130 143 144 0.0218 2.10E+11 7.99E-04 $LNTrans;
element elasticBeamColumn 131 144 145 0.0218 2.10E+11 7.99E-04 $LNTrans;
element elasticBeamColumn 132 146 147 0.0218 2.10E+11 7.99E-04 $LNTrans;
element elasticBeamColumn 133 147 148 0.0218 2.10E+11 7.99E-04 $LNTrans;

#	5th	floor
element elasticBeamColumn 134 149 150 0.0218 2.10E+11 7.99E-04 $LNTrans;
element elasticBeamColumn 135 150 151 0.0218 2.10E+11 7.99E-04 $LNTrans;
element elasticBeamColumn 136 152 153 0.0218 2.10E+11 7.99E-04 $LNTrans;
element elasticBeamColumn 137 153 154 0.0218 2.10E+11 7.99E-04 $LNTrans;
element elasticBeamColumn 138 155 156 0.0218 2.10E+11 7.99E-04 $LNTrans;
element elasticBeamColumn 139 156 157 0.0218 2.10E+11 7.99E-04 $LNTrans;
element elasticBeamColumn 140 158 159 0.0218 2.10E+11 7.99E-04 $LNTrans;
element elasticBeamColumn 141 159 160 0.0218 2.10E+11 7.99E-04 $LNTrans;


# Define Beam column interface rigid elements


#	x1CR

#	y2

#	Top

element elasticBeamColumn 142 103 181 0.0218 2.10E+11 7.99E-04 $LNTrans;
element elasticBeamColumn 143 181 182 0.0218 2.10E+11 7.99E-04 $LNTrans;
element elasticBeamColumn 144 182 183 0.0218 2.10E+11 7.99E-04 $LNTrans;
element elasticBeamColumn 145 183 184 0.0218 2.10E+11 7.99E-04 $LNTrans;
element elasticBeamColumn 146 41 185 0.0218 2.10E+11 7.99E-04 $LNTrans;
element elasticBeamColumn 147 185 186 0.0218 2.10E+11 7.99E-04 $LNTrans;
element elasticBeamColumn 148 186 187 0.0218 2.10E+11 7.99E-04 $LNTrans;
element elasticBeamColumn 149 187 188 0.0218 2.10E+11 7.99E-04 $LNTrans;

#	Bottom

element elasticBeamColumn 150 103 189 0.0218 2.10E+11 7.99E-04 $LNTrans;
element elasticBeamColumn 151 189 190 0.0218 2.10E+11 7.99E-04 $LNTrans;
element elasticBeamColumn 152 190 191 0.0218 2.10E+11 7.99E-04 $LNTrans;
element elasticBeamColumn 153 191 192 0.0218 2.10E+11 7.99E-04 $LNTrans;
element elasticBeamColumn 154 41 193 0.0218 2.10E+11 7.99E-04 $LNTrans;
element elasticBeamColumn 155 193 194 0.0218 2.10E+11 7.99E-04 $LNTrans;
element elasticBeamColumn 156 194 195 0.0218 2.10E+11 7.99E-04 $LNTrans;
element elasticBeamColumn 157 195 196 0.0218 2.10E+11 7.99E-04 $LNTrans;

#	y3

#	Top

element elasticBeamColumn 158 115 197 0.0218 2.10E+11 7.99E-04 $LNTrans;
element elasticBeamColumn 159 197 198 0.0218 2.10E+11 7.99E-04 $LNTrans;
element elasticBeamColumn 160 198 199 0.0218 2.10E+11 7.99E-04 $LNTrans;
element elasticBeamColumn 161 199 200 0.0218 2.10E+11 7.99E-04 $LNTrans;
element elasticBeamColumn 162 53 201 0.0218 2.10E+11 7.99E-04 $LNTrans;
element elasticBeamColumn 163 201 202 0.0218 2.10E+11 7.99E-04 $LNTrans;
element elasticBeamColumn 164 202 203 0.0218 2.10E+11 7.99E-04 $LNTrans;
element elasticBeamColumn 165 203 204 0.0218 2.10E+11 7.99E-04 $LNTrans;

#	Bottom

element elasticBeamColumn 166 115 205 0.0218 2.10E+11 7.99E-04 $LNTrans;
element elasticBeamColumn 167 205 206 0.0218 2.10E+11 7.99E-04 $LNTrans;
element elasticBeamColumn 168 206 207 0.0218 2.10E+11 7.99E-04 $LNTrans;
element elasticBeamColumn 169 207 208 0.0218 2.10E+11 7.99E-04 $LNTrans;
element elasticBeamColumn 170 53 209 0.0218 2.10E+11 7.99E-04 $LNTrans;
element elasticBeamColumn 171 209 210 0.0218 2.10E+11 7.99E-04 $LNTrans;
element elasticBeamColumn 172 210 211 0.0218 2.10E+11 7.99E-04 $LNTrans;
element elasticBeamColumn 173 211 212 0.0218 2.10E+11 7.99E-04 $LNTrans;
```

```
#       y4

#       Top

element elasticBeamColumn 174       127       213       0.0218    2.10E+11  7.99E-04  $LNTrans;
element elasticBeamColumn 175       213       214       0.0218    2.10E+11  7.99E-04  $LNTrans;
element elasticBeamColumn 176       214       215       0.0218    2.10E+11  7.99E-04  $LNTrans;
element elasticBeamColumn 177       215       216       0.0218    2.10E+11  7.99E-04  $LNTrans;
element elasticBeamColumn 178       65        217       0.0218    2.10E+11  7.99E-04  $LNTrans;
element elasticBeamColumn 179       217       218       0.0218    2.10E+11  7.99E-04  $LNTrans;
element elasticBeamColumn 180       218       219       0.0218    2.10E+11  7.99E-04  $LNTrans;
element elasticBeamColumn 181       219       220       0.0218    2.10E+11  7.99E-04  $LNTrans;

#       Bottom

element elasticBeamColumn 182       127       221       0.0218    2.10E+11  7.99E-04  $LNTrans;
element elasticBeamColumn 183       221       222       0.0218    2.10E+11  7.99E-04  $LNTrans;
element elasticBeamColumn 184       222       223       0.0218    2.10E+11  7.99E-04  $LNTrans;
element elasticBeamColumn 185       223       224       0.0218    2.10E+11  7.99E-04  $LNTrans;
element elasticBeamColumn 186       65        225       0.0218    2.10E+11  7.99E-04  $LNTrans;
element elasticBeamColumn 187       225       226       0.0218    2.10E+11  7.99E-04  $LNTrans;
element elasticBeamColumn 188       226       227       0.0218    2.10E+11  7.99E-04  $LNTrans;
element elasticBeamColumn 189       227       228       0.0218    2.10E+11  7.99E-04  $LNTrans;

#       y5

#       Top

element elasticBeamColumn 190       139       229       0.0218    2.10E+11  7.99E-04  $LNTrans;
element elasticBeamColumn 191       229       230       0.0218    2.10E+11  7.99E-04  $LNTrans;
element elasticBeamColumn 192       230       231       0.0218    2.10E+11  7.99E-04  $LNTrans;
element elasticBeamColumn 193       231       232       0.0218    2.10E+11  7.99E-04  $LNTrans;
element elasticBeamColumn 194       77        233       0.0218    2.10E+11  7.99E-04  $LNTrans;
element elasticBeamColumn 195       233       234       0.0218    2.10E+11  7.99E-04  $LNTrans;
element elasticBeamColumn 196       234       235       0.0218    2.10E+11  7.99E-04  $LNTrans;
element elasticBeamColumn 197       235       236       0.0218    2.10E+11  7.99E-04  $LNTrans;

#       Bottom

element elasticBeamColumn 198       139       237       0.0218    2.10E+11  7.99E-04  $LNTrans;
element elasticBeamColumn 199       237       238       0.0218    2.10E+11  7.99E-04  $LNTrans;
element elasticBeamColumn 200       238       239       0.0218    2.10E+11  7.99E-04  $LNTrans;
element elasticBeamColumn 201       239       240       0.0218    2.10E+11  7.99E-04  $LNTrans;
element elasticBeamColumn 202       77        241       0.0218    2.10E+11  7.99E-04  $LNTrans;
element elasticBeamColumn 203       241       242       0.0218    2.10E+11  7.99E-04  $LNTrans;
element elasticBeamColumn 204       242       243       0.0218    2.10E+11  7.99E-04  $LNTrans;
element elasticBeamColumn 205       243       244       0.0218    2.10E+11  7.99E-04  $LNTrans;

#       y6

#       Top

element elasticBeamColumn 206       151       245       0.0218    2.10E+11  7.99E-04  $LNTrans;
element elasticBeamColumn 207       245       246       0.0218    2.10E+11  7.99E-04  $LNTrans;
element elasticBeamColumn 208       246       247       0.0218    2.10E+11  7.99E-04  $LNTrans;
element elasticBeamColumn 209       247       248       0.0218    2.10E+11  7.99E-04  $LNTrans;
element elasticBeamColumn 210       89        249       0.0218    2.10E+11  7.99E-04  $LNTrans;
element elasticBeamColumn 211       249       250       0.0218    2.10E+11  7.99E-04  $LNTrans;
element elasticBeamColumn 212       250       251       0.0218    2.10E+11  7.99E-04  $LNTrans;
element elasticBeamColumn 213       251       252       0.0218    2.10E+11  7.99E-04  $LNTrans;

#       Bottom

element elasticBeamColumn 214       151       253       0.0218    2.10E+11  7.99E-04  $LNTrans;
element elasticBeamColumn 215       253       254       0.0218    2.10E+11  7.99E-04  $LNTrans;
element elasticBeamColumn 216       254       255       0.0218    2.10E+11  7.99E-04  $LNTrans;
element elasticBeamColumn 217       255       256       0.0218    2.10E+11  7.99E-04  $LNTrans;
element elasticBeamColumn 218       89        257       0.0218    2.10E+11  7.99E-04  $LNTrans;
element elasticBeamColumn 219       257       258       0.0218    2.10E+11  7.99E-04  $LNTrans;
element elasticBeamColumn 220       258       259       0.0218    2.10E+11  7.99E-04  $LNTrans;
element elasticBeamColumn 221       259       260       0.0218    2.10E+11  7.99E-04  $LNTrans;

#       x2CL
```

```
#       y2

#       Top

element elasticBeamColumn 222       104       261       0.0218    2.10E+11  7.99E-04  $LNTrans;
element elasticBeamColumn 223       261       262       0.0218    2.10E+11  7.99E-04  $LNTrans;
element elasticBeamColumn 224       262       263       0.0218    2.10E+11  7.99E-04  $LNTrans;
element elasticBeamColumn 225       263       264       0.0218    2.10E+11  7.99E-04  $LNTrans;
element elasticBeamColumn 226       44        265       0.0218    2.10E+11  7.99E-04  $LNTrans;
element elasticBeamColumn 227       265       266       0.0218    2.10E+11  7.99E-04  $LNTrans;
element elasticBeamColumn 228       266       267       0.0218    2.10E+11  7.99E-04  $LNTrans;
element elasticBeamColumn 229       267       268       0.0218    2.10E+11  7.99E-04  $LNTrans;

#       Bottom

element elasticBeamColumn 230       104       269       0.0218    2.10E+11  7.99E-04  $LNTrans;
element elasticBeamColumn 231       269       270       0.0218    2.10E+11  7.99E-04  $LNTrans;
element elasticBeamColumn 232       270       271       0.0218    2.10E+11  7.99E-04  $LNTrans;
element elasticBeamColumn 233       271       272       0.0218    2.10E+11  7.99E-04  $LNTrans;
element elasticBeamColumn 234       44        273       0.0218    2.10E+11  7.99E-04  $LNTrans;
element elasticBeamColumn 235       273       274       0.0218    2.10E+11  7.99E-04  $LNTrans;
element elasticBeamColumn 236       274       275       0.0218    2.10E+11  7.99E-04  $LNTrans;
element elasticBeamColumn 237       275       276       0.0218    2.10E+11  7.99E-04  $LNTrans;

#       y3

#       Top

element elasticBeamColumn 238       116       277       0.0218    2.10E+11  7.99E-04  $LNTrans;
element elasticBeamColumn 239       277       278       0.0218    2.10E+11  7.99E-04  $LNTrans;
element elasticBeamColumn 240       278       279       0.0218    2.10E+11  7.99E-04  $LNTrans;
element elasticBeamColumn 241       279       280       0.0218    2.10E+11  7.99E-04  $LNTrans;
element elasticBeamColumn 242       56        281       0.0218    2.10E+11  7.99E-04  $LNTrans;
element elasticBeamColumn 243       281       282       0.0218    2.10E+11  7.99E-04  $LNTrans;
element elasticBeamColumn 244       282       283       0.0218    2.10E+11  7.99E-04  $LNTrans;
element elasticBeamColumn 245       283       284       0.0218    2.10E+11  7.99E-04  $LNTrans;

#       Bottom

element elasticBeamColumn 246       116       285       0.0218    2.10E+11  7.99E-04  $LNTrans;
element elasticBeamColumn 247       285       286       0.0218    2.10E+11  7.99E-04  $LNTrans;
element elasticBeamColumn 248       286       287       0.0218    2.10E+11  7.99E-04  $LNTrans;
element elasticBeamColumn 249       287       288       0.0218    2.10E+11  7.99E-04  $LNTrans;
element elasticBeamColumn 250       56        289       0.0218    2.10E+11  7.99E-04  $LNTrans;
element elasticBeamColumn 251       289       290       0.0218    2.10E+11  7.99E-04  $LNTrans;
element elasticBeamColumn 252       290       291       0.0218    2.10E+11  7.99E-04  $LNTrans;
element elasticBeamColumn 253       291       292       0.0218    2.10E+11  7.99E-04  $LNTrans;

#       y4

#       Top

element elasticBeamColumn 254       128       293       0.0218    2.10E+11  7.99E-04  $LNTrans;
element elasticBeamColumn 255       293       294       0.0218    2.10E+11  7.99E-04  $LNTrans;
element elasticBeamColumn 256       294       295       0.0218    2.10E+11  7.99E-04  $LNTrans;
element elasticBeamColumn 257       295       296       0.0218    2.10E+11  7.99E-04  $LNTrans;
element elasticBeamColumn 258       68        297       0.0218    2.10E+11  7.99E-04  $LNTrans;
element elasticBeamColumn 259       297       298       0.0218    2.10E+11  7.99E-04  $LNTrans;
element elasticBeamColumn 260       298       299       0.0218    2.10E+11  7.99E-04  $LNTrans;
element elasticBeamColumn 261       299       300       0.0218    2.10E+11  7.99E-04  $LNTrans;

#       Bottom

element elasticBeamColumn 262       128       301       0.0218    2.10E+11  7.99E-04  $LNTrans;
element elasticBeamColumn 263       301       302       0.0218    2.10E+11  7.99E-04  $LNTrans;
element elasticBeamColumn 264       302       303       0.0218    2.10E+11  7.99E-04  $LNTrans;
element elasticBeamColumn 265       303       304       0.0218    2.10E+11  7.99E-04  $LNTrans;
element elasticBeamColumn 266       68        305       0.0218    2.10E+11  7.99E-04  $LNTrans;
element elasticBeamColumn 267       305       306       0.0218    2.10E+11  7.99E-04  $LNTrans;
element elasticBeamColumn 268       306       307       0.0218    2.10E+11  7.99E-04  $LNTrans;
element elasticBeamColumn 269       307       308       0.0218    2.10E+11  7.99E-04  $LNTrans;

#       y5

#       Top
```

```
element elasticBeamColumn 270 140 309 0.0218 2.10E+11 7.99E-04 $LNTrans;
element elasticBeamColumn 271 309 310 0.0218 2.10E+11 7.99E-04 $LNTrans;
element elasticBeamColumn 272 310 311 0.0218 2.10E+11 7.99E-04 $LNTrans;
element elasticBeamColumn 273 311 312 0.0218 2.10E+11 7.99E-04 $LNTrans;
element elasticBeamColumn 274 80 313 0.0218 2.10E+11 7.99E-04 $LNTrans;
element elasticBeamColumn 275 313 314 0.0218 2.10E+11 7.99E-04 $LNTrans;
element elasticBeamColumn 276 314 315 0.0218 2.10E+11 7.99E-04 $LNTrans;
element elasticBeamColumn 277 315 316 0.0218 2.10E+11 7.99E-04 $LNTrans;

#	Bottom

element elasticBeamColumn 278 140 317 0.0218 2.10E+11 7.99E-04 $LNTrans;
element elasticBeamColumn 279 317 318 0.0218 2.10E+11 7.99E-04 $LNTrans;
element elasticBeamColumn 280 318 319 0.0218 2.10E+11 7.99E-04 $LNTrans;
element elasticBeamColumn 281 319 320 0.0218 2.10E+11 7.99E-04 $LNTrans;
element elasticBeamColumn 282 80 321 0.0218 2.10E+11 7.99E-04 $LNTrans;
element elasticBeamColumn 283 321 322 0.0218 2.10E+11 7.99E-04 $LNTrans;
element elasticBeamColumn 284 322 323 0.0218 2.10E+11 7.99E-04 $LNTrans;
element elasticBeamColumn 285 323 324 0.0218 2.10E+11 7.99E-04 $LNTrans;

#	y6

#	Top

element elasticBeamColumn 286 152 325 0.0218 2.10E+11 7.99E-04 $LNTrans;
element elasticBeamColumn 287 325 326 0.0218 2.10E+11 7.99E-04 $LNTrans;
element elasticBeamColumn 288 326 327 0.0218 2.10E+11 7.99E-04 $LNTrans;
element elasticBeamColumn 289 327 328 0.0218 2.10E+11 7.99E-04 $LNTrans;
element elasticBeamColumn 290 92 329 0.0218 2.10E+11 7.99E-04 $LNTrans;
element elasticBeamColumn 291 329 330 0.0218 2.10E+11 7.99E-04 $LNTrans;
element elasticBeamColumn 292 330 331 0.0218 2.10E+11 7.99E-04 $LNTrans;
element elasticBeamColumn 293 331 332 0.0218 2.10E+11 7.99E-04 $LNTrans;

#	Bottom

element elasticBeamColumn 294 152 333 0.0218 2.10E+11 7.99E-04 $LNTrans;
element elasticBeamColumn 295 333 334 0.0218 2.10E+11 7.99E-04 $LNTrans;
element elasticBeamColumn 296 334 335 0.0218 2.10E+11 7.99E-04 $LNTrans;
element elasticBeamColumn 297 335 336 0.0218 2.10E+11 7.99E-04 $LNTrans;
element elasticBeamColumn 298 92 337 0.0218 2.10E+11 7.99E-04 $LNTrans;
element elasticBeamColumn 299 337 338 0.0218 2.10E+11 7.99E-04 $LNTrans;
element elasticBeamColumn 300 338 339 0.0218 2.10E+11 7.99E-04 $LNTrans;
element elasticBeamColumn 301 339 340 0.0218 2.10E+11 7.99E-04 $LNTrans;

#	x2CR

#	y2

#	Top

element elasticBeamColumn 302 106 341 0.0218 2.10E+11 7.99E-04 $LNTrans;
element elasticBeamColumn 303 341 342 0.0218 2.10E+11 7.99E-04 $LNTrans;
element elasticBeamColumn 304 342 343 0.0218 2.10E+11 7.99E-04 $LNTrans;
element elasticBeamColumn 305 343 344 0.0218 2.10E+11 7.99E-04 $LNTrans;
element elasticBeamColumn 306 45 345 0.0218 2.10E+11 7.99E-04 $LNTrans;
element elasticBeamColumn 307 345 346 0.0218 2.10E+11 7.99E-04 $LNTrans;
element elasticBeamColumn 308 346 347 0.0218 2.10E+11 7.99E-04 $LNTrans;
element elasticBeamColumn 309 347 348 0.0218 2.10E+11 7.99E-04 $LNTrans;

#	Bottom

element elasticBeamColumn 310 106 349 0.0218 2.10E+11 7.99E-04 $LNTrans;
element elasticBeamColumn 311 349 350 0.0218 2.10E+11 7.99E-04 $LNTrans;
element elasticBeamColumn 312 350 351 0.0218 2.10E+11 7.99E-04 $LNTrans;
element elasticBeamColumn 313 351 352 0.0218 2.10E+11 7.99E-04 $LNTrans;
element elasticBeamColumn 314 45 353 0.0218 2.10E+11 7.99E-04 $LNTrans;
element elasticBeamColumn 315 353 354 0.0218 2.10E+11 7.99E-04 $LNTrans;
element elasticBeamColumn 316 354 355 0.0218 2.10E+11 7.99E-04 $LNTrans;
element elasticBeamColumn 317 355 356 0.0218 2.10E+11 7.99E-04 $LNTrans;

#	y3

#	Top
```

```
element elasticBeamColumn 318 118 357 0.0218 2.10E+11 7.99E-04 $LNTrans;
element elasticBeamColumn 319 357 358 0.0218 2.10E+11 7.99E-04 $LNTrans;
element elasticBeamColumn 320 358 359 0.0218 2.10E+11 7.99E-04 $LNTrans;
element elasticBeamColumn 321 359 360 0.0218 2.10E+11 7.99E-04 $LNTrans;
element elasticBeamColumn 322 57 361 0.0218 2.10E+11 7.99E-04 $LNTrans;
element elasticBeamColumn 323 361 362 0.0218 2.10E+11 7.99E-04 $LNTrans;
element elasticBeamColumn 324 362 363 0.0218 2.10E+11 7.99E-04 $LNTrans;
element elasticBeamColumn 325 363 364 0.0218 2.10E+11 7.99E-04 $LNTrans;

#	Bottom

element elasticBeamColumn 326 118 365 0.0218 2.10E+11 7.99E-04 $LNTrans;
element elasticBeamColumn 327 365 366 0.0218 2.10E+11 7.99E-04 $LNTrans;
element elasticBeamColumn 328 366 367 0.0218 2.10E+11 7.99E-04 $LNTrans;
element elasticBeamColumn 329 367 368 0.0218 2.10E+11 7.99E-04 $LNTrans;
element elasticBeamColumn 330 57 369 0.0218 2.10E+11 7.99E-04 $LNTrans;
element elasticBeamColumn 331 369 370 0.0218 2.10E+11 7.99E-04 $LNTrans;
element elasticBeamColumn 332 370 371 0.0218 2.10E+11 7.99E-04 $LNTrans;
element elasticBeamColumn 333 371 372 0.0218 2.10E+11 7.99E-04 $LNTrans;

#	y4

#	Top

element elasticBeamColumn 334 130 373 0.0218 2.10E+11 7.99E-04 $LNTrans;
element elasticBeamColumn 335 373 374 0.0218 2.10E+11 7.99E-04 $LNTrans;
element elasticBeamColumn 336 374 375 0.0218 2.10E+11 7.99E-04 $LNTrans;
element elasticBeamColumn 337 375 376 0.0218 2.10E+11 7.99E-04 $LNTrans;
element elasticBeamColumn 338 69 377 0.0218 2.10E+11 7.99E-04 $LNTrans;
element elasticBeamColumn 339 377 378 0.0218 2.10E+11 7.99E-04 $LNTrans;
element elasticBeamColumn 340 378 379 0.0218 2.10E+11 7.99E-04 $LNTrans;
element elasticBeamColumn 341 379 380 0.0218 2.10E+11 7.99E-04 $LNTrans;

#	Bottom

element elasticBeamColumn 342 130 381 0.0218 2.10E+11 7.99E-04 $LNTrans;
element elasticBeamColumn 343 381 382 0.0218 2.10E+11 7.99E-04 $LNTrans;
element elasticBeamColumn 344 382 383 0.0218 2.10E+11 7.99E-04 $LNTrans;
element elasticBeamColumn 345 383 384 0.0218 2.10E+11 7.99E-04 $LNTrans;
element elasticBeamColumn 346 69 385 0.0218 2.10E+11 7.99E-04 $LNTrans;
element elasticBeamColumn 347 385 386 0.0218 2.10E+11 7.99E-04 $LNTrans;
element elasticBeamColumn 348 386 387 0.0218 2.10E+11 7.99E-04 $LNTrans;
element elasticBeamColumn 349 387 388 0.0218 2.10E+11 7.99E-04 $LNTrans;

#	y5

#	Top

element elasticBeamColumn 350 142 389 0.0218 2.10E+11 7.99E-04 $LNTrans;
element elasticBeamColumn 351 389 390 0.0218 2.10E+11 7.99E-04 $LNTrans;
element elasticBeamColumn 352 390 391 0.0218 2.10E+11 7.99E-04 $LNTrans;
element elasticBeamColumn 353 391 392 0.0218 2.10E+11 7.99E-04 $LNTrans;
element elasticBeamColumn 354 81 393 0.0218 2.10E+11 7.99E-04 $LNTrans;
element elasticBeamColumn 355 393 394 0.0218 2.10E+11 7.99E-04 $LNTrans;
element elasticBeamColumn 356 394 395 0.0218 2.10E+11 7.99E-04 $LNTrans;
element elasticBeamColumn 357 395 396 0.0218 2.10E+11 7.99E-04 $LNTrans;

#	Bottom

element elasticBeamColumn 358 142 397 0.0218 2.10E+11 7.99E-04 $LNTrans;
element elasticBeamColumn 359 397 398 0.0218 2.10E+11 7.99E-04 $LNTrans;
element elasticBeamColumn 360 398 399 0.0218 2.10E+11 7.99E-04 $LNTrans;
element elasticBeamColumn 361 399 400 0.0218 2.10E+11 7.99E-04 $LNTrans;
element elasticBeamColumn 362 81 401 0.0218 2.10E+11 7.99E-04 $LNTrans;
element elasticBeamColumn 363 401 402 0.0218 2.10E+11 7.99E-04 $LNTrans;
element elasticBeamColumn 364 402 403 0.0218 2.10E+11 7.99E-04 $LNTrans;
element elasticBeamColumn 365 403 404 0.0218 2.10E+11 7.99E-04 $LNTrans;

#	y6

#	Top

element elasticBeamColumn 366 154 405 0.0218 2.10E+11 7.99E-04 $LNTrans;
element elasticBeamColumn 367 405 406 0.0218 2.10E+11 7.99E-04 $LNTrans;
element elasticBeamColumn 368 406 407 0.0218 2.10E+11 7.99E-04 $LNTrans;
```

```
element elasticBeamColumn 369 407 408 0.0218 2.10E+11 7.99E-04 $LNTrans;
element elasticBeamColumn 370 93 409 0.0218 2.10E+11 7.99E-04 $LNTrans;
element elasticBeamColumn 371 409 410 0.0218 2.10E+11 7.99E-04 $LNTrans;
element elasticBeamColumn 372 410 411 0.0218 2.10E+11 7.99E-04 $LNTrans;
element elasticBeamColumn 373 411 412 0.0218 2.10E+11 7.99E-04 $LNTrans;

#	Bottom

element elasticBeamColumn 374 154 413 0.0218 2.10E+11 7.99E-04 $LNTrans;
element elasticBeamColumn 375 413 414 0.0218 2.10E+11 7.99E-04 $LNTrans;
element elasticBeamColumn 376 414 415 0.0218 2.10E+11 7.99E-04 $LNTrans;
element elasticBeamColumn 377 415 416 0.0218 2.10E+11 7.99E-04 $LNTrans;
element elasticBeamColumn 378 93 417 0.0218 2.10E+11 7.99E-04 $LNTrans;
element elasticBeamColumn 379 417 418 0.0218 2.10E+11 7.99E-04 $LNTrans;
element elasticBeamColumn 380 418 419 0.0218 2.10E+11 7.99E-04 $LNTrans;
element elasticBeamColumn 381 419 420 0.0218 2.10E+11 7.99E-04 $LNTrans;

#	x3CL

#	y2

#	Top

element elasticBeamColumn 382 107 421 0.0218 2.10E+11 7.99E-04 $LNTrans;
element elasticBeamColumn 383 421 422 0.0218 2.10E+11 7.99E-04 $LNTrans;
element elasticBeamColumn 384 422 423 0.0218 2.10E+11 7.99E-04 $LNTrans;
element elasticBeamColumn 385 423 424 0.0218 2.10E+11 7.99E-04 $LNTrans;
element elasticBeamColumn 386 48 425 0.0218 2.10E+11 7.99E-04 $LNTrans;
element elasticBeamColumn 387 425 426 0.0218 2.10E+11 7.99E-04 $LNTrans;
element elasticBeamColumn 388 426 427 0.0218 2.10E+11 7.99E-04 $LNTrans;
element elasticBeamColumn 389 427 428 0.0218 2.10E+11 7.99E-04 $LNTrans;

#	Bottom

element elasticBeamColumn 390 107 429 0.0218 2.10E+11 7.99E-04 $LNTrans;
element elasticBeamColumn 391 429 430 0.0218 2.10E+11 7.99E-04 $LNTrans;
element elasticBeamColumn 392 430 431 0.0218 2.10E+11 7.99E-04 $LNTrans;
element elasticBeamColumn 393 431 432 0.0218 2.10E+11 7.99E-04 $LNTrans;
element elasticBeamColumn 394 48 433 0.0218 2.10E+11 7.99E-04 $LNTrans;
element elasticBeamColumn 395 433 434 0.0218 2.10E+11 7.99E-04 $LNTrans;
element elasticBeamColumn 396 434 435 0.0218 2.10E+11 7.99E-04 $LNTrans;
element elasticBeamColumn 397 435 436 0.0218 2.10E+11 7.99E-04 $LNTrans;

#	y3

#	Top

element elasticBeamColumn 398 119 437 0.0218 2.10E+11 7.99E-04 $LNTrans;
element elasticBeamColumn 399 437 438 0.0218 2.10E+11 7.99E-04 $LNTrans;
element elasticBeamColumn 400 438 439 0.0218 2.10E+11 7.99E-04 $LNTrans;
element elasticBeamColumn 401 439 440 0.0218 2.10E+11 7.99E-04 $LNTrans;
element elasticBeamColumn 402 60 441 0.0218 2.10E+11 7.99E-04 $LNTrans;
element elasticBeamColumn 403 441 442 0.0218 2.10E+11 7.99E-04 $LNTrans;
element elasticBeamColumn 404 442 443 0.0218 2.10E+11 7.99E-04 $LNTrans;
element elasticBeamColumn 405 443 444 0.0218 2.10E+11 7.99E-04 $LNTrans;

#	Bottom

element elasticBeamColumn 406 119 445 0.0218 2.10E+11 7.99E-04 $LNTrans;
element elasticBeamColumn 407 445 446 0.0218 2.10E+11 7.99E-04 $LNTrans;
element elasticBeamColumn 408 446 447 0.0218 2.10E+11 7.99E-04 $LNTrans;
element elasticBeamColumn 409 447 448 0.0218 2.10E+11 7.99E-04 $LNTrans;
element elasticBeamColumn 410 60 449 0.0218 2.10E+11 7.99E-04 $LNTrans;
element elasticBeamColumn 411 449 450 0.0218 2.10E+11 7.99E-04 $LNTrans;
element elasticBeamColumn 412 450 451 0.0218 2.10E+11 7.99E-04 $LNTrans;
element elasticBeamColumn 413 451 452 0.0218 2.10E+11 7.99E-04 $LNTrans;

#	y4

#	Top

element elasticBeamColumn 414 131 453 0.0218 2.10E+11 7.99E-04 $LNTrans;
element elasticBeamColumn 415 453 454 0.0218 2.10E+11 7.99E-04 $LNTrans;
element elasticBeamColumn 416 454 455 0.0218 2.10E+11 7.99E-04 $LNTrans;
element elasticBeamColumn 417 455 456 0.0218 2.10E+11 7.99E-04 $LNTrans;
```

```
element elasticBeamColumn 418 72 457 0.0218 2.10E+11 7.99E-04 $LNTrans;
element elasticBeamColumn 419 457 458 0.0218 2.10E+11 7.99E-04 $LNTrans;
element elasticBeamColumn 420 458 459 0.0218 2.10E+11 7.99E-04 $LNTrans;
element elasticBeamColumn 421 459 460 0.0218 2.10E+11 7.99E-04 $LNTrans;

#	Bottom

element elasticBeamColumn 422 131 461 0.0218 2.10E+11 7.99E-04 $LNTrans;
element elasticBeamColumn 423 461 462 0.0218 2.10E+11 7.99E-04 $LNTrans;
element elasticBeamColumn 424 462 463 0.0218 2.10E+11 7.99E-04 $LNTrans;
element elasticBeamColumn 425 463 464 0.0218 2.10E+11 7.99E-04 $LNTrans;
element elasticBeamColumn 426 72 465 0.0218 2.10E+11 7.99E-04 $LNTrans;
element elasticBeamColumn 427 465 466 0.0218 2.10E+11 7.99E-04 $LNTrans;
element elasticBeamColumn 428 466 467 0.0218 2.10E+11 7.99E-04 $LNTrans;
element elasticBeamColumn 429 467 468 0.0218 2.10E+11 7.99E-04 $LNTrans;

#	y5

#	Top

element elasticBeamColumn 430 143 469 0.0218 2.10E+11 7.99E-04 $LNTrans;
element elasticBeamColumn 431 469 470 0.0218 2.10E+11 7.99E-04 $LNTrans;
element elasticBeamColumn 432 470 471 0.0218 2.10E+11 7.99E-04 $LNTrans;
element elasticBeamColumn 433 471 472 0.0218 2.10E+11 7.99E-04 $LNTrans;
element elasticBeamColumn 434 84 473 0.0218 2.10E+11 7.99E-04 $LNTrans;
element elasticBeamColumn 435 473 474 0.0218 2.10E+11 7.99E-04 $LNTrans;
element elasticBeamColumn 436 474 475 0.0218 2.10E+11 7.99E-04 $LNTrans;
element elasticBeamColumn 437 475 476 0.0218 2.10E+11 7.99E-04 $LNTrans;

#	Bottom

element elasticBeamColumn 438 143 477 0.0218 2.10E+11 7.99E-04 $LNTrans;
element elasticBeamColumn 439 477 478 0.0218 2.10E+11 7.99E-04 $LNTrans;
element elasticBeamColumn 440 478 479 0.0218 2.10E+11 7.99E-04 $LNTrans;
element elasticBeamColumn 441 479 480 0.0218 2.10E+11 7.99E-04 $LNTrans;
element elasticBeamColumn 442 84 481 0.0218 2.10E+11 7.99E-04 $LNTrans;
element elasticBeamColumn 443 481 482 0.0218 2.10E+11 7.99E-04 $LNTrans;
element elasticBeamColumn 444 482 483 0.0218 2.10E+11 7.99E-04 $LNTrans;
element elasticBeamColumn 445 483 484 0.0218 2.10E+11 7.99E-04 $LNTrans;

#	y6

#	Top

element elasticBeamColumn 446 155 485 0.0218 2.10E+11 7.99E-04 $LNTrans;
element elasticBeamColumn 447 485 486 0.0218 2.10E+11 7.99E-04 $LNTrans;
element elasticBeamColumn 448 486 487 0.0218 2.10E+11 7.99E-04 $LNTrans;
element elasticBeamColumn 449 487 488 0.0218 2.10E+11 7.99E-04 $LNTrans;
element elasticBeamColumn 450 96 489 0.0218 2.10E+11 7.99E-04 $LNTrans;
element elasticBeamColumn 451 489 490 0.0218 2.10E+11 7.99E-04 $LNTrans;
element elasticBeamColumn 452 490 491 0.0218 2.10E+11 7.99E-04 $LNTrans;
element elasticBeamColumn 453 491 492 0.0218 2.10E+11 7.99E-04 $LNTrans;

#	Bottom

element elasticBeamColumn 454 155 493 0.0218 2.10E+11 7.99E-04 $LNTrans;
element elasticBeamColumn 455 493 494 0.0218 2.10E+11 7.99E-04 $LNTrans;
element elasticBeamColumn 456 494 495 0.0218 2.10E+11 7.99E-04 $LNTrans;
element elasticBeamColumn 457 495 496 0.0218 2.10E+11 7.99E-04 $LNTrans;
element elasticBeamColumn 458 96 497 0.0218 2.10E+11 7.99E-04 $LNTrans;
element elasticBeamColumn 459 497 498 0.0218 2.10E+11 7.99E-04 $LNTrans;
element elasticBeamColumn 460 498 499 0.0218 2.10E+11 7.99E-04 $LNTrans;
element elasticBeamColumn 461 499 500 0.0218 2.10E+11 7.99E-04 $LNTrans;

#	x3CR

#	y2

#	Top

element elasticBeamColumn 462 109 501 0.0218 2.10E+11 7.99E-04 $LNTrans;
element elasticBeamColumn 463 501 502 0.0218 2.10E+11 7.99E-04 $LNTrans;
element elasticBeamColumn 464 502 503 0.0218 2.10E+11 7.99E-04 $LNTrans;
element elasticBeamColumn 465 503 504 0.0218 2.10E+11 7.99E-04 $LNTrans;
element elasticBeamColumn 466 49 505 0.0218 2.10E+11 7.99E-04 $LNTrans;
```

```
element elasticBeamColumn 467 505 506 0.0218 2.10E+11 7.99E-04 $LNTrans;
element elasticBeamColumn 468 506 507 0.0218 2.10E+11 7.99E-04 $LNTrans;
element elasticBeamColumn 469 507 508 0.0218 2.10E+11 7.99E-04 $LNTrans;

#	Bottom

element elasticBeamColumn 470 109 509 0.0218 2.10E+11 7.99E-04 $LNTrans;
element elasticBeamColumn 471 509 510 0.0218 2.10E+11 7.99E-04 $LNTrans;
element elasticBeamColumn 472 510 511 0.0218 2.10E+11 7.99E-04 $LNTrans;
element elasticBeamColumn 473 511 512 0.0218 2.10E+11 7.99E-04 $LNTrans;
element elasticBeamColumn 474 49 513 0.0218 2.10E+11 7.99E-04 $LNTrans;
element elasticBeamColumn 475 513 514 0.0218 2.10E+11 7.99E-04 $LNTrans;
element elasticBeamColumn 476 514 515 0.0218 2.10E+11 7.99E-04 $LNTrans;
element elasticBeamColumn 477 515 516 0.0218 2.10E+11 7.99E-04 $LNTrans;

#	y3

#	Top

element elasticBeamColumn 478 121 517 0.0218 2.10E+11 7.99E-04 $LNTrans;
element elasticBeamColumn 479 517 518 0.0218 2.10E+11 7.99E-04 $LNTrans;
element elasticBeamColumn 480 518 519 0.0218 2.10E+11 7.99E-04 $LNTrans;
element elasticBeamColumn 481 519 520 0.0218 2.10E+11 7.99E-04 $LNTrans;
element elasticBeamColumn 482 61 521 0.0218 2.10E+11 7.99E-04 $LNTrans;
element elasticBeamColumn 483 521 522 0.0218 2.10E+11 7.99E-04 $LNTrans;
element elasticBeamColumn 484 522 523 0.0218 2.10E+11 7.99E-04 $LNTrans;
element elasticBeamColumn 485 523 524 0.0218 2.10E+11 7.99E-04 $LNTrans;

#	Bottom

element elasticBeamColumn 486 121 525 0.0218 2.10E+11 7.99E-04 $LNTrans;
element elasticBeamColumn 487 525 526 0.0218 2.10E+11 7.99E-04 $LNTrans;
element elasticBeamColumn 488 526 527 0.0218 2.10E+11 7.99E-04 $LNTrans;
element elasticBeamColumn 489 527 528 0.0218 2.10E+11 7.99E-04 $LNTrans;
element elasticBeamColumn 490 61 529 0.0218 2.10E+11 7.99E-04 $LNTrans;
element elasticBeamColumn 491 529 530 0.0218 2.10E+11 7.99E-04 $LNTrans;
element elasticBeamColumn 492 530 531 0.0218 2.10E+11 7.99E-04 $LNTrans;
element elasticBeamColumn 493 531 532 0.0218 2.10E+11 7.99E-04 $LNTrans;

#	y4

#	Top

element elasticBeamColumn 494 133 533 0.0218 2.10E+11 7.99E-04 $LNTrans;
element elasticBeamColumn 495 533 534 0.0218 2.10E+11 7.99E-04 $LNTrans;
element elasticBeamColumn 496 534 535 0.0218 2.10E+11 7.99E-04 $LNTrans;
element elasticBeamColumn 497 535 536 0.0218 2.10E+11 7.99E-04 $LNTrans;
element elasticBeamColumn 498 73 537 0.0218 2.10E+11 7.99E-04 $LNTrans;
element elasticBeamColumn 499 537 538 0.0218 2.10E+11 7.99E-04 $LNTrans;
element elasticBeamColumn 500 538 539 0.0218 2.10E+11 7.99E-04 $LNTrans;
element elasticBeamColumn 501 539 540 0.0218 2.10E+11 7.99E-04 $LNTrans;

#	Bottom

element elasticBeamColumn 502 133 541 0.0218 2.10E+11 7.99E-04 $LNTrans;
element elasticBeamColumn 503 541 542 0.0218 2.10E+11 7.99E-04 $LNTrans;
element elasticBeamColumn 504 542 543 0.0218 2.10E+11 7.99E-04 $LNTrans;
element elasticBeamColumn 505 543 544 0.0218 2.10E+11 7.99E-04 $LNTrans;
element elasticBeamColumn 506 73 545 0.0218 2.10E+11 7.99E-04 $LNTrans;
element elasticBeamColumn 507 545 546 0.0218 2.10E+11 7.99E-04 $LNTrans;
element elasticBeamColumn 508 546 547 0.0218 2.10E+11 7.99E-04 $LNTrans;
element elasticBeamColumn 509 547 548 0.0218 2.10E+11 7.99E-04 $LNTrans;

#	y5

#	Top

element elasticBeamColumn 510 145 549 0.0218 2.10E+11 7.99E-04 $LNTrans;
element elasticBeamColumn 511 549 550 0.0218 2.10E+11 7.99E-04 $LNTrans;
element elasticBeamColumn 512 550 551 0.0218 2.10E+11 7.99E-04 $LNTrans;
element elasticBeamColumn 513 551 552 0.0218 2.10E+11 7.99E-04 $LNTrans;
element elasticBeamColumn 514 85 553 0.0218 2.10E+11 7.99E-04 $LNTrans;
element elasticBeamColumn 515 553 554 0.0218 2.10E+11 7.99E-04 $LNTrans;
element elasticBeamColumn 516 554 555 0.0218 2.10E+11 7.99E-04 $LNTrans;
element elasticBeamColumn 517 555 556 0.0218 2.10E+11 7.99E-04 $LNTrans;
```

```
#       Bottom

element elasticBeamColumn 518       145       557       0.0218    2.10E+11  7.99E-04  $LNTrans;
element elasticBeamColumn 519       557       558       0.0218    2.10E+11  7.99E-04  $LNTrans;
element elasticBeamColumn 520       558       559       0.0218    2.10E+11  7.99E-04  $LNTrans;
element elasticBeamColumn 521       559       560       0.0218    2.10E+11  7.99E-04  $LNTrans;
element elasticBeamColumn 522       85        561       0.0218    2.10E+11  7.99E-04  $LNTrans;
element elasticBeamColumn 523       561       562       0.0218    2.10E+11  7.99E-04  $LNTrans;
element elasticBeamColumn 524       562       563       0.0218    2.10E+11  7.99E-04  $LNTrans;
element elasticBeamColumn 525       563       564       0.0218    2.10E+11  7.99E-04  $LNTrans;

#       y6

#       Top

element elasticBeamColumn 526       157       565       0.0218    2.10E+11  7.99E-04  $LNTrans;
element elasticBeamColumn 527       565       566       0.0218    2.10E+11  7.99E-04  $LNTrans;
element elasticBeamColumn 528       566       567       0.0218    2.10E+11  7.99E-04  $LNTrans;
element elasticBeamColumn 529       567       568       0.0218    2.10E+11  7.99E-04  $LNTrans;
element elasticBeamColumn 530       97        569       0.0218    2.10E+11  7.99E-04  $LNTrans;
element elasticBeamColumn 531       569       570       0.0218    2.10E+11  7.99E-04  $LNTrans;
element elasticBeamColumn 532       570       571       0.0218    2.10E+11  7.99E-04  $LNTrans;
element elasticBeamColumn 533       571       572       0.0218    2.10E+11  7.99E-04  $LNTrans;

#       Bottom

element elasticBeamColumn 534       157       573       0.0218    2.10E+11  7.99E-04  $LNTrans;
element elasticBeamColumn 535       573       574       0.0218    2.10E+11  7.99E-04  $LNTrans;
element elasticBeamColumn 536       574       575       0.0218    2.10E+11  7.99E-04  $LNTrans;
element elasticBeamColumn 537       575       576       0.0218    2.10E+11  7.99E-04  $LNTrans;
element elasticBeamColumn 538       97        577       0.0218    2.10E+11  7.99E-04  $LNTrans;
element elasticBeamColumn 539       577       578       0.0218    2.10E+11  7.99E-04  $LNTrans;
element elasticBeamColumn 540       578       579       0.0218    2.10E+11  7.99E-04  $LNTrans;
element elasticBeamColumn 541       579       580       0.0218    2.10E+11  7.99E-04  $LNTrans;

#       x4CL

#       y2

#       Top

element elasticBeamColumn 542       110       581       0.0218    2.10E+11  7.99E-04  $LNTrans;
element elasticBeamColumn 543       581       582       0.0218    2.10E+11  7.99E-04  $LNTrans;
element elasticBeamColumn 544       582       583       0.0218    2.10E+11  7.99E-04  $LNTrans;
element elasticBeamColumn 545       583       584       0.0218    2.10E+11  7.99E-04  $LNTrans;
element elasticBeamColumn 546       52        585       0.0218    2.10E+11  7.99E-04  $LNTrans;
element elasticBeamColumn 547       585       586       0.0218    2.10E+11  7.99E-04  $LNTrans;
element elasticBeamColumn 548       586       587       0.0218    2.10E+11  7.99E-04  $LNTrans;
element elasticBeamColumn 549       587       588       0.0218    2.10E+11  7.99E-04  $LNTrans;

#       Bottom

element elasticBeamColumn 550       110       589       0.0218    2.10E+11  7.99E-04  $LNTrans;
element elasticBeamColumn 551       589       590       0.0218    2.10E+11  7.99E-04  $LNTrans;
element elasticBeamColumn 552       590       591       0.0218    2.10E+11  7.99E-04  $LNTrans;
element elasticBeamColumn 553       591       592       0.0218    2.10E+11  7.99E-04  $LNTrans;
element elasticBeamColumn 554       52        593       0.0218    2.10E+11  7.99E-04  $LNTrans;
element elasticBeamColumn 555       593       594       0.0218    2.10E+11  7.99E-04  $LNTrans;
element elasticBeamColumn 556       594       595       0.0218    2.10E+11  7.99E-04  $LNTrans;
element elasticBeamColumn 557       595       596       0.0218    2.10E+11  7.99E-04  $LNTrans;

#       y3

#       Top

element elasticBeamColumn 558       122       597       0.0218    2.10E+11  7.99E-04  $LNTrans;
element elasticBeamColumn 559       597       598       0.0218    2.10E+11  7.99E-04  $LNTrans;
element elasticBeamColumn 560       598       599       0.0218    2.10E+11  7.99E-04  $LNTrans;
element elasticBeamColumn 561       599       600       0.0218    2.10E+11  7.99E-04  $LNTrans;
element elasticBeamColumn 562       64        601       0.0218    2.10E+11  7.99E-04  $LNTrans;
element elasticBeamColumn 563       601       602       0.0218    2.10E+11  7.99E-04  $LNTrans;
element elasticBeamColumn 564       602       603       0.0218    2.10E+11  7.99E-04  $LNTrans;
element elasticBeamColumn 565       603       604       0.0218    2.10E+11  7.99E-04  $LNTrans;
```

```
#       Bottom

element elasticBeamColumn 566       122       605       0.0218    2.10E+11  7.99E-04  $LNTrans;
element elasticBeamColumn 567       605       606       0.0218    2.10E+11  7.99E-04  $LNTrans;
element elasticBeamColumn 568       606       607       0.0218    2.10E+11  7.99E-04  $LNTrans;
element elasticBeamColumn 569       607       608       0.0218    2.10E+11  7.99E-04  $LNTrans;
element elasticBeamColumn 570       64        609       0.0218    2.10E+11  7.99E-04  $LNTrans;
element elasticBeamColumn 571       609       610       0.0218    2.10E+11  7.99E-04  $LNTrans;
element elasticBeamColumn 572       610       611       0.0218    2.10E+11  7.99E-04  $LNTrans;
element elasticBeamColumn 573       611       612       0.0218    2.10E+11  7.99E-04  $LNTrans;

#       y4

#       Top

element elasticBeamColumn 574       134       613       0.0218    2.10E+11  7.99E-04  $LNTrans;
element elasticBeamColumn 575       613       614       0.0218    2.10E+11  7.99E-04  $LNTrans;
element elasticBeamColumn 576       614       615       0.0218    2.10E+11  7.99E-04  $LNTrans;
element elasticBeamColumn 577       615       616       0.0218    2.10E+11  7.99E-04  $LNTrans;
element elasticBeamColumn 578       76        617       0.0218    2.10E+11  7.99E-04  $LNTrans;
element elasticBeamColumn 579       617       618       0.0218    2.10E+11  7.99E-04  $LNTrans;
element elasticBeamColumn 580       618       619       0.0218    2.10E+11  7.99E-04  $LNTrans;
element elasticBeamColumn 581       619       620       0.0218    2.10E+11  7.99E-04  $LNTrans;

#       Bottom

element elasticBeamColumn 582       134       621       0.0218    2.10E+11  7.99E-04  $LNTrans;
element elasticBeamColumn 583       621       622       0.0218    2.10E+11  7.99E-04  $LNTrans;
element elasticBeamColumn 584       622       623       0.0218    2.10E+11  7.99E-04  $LNTrans;
element elasticBeamColumn 585       623       624       0.0218    2.10E+11  7.99E-04  $LNTrans;
element elasticBeamColumn 586       76        625       0.0218    2.10E+11  7.99E-04  $LNTrans;
element elasticBeamColumn 587       625       626       0.0218    2.10E+11  7.99E-04  $LNTrans;
element elasticBeamColumn 588       626       627       0.0218    2.10E+11  7.99E-04  $LNTrans;
element elasticBeamColumn 589       627       628       0.0218    2.10E+11  7.99E-04  $LNTrans;

#       y5

#       Top

element elasticBeamColumn 590       146       629       0.0218    2.10E+11  7.99E-04  $LNTrans;
element elasticBeamColumn 591       629       630       0.0218    2.10E+11  7.99E-04  $LNTrans;
element elasticBeamColumn 592       630       631       0.0218    2.10E+11  7.99E-04  $LNTrans;
element elasticBeamColumn 593       631       632       0.0218    2.10E+11  7.99E-04  $LNTrans;
element elasticBeamColumn 594       88        633       0.0218    2.10E+11  7.99E-04  $LNTrans;
element elasticBeamColumn 595       633       634       0.0218    2.10E+11  7.99E-04  $LNTrans;
element elasticBeamColumn 596       634       635       0.0218    2.10E+11  7.99E-04  $LNTrans;
element elasticBeamColumn 597       635       636       0.0218    2.10E+11  7.99E-04  $LNTrans;

#       Bottom

element elasticBeamColumn 598       146       637       0.0218    2.10E+11  7.99E-04  $LNTrans;
element elasticBeamColumn 599       637       638       0.0218    2.10E+11  7.99E-04  $LNTrans;
element elasticBeamColumn 600       638       639       0.0218    2.10E+11  7.99E-04  $LNTrans;
element elasticBeamColumn 601       639       640       0.0218    2.10E+11  7.99E-04  $LNTrans;
element elasticBeamColumn 602       88        641       0.0218    2.10E+11  7.99E-04  $LNTrans;
element elasticBeamColumn 603       641       642       0.0218    2.10E+11  7.99E-04  $LNTrans;
element elasticBeamColumn 604       642       643       0.0218    2.10E+11  7.99E-04  $LNTrans;
element elasticBeamColumn 605       643       644       0.0218    2.10E+11  7.99E-04  $LNTrans;

#       y6

#       Top

element elasticBeamColumn 606       158       645       0.0218    2.10E+11  7.99E-04  $LNTrans;
element elasticBeamColumn 607       645       646       0.0218    2.10E+11  7.99E-04  $LNTrans;
element elasticBeamColumn 608       646       647       0.0218    2.10E+11  7.99E-04  $LNTrans;
element elasticBeamColumn 609       647       648       0.0218    2.10E+11  7.99E-04  $LNTrans;
element elasticBeamColumn 610       100       649       0.0218    2.10E+11  7.99E-04  $LNTrans;
element elasticBeamColumn 611       649       650       0.0218    2.10E+11  7.99E-04  $LNTrans;
element elasticBeamColumn 612       650       651       0.0218    2.10E+11  7.99E-04  $LNTrans;
element elasticBeamColumn 613       651       652       0.0218    2.10E+11  7.99E-04  $LNTrans;

#       Bottom

element elasticBeamColumn 614       158       653       0.0218    2.10E+11  7.99E-04  $LNTrans;
```

```
element elasticBeamColumn 615 653 654 0.0218 2.10E+11 7.99E-04 $LNTrans;
element elasticBeamColumn 616 654 655 0.0218 2.10E+11 7.99E-04 $LNTrans;
element elasticBeamColumn 617 655 656 0.0218 2.10E+11 7.99E-04 $LNTrans;
element elasticBeamColumn 618 100 657 0.0218 2.10E+11 7.99E-04 $LNTrans;
element elasticBeamColumn 619 657 658 0.0218 2.10E+11 7.99E-04 $LNTrans;
element elasticBeamColumn 620 658 659 0.0218 2.10E+11 7.99E-04 $LNTrans;
element elasticBeamColumn 621 659 660 0.0218 2.10E+11 7.99E-04 $LNTrans;
```

Define contact zero length elements

```
element zeroLength 622 182 186 -mat $ctTag1 -dir 1;
element zeroLength 623 183 187 -mat $ctTag1 -dir 1;
element zeroLength 624 184 188 -mat $ctTag1 -dir 1;
element zeroLength 625 190 194 -mat $ctTag1 -dir 1;
element zeroLength 626 191 195 -mat $ctTag1 -dir 1;
element zeroLength 627 192 196 -mat $ctTag1 -dir 1;
element zeroLength 628 198 202 -mat $ctTag2 -dir 1;
element zeroLength 629 199 203 -mat $ctTag2 -dir 1;
element zeroLength 630 200 204 -mat $ctTag2 -dir 1;
element zeroLength 631 206 210 -mat $ctTag2 -dir 1;
element zeroLength 632 207 211 -mat $ctTag2 -dir 1;
element zeroLength 633 208 212 -mat $ctTag2 -dir 1;
element zeroLength 634 214 218 -mat $ctTag3 -dir 1;
element zeroLength 635 215 219 -mat $ctTag3 -dir 1;
element zeroLength 636 216 220 -mat $ctTag3 -dir 1;
element zeroLength 637 222 226 -mat $ctTag3 -dir 1;
element zeroLength 638 223 227 -mat $ctTag3 -dir 1;
element zeroLength 639 224 228 -mat $ctTag3 -dir 1;
element zeroLength 640 230 234 -mat $ctTag4 -dir 1;
element zeroLength 641 231 235 -mat $ctTag4 -dir 1;
element zeroLength 642 232 236 -mat $ctTag4 -dir 1;
element zeroLength 643 238 242 -mat $ctTag4 -dir 1;
element zeroLength 644 239 243 -mat $ctTag4 -dir 1;
element zeroLength 645 240 244 -mat $ctTag4 -dir 1;
element zeroLength 646 246 250 -mat $ctTag5 -dir 1;
element zeroLength 647 247 251 -mat $ctTag5 -dir 1;
element zeroLength 648 248 252 -mat $ctTag5 -dir 1;
element zeroLength 649 254 258 -mat $ctTag5 -dir 1;
element zeroLength 650 255 259 -mat $ctTag5 -dir 1;
element zeroLength 651 256 260 -mat $ctTag5 -dir 1;
element zeroLength 652 266 262 -mat $ctTag1 -dir 1;
element zeroLength 653 267 263 -mat $ctTag1 -dir 1;
element zeroLength 654 268 264 -mat $ctTag1 -dir 1;
element zeroLength 655 274 270 -mat $ctTag1 -dir 1;
element zeroLength 656 275 271 -mat $ctTag1 -dir 1;
element zeroLength 657 276 272 -mat $ctTag1 -dir 1;
element zeroLength 658 282 278 -mat $ctTag2 -dir 1;
element zeroLength 659 283 279 -mat $ctTag2 -dir 1;
element zeroLength 660 284 280 -mat $ctTag2 -dir 1;
element zeroLength 661 290 286 -mat $ctTag2 -dir 1;
element zeroLength 662 291 287 -mat $ctTag2 -dir 1;
element zeroLength 663 292 288 -mat $ctTag2 -dir 1;
element zeroLength 664 298 294 -mat $ctTag3 -dir 1;
element zeroLength 665 299 295 -mat $ctTag3 -dir 1;
element zeroLength 666 300 296 -mat $ctTag3 -dir 1;
element zeroLength 667 306 302 -mat $ctTag3 -dir 1;
element zeroLength 668 307 303 -mat $ctTag3 -dir 1;
element zeroLength 669 308 304 -mat $ctTag3 -dir 1;
element zeroLength 670 314 310 -mat $ctTag4 -dir 1;
element zeroLength 671 315 311 -mat $ctTag4 -dir 1;
element zeroLength 672 316 312 -mat $ctTag4 -dir 1;
element zeroLength 673 322 318 -mat $ctTag4 -dir 1;
element zeroLength 674 323 319 -mat $ctTag4 -dir 1;
element zeroLength 675 324 320 -mat $ctTag4 -dir 1;
element zeroLength 676 330 326 -mat $ctTag5 -dir 1;
element zeroLength 677 331 327 -mat $ctTag5 -dir 1;
element zeroLength 678 332 328 -mat $ctTag5 -dir 1;
element zeroLength 679 338 334 -mat $ctTag5 -dir 1;
element zeroLength 680 339 335 -mat $ctTag5 -dir 1;
element zeroLength 681 340 336 -mat $ctTag5 -dir 1;
element zeroLength 682 342 346 -mat $ctTag1 -dir 1;
element zeroLength 683 343 347 -mat $ctTag1 -dir 1;
element zeroLength 684 344 348 -mat $ctTag1 -dir 1;
element zeroLength 685 350 354 -mat $ctTag1 -dir 1;
```

```
element zeroLength 686 351 355 -mat $ctTag1 -dir 1;
element zeroLength 687 352 356 -mat $ctTag1 -dir 1;
element zeroLength 688 358 362 -mat $ctTag2 -dir 1;
element zeroLength 689 359 363 -mat $ctTag2 -dir 1;
element zeroLength 690 360 364 -mat $ctTag2 -dir 1;
element zeroLength 691 366 370 -mat $ctTag2 -dir 1;
element zeroLength 692 367 371 -mat $ctTag2 -dir 1;
element zeroLength 693 368 372 -mat $ctTag2 -dir 1;
element zeroLength 694 374 378 -mat $ctTag3 -dir 1;
element zeroLength 695 375 379 -mat $ctTag3 -dir 1;
element zeroLength 696 376 380 -mat $ctTag3 -dir 1;
element zeroLength 697 382 386 -mat $ctTag3 -dir 1;
element zeroLength 698 383 387 -mat $ctTag3 -dir 1;
element zeroLength 699 384 388 -mat $ctTag3 -dir 1;
element zeroLength 700 390 394 -mat $ctTag4 -dir 1;
element zeroLength 701 391 395 -mat $ctTag4 -dir 1;
element zeroLength 702 392 396 -mat $ctTag4 -dir 1;
element zeroLength 703 398 402 -mat $ctTag4 -dir 1;
element zeroLength 704 399 403 -mat $ctTag4 -dir 1;
element zeroLength 705 400 404 -mat $ctTag4 -dir 1;
element zeroLength 706 406 410 -mat $ctTag5 -dir 1;
element zeroLength 707 407 411 -mat $ctTag5 -dir 1;
element zeroLength 708 408 412 -mat $ctTag5 -dir 1;
element zeroLength 709 414 418 -mat $ctTag5 -dir 1;
element zeroLength 710 415 419 -mat $ctTag5 -dir 1;
element zeroLength 711 416 420 -mat $ctTag5 -dir 1;
element zeroLength 712 426 422 -mat $ctTag1 -dir 1;
element zeroLength 713 427 423 -mat $ctTag1 -dir 1;
element zeroLength 714 428 424 -mat $ctTag1 -dir 1;
element zeroLength 715 434 430 -mat $ctTag1 -dir 1;
element zeroLength 716 435 431 -mat $ctTag1 -dir 1;
element zeroLength 717 436 432 -mat $ctTag1 -dir 1;
element zeroLength 718 442 438 -mat $ctTag2 -dir 1;
element zeroLength 719 443 439 -mat $ctTag2 -dir 1;
element zeroLength 720 444 440 -mat $ctTag2 -dir 1;
element zeroLength 721 450 446 -mat $ctTag2 -dir 1;
element zeroLength 722 451 447 -mat $ctTag2 -dir 1;
element zeroLength 723 452 448 -mat $ctTag2 -dir 1;
element zeroLength 724 458 454 -mat $ctTag3 -dir 1;
element zeroLength 725 459 455 -mat $ctTag3 -dir 1;
element zeroLength 726 460 456 -mat $ctTag3 -dir 1;
element zeroLength 727 466 462 -mat $ctTag3 -dir 1;
element zeroLength 728 467 463 -mat $ctTag3 -dir 1;
element zeroLength 729 468 464 -mat $ctTag3 -dir 1;
element zeroLength 730 474 470 -mat $ctTag4 -dir 1;
element zeroLength 731 475 471 -mat $ctTag4 -dir 1;
element zeroLength 732 476 472 -mat $ctTag4 -dir 1;
element zeroLength 733 482 478 -mat $ctTag4 -dir 1;
element zeroLength 734 483 479 -mat $ctTag4 -dir 1;
element zeroLength 735 484 480 -mat $ctTag4 -dir 1;
element zeroLength 736 490 486 -mat $ctTag5 -dir 1;
element zeroLength 737 491 487 -mat $ctTag5 -dir 1;
element zeroLength 738 492 488 -mat $ctTag5 -dir 1;
element zeroLength 739 498 494 -mat $ctTag5 -dir 1;
element zeroLength 740 499 495 -mat $ctTag5 -dir 1;
element zeroLength 741 500 496 -mat $ctTag5 -dir 1;
element zeroLength 742 502 506 -mat $ctTag1 -dir 1;
element zeroLength 743 503 507 -mat $ctTag1 -dir 1;
element zeroLength 744 504 508 -mat $ctTag1 -dir 1;
element zeroLength 745 510 514 -mat $ctTag1 -dir 1;
element zeroLength 746 511 515 -mat $ctTag1 -dir 1;
element zeroLength 747 512 516 -mat $ctTag1 -dir 1;
element zeroLength 748 518 522 -mat $ctTag2 -dir 1;
element zeroLength 749 519 523 -mat $ctTag2 -dir 1;
element zeroLength 750 520 524 -mat $ctTag2 -dir 1;
element zeroLength 751 526 530 -mat $ctTag2 -dir 1;
element zeroLength 752 527 531 -mat $ctTag2 -dir 1;
element zeroLength 753 528 532 -mat $ctTag2 -dir 1;
element zeroLength 754 534 538 -mat $ctTag3 -dir 1;
element zeroLength 755 535 539 -mat $ctTag3 -dir 1;
element zeroLength 756 536 540 -mat $ctTag3 -dir 1;
element zeroLength 757 542 546 -mat $ctTag3 -dir 1;
element zeroLength 758 543 547 -mat $ctTag3 -dir 1;
element zeroLength 759 544 548 -mat $ctTag3 -dir 1;
element zeroLength 760 550 554 -mat $ctTag4 -dir 1;
```

```
element zeroLength 761 551 555 -mat $ctTag4 -dir 1;
element zeroLength 762 552 556 -mat $ctTag4 -dir 1;
element zeroLength 763 558 562 -mat $ctTag4 -dir 1;
element zeroLength 764 559 563 -mat $ctTag4 -dir 1;
element zeroLength 765 560 564 -mat $ctTag4 -dir 1;
element zeroLength 766 566 570 -mat $ctTag5 -dir 1;
element zeroLength 767 567 571 -mat $ctTag5 -dir 1;
element zeroLength 768 568 572 -mat $ctTag5 -dir 1;
element zeroLength 769 574 578 -mat $ctTag5 -dir 1;
element zeroLength 770 575 579 -mat $ctTag5 -dir 1;
element zeroLength 771 576 580 -mat $ctTag5 -dir 1;
element zeroLength 772 586 582 -mat $ctTag1 -dir 1;
element zeroLength 773 587 583 -mat $ctTag1 -dir 1;
element zeroLength 774 588 584 -mat $ctTag1 -dir 1;
element zeroLength 775 594 590 -mat $ctTag1 -dir 1;
element zeroLength 776 595 591 -mat $ctTag1 -dir 1;
element zeroLength 777 596 592 -mat $ctTag1 -dir 1;
element zeroLength 778 602 598 -mat $ctTag2 -dir 1;
element zeroLength 779 603 599 -mat $ctTag2 -dir 1;
element zeroLength 780 604 600 -mat $ctTag2 -dir 1;
element zeroLength 781 610 606 -mat $ctTag2 -dir 1;
element zeroLength 782 611 607 -mat $ctTag2 -dir 1;
element zeroLength 783 612 608 -mat $ctTag2 -dir 1;
element zeroLength 784 618 614 -mat $ctTag3 -dir 1;
element zeroLength 785 619 615 -mat $ctTag3 -dir 1;
element zeroLength 786 620 616 -mat $ctTag3 -dir 1;
element zeroLength 787 626 622 -mat $ctTag3 -dir 1;
element zeroLength 788 627 623 -mat $ctTag3 -dir 1;
element zeroLength 789 628 624 -mat $ctTag3 -dir 1;
element zeroLength 790 634 630 -mat $ctTag4 -dir 1;
element zeroLength 791 635 631 -mat $ctTag4 -dir 1;
element zeroLength 792 636 632 -mat $ctTag4 -dir 1;
element zeroLength 793 642 638 -mat $ctTag4 -dir 1;
element zeroLength 794 643 639 -mat $ctTag4 -dir 1;
element zeroLength 795 644 640 -mat $ctTag4 -dir 1;
element zeroLength 796 650 646 -mat $ctTag5 -dir 1;
element zeroLength 797 651 647 -mat $ctTag5 -dir 1;
element zeroLength 798 652 648 -mat $ctTag5 -dir 1;
element zeroLength 799 658 654 -mat $ctTag5 -dir 1;
element zeroLength 800 659 655 -mat $ctTag5 -dir 1;
element zeroLength 801 660 656 -mat $ctTag5 -dir 1;

# PT bars (Truss elements)

element truss 802 679 112 [expr 2*3.14*0.043*0.043/4] $PT1;
element truss 803 680 124 [expr 2*3.14*0.050*0.050/4] $PT2;
element truss 804 681 136 [expr 2*3.14*0.043*0.043/4] $PT3;
element truss 805 682 148 [expr 2*3.14*0.037*0.037/4] $PT4;
element truss 806 683 160 [expr 2*3.14*0.035*0.035/4] $PT5;

# Panel zones rotational springs (both for panel and flange)

element zeroLength 807 161 102 -mat $Spanel1 -dir 6;
element zeroLength 808 162 105 -mat $Spanel1 -dir 6;
element zeroLength 809 163 108 -mat $Spanel1 -dir 6;
element zeroLength 810 164 111 -mat $Spanel1 -dir 6;

element zeroLength 811 165 114 -mat $Spanel2 -dir 6;
element zeroLength 812 166 117 -mat $Spanel2 -dir 6;
element zeroLength 813 167 120 -mat $Spanel2 -dir 6;
element zeroLength 814 168 123 -mat $Spanel2 -dir 6;

element zeroLength 815 169 126 -mat $Spanel3 -dir 6;
element zeroLength 816 170 129 -mat $Spanel3 -dir 6;
element zeroLength 817 171 132 -mat $Spanel3 -dir 6;
element zeroLength 818 172 135 -mat $Spanel3 -dir 6;

element zeroLength 819 173 138 -mat $Spanel4 -dir 6;
element zeroLength 820 174 141 -mat $Spanel4 -dir 6;
element zeroLength 821 175 144 -mat $Spanel4 -dir 6;
element zeroLength 822 176 147 -mat $Spanel4 -dir 6;

element zeroLength 823 177 150 -mat $Spanel5 -dir 6;
element zeroLength 824 178 153 -mat $Spanel5 -dir 6;
element zeroLength 825 179 156 -mat $Spanel5 -dir 6;
```

```
element zeroLength 826 180 159 -mat $Spanel5 -dir 6;

element zeroLength 827 161 102 -mat $Sflange1 -dir 6;
element zeroLength 828 162 105 -mat $Sflange1 -dir 6;
element zeroLength 829 163 108 -mat $Sflange1 -dir 6;
element zeroLength 830 164 111 -mat $Sflange1 -dir 6;

element zeroLength 831 165 114 -mat $Sflange2 -dir 6;
element zeroLength 832 166 117 -mat $Sflange2 -dir 6;
element zeroLength 833 167 120 -mat $Sflange2 -dir 6;
element zeroLength 834 168 123 -mat $Sflange2 -dir 6;

element zeroLength 835 169 126 -mat $Sflange3 -dir 6;
element zeroLength 836 170 129 -mat $Sflange3 -dir 6;
element zeroLength 837 171 132 -mat $Sflange3 -dir 6;
element zeroLength 838 172 135 -mat $Sflange3 -dir 6;

element zeroLength 839 173 138 -mat $Sflange4 -dir 6;
element zeroLength 840 174 141 -mat $Sflange4 -dir 6;
element zeroLength 841 175 144 -mat $Sflange4 -dir 6;
element zeroLength 842 176 147 -mat $Sflange4 -dir 6;

element zeroLength 843 177 150 -mat $Sflange5 -dir 6;
element zeroLength 844 178 153 -mat $Sflange5 -dir 6;
element zeroLength 845 179 156 -mat $Sflange5 -dir 6;
element zeroLength 846 180 159 -mat $Sflange5 -dir 6;

# WHPs (Translational springs)

element zeroLength 847 181 185 -mat $whpTag1 -dir 1;
element zeroLength 848 189 193 -mat $whpTag1 -dir 1;
element zeroLength 849 197 201 -mat $whpTag2 -dir 1;
element zeroLength 850 205 209 -mat $whpTag2 -dir 1;
element zeroLength 851 213 217 -mat $whpTag3 -dir 1;
element zeroLength 852 221 225 -mat $whpTag3 -dir 1;
element zeroLength 853 229 233 -mat $whpTag4 -dir 1;
element zeroLength 854 237 241 -mat $whpTag4 -dir 1;
element zeroLength 855 245 249 -mat $whpTag5 -dir 1;
element zeroLength 856 253 257 -mat $whpTag5 -dir 1;
element zeroLength 857 265 261 -mat $whpTag1 -dir 1;
element zeroLength 858 273 269 -mat $whpTag1 -dir 1;
element zeroLength 859 281 277 -mat $whpTag2 -dir 1;
element zeroLength 860 289 285 -mat $whpTag2 -dir 1;
element zeroLength 861 297 293 -mat $whpTag3 -dir 1;
element zeroLength 862 305 301 -mat $whpTag3 -dir 1;
element zeroLength 863 313 309 -mat $whpTag4 -dir 1;
element zeroLength 864 321 317 -mat $whpTag4 -dir 1;
element zeroLength 865 329 325 -mat $whpTag5 -dir 1;
element zeroLength 866 337 333 -mat $whpTag5 -dir 1;
element zeroLength 867 341 345 -mat $whpTag1 -dir 1;
element zeroLength 868 349 353 -mat $whpTag1 -dir 1;
element zeroLength 869 357 361 -mat $whpTag2 -dir 1;
element zeroLength 870 365 369 -mat $whpTag2 -dir 1;
element zeroLength 871 373 377 -mat $whpTag3 -dir 1;
element zeroLength 872 381 385 -mat $whpTag3 -dir 1;
element zeroLength 873 389 393 -mat $whpTag4 -dir 1;
element zeroLength 874 397 401 -mat $whpTag4 -dir 1;
element zeroLength 875 405 409 -mat $whpTag5 -dir 1;
element zeroLength 876 413 417 -mat $whpTag5 -dir 1;
element zeroLength 877 425 421 -mat $whpTag1 -dir 1;
element zeroLength 878 433 429 -mat $whpTag1 -dir 1;
element zeroLength 879 441 437 -mat $whpTag2 -dir 1;
element zeroLength 880 449 445 -mat $whpTag2 -dir 1;
element zeroLength 881 457 453 -mat $whpTag3 -dir 1;
element zeroLength 882 465 461 -mat $whpTag3 -dir 1;
element zeroLength 883 473 469 -mat $whpTag4 -dir 1;
element zeroLength 884 481 477 -mat $whpTag4 -dir 1;
element zeroLength 885 489 485 -mat $whpTag5 -dir 1;
element zeroLength 886 497 493 -mat $whpTag5 -dir 1;
element zeroLength 887 501 505 -mat $whpTag1 -dir 1;
element zeroLength 888 509 513 -mat $whpTag1 -dir 1;
element zeroLength 889 517 521 -mat $whpTag2 -dir 1;
element zeroLength 890 525 529 -mat $whpTag2 -dir 1;
element zeroLength 891 533 537 -mat $whpTag3 -dir 1;
element zeroLength 892 541 545 -mat $whpTag3 -dir 1;
```

```
element zeroLength 893 549 553 -mat $whpTag4 -dir 1;
element zeroLength 894 557 561 -mat $whpTag4 -dir 1;
element zeroLength 895 565 569 -mat $whpTag5 -dir 1;
element zeroLength 896 573 577 -mat $whpTag5 -dir 1;
element zeroLength 897 585 581 -mat $whpTag1 -dir 1;
element zeroLength 898 593 589 -mat $whpTag1 -dir 1;
element zeroLength 899 601 597 -mat $whpTag2 -dir 1;
element zeroLength 900 609 605 -mat $whpTag2 -dir 1;
element zeroLength 901 617 613 -mat $whpTag3 -dir 1;
element zeroLength 902 625 621 -mat $whpTag3 -dir 1;
element zeroLength 903 633 629 -mat $whpTag4 -dir 1;
element zeroLength 904 641 637 -mat $whpTag4 -dir 1;
element zeroLength 905 649 645 -mat $whpTag5 -dir 1;
element zeroLength 906 657 653 -mat $whpTag5 -dir 1;

# Lean on columns elements

set AL1 [expr 8*0.0106/3];
set IL1 [expr 8*0.00011260/3];

set AL2 [expr 8*0.0091/3];
set IL2 [expr 8*0.00008091/3];

element elasticBeamColumn 907 661 662 $AL1 $E2 $IL1 $PDTrans;
element elasticBeamColumn 908 662 663 $AL1 $E2 $IL1 $PDTrans;
element elasticBeamColumn 909 663 664 $AL1 $E2 $IL1 $PDTrans;
element elasticBeamColumn 910 664 665 $AL2 $E2 $IL2 $PDTrans;
element elasticBeamColumn 911 665 666 $AL2 $E2 $IL2 $PDTrans;

element elasticBeamColumn 912 667 668 $AL1 $E2 $IL1 $PDTrans;
element elasticBeamColumn 913 668 669 $AL1 $E2 $IL1 $PDTrans;
element elasticBeamColumn 914 669 670 $AL1 $E2 $IL1 $PDTrans;
element elasticBeamColumn 915 670 671 $AL2 $E2 $IL2 $PDTrans;
element elasticBeamColumn 916 671 672 $AL2 $E2 $IL2 $PDTrans;

element elasticBeamColumn 917 673 674 $AL1 $E2 $IL1 $PDTrans;
element elasticBeamColumn 918 674 675 $AL1 $E2 $IL1 $PDTrans;
element elasticBeamColumn 919 675 676 $AL1 $E2 $IL1 $PDTrans;
element elasticBeamColumn 920 676 677 $AL2 $E2 $IL2 $PDTrans;
element elasticBeamColumn 921 677 678 $AL2 $E2 $IL2 $PDTrans;

# Lignos elements

element zeroLength 922 42 684 -mat $lignos1 -dir 6;
element zeroLength 923 685 43 -mat $lignos1 -dir 6;
element zeroLength 924 46 686 -mat $lignos1 -dir 6;
element zeroLength 925 687 47 -mat $lignos1 -dir 6;
element zeroLength 926 50 688 -mat $lignos1 -dir 6;
element zeroLength 927 689 51 -mat $lignos1 -dir 6;
element zeroLength 928 54 690 -mat $lignos2 -dir 6;
element zeroLength 929 691 55 -mat $lignos2 -dir 6;
element zeroLength 930 58 692 -mat $lignos2 -dir 6;
element zeroLength 931 693 59 -mat $lignos2 -dir 6;
element zeroLength 932 62 694 -mat $lignos2 -dir 6;
element zeroLength 933 695 63 -mat $lignos2 -dir 6;
element zeroLength 934 66 696 -mat $lignos3 -dir 6;
element zeroLength 935 697 67 -mat $lignos3 -dir 6;
element zeroLength 936 70 698 -mat $lignos3 -dir 6;
element zeroLength 937 699 71 -mat $lignos3 -dir 6;
element zeroLength 938 74 700 -mat $lignos3 -dir 6;
element zeroLength 939 701 75 -mat $lignos3 -dir 6;
element zeroLength 940 78 702 -mat $lignos4 -dir 6;
element zeroLength 941 703 79 -mat $lignos4 -dir 6;
element zeroLength 942 82 704 -mat $lignos4 -dir 6;
element zeroLength 943 705 83 -mat $lignos4 -dir 6;
element zeroLength 944 86 706 -mat $lignos4 -dir 6;
element zeroLength 945 707 87 -mat $lignos4 -dir 6;
element zeroLength 946 90 708 -mat $lignos5 -dir 6;
element zeroLength 947 709 91 -mat $lignos5 -dir 6;
element zeroLength 948 94 710 -mat $lignos5 -dir 6;
element zeroLength 949 711 95 -mat $lignos5 -dir 6;
element zeroLength 950 98 712 -mat $lignos5 -dir 6;
element zeroLength 951 713 99 -mat $lignos5 -dir 6;

# Recorder definition for the axial forces on the PT bars
```

```
recorder Element -file FStrand.out -ele 802 803 804 805 806 force;

# Application of Vertical loads

pattern Plain 1 Linear {
load    161     0       -126.2      0;
load    162     0       -67.20      0;
load    163     0       -67.20      0;
load    164     0       -126.2      0;
load    165     0       -112.76     0;
load    166     0       -53.76      0;
load    167     0       -53.76      0;
load    168     0       -112.76     0;
load    169     0       -112.76     0;
load    170     0       -53.76      0;
load    171     0       -53.76      0;
load    172     0       -112.76     0;
load    173     0       -112.76     0;
load    174     0       -53.76      0;
load    175     0       -53.76      0;
load    176     0       -112.76     0;
load    177     0       -112.76     0;
load    178     0       -53.76      0;
load    179     0       -53.76      0;
load    180     0       -112.76     0;

load    42      0       [expr -14.75*(8-$dc1)/2]        0;
load    43      0       [expr -14.75*(8-$dc1)/2]        0;
load    46      0       [expr -14.75*(8-$dc1)/2]        0;
load    47      0       [expr -14.75*(8-$dc1)/2]        0;
load    50      0       [expr -14.75*(8-$dc1)/2]        0;
load    51      0       [expr -14.75*(8-$dc1)/2]        0;

load    54      0       [expr -14.75*(8-$dc1)/2]        0;
load    55      0       [expr -14.75*(8-$dc1)/2]        0;
load    58      0       [expr -14.75*(8-$dc1)/2]        0;
load    59      0       [expr -14.75*(8-$dc1)/2]        0;
load    62      0       [expr -14.75*(8-$dc1)/2]        0;
load    63      0       [expr -14.75*(8-$dc1)/2]        0;

load    66      0       [expr -14.75*(8-$dc1)/2]        0;
load    67      0       [expr -14.75*(8-$dc1)/2]        0;
load    70      0       [expr -14.75*(8-$dc1)/2]        0;
load    71      0       [expr -14.75*(8-$dc1)/2]        0;
load    74      0       [expr -14.75*(8-$dc1)/2]        0;
load    75      0       [expr -14.75*(8-$dc1)/2]        0;

load    78      0       [expr -14.75*(8-$dc2)/2]        0;
load    79      0       [expr -14.75*(8-$dc2)/2]        0;
load    82      0       [expr -14.75*(8-$dc2)/2]        0;
load    83      0       [expr -14.75*(8-$dc2)/2]        0;
load    86      0       [expr -14.75*(8-$dc2)/2]        0;
load    87      0       [expr -14.75*(8-$dc2)/2]        0;

load    90      0       [expr -14.75*(8-$dc2)/2]        0;
load    91      0       [expr -14.75*(8-$dc2)/2]        0;
load    94      0       [expr -14.75*(8-$dc2)/2]        0;
load    95      0       [expr -14.75*(8-$dc2)/2]        0;
load    98      0       [expr -14.75*(8-$dc2)/2]        0;
load    99      0       [expr -14.75*(8-$dc2)/2]        0;

load    662     0       [expr -1491.27/3]       0;
load    663     0       [expr -1452.62/3]       0;
load    664     0       [expr -1452.62/3]       0;
load    665     0       [expr -1452.62/3]       0;
load    666     0       [expr -1452.62/3]       0;
load    668     0       [expr -1491.27/3]       0;
load    669     0       [expr -1452.62/3]       0;
load    670     0       [expr -1452.62/3]       0;
load    671     0       [expr -1452.62/3]       0;
load    672     0       [expr -1452.62/3]       0;
load    674     0       [expr -1491.27/3]       0;
load    675     0       [expr -1452.62/3]       0;
load    676     0       [expr -1452.62/3]       0;
```

```
load      677       0         [expr -1452.62/3]     0;
load      678       0         [expr -1452.62/3]     0;
}

constraints Transformation;
numberer RCM;
system BandGeneral;
analysis Static;
test NormDispIncr 1.0e-4 400 1;
algorithm Newton;
integrator LoadControl 1; analyze 1;
loadConst -time 0.0;          # hold gravity constant and restart time

# Instert trusses simulating diaphragmatic action (after the application of vertical loads)

element truss     957       41        662       4.269285714       $Diaph;
element truss     958       42        662       4.490077551       $Diaph;
element truss     959       43        662       5.338493878       $Diaph;
element truss     960       44        662       5.559285714       $Diaph;
element truss     961       45        668       4.269285714       $Diaph;
element truss     962       46        668       4.490077551       $Diaph;
element truss     963       47        668       5.338493878       $Diaph;
element truss     964       48        668       5.559285714       $Diaph;
element truss     965       49        674       4.269285714       $Diaph;
element truss     966       50        674       4.490077551       $Diaph;
element truss     967       51        674       5.338493878       $Diaph;
element truss     968       52        674       5.559285714       $Diaph;
element truss     969       53        663       4.997380952       $Diaph;
element truss     970       54        663       5.297531973       $Diaph;
element truss     971       55        663       6.207229932       $Diaph;
element truss     972       56        663       6.507380952       $Diaph;
element truss     973       57        669       4.997380952       $Diaph;
element truss     974       58        669       5.297531973       $Diaph;
element truss     975       59        669       6.207229932       $Diaph;
element truss     976       60        669       6.507380952       $Diaph;
element truss     977       61        675       4.997380952       $Diaph;
element truss     978       62        675       5.297531973       $Diaph;
element truss     979       63        675       6.207229932       $Diaph;
element truss     980       64        675       6.507380952       $Diaph;
element truss     981       65        664       4.269285714       $Diaph;
element truss     982       66        664       4.499379592       $Diaph;
element truss     983       67        664       5.329191837       $Diaph;
element truss     984       68        664       5.559285714       $Diaph;
element truss     985       69        670       4.269285714       $Diaph;
element truss     986       70        670       4.499379592       $Diaph;
element truss     987       71        670       5.329191837       $Diaph;
element truss     988       72        670       5.559285714       $Diaph;
element truss     989       73        676       4.269285714       $Diaph;
element truss     990       74        676       4.499379592       $Diaph;
element truss     991       75        676       5.329191837       $Diaph;
element truss     992       76        676       5.559285714       $Diaph;
element truss     993       77        665       3.677837838       $Diaph;
element truss     994       78        665       3.840237838       $Diaph;
element truss     995       79        665       4.635437838       $Diaph;
element truss     996       80        665       4.797837838       $Diaph;
element truss     997       81        671       3.677837838       $Diaph;
element truss     998       82        671       3.840237838       $Diaph;
element truss     999       83        671       4.635437838       $Diaph;
element truss     1000      84        671       4.797837838       $Diaph;
element truss     1001      85        677       3.677837838       $Diaph;
element truss     1002      86        677       3.840237838       $Diaph;
element truss     1003      87        677       4.635437838       $Diaph;
element truss     1004      88        677       4.797837838       $Diaph;
element truss     1005      89        666       3.677837838       $Diaph;
element truss     1006      90        666       3.787416216       $Diaph;
element truss     1007      91        666       4.688259459       $Diaph;
element truss     1008      92        666       4.797837838       $Diaph;
element truss     1009      93        672       3.677837838       $Diaph;
element truss     1010      94        672       3.787416216       $Diaph;
element truss     1011      95        672       4.688259459       $Diaph;
element truss     1012      96        672       4.797837838       $Diaph;
element truss     1013      97        678       3.677837838       $Diaph;
element truss     1014      98        678       3.300317852       $Diaph;
element truss     1015      99        678       4.126259329       $Diaph;
element truss     1016      100       678       4.207288591       $Diaph;
```

```
# Recorder definition for floors diplacements

recorder Node -file displ.out -time -node 188 189 190 191 192 -dof 1 disp;

# Pushover loading

pattern Plain 2 Linear {
load 662  4.00 0 0;
load 663  7.20 0 0;
load 664  10.4 0 0;
load 665  13.6 0 0;
load 666  16.8 0 0;
load 668  4.00 0 0;
load 669  7.20 0 0;
load 670  10.4 0 0;
load 671  13.6 0 0;
load 672  16.8 0 0;
load 674  4.00 0 0;
load 675  7.20 0 0;
load 676  10.4 0 0;
load 677  13.6 0 0;
load 678  16.8 0 0;
}

constraints Transformation;
numberer RCM;
system BandGeneral;
analysis Static;
test NormDispIncr 1.0e-6 700 1;
algorithm Newton -initial;

integrator DisplacementControl 672 1 +0.0004; analyze 427;
```

Annex B. Matlab code for incremental dynamic analysis (IDA)

```
%% IDA - Multiple ground motion analysis
% Written by Angelos Tzimas & Nasos Dimopoulos

clear all
close all
clc



%% Ground Motion Characteristics

    name1='DT_STEPS.txt';              % time step dt and numberr of steps of each
ground motions
    str109=sprintf('%s',name1);

    x_dt_s=load(str109);

    Sa_T=load ('v100mrf_sa_T1.txt');     % Sa at the fundamental period of each
seismic excitation - Sa(Ti) in m/s2

    fclose('all');

    clear name1 str109

%% IDA - Loop through ground motions

    SF=1; % Scale factor

    Mult=[1 10 20 50 100 500 1000];      % Intervals of each time step


for i=1:44                    % Quakes (= 91)

   Sd=0;                    % Index that shows The factor that reduces the time step
intervals

   k101=0;

   for z2=0.02:0.02:20        % Sa_target steps in g

      k101=k101+1;

      name2='Quake';
      FILE1=sprintf('%s%d.txt',name2,i);

      dt=x_dt_s(i,1);
      points=round(x_dt_s(i,2));
```

```
        SF=z2*9.81/Sa_T(i);                 % Scaling factor of the curent Sa_target =
z2, in g

        if Sd>0
           Sd=Sd-1;
        else
           Sd=0;
        end

        for klp=1:length(Mult)

           Sd=Sd+1;
           incr=round(Mult(Sd)+0.00001);

           [ok]=MotionD(incr,SF,points,dt,FILE1,i);    % Run OpenSees - Return ok
variable, which indicates if the analysis was successful

           if ok==0, break, end
           if (ok~=0) & (Sd==length(Mult)), break, end

        end

        if ok<0 | ok>0

              check_Run1=1.0;           % Not successful

              IDR_max(k101,5)=0;        % Maximum IDR for various seismic
intensities SF
              Roof_Drift_max(k101,1)=0;  % Maximum roof IDR for various seismic
intensities SF
              R_Roof_Drift(k101,1)=0;    % Residual roof IDR for various seismic
intensities SF
              R_floor_IDR(k101,5)=0;     % Residual floor IDR for various seismic
intensities SF
              Accel(k101,5)=0;          % Maximum floor acceleration for various
seismic intensities SF
              Base_Shear(k101,1)=0;      % Base Shear (kN) for various seismic
intensities SF

        else

              str1=sprintf('disp_%d.out',i);
              fid1=fopen(str1,'r');
              n_lines=0;

              while 15
                 tline = fgetl(fid1);
                 if ~ischar(tline),   break,   end
```

```
            n_lines=n_lines+1;              % Number of lines
        end

        fclose(fid1);
        clear tline str1 fid1

        check_Run1=0.0;


[A1,A2,A3,A4,A5,A6]=Scan_Results_Last_Fast(dt,n_lines,Sd,i,check_Run1,incr);

        IDR_max(k101,:)=A1;         % Maximum IDR for various seismic
intensities SF
        Roof_Drift_max(k101,1)=A4;  % Maximum roof IDR for various seismic
intensities SF
        R_Roof_Drift(k101,1)=A3;    % Residual roof IDR for various seismic
intensities SF
        R_floor_IDR(k101,:)=A2;     % Residual floor IDR for various seismic
intensities SF
        Accel(k101,:)=A5;           % Maximum floor acceleration for various
seismic intensities SF
        Base_Shear(k101,1)=A6;      % Base Shear (kN) for various seismic
intensities SF
    end




    kk=k101;
    SF_LINES(kk,1)=z2;              % Sa_Target = z2, in g
    SF_LINES(kk,2)=n_lines;
    SF_LINES(kk,3)=Sd;

    if kk<2
       IDR11=max(IDR_max(1,:));          % Maximum IDR of the 1st step
       Slope_I=SF_LINES(1,1)/IDR11;      % Initial slope
       IDR22(1,1)=IDR11;
       Check_Slope(kk,1)=1;
    else
       IDR22(kk,1)=(max(IDR_max(kk,:)));                    % Maximum
IDR of the current step
       Slope_C=(SF_LINES(kk,1)-SF_LINES((kk-1),1))/(IDR22(kk,1)-IDR22((kk-
1),1));  % Current slope
       Check_Slope(kk,1)=Slope_C/Slope_I;                   % Slope
    end

    if check_Run1==1.0, break, end
    if IDR11>0.15 | IDR22(kk)>0.15, break, end
    if Check_Slope(kk)<0.10 & Check_Slope(kk)>0, break, end
```

```
    end

    xlswrite(sprintf('Quake%d.xls',i),SF_LINES,'Sa_Lines')
    xlswrite(sprintf('Quake%d.xls',i),IDR_max,'IDR')
    xlswrite(sprintf('Quake%d.xls',i),Roof_Drift_max,'Roof_Drift')

    xlswrite(sprintf('Quake%d.xls',i),R_Roof_Drift,'R_Roof_Drift')
    xlswrite(sprintf('Quake%d.xls',i),R_floor_IDR,'R_Floor_Drift')
    xlswrite(sprintf('Quake%d.xls',i),Accel,'ABS_Accel')
    xlswrite(sprintf('Quake%d.xls',i),Base_Shear,'Shear')
    xlswrite(sprintf('Quake%d.xls',i),Check_Slope,'Slope_Ratio')

    clear SF_LINES IDR_max Roof_Drift_max R_Roof_Drift R_floor_IDR Accel
Local_d Base_Shear Check_Slope

end


    LINP_Anal_sec = fopen('Anal_sec.txt','r');
    %Anal_sec = fgets(LINP_Anal_sec)
    Anal_sec = fscanf(LINP_Anal_sec,'%f',1);
    fclose(LINP_Anal_sec)
    delete('Anal_sec.txt');
    analisis_sec(i,1)=Anal_sec;

    LINP_TIMEE = fopen('Timee.txt','r');
    Timee(i,1) = fscanf(LINP_TIMEE,'%f',1);
    fclose(LINP_TIMEE)
    delete('Timee.txt');


% save ('Check_Run.txt','check_Run1','-ascii');
```